**Fermilab**

THE UNIVERSITY OF CHICAGO

THE SEARCH FOR THE DECAYS $K_L \to \pi^0 \ell^+ \ell^-$

A DISSERTATION SUBMITTED TO

THE FACULTY OF THE DIVISION OF THE PHYSICAL SCIENCES

IN CANDIDACY FOR THE DEGREE OF

DOCTOR OF PHILOSOPHY

DEPARTMENT OF PHYSICS

BY

DEBORAH APPEL HARRIS

CHICAGO, ILLINOIS

JUNE 1994

# Acknowledgements

Although there is only one name on the cover of this document, the work and influence of many different people are represented in its pages. Unfortunately, space does not allow their names to be on the cover, but at least I can thank these people here, which is, after all, not too far from the front.

First of all, I would like to thank my advisor Yau Wai Wah for his continuous support and enthusiasm for my work. I thank Bruce Winstein for his exacting and critical eye, and for stressing the importance of clear explanations, without which I might not have ever finished a sentence in a public presentation.

I am indebted to all of my colleagues on experiment E799 who have taken part in the struggles of taking data, splitting it, stripping it, crunching it, and all those other violent-sounding processes that can fill a few years. In particular, I would like to thank Bernhard Schwingenheuer for his kindness, patience, and willingness to share his linguistic expertise. I thank Roy A. Briere for ensuring that I leave Chicago knowing what a precision measurement is. I thank Bob Tschirhart for his generosity and his minimum ionizing help, without which this thesis would be only half of what it is now. I thank Sunil V. Somalwar for many interesting discussions about matters political and otherwise, and a fair number of good sets.

Special thanks go to Richard Armstrong, who kept the Barium Fluoride efforts based in reality, and who renewed my appreciation of thoughtful mechanical design. I would also like to thank Hitoshi Yamamoto for his fine introduction into the world of high-resolution calorimetry, and his crystal legacy.

To my friends who remind me that not all physicists are in high energy physics, I give thanks. To Mark Abney for his inspired devotion to keeping the body healthy as well as the mind, to Arthur Kosowsky for his appreciation of the finer things in life, to Monica Tecchio for her pronunciation of the word "please", to Jim Amundson for being a theorist

who knows experiments. To my friends who remind me that not all people are physicists, and have listened to my trials and tribulations with extremely sympathetic and partial ears: Nancy Billings, Chana Monyek, Elizabeth McSweeney, Theresa Brown, and Jaimie Yeh, I owe you all the remains of my sanity.

For his mysterious abilities to listen critically while always being on my side, to wield a spray-paint can with flair, to inspire both laughter and poetry in exhausted souls, and to reach Starbucks in a single bound, I am indebted to Kevin Scott McFarland-Porter as both a collaborator [1] and a friend. It has been both a privilege and a pleasure to play Rosencrantz to your Guildenstern.

For commuting at least two hours a day for over four and a half years, just so he could suffer all the abuse and neglect that he knows graduate students are capable of, including totally inadequate thanks in thesis acknowlegements, I thank my wonderful husband, Robert Mendy Harris.

Finally, I could not be writing these acknowlegements today without the love, encouragement, and fashion consultation of my parents, Marjorie Ruth Appel and Jeffrey Alan Appel. No words I can write here would even approach the level of thanks that I owe them.

# THE FNAL-E799 COLLABORATION

Katsushi Arisaka, Doug Roberts, William Slater, Matt Spencer, Matt Weaver
*University of California at Los Angeles*

Roy Briere, Elliott Cheu, Deborah Harris, Pat Krolak, Greg Makoff, Kevin McFarland,
Aaron Roodman, Bernhard Schwingenheuer, Yau Wah, Bruce Winstein, Roland Winston
*University of Chicago and The Enrico Fermi Institute*

Tony Barker
*University of Colorado*

Earl Swallow
*Elmhurst College and The Enrico Fermi Institute*

Greg Bock, Rick Coleman, Mike Crisler, Janice Enagonio, Rick Ford, Yee Bob Hsiung,
Doug Jensen, Erik Ramberg, Bob Tschirhart
*Fermi National Accelerator Laboratory*

Eric Collins, George Gollin
*University of Illinois*

Tsuyoshi Nakaya, Taku Yamanaka
*Osaka University*

Peter Haas, William P. Hogan, Sunkee Kim, John N. Matthews, Seong Sook Myung, Ping Gu,
Steve Schnetzer, Sunil Somalwar, Gordon Thomson, Yu Zou
*Rutgers University*

# TABLE OF CONTENTS

# LIST OF TABLES

# LIST OF ILLUSTRATIONS

xiii

For Marchou and le Foie

# ABSTRACT

This thesis describes the search for the decays $K_L \to \pi^0 \ell^+ \ell^-$ carried out by the E799 experiment at the Fermi National Accelerator Laboratory (Fermilab). The largest contribution to these decay modes is expected to be CP-violating and a measurement of the branching ratio could either confirm the mecanisms of CP-violation in the Standard Model or point to new physics. No such events were seen and we determine the following 90% confidence level upper limits:

$$BR(K_L \to \pi^0 e^+ e^-) < 4.3 \times 10^{-9}$$

and

$$BR(K_L \to \pi^0 \mu^+ \mu^-) < 5.1 \times 10^{-9}.$$

This experiment represents the most sensitive search performed thus far for either of these modes.

# CHAPTER 1

# INTRODUCTION

"We have no clear idea of what the hell is going on"—*Roberto Peccei, "Open Questions in CP Violation", talk given at the Enrico Fermi Institute on 2/14/94*

"The scientific approach to the examination of phenomena is a defense against the pure emotion of fear."—*Tom Stoppard, Rosencrantz & Guildenstern are Dead"*

## 1.1   Symmetries in Nature

Starting with Galileo there have always been dire consequences to rejecting the assumption that the world we inhabit is somehow unique or special. In spite of this, Einstein rejected this assumption even more rigorously by postulating that the laws of physics were independent of the inertial reference frame in which one was examining the physics. Mathematically speaking, this means that any theory which describes particle interactions must be Lorentz Invariant. The Lorentz invariance of the theory implies that it must also be invariant under the set of operations C (charge conjugation), P (parity reversal), and T (time reversal) [23][39].

### 1.1.1   Important Symmetries in Particle Interactions

The operation C, or charge conjugation, changes particles to their anti-particles. Particles that are their own anti-particles, for example the photon and neutral pion, are eigenstates of the C operator. Since the operation C performed twice on a given state must give back the state itself, the eigenvalues of C are $\pm 1$. The photon, which mediates the electro-magnetic interaction, is an eigenstate of C, with eigenvalue $-1$. A state consisting of $n$ photons has the C eigenvalue of $(-1)^n$. A neutral pion, since it can decay into two photons, is an

eigenstate of C with +1 eigenvalue. Mathematically, the C operation, when performed on a wave function describing some state, replaces that state with its Hermitian conjugate [71].

The parity operator (P) changes the spatial coordinates of a given state $(x, y, z, t)$ to $(-x, -y, -z, t)$. As a convention, states which have parity eigenvalues of $+1$ are called even states, and states with eigenvalues of $-1$ are said to be odd. Again, since this operator, when used twice on a state, must return the original state, its eigenvalues are also $\pm 1$. The parity of the neutral pion was determined to be odd [18] by the measurement of the angular distribution of the 4 electrons in the decay,

$$\pi^0 \rightarrow (e^+ + e^-) + (e^+ + e^-)$$

using the fact that parity is conserved in electromagnetic interactions.

Finally, the operation of time reversal (T) changes the coordinates of a given state from (x,y,z,t) to (x,y,z,-t). Although many forces encountered in the macroscopic world, such as friction, are not time-invariant (because they depend on the first derivative of time), forces that depend on the second derivative with respect to time are T invariant.

## 1.1.2   Charge Conjugation and Parity Violation

In 1956 Lee and Yang concluded that there was no experimental evidence showing that parity was conserved in weak interactions [69], and in 1957 C. S. Wu *et al* discovered by looking at the angular distribution of electrons emitted from polarized $^{60}$Co that in fact parity was not conserved in $\beta$-decay [70]. The discovery that parity was not conserved also lead to the solution of (and it was in fact most likely inspired by) what was called the "$\tau - \theta$ puzzle", namely, the fact that two particles with the same mass and lifetime, decayed into both a two-pion, P-even final state ($\theta^+$ decays) and a three-pion, P-odd final state ($\tau^+$ decays). If parity is not conserved in those decays, then the $\tau^+$ and $\theta^+$ were presumably the same particle, and were identified as the $K^+$.

Lee, Oehme, and Yang later described how it follows from the CPT theorem that if one of the three operators, C, P, or T, is not conserved, then at least one other of those is also not conserved [71]. Ultimately it is the fact that the W boson, the particle that mediates the weak interaction, couples only to left-handed fermions and right-handed anti-fermions

that precludes either C or P being a conserved quantity in the weak interaction. However, it is possible for the product CP to be conserved in weak interactions although C and P individually are not.

One way to see the violation of both C and P but not CP together is the neutrino sector. The neutrino is left-handed, in other words, its spin opposite to the direction of its momentum. When the Parity operation is performed on the neutrino, the spin, being an axial vector, doesn't change, but the momentum does. The resulting neutrino state is right-handed, and as such is not found in nature. When charge conjugation is performed on that state, however, the right-handed neutrino turns into a right handed anti-neutrino, which is found in nature.

## 1.2   The Neutral Kaon System

Once the operation CP was postulated to be a good symmetry, the neutral Kaon system was a natural place to test its effects. Since both the $K^0$ and the $\bar{K}^0$ could decay into either a two or three-pion final state, then a $K^0$ could turn into a $\bar{K}^0$ via the same two or three pion intermediate state. Gell-Mann and Pais suggested that when a beam of $K^0$'s were produced, then they could mix to a superposition of $K^0$'s and $\bar{K}^0$'s, and one combination would decay quickly to two-pion final states, and the other would be long lived and decay into three-pion final states [22]. Currently it is thought that the W-boson mediates this mixing process, as is shown in figure 1.

Since the CP of a $\pi^0\pi^0$ or $\pi^+\pi^-$ final state is even, and the CP of a $\pi^0\pi^0\pi^0$ final state is odd (the $\pi^+\pi^-\pi^0$ state can be either even or odd, depending on the angular momentum of the $\pi^+\pi^-$ system) , then the short-lived neutral kaon should be CP-even, and the long-lived one CP-odd. If the CP of the $K^0$ and $\bar{K}^0$ are defined as follows:

$$CP|K^0 > \ = \ |\overline{K}^0 >$$
$$CP|\overline{K}^0 > \ = \ |K^0 >$$

the CP-eigenstates containing the $K^0$ and the $\bar{K}^0$ are then:

$$|K_1 > \ = \ \frac{1}{\sqrt{2}}\left(|K^0 > +|\bar{K}^0 >\right)$$

$$|K_2 > = \frac{1}{\sqrt{2}} \left( |K^0 > -|\bar{K}^0 > \right)$$

And if CP were always conserved, the short-lived neutral kaon would correspond to the $K_1$, and the long-lived neutral kaon would be the $K_2$.

## 1.3    CP-Violation observed in Nature

The discovery of CP-violation occurred in 1964 when Christenson, Cronin, Fitch and Turlay observed the decay of the long-lived kaon into a two-pion final state [38]. To explain this decay it was postulated that the eigenstates of the weak decay were in fact superpositions of both $K_1$ and $K_2$, namely, that

$$|K_S > = \frac{1}{\sqrt{1 + |\epsilon|^2}} \left( |K_1 > +\epsilon|K_2 > \right)$$

$$|K_L > = \frac{1}{\sqrt{1 + |\epsilon|^2}} \left( |K_2 > +\epsilon|K_1 > \right)$$

and that the CP-violating decay was simply the consequence of the long-lived neutral kaon being a superposition of mostly $K_2$, and a small fraction of $K_1$. The part of $K_L$ which decayed to two pions, was then just the $K_1$ contamination. This process is now called "indirect CP violation". Other ways to look for this indirect CP-violation are in the decay asymmetries:
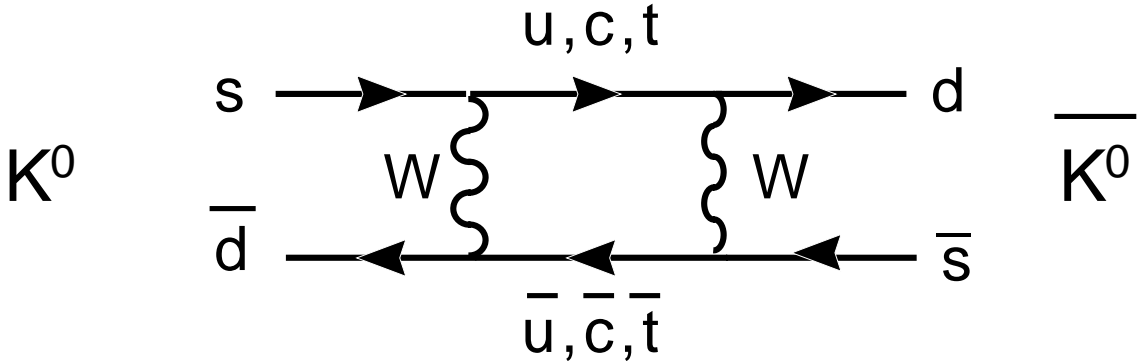


Figure 1. An example of a $K^0$ mixing to a $\overline{K}^0$ through a "box" diagram.

$$A_e = \frac{\Gamma(K_L \to \pi^- e^+ \nu_e) - \Gamma(K_L \to \pi^+ e^- \overline{\nu}_e)}{\Gamma(K_L \to \pi^- e^+ \nu_e) + \Gamma(K_L \to \pi^+ e^- \overline{\nu}_e)}, \text{and}$$

$$A_\mu = \frac{\Gamma(K_L \to \pi^- \mu^+ \nu_\mu) - \Gamma(K_L \to \pi^+ \mu^- \overline{\nu}_\mu)}{\Gamma(K_L \to \pi^- \mu^+ \nu_\mu) + \Gamma(K_L \to \pi^+ \mu^- \overline{\nu}_\mu)}$$

The asymmetries thus defined are equal to twice the real part of $\epsilon$. Experimentally [18],

$$A_e = (0.333 \pm 0.014) \times 10^{-2}$$

$$A_\mu = (0.304 \pm 0.025) \times 10^{-2}$$

These measurements, along with the measurements of $K_L \to \pi\pi$ decays are consistent with the model that the $K_L$ is a superposition of $K_1$ and $K_2$, where the CP-contamination is measured to be [18]:

$$|\epsilon| = (2.27 \pm 0.02) \times 10^{-3}$$

The question of whether or not the $K_2$ can decay into the two-pion final state has yet to be answered. Another way of stating this problem is whether or not a CP eigenstate of one type can decay into a CP eigenstate of another type, which is also referred to as "direct CP violation".

The decays $K_L \to \pi^0 \ell^+ \ell^-$ promise to give long-awaited clues about whether or not direct CP-violation exists because even at the level of Standard Model predictions, the Direct CP-violating contributions to these decays are expected to be as large as or larger than other contributions. Before describing the different components to the decay, other systems which have also been studied in hopes of finding Direct CP-violation are discussed. In contrast to the $K_L \to \pi^0 \ell^+ \ell^-$ decay, however, the CP-Violating processes listed here are expected to be a factor of $10^3$ smaller than the indirect CP-violating or CP-conserving processes.

## $K \to \pi\pi$ Searches

One way to search for direct CP-violation is to look at the decays $K_{L,S} \to \pi\pi$, since the two $\pi^0$ system is a CP-eigenstate, and the $\pi^+\pi^-$ state is simply an isospin rotation of the $\pi^0\pi^0$ state. To measure direct CP violation one simply has to determine how much of the decay is due to the $K_1$ decaying to the two-pion state, and how much of the $K_2$ decays to that state. This strategy has been used in previous experiments to search for direct CP-violation

[43][44] in the kaon system, where in fact reference [43] used almost the same detector (and was done by the same group of physicists) as were used for the analyses described in this thesis. In references [43] and [44] both $K_L$ and $K_S$ decays into the final states $\pi^+\pi^-$ and $\pi^0\pi^0$ were used to measure the real part of $\epsilon'/\epsilon$, which can be expressed as [4]:

$$Re\left(\frac{\epsilon'}{\epsilon}\right) \approx \frac{1 - R}{6}$$

where

$$R \equiv \frac{\frac{\Gamma(K_L \to \pi^0\pi^0)}{\Gamma(K_S \to \pi^0\pi^0)}}{\frac{\Gamma(K_L \to \pi^+\pi^-)}{\Gamma(K_S \to \pi^+\pi^-)}}$$

Here, $\epsilon'$ parameterizes the size of direct CP violation, just as before, $\epsilon$ was the size of indirect CP-violation. The most recent results from these two searches are

$$Re\left(\frac{\epsilon'}{\epsilon}\right) = (7.4 \pm 2.9(syst) \pm 5.2(stat)) \times 10^{-4}[43]$$
$$Re\left(\frac{\epsilon'}{\epsilon}\right) = (23 \pm 5.5(syst) \pm 3.4(stat)) \times 10^{-4}[44].$$

Theoretical predictions which include direct CP-violation are at the several $10^{-4}$ to a few $\times 10^{-3}$ level [31][32]. The largest uncertainties in these predictions are from hadronic effects.

### 1.3.1 Other Avenues in the Pursuit of CP-violation

There are many ways to look for CP-violating effects, of which the decays $K_L \to \pi^0\ell^+\ell^-$ are only two. Table 1 is a partial listing of some observables (and the associated measurements) which would indicate direct CP-violation. Typically, the asymmetries listed above are expected to occur in the Standard Model at the $\sim 10^{-5}$ level [35][41] [42].

So far, the only experiment which has seen direct CP-violation inconsistent with zero at the $3\sigma$ level has been experiment NA31 at CERN [44]. This result is inconsistent at the $2\sigma$ level with the E731 result, however, and even if direct CP-violation is measured in the $K \to \pi\pi$ system, the mystery of the origin of CP violation will still be far from solved.

Table 1. Other Searches for CP-Violation

| CP-Violating Observable | Result |
|---|---|
| Partial Decay Rate Differences <br> $[\Gamma(K^+ \to \pi^+\pi^-\pi^-) - \Gamma(K^- \to \pi^-\pi^+\pi^+)]/[\Gamma(K^+_{\pi\pi\pi}) + \Gamma(K^-_{\pi\pi\pi})]$ [35] | $(0.8 \pm 1.2) \times 10^{-3}$ |
| Dalitz slopes in $K^+ \to \pi^+\pi^-\pi^-$ decays <br> $(a_+ - a_-)/(a_+ + a_-)$ [35] | $(-7.0 \pm 5.3) \times 10^{-3}$ |
| $mu$ polarization transverse to decay plane <br> $K_L \to \pi^+\mu^-\nu$ | $(2.1 \pm 4.8) \times 10^{-3}$ |
| T odd correlation in semi-leptonic baryon decay <br> $(\sigma_n \cdot \vec{p_e} \times \vec{p_\nu})$ of neutron $\beta$ decay [41] | $(-1.1 \pm 1.7) \times 10^{-3}$ |
| Electric Dipole Moment of the Neutron [40] | $< 12 \times 10^{-26} e - cm$ |
| Decay Asymmetry parameter in $\Lambda - \overline{\Lambda}$ decays [42] | $-7.0 \pm 9.0 \times 10^{-2}$ |

## 1.4   CP-Violation in the Standard Model

The way these CP-violating processes can occur in the Standard Model is through the charged current interaction, which mixes different generations of quarks. This mixing is defined in the following way:

$$J_{cc} = (\overline{u}, \overline{c}, \overline{t})\mathcal{M} \begin{pmatrix} d \\ s \\ b \end{pmatrix}$$

where $\mathcal{M}$ is the Cabibbo-Kobayashi-Maskawa (CKM) Matrix. The elements of the matrix correspond to the mixing angles between the different quarks. The elements of $\mathcal{M}$ are defined as follows:

$$\mathcal{M} = \begin{pmatrix} V_{ud} & V_{us} & V_{ub} \\ V_{cd} & V_{cs} & V_{cb} \\ V_{td} & V_{ts} & V_{tb} \end{pmatrix}$$

CP-violation arises if there is a phase difference between two different matrix elements. The matrix itself must be unitary, and this constrains the various elements of the matrix. Two examples of such constraints are:

$$V_{ud}V_{ud}^* + V_{cd}V_{cd}^* + V_{td}V_{td}^* = 1$$

$$V_{ud}V_{us}^* + V_{cd}V_{cs}^* + V_{td}V_{ts}^* = 0$$

Without this constraint there would be 18 free parameters corresponding to the 9 complex elements of the matrix. Wolfenstein realized that $V_{cb} \approx \lambda^2$ and that $V_{ub} \approx \lambda^3$, where $\lambda$ is the sine of the Cabibbo angle ($\lambda \approx 0.23$). The matrix, to order $\lambda^3$ can be described in the following way [33]:

$$\mathcal{M} = \begin{pmatrix} 1 - \lambda^2/2 & \lambda & A\lambda^3(\rho - i\eta) \\ -\lambda & 1 - \lambda^2/2 & A\lambda^2 \\ A\lambda^3(1 - \rho - i\eta) & -A\lambda^2 & 1 \end{pmatrix}$$

where now there are only four parameters which describe the matrix, to this order in $\lambda$. If $\eta$ is non-zero then CP-violation can occur in the Standard Model.

## 1.4.1 Experimental Constraints on the CKM Matrix

To directly measure the elements in the CKM matrix one would have to measure processes at the quark level. Unfortunately, we can only measure processes with hadrons in the initial and final states. Nevertheless, there are experimental constraints on the CKM matrix elements, and a better understanding of hadronic effects (QCD) will reduce theoretical uncertainties in relating experimental measurements to the matrix elements themselves. As mentioned earlier, direct CP-violation gives information about the relative phase between two matrix elements, or $\eta$. By looking at decays of the type $K \to \pi e \nu$, $|V_{us}|$, or $\lambda$ in the Wolfenstein parameterization, can be determined [29]. Similarly, by looking at decays of the type $B \to D\ell\nu$ the matrix element $|V_{cb}|$ can be determined to measure $A$ in the Wolfenstein parameterization [30]. Finally, the quantity $|V_{ub}/V_{cb}|$, or $\sqrt{\eta^2 + \rho^2}$ can be measured by looking at the lepton energy spectrum in semileptonic B decays and fitting for how many events are due to $b \to u$ processes and how many are due to $b \to c$ transitions [14]. To determine $\eta$ by itself, however, one must observe direct CP-violation.

## 1.5  $K_L \to \pi^0 \ell^+ \ell^-$ Contributions

Given that the $K_L$ is a superposition of both the CP-even and CP-odd combinations of $K^0$ and $\bar{K}^0$, there are a number of ways in the Standard Model that the decay $K_L \to \pi^0 \ell^+ \ell^-$ can proceed. The final state $\pi^0 \ell^+ \ell^-$ is not intrinsically a CP-eigenstate, but the decay $K_L \to \pi^0 \ell^+ \ell^-$ can proceed through two different intermediate states which are themselves CP-eigenstates. To decay to $\pi^0 \ell^+ \ell^-$ the $K_L$ proceeds through what is effectively either a $\pi^0 \gamma^*$ or a $\pi^0 \gamma^* \gamma^*$ intermediate state. Given that there are two CP eigenstates in the $K_L$ and the two intermediate states allowed, there are four decay combinations, as shown in figure 2.

The process labeled with an "a" in figure 2 is a CP-conserving process. The $K_1$ is a CP-even state, as is the $\pi^0 \gamma$ state. When the $K_1$ is part of a $K_L$, however, this small admixture of a CP-even state into a primarily CP-odd state is referred to as "Indirect CP-violation". The process indicated by a "b", when occurring in the $K_L$ particle is directly CP-violating, but is reduced by a factor of $\epsilon$ from the definition of the $K_L$ particle, and so its process is likely to be negligible compared to the CP-violating process "c". The process indicated by a "c", is directly CP-violating since $K_2$ is CP-odd and $\pi^0 \gamma^*$ state is CP-even, and finally, the process indicated by a "d" is CP-conserving.

The next sections describe each of these contributions to the decay rate $K_L \to \pi^0 \ell^+ \ell^-$,
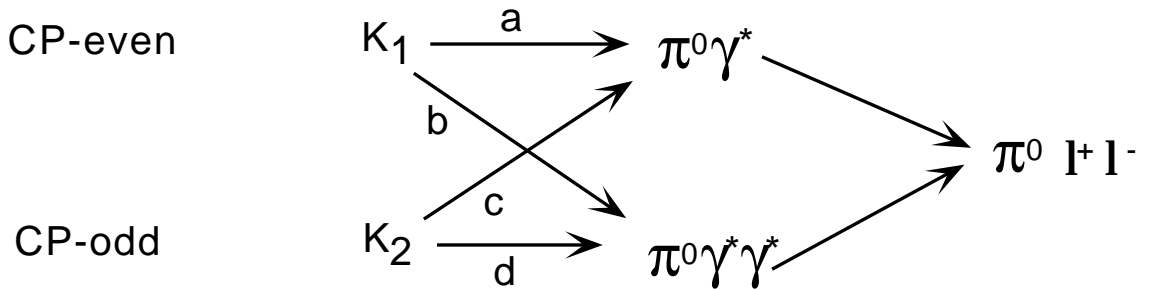


Figure 2. The four different processes by which a $K_L$ can decay to a pion and two leptons, as labeled by arrows $a, b, c$, and $d$. Arrows $b$ and $c$ represent direct CP-violating processes and arrows $a$ and $d$ represent CP-conserving processes

the theoretical predictions for these rates, and finally, experimental constraints on each of these processes.

### 1.5.1 CP-conserving Contributions

The reason the decay $K_L \to \pi^0 \ell^+ \ell^-$ has generated so much interest is its possibilities for finding direct CP-violation is because the CP-conserving contribution is expected to be either the same size or smaller than that for the CP-violating processes. This is because first, the decay $K \to \pi\gamma\gamma$ is suppressed from the decay $K \to \pi\gamma$ by a factor of the electromagnetic coupling constant $\alpha$, and second, the $\gamma\gamma$ coupling to the electron-positron pair is suppressed by helicity. A similar suppression is observed in $\eta$ decay. The fully-leptonic $\eta$ decays proceed electromagnetically through an intermediate two-photon state, and because $m_e \ll m_\mu \leq m_\eta$ the rate of $\eta \to \mu^+\mu^-$ is much greater than the rate of $\eta \to e^+e^-$[18].

In Chiral Perturbation Theory, the leading low energy QCD theory, there are two diagrams which contribute to the CP-conserving process, which are shown in figure 3. The first diagram, A, is suppressed in $\pi^0 e^+ e^-$ decay from helicity arguments, and the amplitude for the diagram labeled B has extra powers of momentum, leading to an angular momentum barrier. Reference [52] estimates the CP-conserving contribution to the branching ratio to be on the order of $10^{-14}$.

However, other theories predict different rates. Figure 4 shows two diagrams which
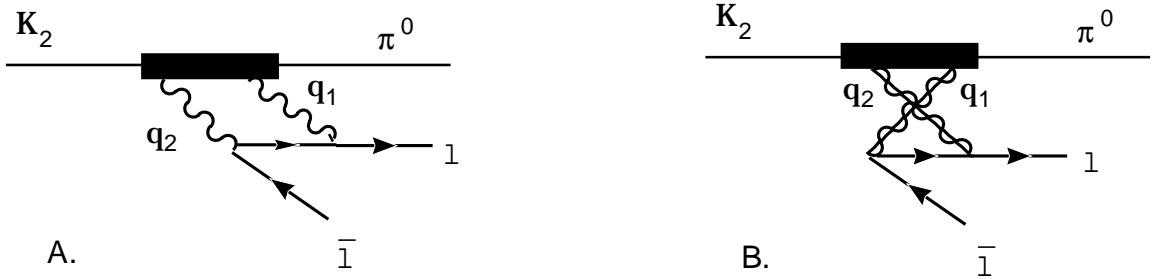


Figure 3. Two Contributions to the $K_L \to \pi^0\gamma\gamma$ decay in Chiral Perturbation Theory, where $q_1$ and $q_2$ are the photon four-vectors

contribute to the process $K_L \rightarrow \pi^0 \gamma \gamma$ considered in reference [48]. The first contribution is the Pion Loop contribution, and the second is the Vector Meson Dominance (VMD) term. The $\gamma\gamma$ mass spectrum resulting from these two diagrams differ significantly, and depending on whether they interfere constructively or destructively the $\gamma\gamma$ invariant mass spectrum could be quite different [48]. By measuring the decay $K_L \rightarrow \pi^0 \gamma \gamma$ and mapping out the $\gamma\gamma$ invariant mass spectrum the prediction for the on-shell contribution to $K_L \rightarrow \pi^0 \ell^+ \ell^-$ can be calculated.

There still remains some controversy as to the overall CP-conserving rate for either the $\pi^0 e^+ e^-$ or the $\pi^0 \mu^+ \mu^-$ process, due to uncertainties in the ultimate $\gamma\gamma$ invariant mass distribution, which is related to the angular momentum of the two photons in the $\pi^0 \gamma \gamma$ intermediate state. Chiral perturbation theory predicts the rate to be $10^{-14}$ for the $\pi^0 e^+ e^-$ process and lower for the $\pi^0 \mu^+ \mu^-$ process [49]. However, reference [48] determines these contributions to be

$$B(K_L \rightarrow \pi^0 e^+ e^-)_{\text{CP} - \text{conserving}} \;=\; 4.1 \times 10^{-12}$$
$$B(K_L \rightarrow \pi^0 \mu^+ \mu^-)_{\text{CP} - \text{conserving}} \;=\; 4.4 \times 10^{-13}.$$

The decay $K_L \rightarrow \pi^0 \gamma \gamma$ has been seen by both E731 and NA31 (references [45] and [46], respectively), but a higher statistics sample is needed to more precisely map out the $\gamma\gamma$ invariant mass $(M_{\gamma\gamma})$ spectrum.
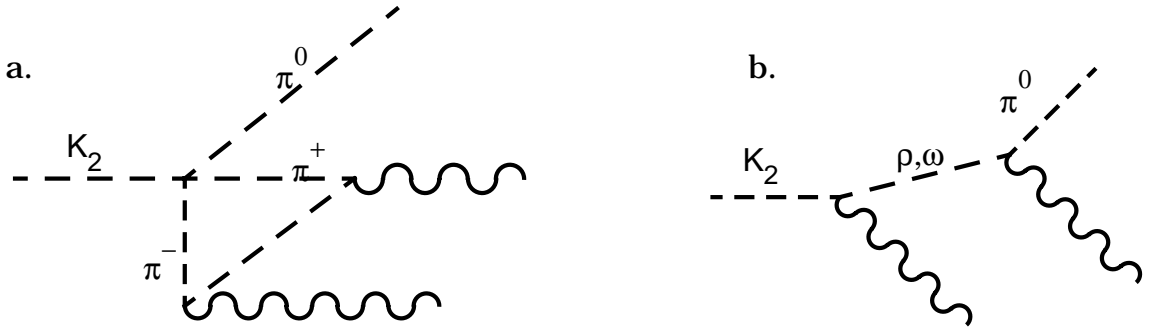


Figure 4. Vector Meson Dominance and Pion Loop diagrams which contribute to the CP-conserving process $K_L \rightarrow \pi^0 \gamma \gamma \rightarrow \pi^0 \ell^+ \ell^-$

### 1.5.2  CP-Violating Contributions

**Indirect CP-violation**

The decay $K_1 \to \pi^0 \gamma^*$ is a CP-allowed decay, and its rate can be estimated by measuring the rate of $K^+ \to \pi^+ l^+ l^-$. To precisely determine the indirect contribution the branching ratio $K_S \to \pi^0 l^+ l^-$, which is dominated by the same intermediate process $K_1 \to \pi^0 \gamma^*$, is needed. The indirect contribution to the branching ratio of $K_L \to \pi^0 \ell^+ \ell^-$ from the admixture of $K_1$ is then simply

$$B(K_L \to \pi^0 \ell^+ \ell^-)_{\text{indirect}} = |\epsilon|^2 \frac{\tau_{K_L}}{\tau_{K_S}} B(K_S \to \pi^0 l^+ l^-)$$

The only limit on either of the branching ratios $B(K_S \to \pi^0 l^+ l^-)$ is [57]:

$$B(K_S \to \pi^0 e^+ e^-) < 4.5 \times 10^{-5}, \tag{1.1}$$

which limits the indirect contribution to the $K_L$ branching ratio to $1.1 \times 10^{-7}$. Theoretical predictions for this limit are at the $10^{-9}$ level.

Currently the branching ratios for $K^+ \to \pi^+ l^+ l^-$ are known to the following precision [54]:

$$
\begin{aligned}
B(K^+ \to \pi^+ e^+ e^-) &= (2.99 \pm 0.22) \times 10^{-7} \\
B(K^+ \to \pi^+ \mu^+ \mu^-) &< (2.3) \times 10^{-7}
\end{aligned}
$$

at the 90% confidence level. The two-muon rate is expected to be about a factor of 10 lower than the two-electron rate because of the reduced phase space [13]. The upper bound on the indirect contributions, given the charged kaon measurements, is:

$$
\begin{aligned}
B(K_L \to \pi^0 e^+ e^-)_{\text{indirect}} &< 1.27 \times 10^{-12} [13] \\
&\leq 1.6 \times 10^{-12} [17] \\
B(K_L \to \pi^0 \mu^+ \mu^-)_{\text{indirect}} &< 2.5 \times 10^{-13} [13]
\end{aligned}
$$

**Direct CP-violation**

Finally, there are two diagrams which contribute to direct CP-violation in the $K_L \to \pi^0 \ell^+ \ell^-$ system, and are shown in figure 5. The $s$ ($\bar{s}$) quark emits a W boson, and becomes either a $u, c,$ or $t$ ($\bar{u}, \bar{c},$ or $\bar{t}$) quark, which then recombines to form a $d$ ($\bar{d}$) quark. The amplitudes for both processes depend on the sine of the phase difference between the matrix elements at each vertex on the quark line, and the mass of the intermediate quark. Since the top quark diagrams dominate these amplitudes, the matrix elements for the processes shown depend on the top quark mass, and the phase difference between $V_{td}$ and $V_{ts}$. An approximate expression for the expected rate, found in reference [13] is:

$$
\begin{aligned}
B(K_L \to \pi^0 e^+ e^-) &= 0.32 \times 10^{-10} \eta^2 A^4 I(m_t), \text{where} \\
I(m_t) &\simeq 0.73 \left( \frac{m_t^2}{m_W^2} \right)^{1.18}.
\end{aligned}
$$

To see how the diagrams in figure 5 relate to $\eta$, consider the fact that the $K_2$ is in fact the sum of $K^0$ and $\bar{K}^0$, and the product $V_{td}^* V_{ts}$ must be subtracted from its complex conjugate to account for the admixture of $K^0$ and $\bar{K}^0$. If there is no direct CP-violation then there is no phase difference between the matrix elements, and the amplitudes for each of the diagrams shown will be canceled when the complex conjugate is subtracted.
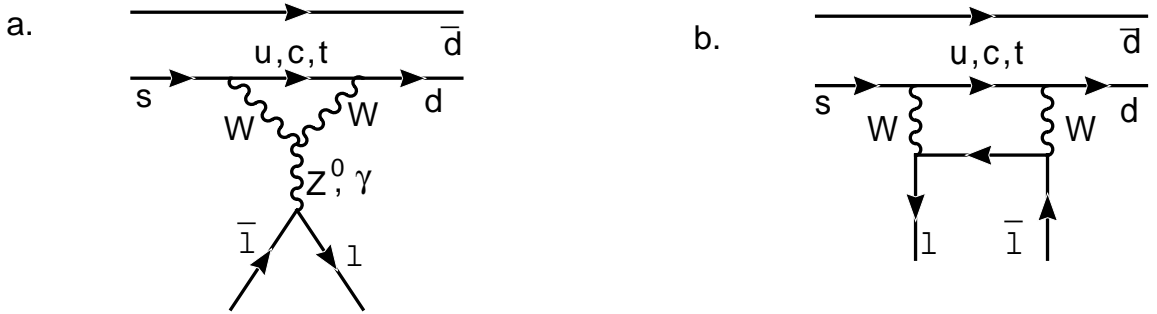


Figure 5. Feynman Diagrams for the Direct CP-violating contributions to the decay $K_L \to \pi^0 \ell^+ \ell^-$. Figure a. is an electroweak penguin diagram, and figure b. is a W-box diagram.

$K_L \to \pi^0 \nu \overline{\nu}$ **Searches**

From the previous discussion of contributions, one might ask if there is a decay mode where the various contributions are not all of comparable size, but where the size of the direct CP-violating channel far surpasses the other two contributions. Such a process is the decay $K_L \to \pi^0 \nu \overline{\nu}$. The W box diagram and the Z penguin diagram, shown in figure 5 can both contribute to the rate since the Z or W can couple to neutrinos instead of charged leptons. However, since photons cannot couple to neutrinos, neither the CP-conserving process nor the indirect CP-violating process described earlier can contribute to the $K_L \to \pi^0 \nu \overline{\nu}$ branching ratio without considering higher order diagrams. This makes the decay $K_L \to \pi^0 \nu \overline{\nu}$ the cleanest signal theoretically of direct CP-violation.

Experimentally, however, the measurement is very challenging since only one of the three final state particles can be detected, and so the possibility for backgrounds is enormous. By searching for decays of the type $K_L \to \pi^0 \nu \overline{\nu}$, where the $\pi^0$ decays to $e^+ e^- \gamma$, one can hope to have additional kinematic handles by which to discriminate signal from background, but at present the experimental limits are far from the Standard Model predictions. Theoretical predictions for this process are at the level of $10^{-10}$ [59], and the current experimental limit, found in E799, is $5.7 \times 10^{-5}$[3].

## 1.5.3   Non-Standard Model Processes

There are several non-Standard Model processes whose direct CP-violating predictions differ from that of the Standard Model. Any non-Standard Model prediction for the indirect CP-violating amplitude is limited experimentally by the measured branching ratio of the decay $K^+ \to \pi^+ e^+ e^-$. A non-standard CP-conserving contribution could be due to some scalar-scalar vertex which involves an $s$ quark emitting some scalar, and becoming a $d$ quark, and then the scalar decays to two leptons. This contribution, however is constrained by the experimental limit on $K_L \to e^+ e^-$. With the current experimental limit of [18]

$$B(K_L \to e^+ e^-) < 1.6 \times 10^{-10} @90\% \text{confidence}, \tag{1.2}$$

a scalar-scalar vertex contribution to the CP-conserving rate is less than $4 \times 10^{-13}$, which is as small as or smaller than Standard Model predictions for the CP-conserving rate [50][51].

We will now discuss other non-Standard Model processes and their predictions for the decays $K_L \to \pi^0 \ell^+ \ell^-$.

## Superweak Prediction

The Superweak hypothesis predicts that the small mixing of $K_1$ and $K_2$ in the $K_L$ and the $K_S$ particles is due to an additional CP-odd term in the weak Hamiltonian [34][37]. There are no other predicted manifestations of CP-violation in the K system. In the Wolfenstein parameterization, this implies that $\eta$ will be zero, and therefore there will be no contribution to the $\pi^0 \ell^+ \ell^-$ branching ratios through either the electroweak penguin or W-box diagrams.

## Leptoquark Models

If there is a leptoquark which decays to a quark-lepton pair, then the decay $K_L \to \pi^0 \ell^+ \ell^-$ can occur at tree-level. For example, consider a leptoquark coupling which is described as $\lambda_{ij} \overline{Q}_i \phi l_j^c$, where $Q$ is a quark doublet and $l$ is a lepton singlet. The $\pi^0 \ell^+ \ell^-$ contribution from the tree-level process is [50][51]:

$$B(K_L \to \pi^0 \ell^+ \ell^-) = 2 \times 10^9 (Im\lambda_{1j}\lambda_{2j}^*)^2 \left(\frac{GeV}{M}\right)^4$$

where $j = 1$ for electrons, and $j = 2$ for muons, and $M$ is the scalar mass. The couplings to muons are expected to be significantly lower than the couplings to electrons, given the branching ratio of the decay $K_L \to \mu^+ \mu^-$ (which is $(7.3 \pm 0.4) \times 10^{-9}$[18]) and the limit on the branching ratio of $K_L \to \mu e$ ($< 9.4 \times 10^{-11}$ at 90% confidence [18]). The helicities of the quark and lepton that the leptoquark couples to determine whether the tree-level contribution violates or conserves CP.

## Exotic Particle Contributions

Still another way that a non-Standard Model contribution can arise is if there are exotic particles which can enter into the penguin or box diagrams shown in figure 5, in place of the W or Z. References [50] and [15] both discuss the effect of super-symmetric contributions to the $\pi^0 \ell^+ \ell^-$ branching ratio from additional box and loop diagrams with supersymmetric particles. In each case the predicted branching ratio can either be considerably larger

than the Standard Model predictions, or the same size, depending on the strengths of the supersymmetric couplings.

Reference [53] discusses a model which includes several Higgs doublets, with an electro-Higgs boson $(H_e)$ which, once it is more massive than twice the muon mass, couples equally to $e^+e^-$ and $\mu^+\mu^-$ pairs. In this case the $\pi^0 e^+ e^-$ and $\pi^0 \mu^+ \mu^-$ branching ratios are expected to be of comparable size, since the process is expected to proceed through a $\pi^0 H_e$ intermediate state.

$$\begin{aligned} B(K_L \to \pi^0 \ell^+ \ell^-) &= B(K_L \to \pi^0 H_e) B(H_e \to \ell^+ \ell^-) \\ &= (10^{-9} - 10^{-6}) \left( \frac{250\,GeV}{<H_e>} \right)^2 \end{aligned}$$

where $<H_e>$ is the electro-Higgs mass. The contributions from this mode are also limited by the charged kaon branching ratio measurements.

## 1.5.4  Dangerous Backgrounds

After the decay $K_L \to e^+ e^- \gamma\gamma$ had been seen it was pointed out by Greenlee that this decay could cause serious background to $K_L \to \pi^0 e^+ e^-$ searches at levels where Standard Model contributions are important [63]. Although there is no expected enhancement of this decay at a $\gamma\gamma$ invariant mass, $M_{\gamma\gamma}$, near the $\pi^0$ mass (see figure 65), there will be a finite amount of background predicted from this process regardless of how tightly an analysis cuts on the $\gamma\gamma$ invariant mass. The decay $K_L \to \mu^+ \mu^- \gamma\gamma$ may also become important at Standard Model levels. Currently the branching ratio $K_L \to e^+ e^- \gamma\gamma$ measured in this experiment, is [16]:

$$B(K_L \to e^+ e^- \gamma\gamma) = (7.5 \pm 1.5(\text{stat}) \pm 0.8(\text{syst})) \times 10^{-7}.$$

While the muon partner of this decay, $K_L \to \mu^+ \mu^- \gamma\gamma$, has not yet been observed, it has been predicted to be about a factor of 100 smaller in overall rate, since the muons in the decay are not as relativistic as the electrons in the $e^+ e^- \gamma\gamma$ decay and hence are not as likely to emit bremsstrahlung photons. The expected background from the $K_L \to \mu^+ \mu^- \gamma\gamma$ decay to the $\pi^0 \mu^+ \mu^-$ signal is about a factor of 11 lower than the expected background in the electron mode, because phase space cuts which optimize the $\pi^0 e^+ e^-$ / $e^+ e^- \gamma\gamma$ signal are not

Table 2. Theoretical Predictions for $K_L \to \pi^0 \ell^+ \ell^-$ Contributions

| Contribution | $K_L \to \pi^0 e^+ e^-$ | $K_L \to \pi^0 \mu^+ \mu^-$ |
|---|---|---|
| CP-violating | $\sim 6 \times 10^{-12}$ [17] | |
| (Direct + Indirect) | $3.7 \times 10^{-12}$ [66] | |
| | $1 - 62 \times 10^{-12}$ [48] | $0.4 - 13 \times 10^{-12}$ [48] |
| | $1.5 - 15 \times 10^{-12}$ [49] | $3 - 30 \times 10^{-13}$ [49] |
| | $10^{-11}$ [52] | |
| CP-conserving | $2.3 \times 10^{-13}$ [66] | |
| | $4.1 \times 10^{-12}$ [48] | $4.4 \times 10^{-12}$ [48] |
| | $8 \times 10^{-13}$ [49] | $5 - 10 \times 10^{-12}$ [49] |
| | $10^{-13} - 10^{-14}$ [52] | |
| Non-Standard Model | potentially large | |
| Radiative Dalitz Background$^\dagger$ | $7 \times 10^{-11}$ | $6 \times 10^{-12}$ |

$^\dagger$ This is the background estimated for a $\pm 2\, MeV/c^2$ cut on $M_{\gamma\gamma}$.

as powerful in optimizing the $\pi^0 \mu^+ \mu^-$ / $\mu^+ \mu^- \gamma\gamma$ signal. Since the overall branching ratio for $K_L \to \pi^0 \mu^+ \mu^-$ is expected to be about a factor of 5 lower than that for $K_L \to \pi^0 e^+ e^-$ the relative background from $\mu^+ \mu^- \gamma\gamma$ to the $\pi^0 \mu^+ \mu^-$ signal is expected to be about a factor of 2 less than the background from $e^+ e^- \gamma\gamma$ to the $\pi^0 e^+ e^-$ signal.

## 1.6   Theoretical Predictions

Table 2 is a list of the different contributions and the corresponding branching ratios predicted by theory. Note that although there is some disagreement between various theories most theories predict levels at around $10^{-11} - 10^{-12}$ for the $\pi^0 e^+ e^-$ branching ratio, and $10^{-12}$ for the $\pi^0 \mu^+ \mu^-$ branching ratio. Since the indirect and direct CP-violating amplitudes interfere, the amplitudes for each mode must be summed and squared before a decay rate can be predicted, and in fact, whether or not this interference is constructive or destructive is unknown.

Table 3. History of Searches for $K_L \to \pi^0 \ell^+ \ell^-$

| Decay Mode | 90% C.L. Limit | Year | Laboratory | Reference |
|---|---|---|---|---|
| $K_L \to \pi^0 \mu^+ \mu^-$ | $< 5.7 \times 10^{-5}$ | 1976 | SLAC | [55] |
| $K_L \to \pi^0 \mu^+ \mu^-$ | $< 1.2 \times 10^{-6}$ | 1980 | Brookhaven | [56] |
| $K_L \to \pi^0 e^+ e^-$ | $< 2.3 \times 10^{-6}$ | 1980 | Brookhaven | [56] |
| $K_L \to \pi^0 e^+ e^-$ | $< 5.5 \times 10^{-9}$ | 1990 | Brookhaven | [60] |
| $K_L \to \pi^0 e^+ e^-$ | $< 7.5 \times 10^{-9}$ | 1990 | Fermilab | [58] |

## 1.7   Experimental Limits

The limits on the $\pi^0 \ell^+ \ell^-$ branching ratios have been improving since the first search for these processes in 1976. Most recently, attention has focused on the $\pi^0 e^+ e^-$ limit, and before this search, no improvement in the $\pi^0 \mu^+ \mu^-$ mode had been made since 1980. Table 3 lists the various branching ratio limits (at the 90% confidence level) for the two different decay modes.

## 1.8   Overview

As can be seen from the comparison of tables 2 and 3 there is much room for non-Standard Model processes to be discovered. In the $\pi^0 e^+ e^-$ decay there are at least 2 orders of magnitude between the Standard Model theoretical predictions and the experimental limits, and in the $\pi^0 \mu^+ \mu^-$ arena there are 6 orders of magnitude. The remainder of this thesis describes the most sensitive searches to date for each of these modes. The following chapter describes how branching ratios are measured in this experiment. The following four chapters describe the detector and how candidate events were selected online, with special attention paid to the electromagnetic calorimeter and the muon identification system, both of which were crucial to these searches. Chapter 7 describes the detector simulation which plays a very important role in the analysis. The next three chapters describe general event reconstruction, signal identification, and how various backgrounds to each signal were min-

imized. Chapter 11 describes the systematic errors associated with both branching ratio measurements, and finally, chapter 12 gives the final results and discusses possible methods of determining the different contributions to the decay, once a signal is seen in the future.

# CHAPTER 2

# TECHNIQUE

"Vous avez toujours tendance à additionner. Mais il faut aussi soustraire. Il ne faut pas uniquement intégrer. Il faut aussi désintégrer. C'est ça la vie. C'est ça la philosophie. C'est ça la science. C'est ça le progrès, la civilisation. "
—*Ionesco, La leçon*

The $K_L \to \pi^0 \ell^+ \ell^-$ branching ratios can be measured by comparing the observed rates of decays of the type $K_L \to \pi^0 \ell^+ \ell^-$ to those of previously measured decays of the $K_L$. This chapter describes the strategy adopted to make the measurement and the previously measured "normalization" decays which were chosen. The choice of normalization decays was made with the goal of introducing as little systematic error as possible into the measurement.

## 2.1   Normalization Procedure

In this experiment, neither the production nor the decays of $K_L$'s are tagged; that is, only the decay itself of the $K_L$ is observed in the detector. Therefore, in order to determine a branching ratio in this experiment one measures a ratio of decay rates. The analysis must include two different decay modes, the signal mode, and the normalization mode. The branching ratio of the signal mode can then be expressed in the following way:

$$BR(\text{signal}) = BR(\text{normalization}) \times \frac{N(\text{signal})}{N(\text{normalization})} \times \frac{A(\text{normalization})}{A(\text{signal})} \qquad (2.1)$$

Where $N(\text{mode})$ is the number of events seen in a given mode, and $A(\text{mode})$ is the acceptance of that mode, which can be calculated in a simulation of the detector response (the Monte Carlo). Since the branching ratio depends critically on the ratio of acceptances rather than on the acceptance of one mode in particular, it is best to chose a normalization

mode which is as similar as possible to the signal mode, and then analyze and reconstruct both signal and normalization modes the same way, using the same cuts, if possible. If this is done, uncertainties in the efficiencies of the cuts will often cancel. For example, if both the signal and normalization decays contain two electrons which are identified in the same way, the overall electron efficiency may cancel. Similarly, during the course of the E799 run the acceptances of various modes changed significantly with time, but if one collects both signal and normalization data simultaneously, again this effect cancels in the ratio of the acceptances.

## 2.2  Normalization Analysis

This section discusses how the normalization modes were chosen and outline how the analyses differed between signal and normalization samples. In general, for each cut described in this thesis there are tables which describe its efficiency If that cut is also made on the normalization sample then this will be indicated in the table. Since for the two different searches the normalization samples are quite different they will be discussed separately.

### 2.2.1  $K_L \to \pi^0 e^+ e^-$ Normalization

For the $K_L \to \pi^0 e^+ e^-$ search the normalization sample used was the decay $K_L \to e^+ e^- \gamma$. The branching ratio for this process has been measured to be

$$BR(K_L \to e^+ e^- \gamma) = (9.1 \pm 0.5) \times 10^{-6}[18]. \qquad (2.2)$$

Although this branching ratio is only known to within 5.5%, the decay $K_L \to e^+ e^- \gamma$ was chosen by virtue of having two electrons in the final state, so uncertainties in the electron efficiencies will approximately cancel. This is the first $K_L \to \pi^0 e^+ e^-$ search with sufficient $K_L$ flux and acceptance to use this rare a decay as a normalization. The same particle identification, fiducial, and detector cuts are made on both samples to minimize the systematic errors. Unfortunately, however, the kinematics of this decay are different, especially in the distribution of the invariant mass of the $e^+ e^-$ pair ($M_{e^+ e^-}$). Figure 6 shows the decay rates as a function of $M_{e^+ e^-}$ for both the $K_L \to e^+ e^- \gamma$ decay and the $K_L \to \pi^0 \mu^+ \mu^-$ decay, as-

suming the $K_L \to \pi^0 e^+ e^-$ decay populates the available phase space evenly. The difference between these two spectra precludes making the same cut on the $e^+ e^-$ invariant mass (if one is made, that is), but other than that, similar kinematic cuts were made in the two analyses.

Another issue associated with the ratio of signal and normalization acceptances is the overall photon identification efficiency—the decay $K_L \to e^+ e^- \gamma$ has only one photon in the final state, while $K_L \to \pi^0 e^+ e^-$ has two photons in the final state. To check for uncertainties in misunderstanding the acceptance difference between one and two photons, we also reconstruct decays of the type $K_L \to \pi^0 \pi^0$, where one $\pi^0$ undergoes a Dalitz decay $(\pi^0 \to e^+ e^- \gamma)$. The branching ratio for this series of decays is

$$
\begin{aligned}
BR(K_L \to \pi^0 \pi^0, \pi^0 \to e^+ e^- \gamma) &= 2 \times BR(K_L \to \pi^0 \pi^0) \times BR(\pi^0 \to e^+ e^- \gamma) \\
&= (2.1 \pm 0.10) \times 10^{-5} [18].
\end{aligned}
$$

As with the $K_L \to e^+ e^- \gamma$ analysis, all the same particle identification cuts can be made on the electrons and photons. However, while this decay has three photons in the final state and therefore serves as a good cross-check, the kinematics of this decay are even
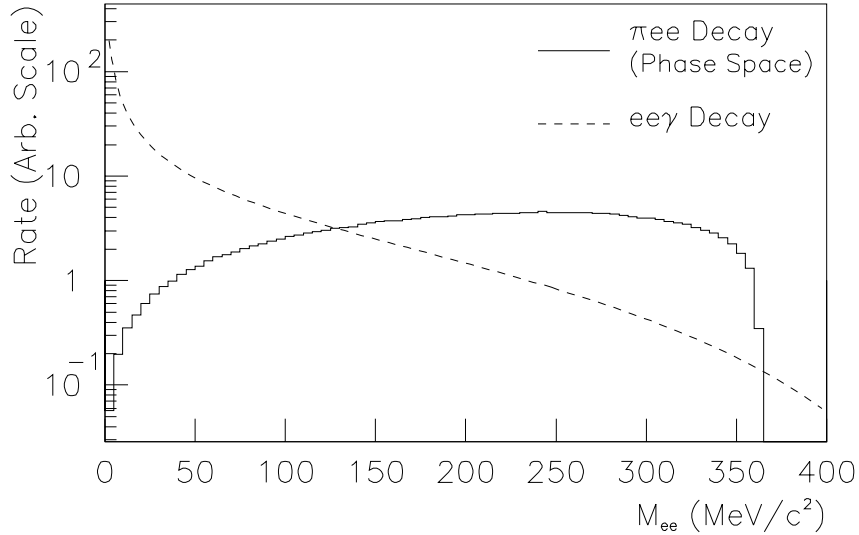


Figure 6. The $M_{e^+ e^-}$ spectra of both $K_L \to \pi^0 e^+ e^-$ and $K_L \to e^+ e^- \gamma$ decays

less similar to the signal mode than the kinematics of $K_L \to e^+e^-\gamma$. Because of this, the reconstruction of these events is also different from the reconstruction of the signal events, as will be discussed in section 8.4.4. Therefore, this decay is only used as a cross-check and does not enter into the final branching ratio calculation. If it is shown that the three and one-photon efficiencies are understood, then we can claim the two-photon efficiency is also well-simulated.

### 2.2.2 $K_L \to \pi^0\mu^+\mu^-$ normalization

Since there is no other well-known decay of the $K_L$ particle containing two muons in the final state, the branching ratio of the decay $K_L \to \pi^0\mu^+\mu^-$ is best measured by using the decay $K_L \to \pi^+\pi^-\pi^0$ as a normalization sample. The only advantage this decay has over the samples chosen for the $K_L \to \pi^0e^+e^-$ decay in that it is almost kinematically identical to the signal decay. Therefore, all of the kinematic and background specific cuts which were made on the signal sample can be made on the normalization sample as well. Also, the process $K_L \to \pi^+\pi^-\pi^0$ has a large branching ratio:

$$BR(K_L \to \pi^+\pi^-\pi^0) = 0.1238 \pm 0.021[18],$$ (2.3)

which means that it is relatively straightforward to get a low-background, large sample of these decays. With such a large sample of events, one can look at the loss of normalization acceptance in the Monte Carlo and compare it with the loss of normalization events to determine how well the cuts are modeled in the Monte Carlo.

The disadvantage of using the decay $K_L \to \pi^+\pi^-\pi^0$ to determine the branching ratio of the decay $K_L \to \pi^0\mu^+\mu^-$ is that since the final state charged particles are different, requiring different trigger and the particle identification cuts. These differences were studied in detail and are accounted for in section 11.3.

## 2.3 Overview

Given the strategy outlined above it is clear that the experiment must be able to trigger on and reconstruct each of the decay modes listed in table 4. A detector is needed for which

Table 4. Decay Modes Used in $K_L \to \pi^0 \ell^+ \ell^-$ Analyses

| Decay Mode | Branching Ratio |
|---|---|
| $K_L \to \pi^0 e^+ e^-$ | $< 5.5 \times 10^{-9}$ |
| $K_L \to e^+ e^- \gamma$ | $9.1 \times 10^{-6}$ |
| $K_L \to \pi^0 \pi^0, \pi^0 \to e^+ e^- \gamma$ | $2.1 \times 10^{-5}$ |
| $K_L \to \pi^0 \mu^+ \mu^-$ | $1.2 \times 10^{-6}$ |
| $K_L \to \pi^+ \pi^- \pi^0$ | $1.2 \times 10^{-1}$ |

the acceptances for four different final state particles and three different multiplicities are both large and well-understood. Given the low levels of the expected rates, the detector must also have sufficient invariant mass resolution and particle identification capability so that an analysis can discriminate against the many backgrounds which may (and in fact did) arise. In the next chapter the E799 detector will be described and the features which enable the measurement to be made will be outlined.

# CHAPTER 3

# THE EXPERIMENT

The detector was originally designed to measure $\epsilon'/\epsilon$ in the $K_L \to \pi\pi$ system (E731 at Fermilab) and hence was optimized to detect four-body final state decays of the $K_L$ particle. Although much of the detector remained the same between E731 and E799 there were different features which were important for the different decays in E799. There are more detailed descriptions of many of the elements listed here in references [1] and [6], but the salient features important to the $K_L \to \pi^0 \ell^+ \ell^-$ measurements are included here.

## 3.1   $K_L$ Beam Production

The Fermilab Tevatron delivered $800\,GeV$ protons in a 22 second period, known as a "spill", and there was one such spill every 58 seconds. The spill itself was divided into many "buckets", where the beginning of each bucket was determined by a Radio Frequency ("RF") signal. The buckets themselves were separated by $18.9\,nsec$, and the protons arrived in a $2\,nsec$ period at the beginning of each bucket. On average the experiment received $\sim 1.5 \times 10^{12}$ protons on the target per spill.

To make a beam of $K_L$ particles the proton beam struck a beryllium target which measured one nuclear interaction length ($36.2\,cm$) long, and had a square cross section of $3.2\,mm$ on a side. The targeting angle was at $4.8\,mrad$, which produced $K_L$'s with the energy spectrum shown in figure 7. The spectrum itself was determined from data in experiment E731, which had the same targeting angle and beam geometry. Downstream of the target there were a series of sweeping magnets and collimators to remove all but the neutral particles, and these are shown in figure 8. The first collimator to shape the beams was the two-hole collimator, which consisted of a $5.8\,m$ thick slab of copper with two

holes, vertically aligned, which ultimately produced beams whose centers were separated by about $23.2\,cm$ when they were $180\,m$ downstream of the target. Following the two-hole collimator was a lead absorber which was placed in the beam to convert photons to electron-positron pairs which would then be removed by another sweeping magnet. The lead absorber was $3\,in$ thick, representing $0.44$ nuclear interaction lengths or $14$ radiation lengths of material. Downstream of the absorber were three sets of collimators and two sweeping magnets sandwiched between the three layers of collimators. After the last collimator there was an $18\,in$ beam-pipe which extended from about $85\,m$ from the target to $115\,m$ from the target, and then the pipe was connected to a series of larger pipes. Because of the long decay volume and the sweeping magnets the only particles which survived the flight from the target to the decay region were $K_L$'s, high energy $\Lambda$ particles, and neutrons. Figure 9 shows the decay volume of the experiment. From the lead absorber to the end of the last beam-pipe, the decay region was in a vacuum of about $15\,mTorr$. There was a $48\,in$ diameter vacuum window on the end of the last beam-pipe to define the end of the decay volume.
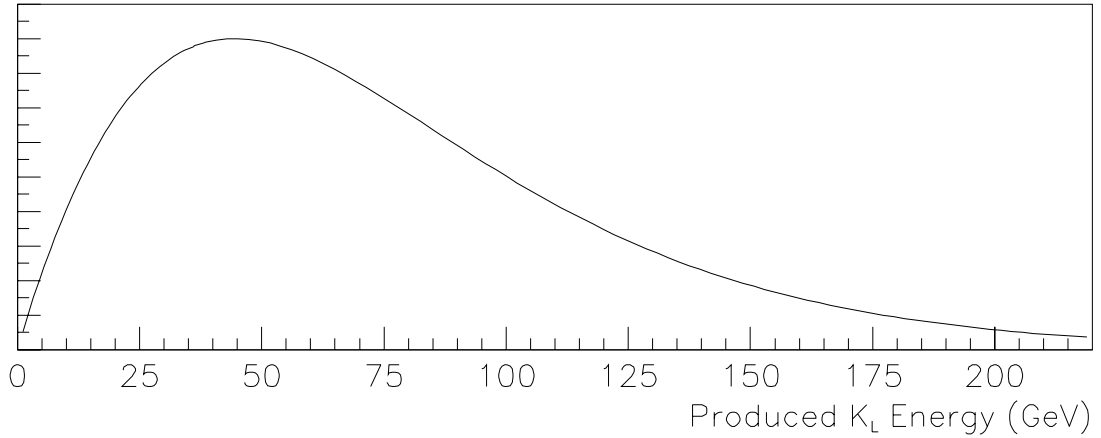


Figure 7. The energy spectrum of $K_L$ particles at the target

MC6

MC7

Slab Collimator

Sweeping Magnet

Absorber

Two-Hole Collimator

Sweeping Magnets

Slab Collimator

Jaw Collimator (H)

Sweeping Magnet

Jaw Collimator (V)

Jaw Collimator (H)
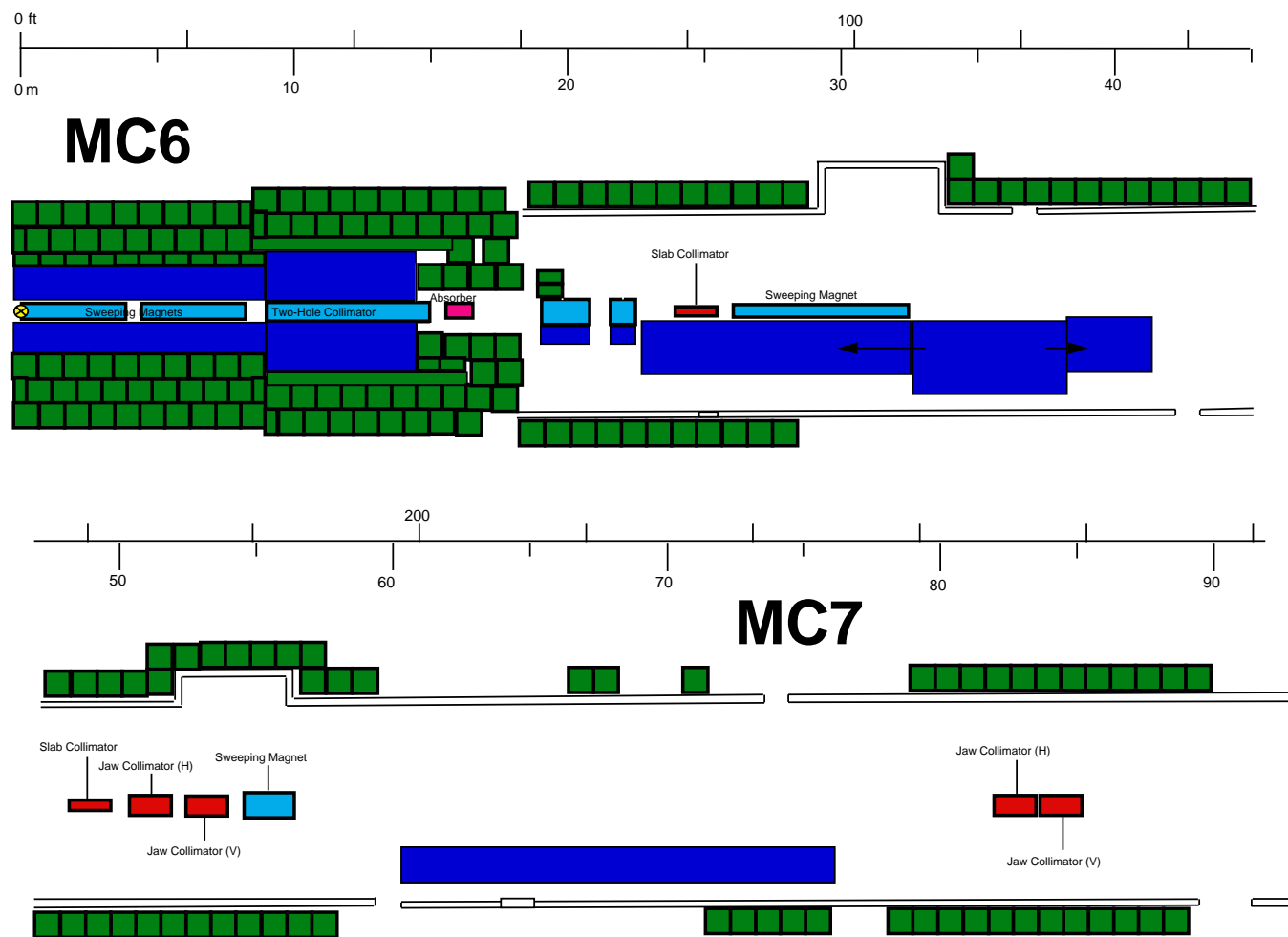
Jaw Collimator (V)

Figure 8. The Collimators and Sweeping Magnets

MC7

300

90      100      110

Jaw Collimators

18" VACUUM PIPE

MC8

117.86m

400

120      130      140

148.98m

500

150

159.14m

160

MC8AN1

VA-1

VA0

MC8REG2 (773)

VA1

VA2

MC8AN2/3

VA3

A/C

VA4

SA

4' Vacuum    Decay    Tank

Vac. pump

DRA

6' Vacuum    Decay    Tank

Chiller

(Steel)
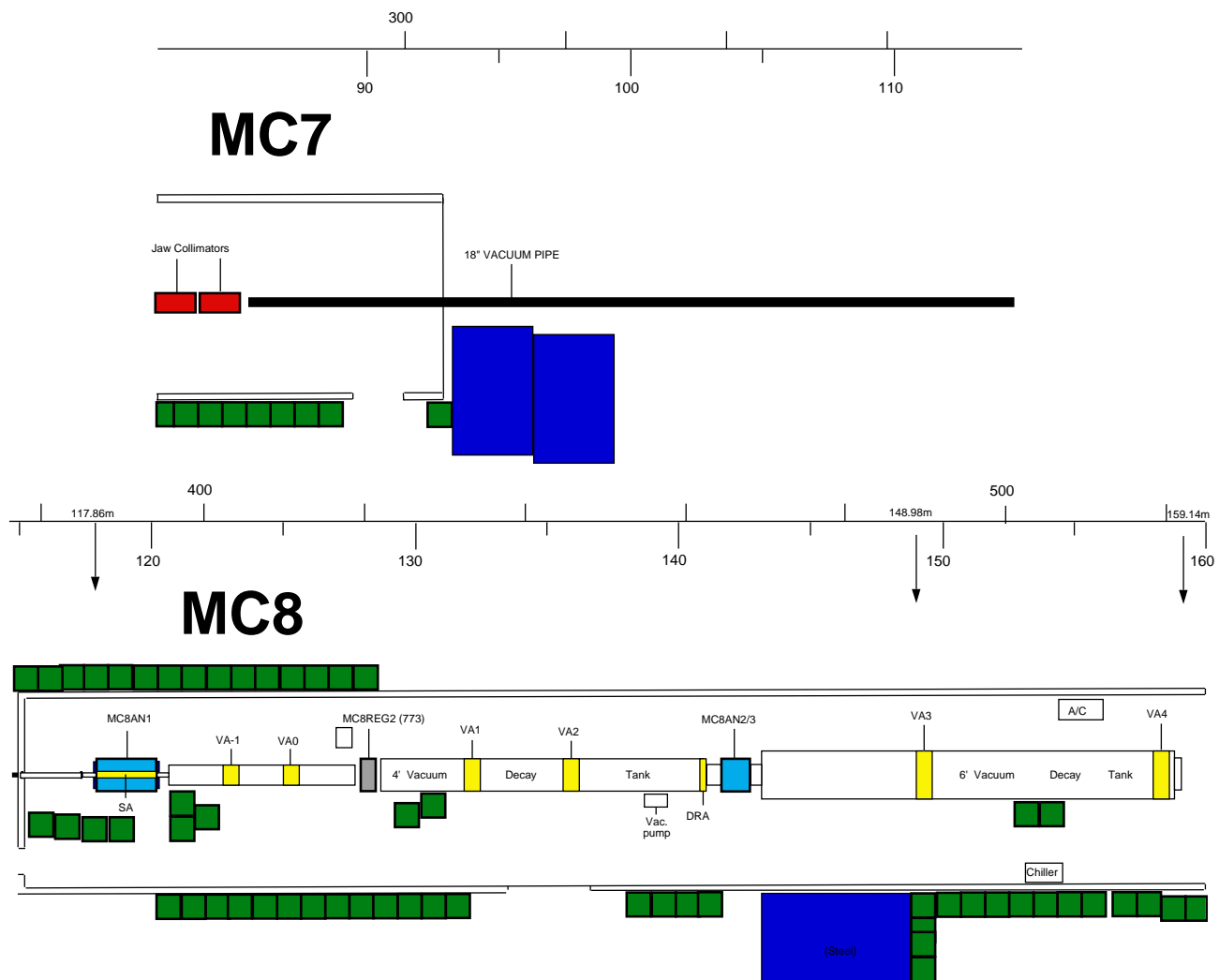
Figure 9. The Decay Volume

## 3.2  Detector Elements and Layout

The most crucial elements of the E799 detector for the analyses described in this thesis are the charged spectrometer, the lead-glass calorimeter, and the muon identification system. There are also several detectors which ensure that no charged particles escaped the detector fiducial region unobserved. In this section we will describe the latter detectors in some detail and give the salient features of the spectrometer, calorimeter, and muon identification system. Reference [1] contains a comprehensive description of the spectrometer and its calibration, and chapters 5 and 6 give more detailed descriptions of the calorimeter and muon identification system, respectively. Figure 10 shows a schematic drawing of all of the elements in the E799 detector.

A global coordinate system was defined to describe the detector element positions and orientations. The z direction is the direction defined by the vector pointing from the center of the target to the very center of the lead-glass calorimeter, and "downstream" is the direction pointing in positive z. The y coordinate was defined to be vertical, with the positive y direction being up, and the positive x (horizontal) direction was defined such that the overall coordinate system was right-handed, and the positive x direction was to the left, as seen by a $K_L$ traveling downstream from the target.

### 3.2.1  Photon Vetoes

Throughout the decay volume there were several stations of photon vetoes which, at trigger level, were used to veto events with charged particles leaving the fiducial region of the detector. These can be seen in both figure 9 and figure 10. Table 5 is a listing of all the photon vetoes, their inner and outer dimensions, and their respective distances from the target.

The vetoes surrounding the vacuum region (the Vacuum Antis or VA's) and the veto located in front of the magnet (the Magnet Anti or MA) all consisted of a thin layer of scintillator followed by two sections of lead-lucite sandwiches. Figure 11 shows a picture of the cross section of one such combination of counters. There are a total of 6 radiation lengths in each photon veto assembly. The Decay Region Anti (DRA) consisted of two

25 cm

Photon Veto
Counters

Photon Veto
Counters

Lead Wall

Muon
Trigger
Planes

Lead Glass

Muon
Filter

$K_L$
beams

Vacuum Window

Calibration magnets

Drift
Chambers

Analysis Magnet Hadron Veto
Trigger Planes

120    130    140    150    160    170    180    190

Distance from Target (m)
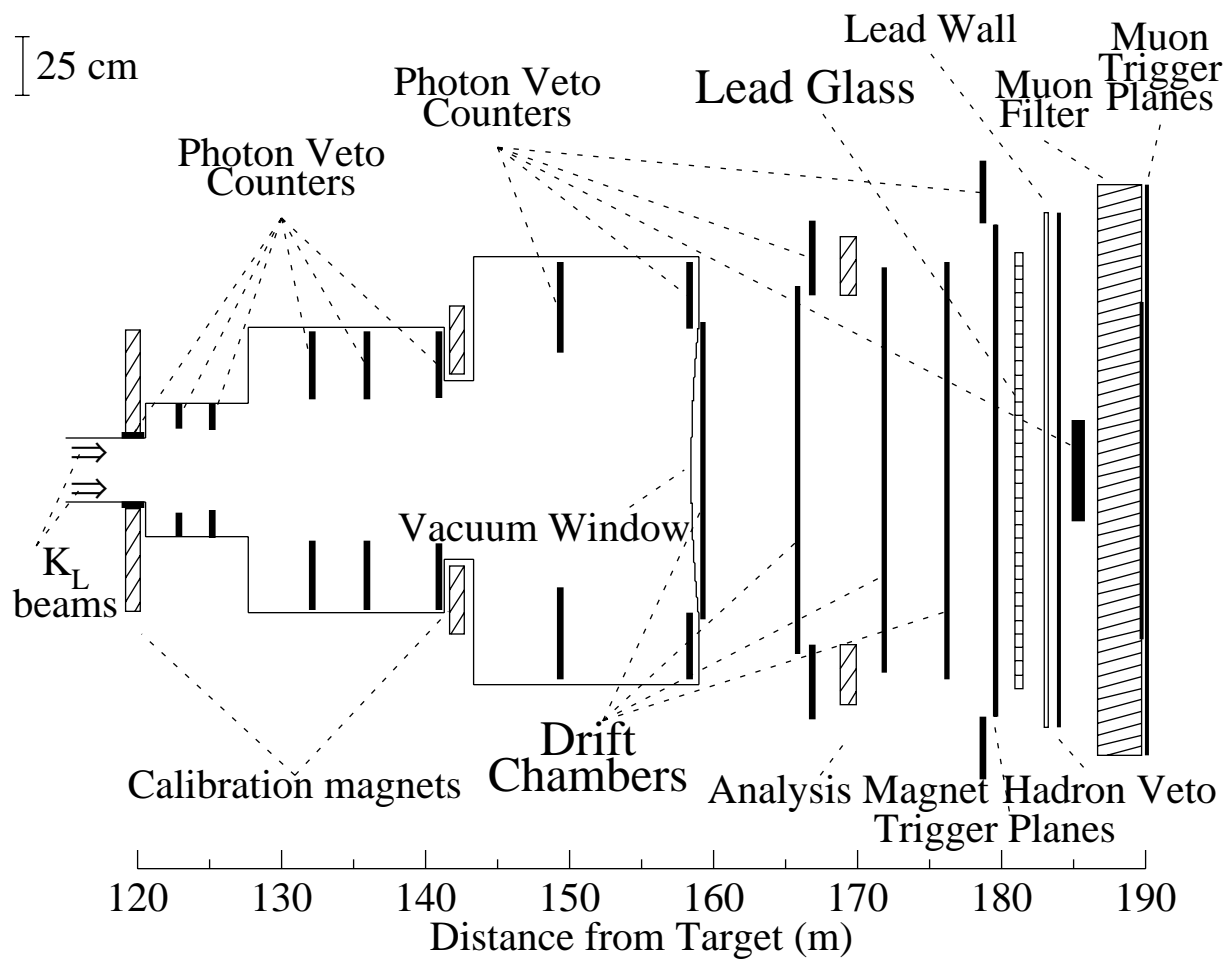
Figure 10. Schematic drawing of the detector

Table 5. Photon Veto Positions. Where there are two dimension entries for a given veto, this means that the veto was rectangular, with the x and y inner and outer dimensions given as specified.

| Photon Veto | Inner Radius (m) | Outer Radius(m) | Target Distance (m) |
|---|---|---|---|
| Vacuum Anti 9(x) | .0947 | .2050 | 122.87 |
| Vacuum Anti 9(y) | .1782 | .2863 | 122.87 |
| Vacuum Anti 0(x) | .0947 | .2050 | 125.18 |
| Vacuum Anti 0(y) | .1721 | .2889 | 122.87 |
| Vacuum Anti 1 | .303 | .595 | 132.17 |
| Vacuum Anti 2 | .303 | .595 | 135.93 |
| DRA | .595 | .310 | 140.95 |
| Vacuum Anti 3 | .502 | .885 | 149.29 |
| Vacuum Anti 4 | .606 | .889 | 158.27 |
| Magnet Anti(x) | .908 | 1.057 | 166.83 |
| Magnet Anti(y) | .743 | 1.067 | 166.83 |
| Lead Glass Anti | .9080 | 1.403 | 178.71 |

planes of scintillator separated by a lead sheet to convert photons. The veto in front of the outer edge of the lead-glass calorimeter, the Lead Glass Anti, had two such sandwiches with no scintillator.

An iron ring located just downstream of the Lead Glass Anti was designed to reject events with high-angle photons escaping through the gap between the lead-glass and the LGA. The ring overlapped with the outer edge of the lead-glass array, and was 2.9 radiation lengths thick. Figure 12 shows the Iron ring, the Lead Glass Anti, and the outermost blocks of the Lead Glass calorimeter to scale in the relative positions as measured in the experiment. Note that the inner edge of the iron ring was closer to the center of the array than the LGA edge, and caused a slight decrease in acceptance.

### 3.2.2   Charged Spectrometer

To determine the momenta of charged particles the experiment used a charged spectrometer consisting of four drift chambers, two on either side of an analysis magnet. The sizes and distances from the target of each of the four drift chambers are listed in table 6.

Each chamber consisted of four planes of sense wires to measure charged particle position, two planes for the (x) direction and two for the (y) direction. Each sense wire was surrounded by a hexagon of field-shaping wires, which were held at $-2650\,V$. To reduce aging in the chambers this voltage was reduced to $-2300\,V$ between spills when no data was being taken. The sense wires of successive planes in the same view were offset by half of the distance between two wires on the same plane to resolve whether the track passed on the left or the right side of a given wire (the "left-right ambiguity"). The configuration of field and sense wires in a single view of a chamber is shown in figure 13. The distance between consecutive sense wires on the same plane was $12.70\,mm$. Between the planes of sense wires were planes of field-shaping wires at negative high voltage.
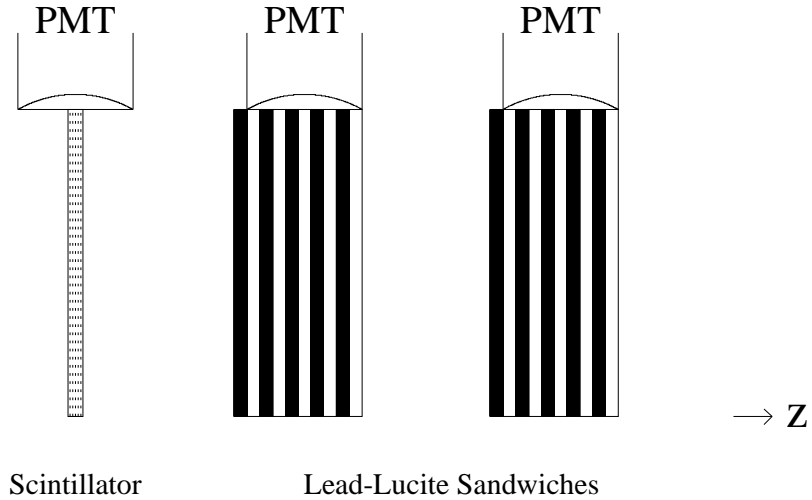


Figure 11. Schematic cross-section of a photon veto

20 cm

20 cm

Outer Ring of
Lead Glass Array     Lead Glass Anti     Iron Ring
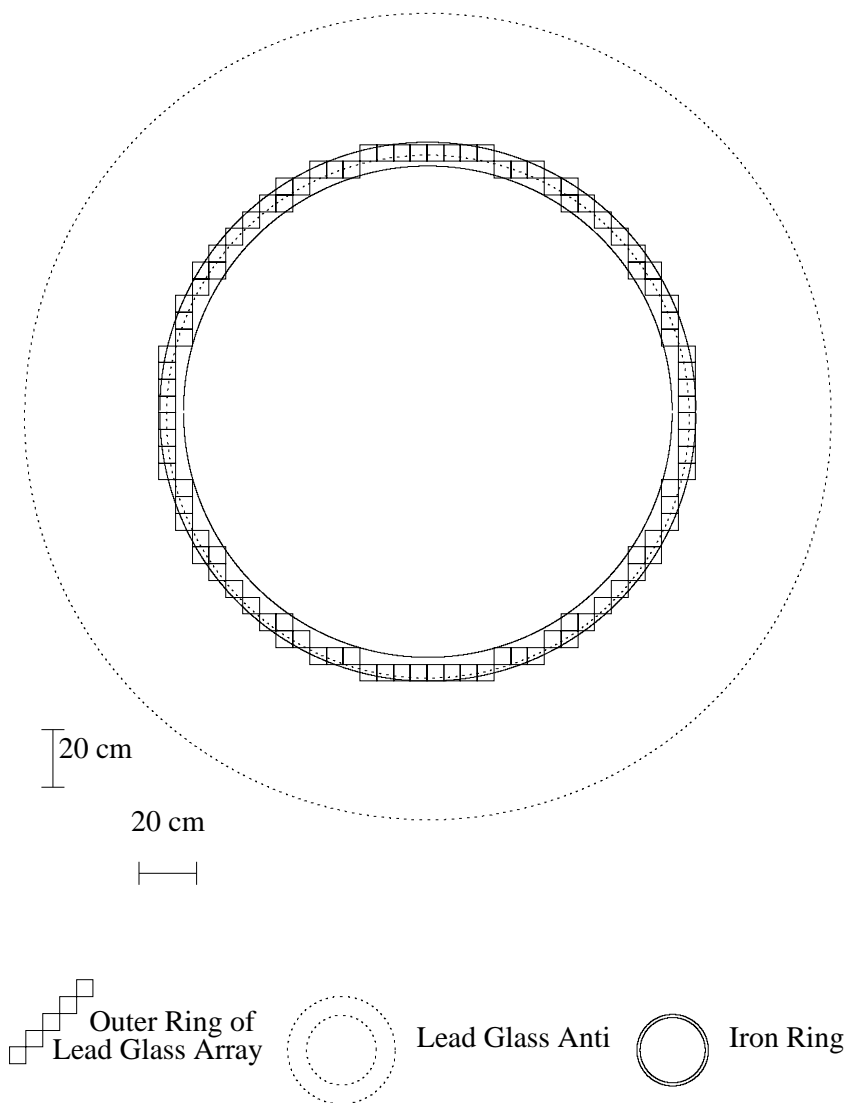
Figure 12. The Lead Glass Anti, the Iron Ring, and the outer blocks of the lead-glass calorimeter

Table 6. Charged Spectrometer Elements and Positions

| Element | Transverse Size (m) | Target Distance (m) | Number of wires |
|---------|---------------------|---------------------|------------------|
| Chamber 1 | 1.27 | 159.29 | 101(x) 101(y) |
| Chamber 2 | 1.57 | 165.87 | 112(x) 128(y) |
| Magnet | 1.49 | 168.4 | |
| Chamber 3 | 1.73 | 171.86 | 128(x) 136(y) |
| Chamber 4 | 1.78 | 176.20 | 140(x) 140(y) |

When a charged particle passed between two sense wires it would ionize the gas in the chambers that was in the path of the particle. The electrons would then drift towards the closest wire in that plane of sense wires, creating a signal (also called a "hit") on that wire. The signal for a hit is the time between the first electron avalanche hitting the wire and a common stop defined by the trigger. To calibrate the drift chambers the relation between the time of a hit on a wire and the distance between the track and the wire must be determined. The calibration procedure is discussed in detail in [1]. Since there are two planes of sense wires in each view for each chamber, a track most often leaves a pair of hits. The single-hit position resolution of the drift chambers, after much careful calibration ranged between 95 and $110\mu m$.

Track segments are then formed by considering various combinations of hit pairs between the two chambers preceding the magnet, and the two chambers after the magnet. Then, an x-track segment upstream of the magnet can be matched to one downstream of the magnet by requiring that for a given track, the segments before and after the magnet extrapolate (within errors) to the same place at the plane of the magnet.

For a given charged particle the (x) track and (y) track through the spectrometer were matched using information from the lead-glass. This will be discussed in chapter 8. Also associated with the drift chambers was a Track Processor which counted the number of hits in each chamber and verified that there were sufficient hits in each chamber to be consistent with the signal from two charged particles.

The magnet gave a $200\,MeV/c$ transverse momentum kick in the (x) direction. Since the magnet was not a perfect dipole, and since the magnetic field was not exactly parallel to the lead-glass calorimeter grid there was also a small kick in the (y) direction but this was ignored. The resulting momentum resolution in the spectrometer is

$$(\sigma_p/p)^2 = (5 \times 10^{-3})^2 + (1.4 \times 10^{-4}(p[GeV/c]))^2 \qquad (3.1)$$

where the first term is due to to multiple scattering and the second is due to the chamber position resolution. Reference [1] contains a section on the intrinsic position resolution of the drift chambers, and the multiple scattering term is a function of the amount of material (chamber gas, wires, chamber windows, etc.) in the spectrometer.
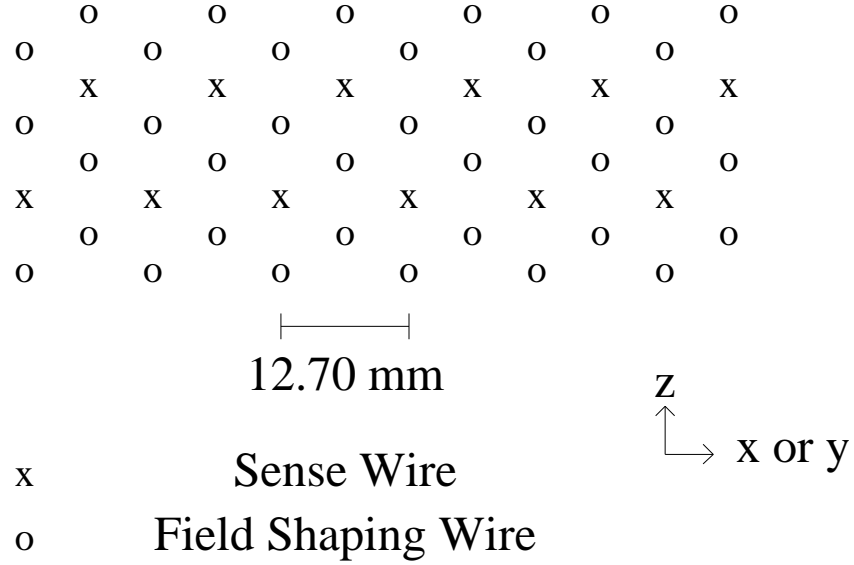


Figure 13. A cross-section of one view of a wire chamber, showing both sense wires and field-shaping wires.

Table 7. B& C Trigger Bank Positions and Sizes

| Bank | Segmentation | Target Distance (m) | Dimensions (x × y) |
|---|---|---|---|
| C Bank | Horizontal | 179.5360 | $1.9\,m \times 1.8\,m$ |
| B Bank | Vertical | 179.6350 | $2.0\,m \times 2.1\,m$ |

### 3.2.3  Charged Particle Trigger Banks

Downstream of the fourth chamber there were two banks, each one made of $1\,cm$ thick plastic scintillator. One bank was segmented vertically and the other horizontally. The segmentation allowed the trigger to select events with at least two charged tracks by requiring that at least two different scintillators in each bank fire in the same bucket. Table 7 lists the banks, their (z) positions, and their transverse dimensions. Figures 14 and 15 show the size and orientation of the counters in the two trigger planes.

### 3.2.4  Lead Glass Array

The Electromagnetic Calorimeter consisted of 804 blocks of Schott F-2 lead glass stacked in a circular array. Each block measured $5.82 \times 5.82 \times 60.17\,cm^3$ and was stacked such that the long dimension was parallel to the beam, resulting in a calorimeter that was 18.7 radiation lengths long. Figure 16 shows a schematic view of the calorimeter.

The Čerenkov light that is produced in the calorimeter was read out by a phototube which was glued to the back of the block. The signal from the phototube was then split, with one eighth of the signal going into a fast energy sum, a small amount to the Hardware Cluster Finder (HCF), and the rest to the ADC's. The fast energy sum was made by summing adjacent groups of 9 blocks in a device called an "Adder". These Adders were then summed to form a signal (total energy, or $E_t$) which was then discriminated at two different thresholds to form a trigger signal. While the ADC gate on each block was $100\,nsec$, the gate on the Adders and $E_t$ was only $30\,nsec$.

An important second-level trigger element that used the lead-glass information was the Hardware Cluster Finder (HCF), which is described in detail in reference [5]. The HCF
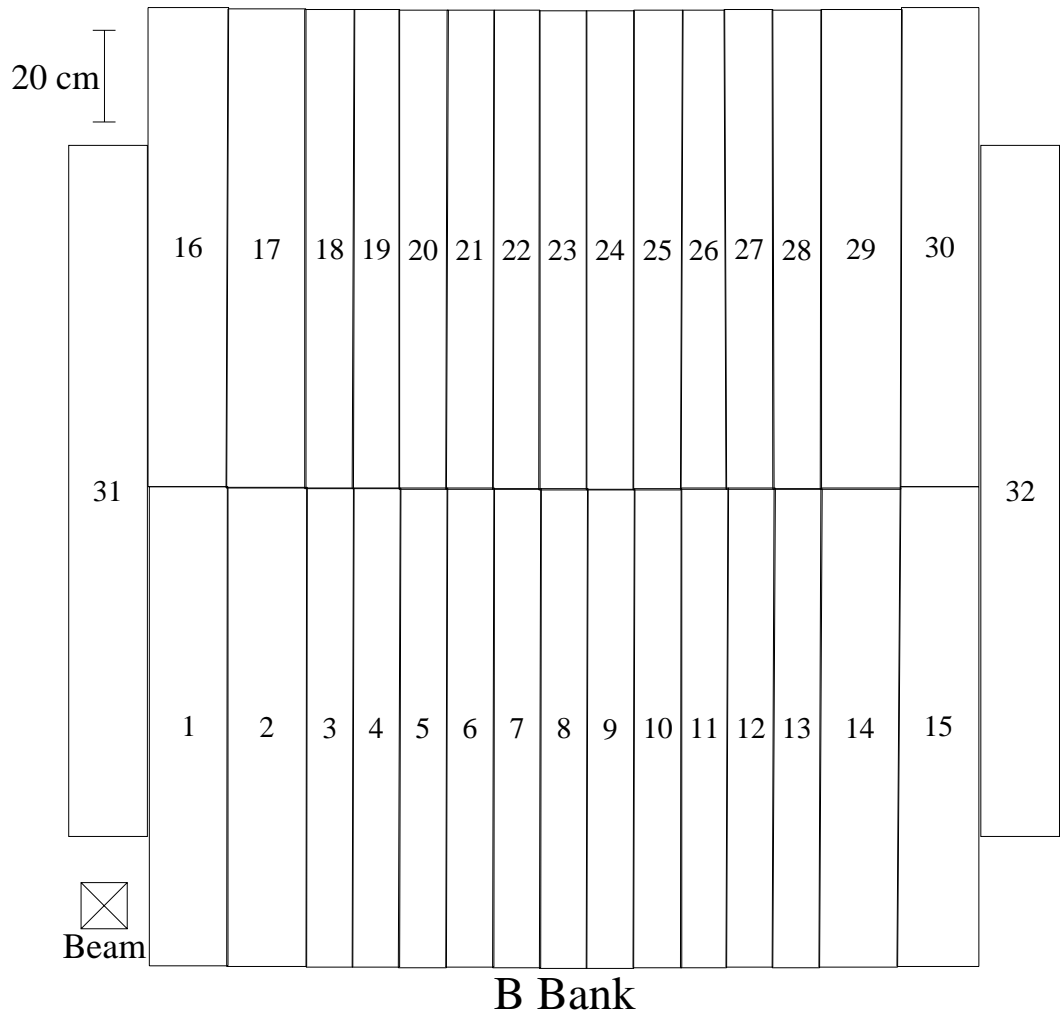
Figure 14. The B Scintillator Bank Counters

20 cm

| 13 | 1 |
|----|----|
| 14 | 2 |
| 15 | 3 |
| 16 | 4 |
| 17 | 5 |
| 18 | 6 |
| 19 | 7 |
| 20 | 8 |
| 21 | 9 |
| 22 | 10 |
| 23 | 11 |
| 24 | 12 |

Beam

## C Bank
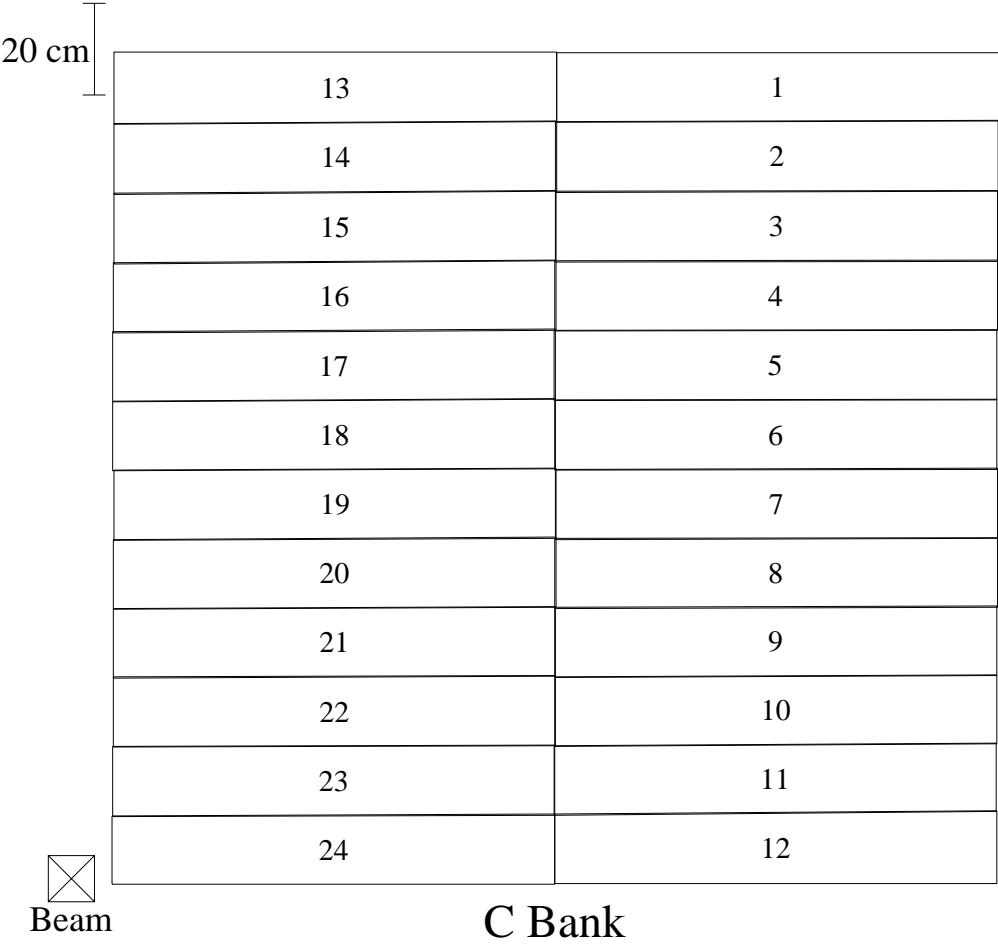
Figure 15. The C Scintillator Bank Counters
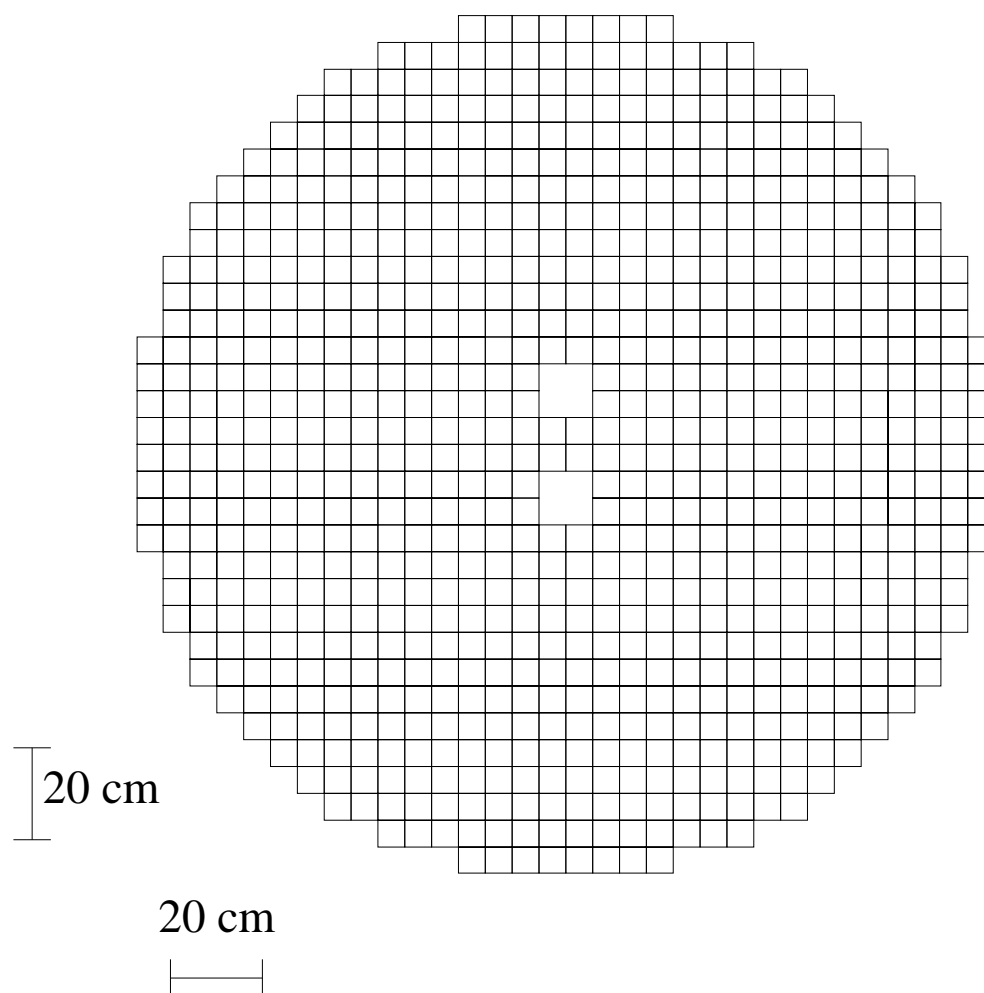
Figure 16. The lead-glass blocks as they were stacked to form the calorimeter

looked for clusters of energy arriving within a gate of $33\,nsec$, and counted the number of these clusters. By triggering on the multiplicity of clusters in a given event the trigger rate could be greatly reduced and the experiment was able to trigger on a large variety of rare decays.

### 3.2.5   Back Anti

Behind the calorimeter beam-holes, $185.047\,m$ from the target, there was a detector set up to veto events with electromagnetic particles going through the beam-holes of the calorimeter. This detector consisted of 48 layers of $0.33\,cm$ thick lead sandwiched between 48 layers of lucite, adding up to a 28.1 radiation length (1.3 interaction length) thick detector. The layers of lucite were alternately segmented horizontally and vertically. The vertically segmented layers were summed in three groups. A schematic drawing of this counter is shown in figure 17.

An electromagnetic shower would be expected to have a large signal in the first two layers but not deposit much energy in the third layer. Hadronic showers, on the other hand, would have large energy depositions in all three layers. A trigger element was formed from the Back Anti by discriminating on the energy in the first two layers, when the energy in the third layer was below $6\,GeV$. If there was more than $3.5\,GeV$ in the first two layers and less than $6\,GeV$ in the last layer then an electromagnetic particle is assumed to have showered in the Back Anti.

### 3.2.6   Hadron Shower Veto System

Behind the Lead Glass calorimeter there was a lead wall which extended past the aperture formed by the calorimeter. The wall measured approximately $2\,m \times 2\,m$ and was $5\,in$ thick, or 22 radiation lengths. Electromagnetic particles were sure to shower and then be absorbed by the combination of the lead glass and lead wall which together measured 42 radiation lengths. Hadronic showers, on the other hand, were not completely contained because there were only 2.4 nuclear interaction lengths in the calorimeter/wall combination (approximately 1.7 interaction lengths in the lead-glass, and 0.7 interaction lengths in the lead wall). Behind the lead wall was a bank of 45 scintillators of varying sizes which

comprised the hadron shower veto, and will be discussed in detail in 6. Figure 18 shows a schematic view of the counters as they appeared in the array.

### 3.2.7 Muon Trigger System

Behind the hadron shower veto was a large block of steel which served as a hadron filter. The steel measured approximately $2.4\,m \times 2.4\,m$ and was approximately $3\,m$ thick, or 20
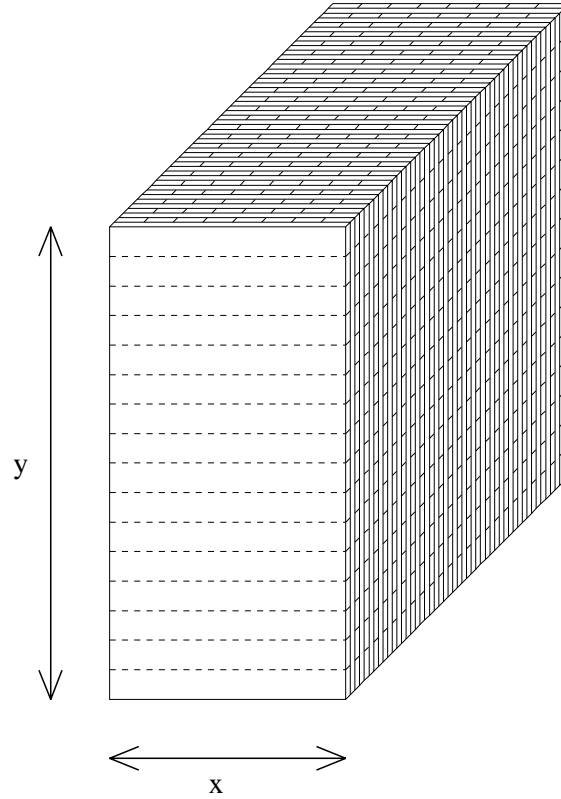


Figure 17. Schematic of the Back Anti counter
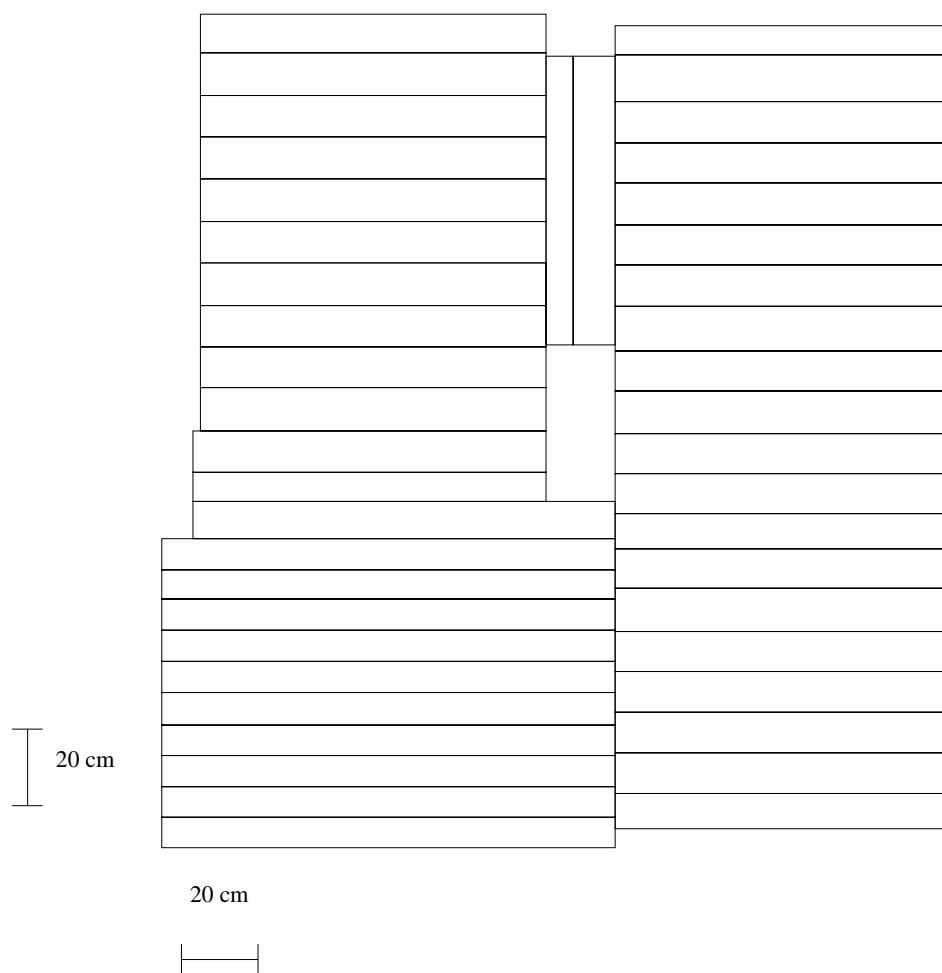
Figure 18. The Hadron Shower Veto

interaction lengths of steel. The filter stopped virtually all hadrons and only allowed the passage of muons with momentum above $5\,GeV/c$.

Behind the hadron filter were two sets of scintillator banks. One of these banks (the Mu3 Bank) consisted of 16 non-overlapping counters, each of which measured approximately $9.1\,cm \times 1.2\,m$. The counters themselves were $0.5\,in$ thick and were vertically oriented, with the phototubes to read out the signal at the bottom of each counter. There was also a bank of overlapping scintillator counters behind the steel filter which could be used at trigger level to detect the presence of at least one muon. This bank (the Mu2 bank) was $2.4\,m \times 2.4\,m$ and covered a larger area than did the muon trigger bank. The two banks and their relative sizes and counter orientations are shown in figure 19.
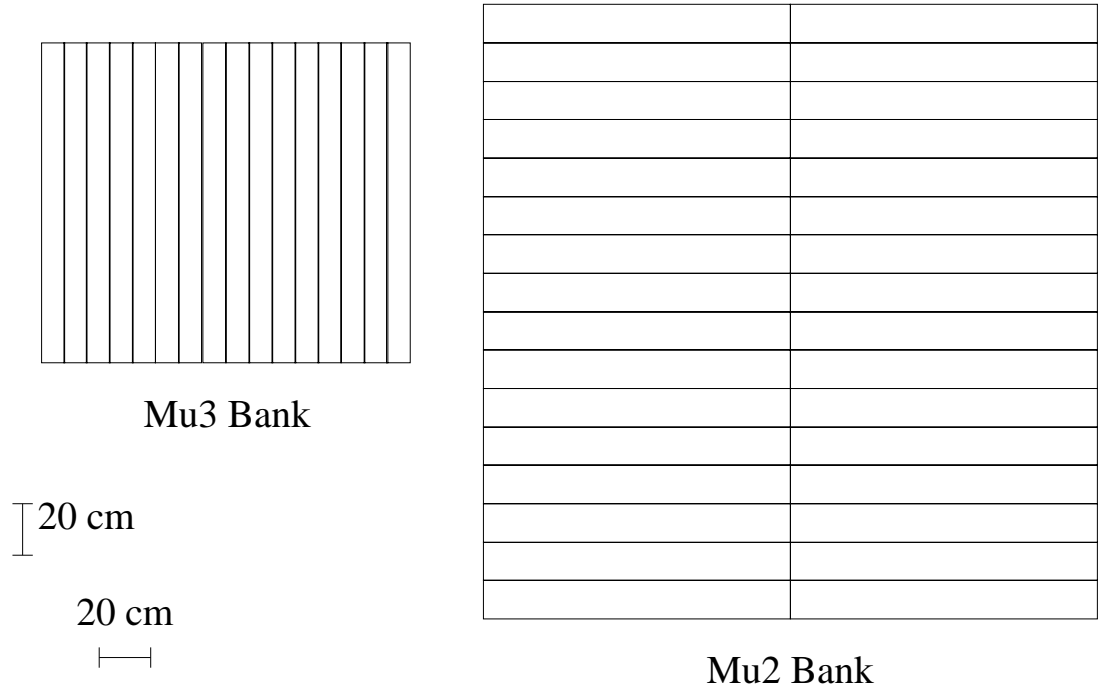


Figure 19. The Muon Trigger Banks

# CHAPTER 4

# TRIGGERS

Since E799 was an experiment designed to look for a variety of rare $K_L$ decays, as many as 15 different triggers were used at any given time. Reference [1] gives a more complete listing of all of the different triggers for various run ranges; this chapter describes only the those which were relevant to the two $K_L \to \pi^0 \ell^+ \ell^-$ searches. There were two kinds of events written to tape—those events which were used for physics analyses (physics triggers) and those taken for calibration purposes. Overall, there were about 405 million physics triggers taken, these two analyses together looked at data samples taken throughout the run which comprise about 57% of all of the data written to tape.

## 4.1   Physics Triggers

The physics triggers for these analyses were used to find either the signal or the normalization decay. In general the normalization mode trigger was designed to be as similar as possible to that of the signal mode. In this section we will describe both types, and where appropriate discuss the similarities between the $\pi^0 \mu^+ \mu^-$ and $\pi^0 e^+ e^-$ triggers.

In general, the E799 triggers were designed to maximize the number of interesting decay modes written to tape while keeping the data-taking rate manageable. For this reason, the trigger which included $K_L \to \pi^0 e^+ e^-$ events also was used to search for the decays $\pi^0 \to e^+ e^-$ and $\pi^0 \to e^+ e^- \gamma$ (from the parent decay $K_L \to \pi^0 \pi^0 \pi^0$), and is referred to as the "two-electron" trigger. The trigger which could accept $K_L \to \pi^0 \mu^+ \mu^-$ decays also could accept $K_L \to \mu^+ \mu^- \gamma$ and $K_L \to \mu^+ \mu^- e^+ e^-$ events and is referred to as the "dimuon" trigger. They were designed to accept two electrons or two muons respectively, and two or more photons and one or more photons respectively.

Table 8. $K_L \to \pi^0 \ell^+ \ell^-$ triggers and prescales. The demarkation 1(*) under the two elec-tron trigger entry represents that fraction of the run when the two electron data accepted $K_L \to \pi^0\pi^0, \pi^0 \to e^+e^-\gamma$ events, and the demarkation 14(**) under the Dalitz trigger en-try represents the small fraction of the run when the Dalitz trigger was slightly altered to increase the $K_L \to e^+e^-\gamma$ acceptance

| Date | Two-electron | Dalitz | Dimuon | Minimum Bias | Fraction of Run |
|------|--------------|--------|--------|--------------|-----------------|
| 10/13-10/19 | 1(*) | - | 1 | - | 8% |
| 10/19-10/19 | 1 | 16 | 1 | - | 14% |
| 11/9-12/28 | 1 | 14 | 1 | 3600 | 67% |
| 12/29-1/9 | 1 | 14(**) | 1 | 3600 | 11% |

For the $K_L \to \pi^0 e^+ e^-$ analysis, the normalization modes considered were $K_L \to e^+e^-\gamma$ and $K_L \to \pi^0\pi^0, \pi^0 \to e^+e^-\gamma$. Since both of these modes involve a Dalitz decay the trigger for these modes was called the "Dalitz trigger" and was prescaled by a various amount as a function of the run number. For the first 8% of the run there was no Dalitz trigger, but the two electron trigger for that part of the run also accepted $K_L \to \pi^0\pi^0, \pi^0 \to e^+e^-\gamma$ decays. For the $K_L \to \pi^0\mu^+\mu^-$ analysis, the normalization mode was $K_L \to \pi^+\pi^-\pi^0$, and these were collected in the minimum bias trigger, which was prescaled by the factor 3600. Although the dimuon trigger was taken for the same amount of time as the two-electron trigger, the minimum bias trigger was only taken for about 78% of the run. The dimuon data analyzed was therefore only that data that was taken at the same time as the minimum bias data.

Table 8 lists the dates that correspond to these different run ranges, and the triggers relevant to the $K_L \to \pi^0 \ell^+ \ell^-$ analyses that were taken during that range, and the prescale on each mode. There is a break in time in this list, and between October 19, 1991 and November 9, 1991 the detector ran in a special configuration to collect data to search for the decays $K_L \to \pi^0\gamma\gamma$ and $K_L \to \pi^0\pi^0\gamma$. These searches are described in reference [2].

### 4.1.1 Signal Modes

In every physics mode discussed in this thesis, there are two charged particles in the final state. Therefore, the charged particle part of each of triggers was the same for both the two-electron and the dimuon physics triggers. In particular, the trigger required that there be at least two hits in both the B and C scintillator banks upstream of the calorimeter ("2B2C"), with the exception of the last small fraction in the run when the Dalitz trigger was changed to require at least one hit in the C bank and at least two hits in the B bank ("2B1C"), (referred to as 14(*) in Table 8). There were also requirements on the number of hits in the drift chambers. A track processor, described in detail in reference [1], required there to be enough hits on the chambers for two charged particles (this was called "Hitcnt$_{2Trk}$"). The trigger also required that no charged particles be observed by the Photon Vetoes leaving the detector fiducial region. In particular, the counters in veto were those listed in table 5: Vacuum Anti 9, Vacuum Antis 0-4, the Magnet Anti, DRA, and the Lead Glass Anti. The thresholds on these counters were set at the signal of one minimum ionization particle at a discriminator. This veto trigger element is abbreviated by the notation

$$\overline{PHV} = \overline{VA-1} \cdot \overline{VA0} \cdot \overline{VA1} \cdot \overline{VA2} \cdot \overline{DRAC} \cdot \overline{VA3} \cdot \overline{VA4} \cdot \overline{LGA}.$$

Similarly, since neither signal mode contained any hadrons in the final state, both the two electron and dimuon triggers had the Hadron Shower Veto in the trigger. This will be discussed in detail in chapter 6.

This is where the similarities between the triggers for the two searches end. We will now discuss in particular the trigger requirements specific to the different lepton triggers. The differences lie in the different signals expected in the lead-glass calorimeter, and also the different requirements on the signal in the muon trigger plane.

**Two Electron Trigger**

The electrons in the decays were required to deposit clusters of energy in the lead-glass. These clusters and clusters from photons in the decay were then required to be found by the Hardware Cluster Finder (HCF). As mentioned in Chapter 3, the HCF had a gate of $33\,nsec$ and a threshold of about $2.4\,GeV$ in a single block. Since this trigger looked

for many decays, including $K_L \to \pi^0 \pi^0 \pi^0, \pi^0 \to e^+ e^- \gamma$, and $K_L \to \pi^0 \pi^0 \pi^0, \pi^0 \to e^+ e^-$, it accepted events with either 4 or more than 5 clusters found by the HCF. For the first 8% of the run the two-electron trigger also accepted 5 cluster events, and this data was used to find $K_L \to \pi^0 \pi^0, \pi^0 \to e^+ e^- \gamma$ events for normalization for that part of the run. Finally, since all the decay products deposit their energy in the lead-glass, and the energies of the Kaons which could be geometrically accepted by the detector were between 35 and 220 $GeV$, there was a trigger requirement of 51 $GeV$ on the fast sum made on the energy in the calorimeter ($E_t$). This trigger requirement will be referred to later as ETHI, and lowered the trigger rate substantially.

To veto on events with electromagnetic particles going through the beam-holes of the calorimeter there was a veto formed on the sum of the energies in the first two layers of the Back Anti counters. When the energy in the third layer of the BA counter was below 6 $GeV$, the sum of energies in the first two layers was checked. If this sum of energies was above 3.5 $GeV$ the event was vetoed. This trigger element will be referred to as the $BA\gamma$ veto.

**Dimuon Trigger**

The requirements made on the calorimeter for the dimuon trigger were significantly less stringent than those made on the two-electron trigger. First of all, there was a much lower minimum requirement on the fast sum of energy in the calorimeter: for the dimuon trigger, this requirement was about 6 $GeV$ and will be referred to later as ETLO. Second of all, although the HCF was turned on for those events and calculated the number of "Hardware Clusters", no requirement was made on the number of those clusters at trigger level.

Finally, in the dimuon trigger there was a requirement on the muon trigger plane (Mu3). The trigger required that two non-adjacent counters in the muon trigger plane behind the hadron filter fire.

### 4.1.2 Normalization Modes

Since the requirements on the normalization mode triggers were almost identical to those used for the signal modes, this section describes only the differences between the normalization and signal triggers for the two different analyses.

**Dalitz Trigger**

Because of the preponderance of low invariant $e^+e^-$ mass pairs in Dalitz decays (shown in figure 6), the Dalitz trigger was a slightly modified version of the two-electron trigger. In particular, a low invariant $e^+e^-$ mass event tends to have two electrons close together, and they often share hits in the first drift chamber. A hit-counting requirement was used, referred to as $rmtHitcnt_{Dalitz}$, which only required one hit in the y-view of the first chamber, Chamber 1. The tracking done in the analysis between the signal and normalization was identical, though, so in this analysis the trigger difference did not have a noticeable affect on the acceptance.

The other two differences in the Dalitz trigger were associated with the calorimeter. The decay $K_L \to \pi^0 \nu \overline{\nu}$, $\pi^0 \to e^+e^-\gamma$ was also searched for using events from the Dalitz trigger. For these decays the neutrinos are expected to carry off some of the $K_L$ energy and so the minimum energy requirement of the $e^+e^-\gamma$ combination should be considerably lower to maintain reasonable acceptance. To account for this there was a lower requirement on the fast sum of energies in the calorimeter, namely $6\,GeV$, or trigger requirement ETLO. In general, however, $K_L \to e^+e^-\gamma$ decays found in this trigger also satisfied the ETHI trigger requirement. Finally, the number of HCF clusters allowed in this trigger were three or five clusters. Because of the lower HCF multiplicity requirement and the lower minimum energy requirement on this trigger the prescale had to be higher than the two-electron trigger, as is shown in table 8.

**Minimum Bias Trigger**

The minimum bias trigger was used to find many of the more common $K_L$ decays, and as the name suggests had very few requirements. Even if one were to design a trigger specifically

for $K_L \to \pi^+ \pi^- \pi^0$ decays it would be different from the dimuon trigger in several ways, due to the presence of hadrons among the final state particles. Since hadrons can shower in the lead-glass or the lead wall, several requirements and vetoes were omitted, not only at trigger level, but at all analysis levels.

First of all, there was no requirement on the amount of energy in the fast energy sum, and no requirement on the Hadron Shower Veto. Finally, there was obviously no requirement on the muon trigger bank. These differences were all studied in detail and systematic checks were performed to quantify the understanding of these differences (see section 11.3).

### 4.1.3 Summary of Physics Triggers

The two electron trigger for most of the run, in summary was:

$$2B \cdot 2C \cdot E_t Hi \cdot \overline{MU1} \cdot \overline{PHV} \cdot \overline{MU3} \cdot \overline{BA_\gamma} \cdot \text{Hitcnt}_{2track} \cdot HCF(4,6,7,8),$$

and for the first 8% of the run was:

$$2B \cdot 2C \cdot E_t Hi \cdot \overline{MU1} \cdot \overline{PHV} \cdot \overline{MU3} \cdot \overline{BA_\gamma} \cdot \text{Hitcnt}_{2track} \cdot HCF(4,5,6,7,8),$$

Averaged over all of the run, this trigger comprised about 33.5% of the total data written to tape. The Dalitz trigger which contained the normalization events for the two electron trigger was

$$2B \cdot 2C \cdot E_t Hi \cdot \overline{MU1} \cdot \overline{PHV} \cdot \overline{MU3} \cdot \overline{BA_\gamma} \cdot \text{Hitcnt}_{Dalitz} \cdot HCF(3,5),$$

for most of the run. For the last section of the run, the Dalitz trigger was:

$$2B \cdot 1C \cdot E_t Hi \cdot \overline{MU1} \cdot \overline{PHV} \cdot \overline{MU3} \cdot \overline{BA_\gamma} \cdot \text{Hitcnt}_{Dalitz} \cdot HCF(3,5),$$

This trigger comprised about 9.7% of the data written to tape during the run. The dimuon trigger is then

$$2B \cdot 2C \cdot E_t Low \cdot MU3 \cdot \overline{MU1} \cdot \overline{PHV} \cdot \text{Hitcnt}_{2Track}.$$

and this data comprised about 12% of the data taken during the run. Finally, the minimum bias trigger is:

$$2B \cdot 2C \cdot \overline{PHV} \cdot \text{Hitcnt}_{2track},$$

and after the prescale of 3600 this trigger comprised only 2.2% of the total number of events written to tape.

## 4.2 Calibration Triggers

Along with the various physics triggers, there was also a lot of data taken for calibration purposes. The calibration data can be classified as being in one of two categories—calibration triggers taken during the physics data-taking runs to track drifts in the electronics, and calibration triggers taken in special runs which tracked overall changes in gains and thresholds. The "during-the-run" triggers constituted only about 1.3% of the data taken during the individual runs , while the special runs were equivalent to about 13% by volume of the total amount of physics data taken during the entire physics run.

### 4.2.1 During the Run Triggers

**Accidental Trigger**

Very important to the searches described in this thesis is the accidental trigger. To do a search for a decay at the $10^{-9}$ level the experiment ran with very high intensity beams. By looking at reconstructed $K_L \to \pi^0 \pi^0 \pi^0$, $\pi^0 \to e^+ e^- \gamma$ decays and the occupancy in the Back Anti, the number of $K_L$'s decaying in flight or arriving at the Back Anti was determined to be 0.05 per bucket [1]. The occupancy of hadron interactions in the last layer of the Back Anti was even higher, however, at 0.09 per bucket.

As was mentioned previously, there were several different types of neutral particles in the beam, whose decay products could eventually hit the detector and cause "accidental" signals. Also, beam neutrons could scatter off the collimators or shower in the B or C scintillator banks and create accidental activity in the detector. To account for this activity a prescaled trigger was taken during normal running which took snapshots of the detector. The trigger for these snapshots was a muon telescope located upstream of the rest of the detector yet outside the remainder of the detector acceptance. The telescope consisted of two scintillators which were on the order of $20\,cm^2$ separated by a few meters, located about $40\,m$ from the target. The telescope was aimed at the target, so these accidental

triggers were correlated with proton beam activity yet uncorrelated with individual $K_L$ decays in the detector. These events were then included in the Monte Carlo simulation for every decay mode studied, and were indispensable for simulating certain backgrounds to the signal modes. Figure 20 shows a schematic picture of the muon telescope used for the accidental trigger.

**Flashers**

During the normal physics data-taking runs the gains on each of the lead-glass blocks were tracked. To do this the light from a xenon flash lamp was split, using optic fibers, and sent to the far end of each lead-glass block. The spectrum from the xenon flash lamp was roughly equivalent to the Čerenkov light spectrum, and the amount of light transmitted to each block was about as much as that resulting from a $38\,GeV$ energy deposition. By looking at the RMS of a flasher signal one can roughly determine the photostatistics of each of the lead-glass blocks, as will be described in section 5.4.2. Events which were comprised of the 804 signals resulting from the xenon flash lamp were called "flasher events", and were taken every 2 seconds.
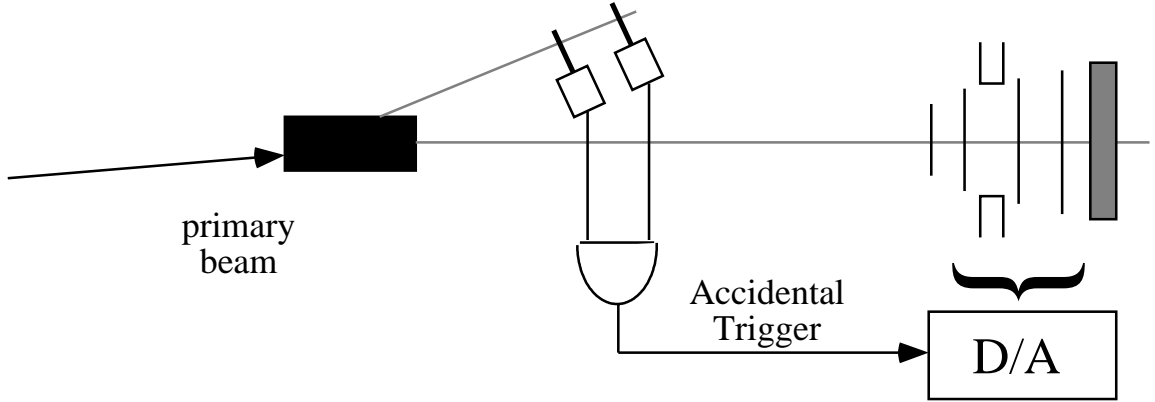


Figure 20. A schematic diagram of the accidental trigger

**Pedestals**

An important parameter to know for every counter digitized by ADC's in the experiment was the ADC pedestal for that counter. This varied on a spill to spill basis due to random electronic noise. Before it was read out the physics data were pedestal subtracted, but in order to study fluctuations on the pedestals there were also events taken every 1 or 2 seconds which contained only pedestal information for each ADC.

## 4.2.2 Special Runs

During the run there were several special data sets which were taken, for which the detector configuration had to be altered dramatically and hence no physics data could be taken concurrently. In this section we describe these runs and the ways in which the configuration of the detector was changed.

**Glass Calibration**

The lead-glass was calibrated by a series of runs where a special beam of electrons and positrons was used to illuminate the glass. These particles were made by first increasing the photon content by removing the lead absorber (which was described in section 3.1) and then placing a copper-titanium sheet in the beam to convert the photons to electron-positron pairs, as will be discussed in detail in section 5.5.1. The intensity for these runs was about a factor of 10 lower than the normal operating intensity to decrease the amount of accidental activity in the lead-glass.

During the glass calibration the trigger was designed to look for two electrons. The trigger for these calibrations was:

$$2B \cdot 2C \cdot \text{Hitcnt}_{2track}.$$

To trigger on more events at the outer edges of the array there was also a special trigger bit set BCPH which was a combination of B and C counters which consisted of a square ring illuminating the rows and columns of the lead-glass several blocks from the center of the array. Overall the experiment took about 19.3 million events for glass calibration.

**Chamber Alignment**

In order to use the drift chambers for precision tracking and optimal momentum resolution, it was necessary to determine their positions accurately. To determine the chamber positions we looked at muon tracks which passed straight through the spectrometer. To get this data the experiment took special runs about once a day where the analysis magnet was turned off and the trigger was simply one hit in any B bank scintillator and one hit in any of the MU2 scintillators. By looking at muons that traveled in a straight line through the apparatus the chambers could be calibrated and their positions understood to a high degree of accuracy. This will is discussed in detail in Reference [1]. There were in total 124 runs which were used for drift chamber position calibrations, summing to 24.8 million events.

**Muon System Calibration**

Finally, to supply a large sample of muons which have been momentum analyzed to use for muon scintillator bank efficiencies, there were several runs which were taken with the beam redirected such that it did not hit the E799 target, but rather, hit a beam stop located 1420 feet upstream of the target. The beam-stop itself was a water cooled copper block which was 18.17 feet long, so for these runs the only particles able to traverse the beam-stop were muons. The trigger for these events was simply one or more counters in both the B and C scintillator banks. There were about 6 such runs taken during the course of the experiment, and are listed in table 12. During the course of the run there were about 10.3 million triggers written to tape for muon calibration.

## 4.3   Data Tapes

There were in total 227 runs where usable physics data was taken, and of these there were 139 runs where usable dimuon data was taken. Overall, there were 405 million different physics triggers written to tape. A run which filled four tapes lasted about 8 hours under ideal conditions and contained about $5 \times 10^6$ events. Each run wrote data to either three or four 8mm tapes, each of which can hold about $2\,Gbytes$ of information. In total there was about $1\,Tbytes$ of data on 1330 tapes. Since there were many analyses which had heavily

prescaled triggers, the raw data on these tapes were split into 8 streams before analysis. In particular, there were three streams whose outputs were used in the searches described here. One stream contained all of the two-electron and Dalitz triggers, and another contained all of the dimuon triggers as well as the minimum bias data. Finally, there was a stream which contained only the accidental events. The two electron data was written onto 227 8mm tapes, the dimuon and minimum bias data was written onto 139 8mm tapes, and the accidental data filled the equivalent of 3 8mm tapes.

### 4.3.1 Two-Electron Data

Once the two-electron data was distilled onto 227 tapes, a further data reduction was completed, called the "crunch". The surviving events from the two-electron crunch fit on 16 8mm tapes, which were then further distilled to very small data sets with both $K_L \to \pi^0 e^+ e^-$ normalization samples and the signal sample separated. The crunch is described in detail in chapter 8.

### 4.3.2 Two-Muon Data

There was also a crunch performed on the dimuon data to distill it from 139 tapes which included candidates for the decay $K_L \to \pi^0 \mu^+ \mu^-$ as well as the decays $K_L \to \pi^0 \mu^\pm e^\mp$ and $K_L \to \pi^0 \pi^0$, $\pi^0 \to \mu^\pm e^\mp$. The surviving events from the muon crunch which included the normalization sample fit onto 3 8mm tapes.

# CHAPTER 5

# Electromagnetic Calorimeter

## 5.1    Overview

The lead glass calorimeter was used to measure the energies and positions of photons and to identify electrons. Due to the short lifetime of the $\pi^0$ particle ($c\tau = 2.5 \times 10^{-8}\,m$), one can assume the photons from the $\pi^0$ decay were produced at the $K_L$ decay point, which is known by reconstructing the vertex from which the $e^+e^-$ or the $\mu^+\mu^-$ pairs originate. $M_{\gamma\gamma}$ can then be measured using the following:

$$M_{\gamma\gamma}^2 = \frac{E_1 E_2 r_{12}^2}{(z_{\text{vertex}} - z_{\text{pbg}})^2} \tag{5.1}$$

In this equation $E_1$ and $E_2$ are the energies of the two photon candidates in the decay, $r_{12}$ is the separation at the lead glass between the two photons, and $(z_{\text{vertex}} - z_{\text{pbg}})$ is the distance between the (z) positions of the track vertex and the lead glass calorimeter.

Our ability to discriminate between neutral pions and random pairs of photons depends crucially on the $\pi^0$ mass resolution. Given equation 5.1, the $M_{\gamma\gamma}$ resolution ($\sigma_{M_{\gamma\gamma}}$) is

$$\frac{\sigma_{M_{\gamma\gamma}}}{M_{\gamma\gamma}} = \frac{1}{2} \left[ \left( \frac{\sigma_{E_1}}{E_1} \right)^2 + \left( \frac{\sigma_{E_2}}{E_2} \right)^2 + 8 \left( \frac{\sigma_x}{r_{12}} \right)^2 + 4 \left( \frac{\sigma_z}{z} \right)^2 \right]^{\frac{1}{2}} \tag{5.2}$$

where $\sigma_{E_{1,2}}$ are the energy resolutions of photons 1 and 2, $\sigma_x$ is the one-dimensional position resolution of photons in the calorimeter, and $\sigma_z$ is the resolution on the (z) position of the vertex. Since the energy resolution dominates the $M_{\gamma\gamma}$ resolution, by optimizing the calorimeter energy resolution through accurate calibration, one optimizes the $M_{\gamma\gamma}$ resolution.

Still another aspect of the glass whose importance cannot be overlooked is its ability to identify electrons. An electron hitting the glass will shower and should leave all of its energy

in the calorimeter. Since the lead-glass is only 1.7 nuclear interaction lengths a hadron, if it showers at all, is not likely to deposit all its energy in the calorimeter. By requiring the ratio of a given particle's cluster energy and its momentum as measured by the spectrometer to be close to unity we ensure that the particle associated with both the track and cluster is an electron. The resolution of this ratio is again dominated by the energy resolution, since the track resolution is several times smaller than the calorimeter energy resolution. Recall that the momentum resolution of the spectrometer is

$$(\sigma_p/p)^2 = (5 \times 10^{-3})^2 + (1.4 \times 10^{-4}(p[GeV/c]))^2 \qquad (5.3)$$

By comparison, the electron energy resolution for a $5\,GeV$ electron is approximately 4.5%. As the electron energy resolution improves, so does the calorimeter's ability to distinguish between electrons and hadrons.

In this chapter the mechanisms responsible for energy measurements in the calorimeter and the corresponding Monte Carlo simulation which was used to characterize the detector will be outlined. The calibration procedure and the resulting energy and position resolutions for both electrons and photons will then be described. Since an extensive description of the lead-glass calorimeter, which was also used in E731, can be found in reference [4], only the most salient features of the detector and new issues pertinent to this experiment will be outlined. The two major differences between this detector and the one described in reference [4] are the extent of the radiation damage of the lead-glass blocks, and the fact that the calorimeter fiducial acceptance was extended closer to the beam-holes. The last section of this chapter describes efforts made in this experiment to instrument one of the beam-holes with $BaF_2$, a new and potentially radiation-hard scintillator.

## 5.2 Physical Attributes of the Calorimeter

The calorimeter consisted of 804 blocks of Schott F-2 lead glass stacked in a circular array (see figure 16). Each block measured $5.82 \times 5.82 \times 60.2\,cm^3$ and was stacked such that the long dimension was parallel to the beam. Since the radiation length of the lead-glass was $3.21\,cm$ the detector was 18.7 radiation lengths long. Relativistic particles (largely electrons)

in the electromagnetic showers emit Čerenkov light. The lead-glass is transparent to the Čerenkov light that is radiated by the charged particles in the shower, and the light is collected by the phototube (PMT) located at the back of the block. The charge output of the phototube is proportional to the amount of light incident on the tube. The signal on the PMT is then split, with a fraction going to an Adder, and the remainder going to an ADC. The Adder gate is $30\,ns$ and the hardware cluster finder gate is $33\,ns$. The ADC gate on each lead-glass block is $100\,ns$.

Other important parts of the calorimeter system were the Adders and the Hardware cluster finder (HCF), which were described in section 3.2.4. The Adders were used to make a fast sum of the total energy in the calorimeter to be used at trigger level. The HCF looked for local clusters of energy in the blocks, and then counted up the number of such clusters. To be efficient, both of these components required that a given PMT signal from a block correspond to roughly the same quantity of energy deposited, independent of which block had the energy deposition. At six different points in the run, the blocks were calibrated and the block gains were matched to $\sim 5\%$ by tuning the voltages on the phototubes. After the run, the calibration data was used to fine-tune these gains. This chapter describes the calibration procedure that was used for gain matching during the run as well as some details of fine-tuning of the gains once the run was over.

## 5.3    Shower Development

In order to understand how to translate the energy of an electromagnetic shower into a particular number of photons incident on the photocathode in the PMT, we have to assume a model for shower development, calculate the amount of light emitted by shower particles, and finally, determine how much of the light gets transmitted through the glass. To understand the shower development we use the program EGS [11]. Based on the chemical composition of the lead-glass, EGS generates electromagnetic showers by simulating Bhabha, Moller, and Compton scattering, pair production, and bremsstrahlung. The incident electron scatters to create a photon which then undergoes pair production to create still more electrons at lower energies which scatter and create more photons. By emitting

Čerenkov radiation the electrons in the shower transfer a fraction of their energy to light. Most of the electrons energy is lost by ionization losses. The distribution of the energy deposited by a given shower can be represented by a function $f(E, x, y, z)$, which is normalized in the following way:

$$\int f(E, x, y, z) dx dy dz = 1$$

The size of the EGS model calorimeter for the lead glass is a $7 \times 7$ block array which is 30 radiation lengths long. The energy depositions for each showering particle are stored in an array which has 35 bins each in (x) and (y) and 60 bins in (z). Given several EGS showers, the average fluctuations in shower energy deposition can be calculated. Although the transverse shower fluctuations are small on the transverse scale of the blocks, in general the longitudinal distribution of energy can be quite different, from shower to shower and as a function of energy. For low energy showers, the depth at which the energy is deposited can fluctuate widely, while for higher energy showers those fluctuations are smaller. Define

$$f(E, z) = \int_{x,y} f(E, x, y, z) dx dy$$

Figure 21 shows a few sample $f(E, z)$ distributions for single showers at four different energies. One can see from these plots how much the showers fluctuate as well as how the (z) position where the most energy is deposited, or the shower maximum, increases for increasing energy. In general the average shower maximum, $t_{max}$, increases as a logarithmic function of energy, in the following way:

$$t_{max} = a + b \log E$$

where $E$ is the energy of the shower. Figure 22 shows the average longitudinal energy deposition for many showers averaged together for several different energies.

EGS showers can also be used to determine how much energy is deposited in the central 9 blocks of the array that are considered as a cluster, as well as how much energy leaks out the back of the blocks. Figure 23a shows the average energy leakage out the back as a function of energy. EGS predicts that only 85% of the total energy is contained in the central block of the shower. To account for the transverse spread of energy deposition, a cluster is defined as the sum of energy in the blocks in a $3 \times 3$ array, with the center block
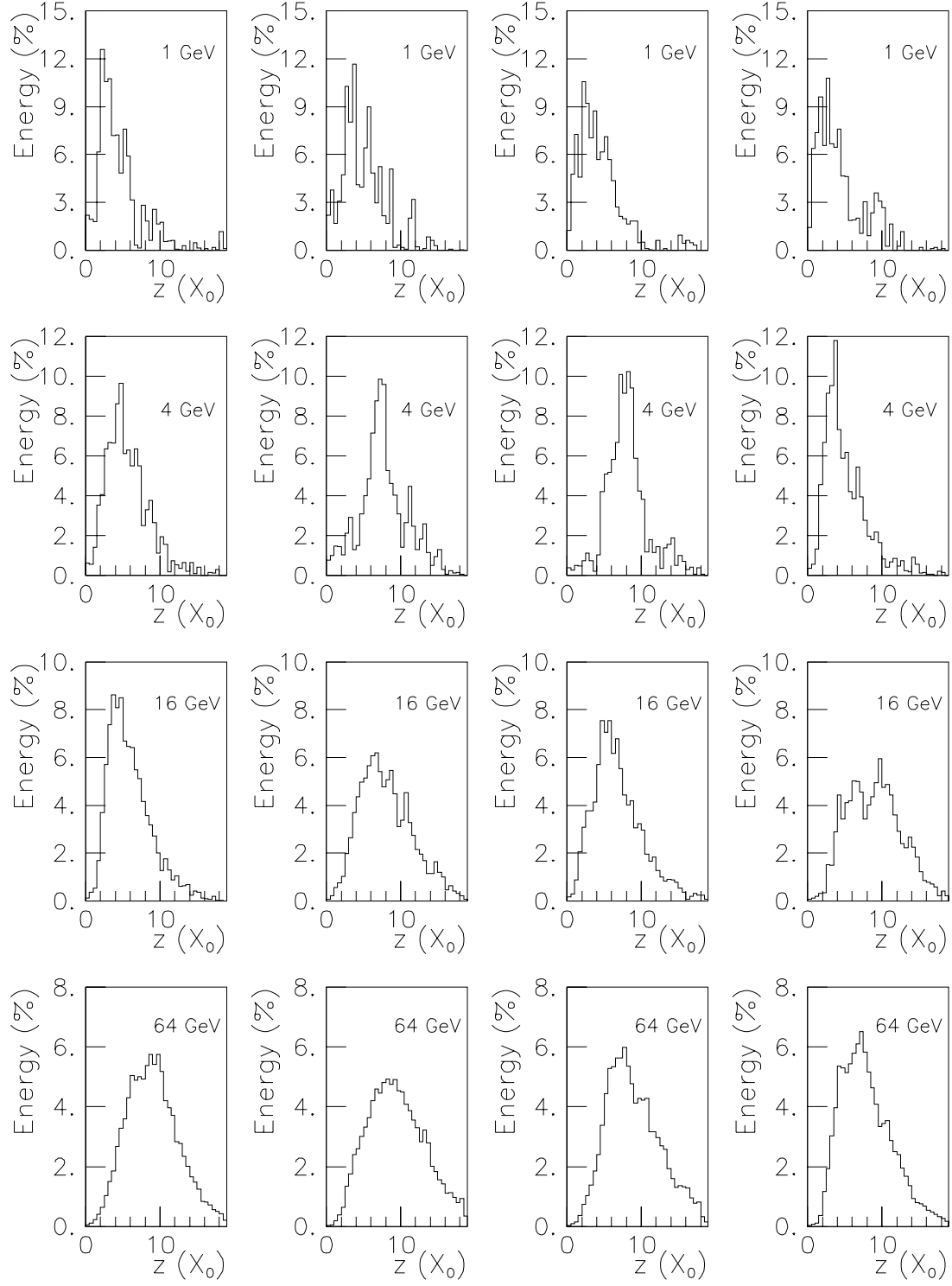
Figure 21. Longitudinal energy distributions (f(E,z)) of a few EGS showers at $1, 4, 16,$ and $64\,GeV$

surrounding the block of maximum energy. Corrections are then put in by hand which account for the extra 2.5% of energy that would leak into blocks that are farther away. Figure 23b shows that the fraction of energy that is contained in a $3 \times 3$ array for showers starting in the center of the central block of the array is constant as a function of shower energy to $\sim 1\%$.

The intrinsic resolution of the calorimeter depends on how much these energy depositions fluctuate. Even if there were no absorption of the Čerenkov light there would still be fluctuations due to the finite size of the calorimeter. Figure 24 shows the RMS on the
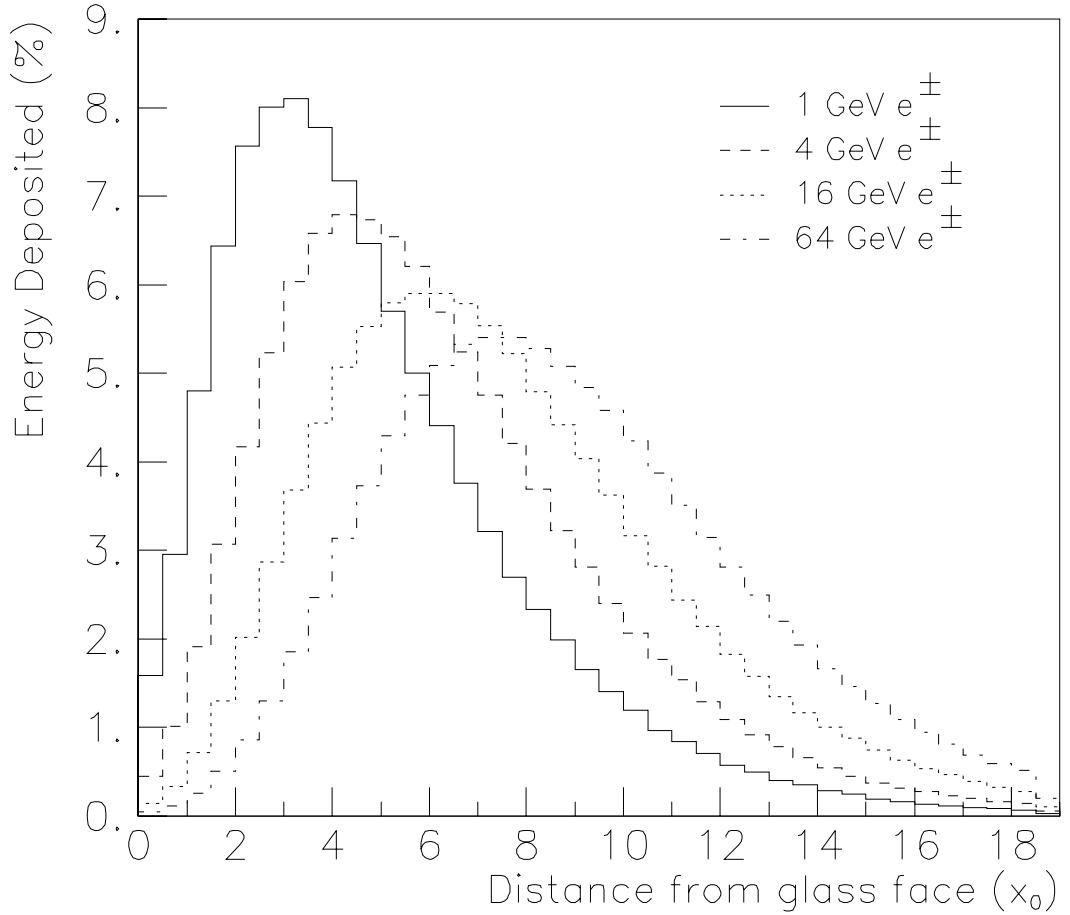


Figure 22. The average longitudinal energy distributions for EGS showers at energies of $1, 4, 16$, and $64 \, GeV$
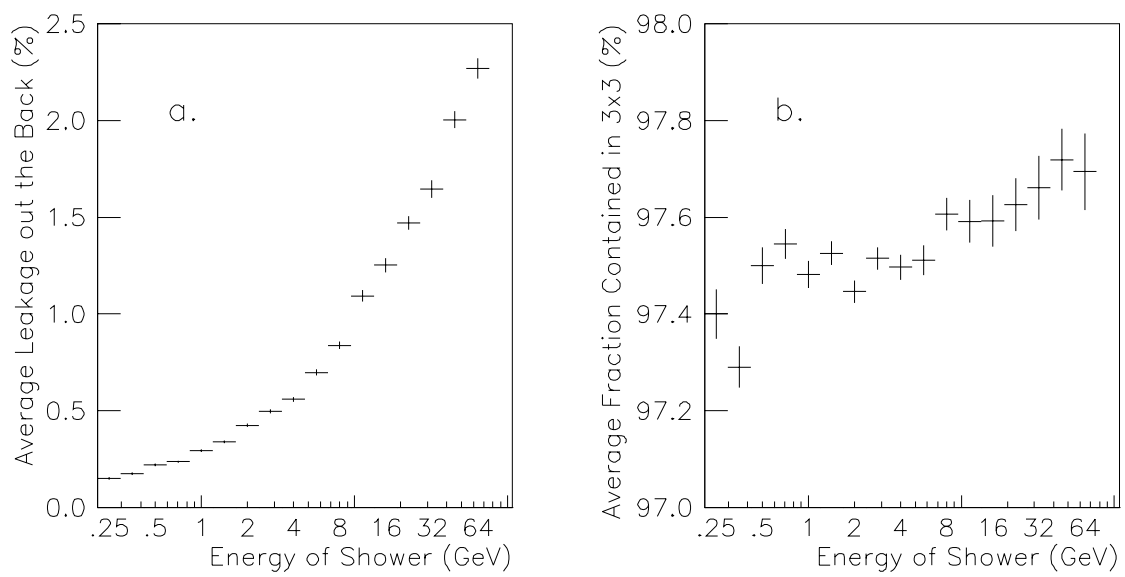
Figure 23. a. The fractional energy leakage out the back of the lead-glass as a function of energy. b. The fraction of the shower contained in a $3 \times 3$ block array of lead-glass as a function of energy

distributions of leakage for different energies. Note that the fluctuations on the leakage out the side of the array are largest for low energy showers, and the fluctuations on the leakage out the back of the array are largest for high energy showers.

## 5.4  Light Production and Collection

Once we have a model for how the electromagnetic shower deposits energy we need to understand how the energy is translated into a light signal, and then how that light is transmitted to the PMT. First of all, the amount of light emitted for a given deposition of energy must be weighted by the probability that the charged particles in question will radiate Čerenkov light, namely

$$1 - \frac{1}{n^2 \beta^2}$$

where n is the index of refraction of the lead-glass (1.6 ) and $\beta$ is the ratio of the particle's speed to the speed of light. The Čerenkov light is then emitted at an angle with respect to
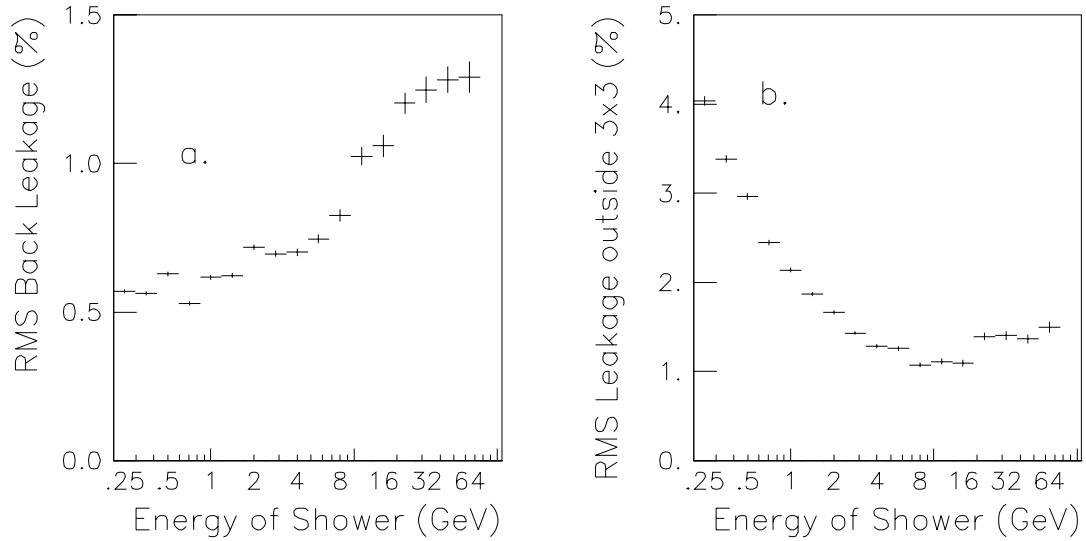


Figure 24. a. The fluctuations (RMS) on the amount of energy that (a) leaks out the back of the lead-glass array and (b) leaks out the sides of a $3 \times 3$ array as a function of energy.

the direction of the radiating particle of $\theta_C$, such that

$$\cos\theta_C = \frac{1}{n\beta}$$

The fact that $\beta$ is always less than 1 ensures that for a charged particle traveling straight through the array, $\theta_C$ is also less than the angle of total internal reflection. Secondary particles in the electromagnetic shower may be traveling at a small angle with respect to the original particle and thus emit light which is above the angle for total internal reflection, but the amount of light lost due to this effect is negligible.

A much larger effect which causes light loss is absorption. The amount of light absorbed is an exponential function of the distance the light travels. For light emitted at some distance $z_e$ from the front of the lead-glass block at an angle $\theta_C$, the total distance traveled before it reaches the PMT is

$$\frac{L - z_e}{\cos\theta_C}.$$

If we define $\alpha_C$ as the absorption in units of fractional amount of energy per radiation length, then the fraction by which a given signal of light will decrease is simply

$$e^{\left(-\alpha_C \frac{L - z_e}{cos\theta_C}\right)},$$

where the quantity $L - z_e$ is measured in radiation lengths. In fact $\alpha_C$, the index of refraction and therefore $\theta_C$, and the quantum efficiency of the photocathode are all wavelength dependent. By integrating over the relevant wavelengths and simplifying the above equation by the notation

$$\alpha = \frac{\alpha_C}{cos\theta_C},$$

we can calculate the total intensity of light reaching the photocathode, $I$, by weighting every fraction of energy deposited at a distance $z_e$ from the front of the block by the absorption factor. This can be written as

$$I = g_0 E \int_0^L f(E, z_e) e^{-\alpha(L - z_e)} dz_e,$$

where $g_0$ is an overall gain constant in photoelectrons per GeV for a $1\,GeV$ shower, and $E$ is the incident particle's energy. If shower development were to be approximated by assuming

all of a shower's energy is deposited at the shower maximum, $t_{max}$, and if $t_{max}$ is a linear function of the log of the energy E, then

$$I \propto E^r$$

where $r$ is a linear function of $\alpha$. However, all of the energy is not deposited at the shower max but is deposited throughout the length of the block. By using the various EGS showers one can determine an average correction due to the absorption of Čerenkov light, in the following way: Define $C(E, \alpha, l)$ as the average over many showers of the expected light output of a block:

$$C(E, \alpha, l) = \frac{\langle \int_0^l f(E, z_e) e^{-\alpha(L-z_e)} dz_e \rangle}{C_\alpha}$$

where $C_\alpha$ is the expected decrease of energy for a $1\,GeV$ shower:

$$C_\alpha = e^{-\alpha(L-z_{1GeV})}, z_{1GeV} = 5.157$$

and $z_{1GeV}$ is defined as the average number of radiation lengths for the shower maximum of a $1\,GeV$ shower. With this normalization, the function $C(E, \alpha, l)$ (also called C-light correction) is close to unity. There is a more extensive discussion of the $C(E, \alpha, l)$ corrections that are done for this experiment in reference [1]. While in the previous experiment, E731, the C-light corrections ranged from between 1.0 (no correction) to 1.15 [4], in E799 these corrections were at times as high as 2.0, within the energy range of 1 to $64\,GeV$. Since electrons start showering at the beginning of the block, $l = 0$, and $I$ is simply

$$I = g_0 C_\alpha E C(E, \alpha, 0).$$

## 5.4.1   Photon Shower Development

Photon showers differ from electron showers only because the photon travels some distance in the lead-glass before converting to an electron-positron pair. The probability of a photon converting after traveling a distance $z_c$, $P(z_c)$, is [18]

$$P(z_c) = \frac{9}{7} e^{-\left(\frac{7z_c}{9}\right)} \tag{5.4}$$

where $z_c$ is measured in radiation lengths. The electron and positron then shower, only the effective lead glass block length is shortened by the distance the photon traveled before

converting ($z_c$). The energies of the electron and positron after the photon converts can be described as $\epsilon E$ and $(1 - \epsilon)E$. The probability for splitting the energy $P(\epsilon)$ is given by the Bethe-Heitler function [10],

$$P(\epsilon) \approx \epsilon^2 + (1 - \epsilon)^2 + \epsilon(1 - \epsilon)\left(\frac{2}{3} - a\right),$$

where $a$ is a constant of the material, ($\approx 0.0297$ for the lead-glass). The signal at the phototube due to a photon of energy $E$ converting in the lead-glass at $z_0$ is described in the following way:

$$I_\gamma = E g_0 C_\alpha \left\langle \epsilon C(\epsilon E, \alpha, L - z_c) + (1 - \epsilon) C((1 - \epsilon)E, \alpha, L - z_c) \right\rangle_{\epsilon, z_c}$$

Therefore, the $C(E, \alpha, l)$ corrections for electrons are different from those for photons. Given that both the photon conversion depth and the energies of the $e^+ e^-$ pair can fluctuate, photon shower energy depositions vary more than electron shower distributions in the (z) direction. As a result the photon energy resolution is about $\sim 50\%$ worse than the electron energy resolution.

## 5.4.2    Energy Resolution

Traditionally, the energy resolution of a calorimeter is expressed as the sum of two terms,

$$\sigma_E / E = a \oplus b/\sqrt{E}. \tag{5.5}$$

The constant term, $a$, is due to fluctuations on the fraction of the shower contained in the calorimeter. As can be seen in figure 24, these fluctuations are not precisely constant with energy, but ignoring absorption effects, the so-called "constant term" for this calorimeter is constant to $\sim 0.5\%$ between 4 and $64\,GeV$. The energy-dependent, or "photostatistics term", is due to the fact that for a given deposition of energy $E$, there are only a finite number of photons which reach the back of the phototube. If one assumes that the number of photons, $n_p$, is large and proportional to the energy of the shower, and the fractional statistical error on the number of photons, $\delta n_p / n_p$ is simply $1/\sqrt{n_p}$, and the statistical error on the energy measurement is proportional to $1/\sqrt{E}$.

The absorption coefficients enter into both the constant term and the photostatistical term because of the C-light corrections. Since the C-light corrections depend on both the $\alpha$ of the central block of the cluster, and the energy of the cluster itself, the resolution can no longer be expressed as the simple functional form in equation 5.5. Figure 25 shows the electron energy resolution seen in the calibration data for all blocks as a function of momentum as well as the functional form in equation 5.5. Clearly equation 5.5 does not characterize the energy resolution. In figure 25 the increase in the RMS for higher energies is due to the fact that higher energy electrons tend to hit blocks closer to the beam-holes of the calorimeter, which are in turn the blocks with the highest absorption coefficients.

**Photostatistics**

To determine how the C-light corrections enter into the photostatistics term, consider the number of photoelectrons, or the intensity of light produced from a shower of energy E.
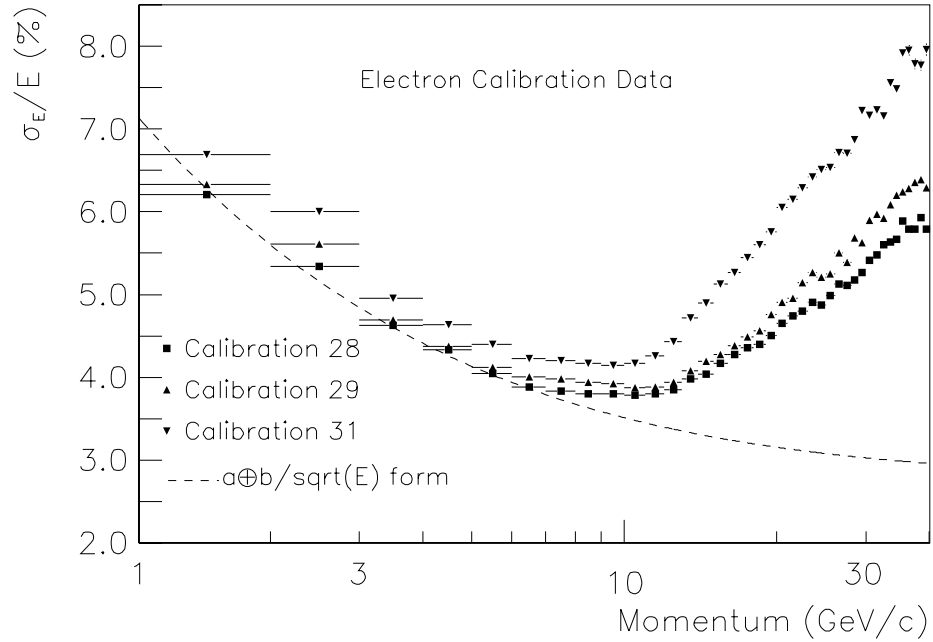


Figure 25. Energy resolution as a function of momentum for calibration electrons. The function $\sigma_E/E = a \oplus b/\sqrt{E}$ with $a = 2.75\%$ and $b = 6.9\%$ is shown for comparison

Earlier in the chapter this intensity was expressed as

$$I = g_0 e^{-\alpha(L-z_{1GeV})} EC(E, \alpha, 0),$$

where $z_{1GeV} = 5.157$, the average number of radiation lengths of the shower maximum of a $1\,GeV$ shower. $g_0$, or the gain in photoelectrons per GeV for a $1\,GeV$ shower, was measured in a previous experiment which used the same calorimeter [4]. By looking at the smearing on the flasher signals, which were a constant signal of light (4.2.1), $g_0$ was determined on average to be 536photoelectrons/$GeV$. The photostatistical resolution, or $1/\sqrt{n_p}$, is then

$$\frac{\delta I}{I} = \frac{1}{\sqrt{g_0 e^{-\alpha(L-z_{1GeV})} EC(E, \alpha, 0)}}$$

$$= \frac{4.32\% e^{\alpha(L-z_{1GeV})/2}}{\sqrt{EC(E, \alpha, 0)}}$$

Figure 26 shows the photostatistics contribution to the energy resolution as a function of energy for a number of different $\alpha$'s, as calculated by the EGS simulation [1].

**Shower Fluctuations**

Without absorption effects the constant term in the energy resolution simply depends on how much of the total energy was deposited in the array. With absorption effects, however, the longitudinal shower fluctuations not only change how much energy is contained in the shower, but also how far from the PMT the energy is deposited. When a shower deposits energy farther into the block, the light that is produced gets absorbed less because it has a shorter path length to travel before it enters the phototube. The larger the $\alpha$, the more important these fluctuations become, and the worse the resolution.

The fluctuations out the back of the array can compensate for the absorption effects, however. Showers which peak closer to the back end of the block and hence have less light signal absorbed, also are those which have more leakage out the back of the block. For low energy showers this compensating effect is negligible because very little light leaks out the back in the first place. For high energy showers, however, this compensation helps, and in general, the resolution for a given $\alpha$ improves as a function of energy. Figure 26 shows the
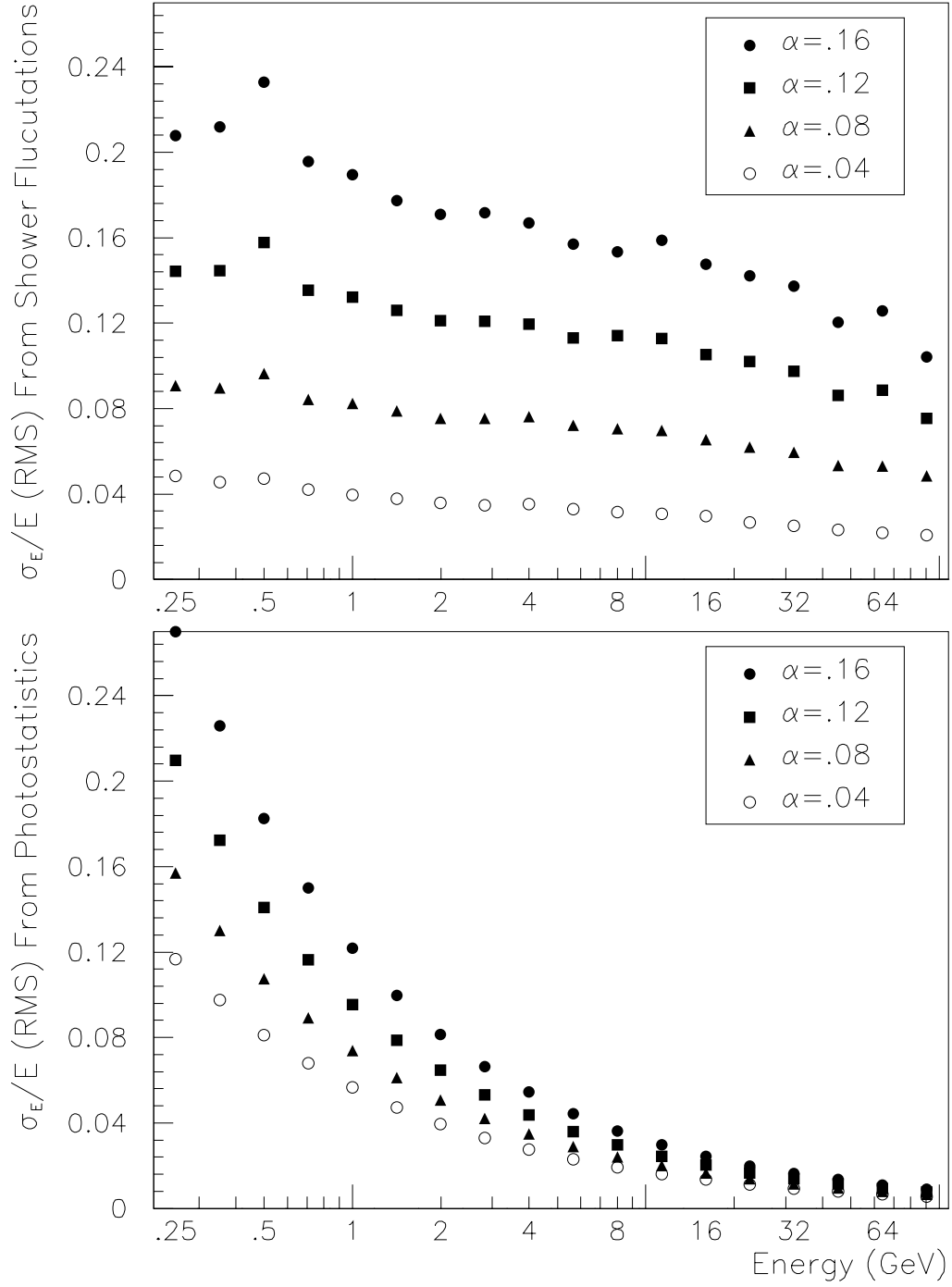
Figure 26. $\sigma_E/E$ from shower fluctuations and from photostatistical smearing as a function of energy for different absorptions ($\alpha$), taken from reference [1]

EGS-calculated energy resolution due to shower fluctuations as a function of energy, for a number of different $\alpha$'s [1].

## 5.5 Calibration

To accurately measure energies and determine the C-light corrections for electromagnetic showers, the gains and the absorption coefficients for each of the 804 blocks must be measured. Interspersed throughout the data-taking run were six different glass calibration runs which were taken to get a sample of electrons of various energies hitting the entire detector. Table 9 shows a list of these runs and when the data were taken. Sometime between each calibration run the central lead-glass blocks were exposed to UV radiation ("cured") for a given amount of time (listed in table 9). After being exposed to UV light, the gains of the blocks change and the absorption coefficients of the lead-glass blocks decrease, thus undoing some of the radiation damage to the blocks. Because of the expected change in the gains and $\alpha$'s during a cure there must be at least one calibration between two successive cures.

The glass calibration required a large flux of electrons and positrons, combined with very little other beam-related activity in the detector. These runs were useful because (i) they enabled the gain-matching of all the blocks, which was important for the operation of the Adders and the Hardware Cluster Finder, and (ii) the gains could also be fine-tuned with optimized analysis cuts to improve the resolution of the calorimeter as a whole.

### 5.5.1 Detector Configuration

To create a beam of electrons and positrons (hereafter referred to only as electrons) the lead absorbers were removed from the beam to increase its photon content. The photons were then converted far upstream of the detector by a sheet consisting of $0.13\,mm$ of copper and $0.08\,mm$ of titanium. The electron pairs were then bent vertically by the AN1 magnet, located at $119\,m$ from the target (see figure 9). Another $19\,m$ downstream of AN1 was still another magnet (AN2) to induce a horizontal momentum kick, and finally the analysis magnet at $159\,m$ gave them an additional momentum kick horizontally. In order to aim electrons at different parts of the glass the currents in the magnets AN1 and AN2 were

Table 9. Glass Calibrations in E799

| Date | Calibration/Cure | Fraction of Two-Electron Data |
|------|------------------|-------------------------------|
| 10/10 | Calibration 27 | 7% |
| 10/15 | Cure (13 hours) | |
| 10/21 | Calibration 28 | 16% |
| 10/29 | Cure (12 hours) | |
| 11/06 | Calibration 29 | 12% |
| 11/12 | Cure (12 hours) | |
| 11/14 | "Mega-Cure" (72 hours) | |
| 12/02 | Calibration 30 | 26% |
| 12/03 | Cure (14 hours) | |
| 12/16 | Calibration 31 | 25% |
| 12/18 | Cure (12 hours) | |
| 12/23 | Calibration 32 | 14% |
| 01/08 | End of Run | |

adjusted during the calibration run to different values. The resulting band of electrons spread across the face of the lead glass; lower energy electrons tended to hit the outer blocks, and higher energy electrons tended to hit the inner blocks. To ensure that each block saw a reasonable range of energies there was more than one set of magnet currents for a given angle. The entire calibration consisted of data at 28 different magnet settings, and usually took about 12 hours to complete. There were between $(3 - 5) \times 10^6$ events written to tape in a calibration.

## 5.5.2  Calibration Data Selection

To select the calibration data that was eventually going to be used in the fitting routine stringent cuts were made on the spectrometer part of the data requiring the two particles to be electrons from a photon conversion. Events were required to have two tracks that

hit the scintillator banks upstream of the lead glass calorimeter, and at least one of those tracks was required to point to an electromagnetic cluster in the calorimeter. Cuts on the quality of the tracks were made (similar to those discussed in chapter 8), and the tracks were not allowed to point to within a half a block size of the beam-holes (those events were used to calibrate the pipe blocks in a separate procedure, as will be explained in section 5.8), or too close to the outside edge of the array. To ensure that the tracks were due to photon conversion in the copper/titanium sheet the invariant mass of the electron pair was calculated by extrapolating tracks back through AN1 and AN2, and the invariant $e^+e^-$ mass was required to be below $14\,MeV/c^2$. As can be seen in figure 27, this cut was loose enough to account for chamber resolution. On average about 25% of the electron calibration data written to tape survived these analysis cuts.

### 5.5.3  Fitting Procedure

The goal of the fitting procedure is to determine the correct gains and absorption coefficients for each of the 804 lead-glass blocks in the calorimeter. The "correct" constants are those
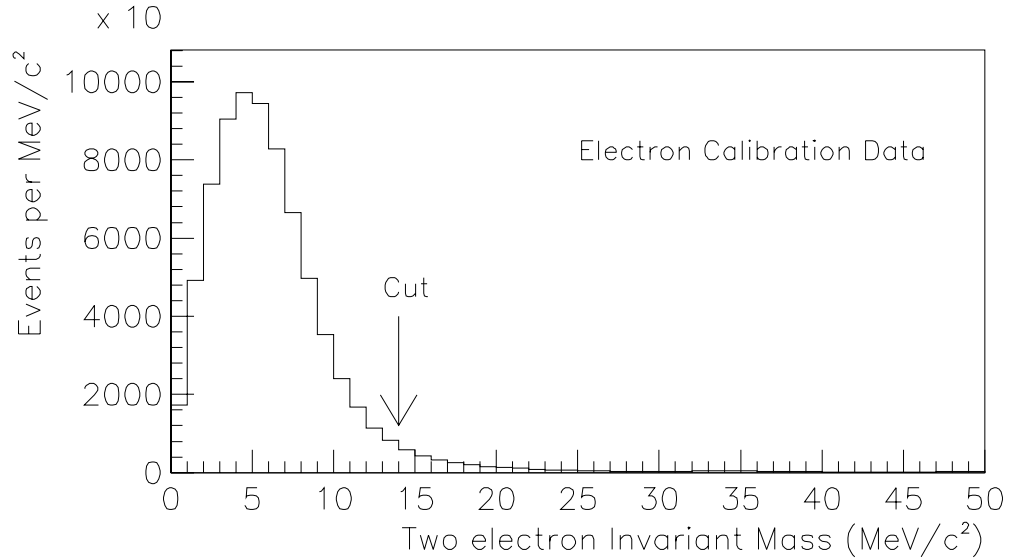
Figure 27. Invariant $e^+e^-$ mass distribution for electron calibration data

which optimize the lead-glass resolution and account for any non-linearity in the lead-glass energy response. Figure 28 shows a plot of the measured electron cluster energy divided by the electron track momentum for one of the electron calibration data sets. A Gaussian curve is superimposed to show the non-Gaussian behavior of this ratio, which is due to the large absorption coefficients. Section 7.2.1 describes the origin of this non-Gaussian behavior, and how it is included in the calorimeter simulation. Figure 29 shows a typical plot of the behavior of the ratio of cluster energy to track momentum as a function of momentum. Notice that the ratio is flat to about a percent within the relevant range of momenta.

As an example of how the absorption parameter $\alpha$ can be seen in the calibration data, figure 30 shows the energy vs. momentum for electrons at the calorimeter for two different cases—the first case is for when the block's absorption is not included in the calculation of the total energy, and the second is for when it is included. This is for a block in the center of the array where the radiation damage was severe and hence the $\alpha$ was large.

One problem concerning $\alpha$ corrections is the following: which $\alpha$ should be used for a given cluster? For this analysis the $\alpha$ of the central block of the cluster was used, but the
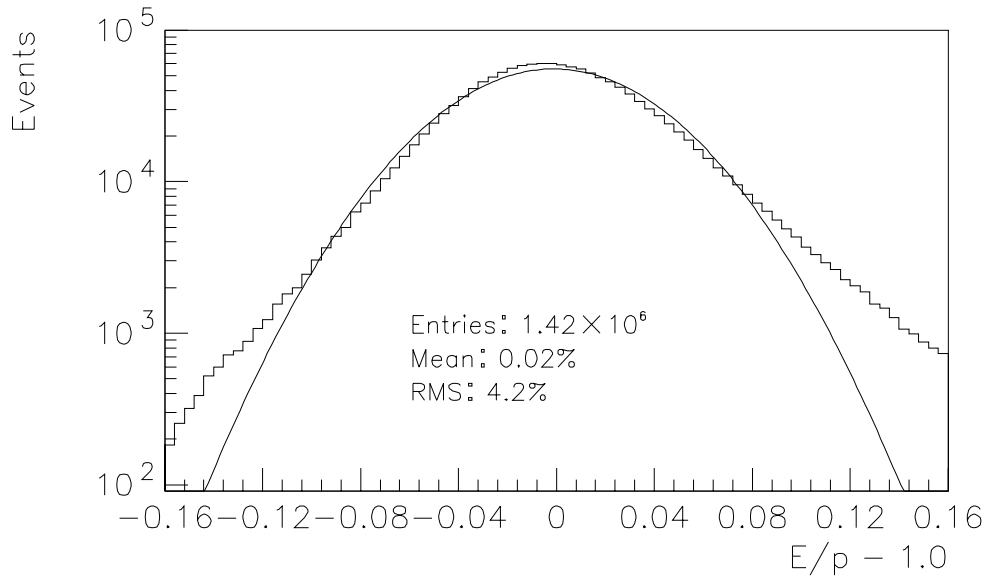


Figure 28. Energy/Momentum - 1 for calibration electrons
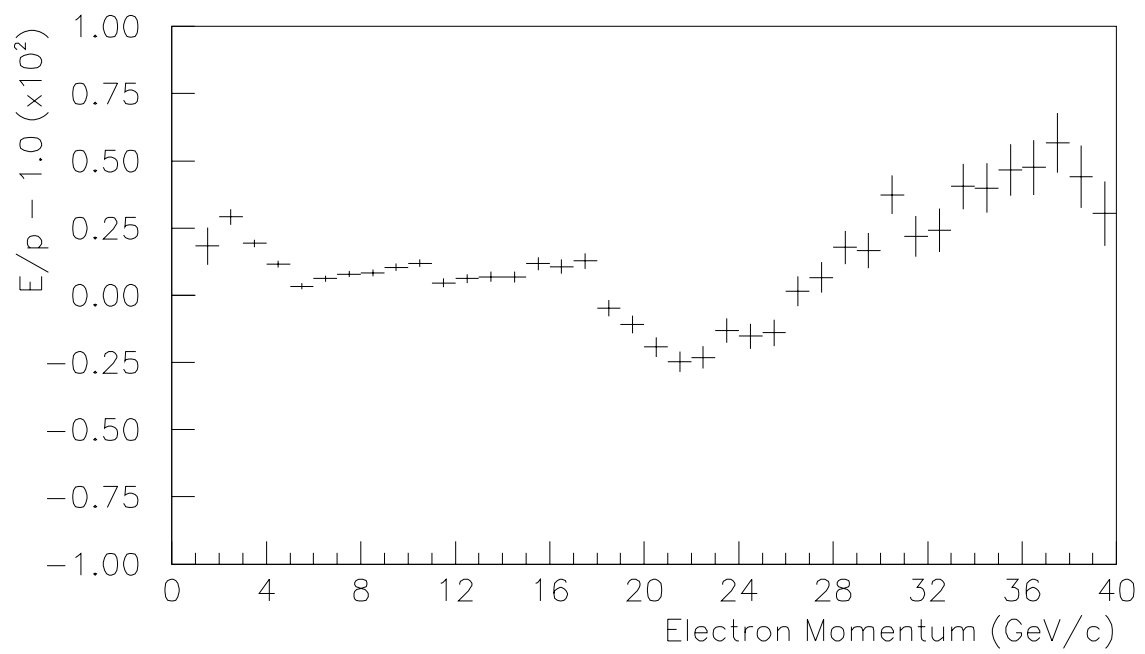
Figure 29. Energy/Momentum - 1 as a function of momentum for calibration electrons

$\alpha$'s themselves varied rather dramatically as a function of distance from the center of the lead-glass array. Also, not only does the $\alpha$ change as a function of block, but it also changes over the course of the run. Figure 31 shows the average $\alpha$ as a function of the distance from the closest beam-hole, for four different calibrations that span the run. For blocks which were more than $0.5\,m$ from the beam-pipes the $\alpha$'s were set to the same values as those which were used in the previous generation of this experiment, E731. This was done because the calibration statistics for those blocks were very low. The $\alpha$'s in the outer region of the calorimeter are expected to be constant because the radiation damage far from the beam-holes is small and the curing between calibrations did not affect the outer blocks.

## 5.6   Radiation Damage of Glass

As the run progressed there was significant damage to the lead-glass. The damage was so severe that by the end of the run some of the central blocks of the calorimeter had absorption coefficients above 17% per radiation length, (typical $\alpha$'s were $\sim 4.3\%$). This
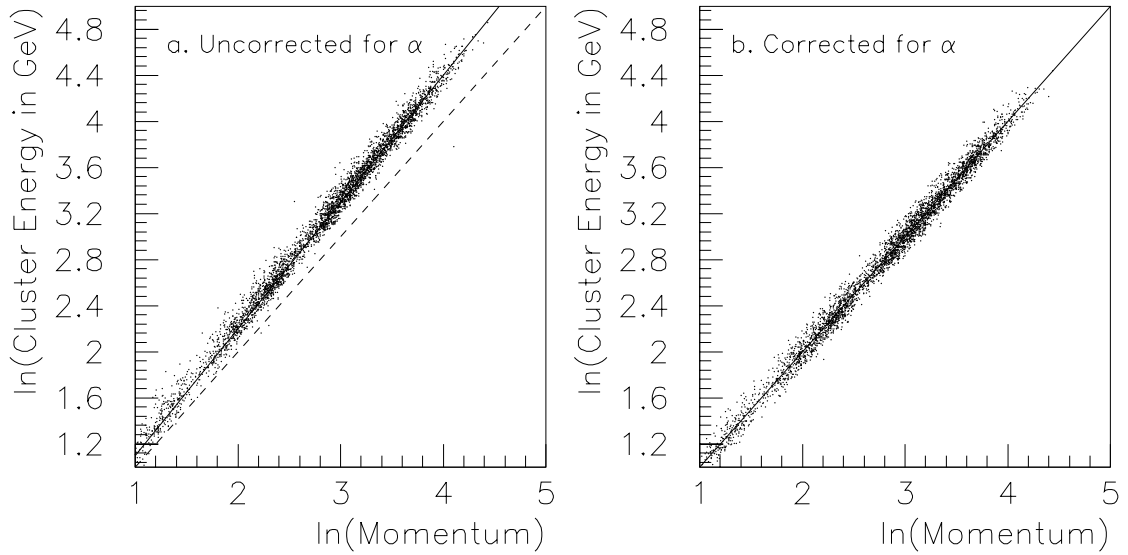


Figure 30. ln(Energy) as a function of ln(momentum) in electron calibration data, for a single block and two different energy calculations: in figure a, the absorption coefficient $\alpha$ is set to zero, in figure b it has the correct value

degraded the energy resolution significantly. As an example, blocks with $\alpha$'s around 4% had energy resolutions of about 4.5%, while the damaged blocks in the center, with $\alpha$'s near 15%, had energy resolutions of about 10%. Figure 32 shows the rate of increase of absorption coefficient as a function of block position between each calibration [1]. Although some radiation damage was expected to occur during the run, the magnitude of the damage incurred in E799 was much larger than expected. During the course of the run some new calorimeter materials which are supposedly much more radiation hard than lead-glass were tested, and one of these tests is described at the end of this chapter.

## 5.7   Position Algorithm

Crudely, a cluster is assumed to be centered somewhere in the block with the maximum energy deposition. By looking at the energies of the eight neighboring blocks; however, a more precise position measurement can be made. For showers in most of the calorimeter, the symmetry in the $3 \times 3$ array of blocks is used to simplify the position algorithm. For
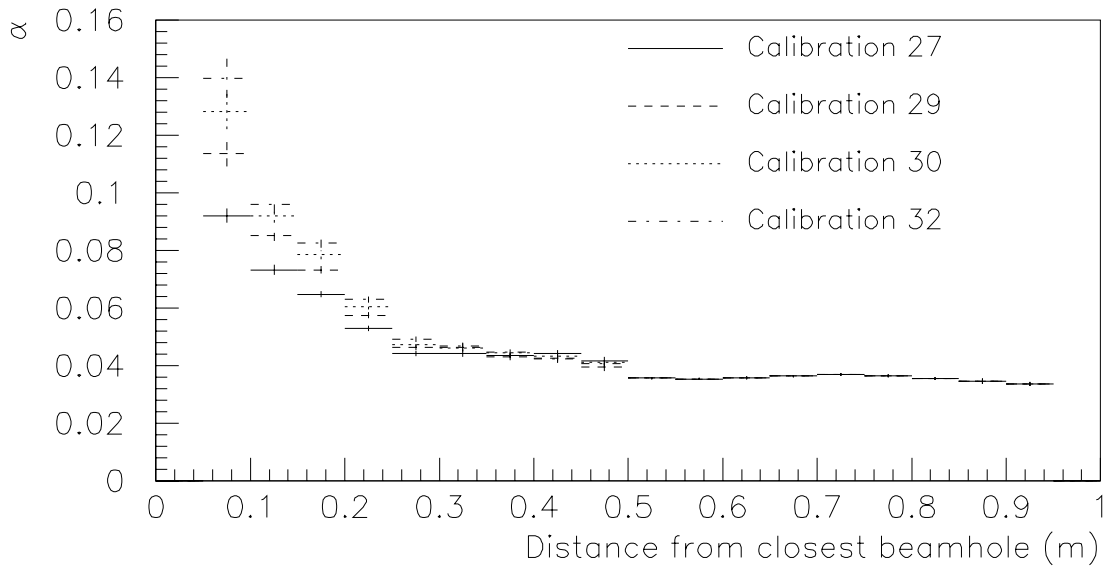


Figure 31. Average absorption coefficient ($\alpha$) in the glass as a function of distance to the closest beam-hole at four different points during the run
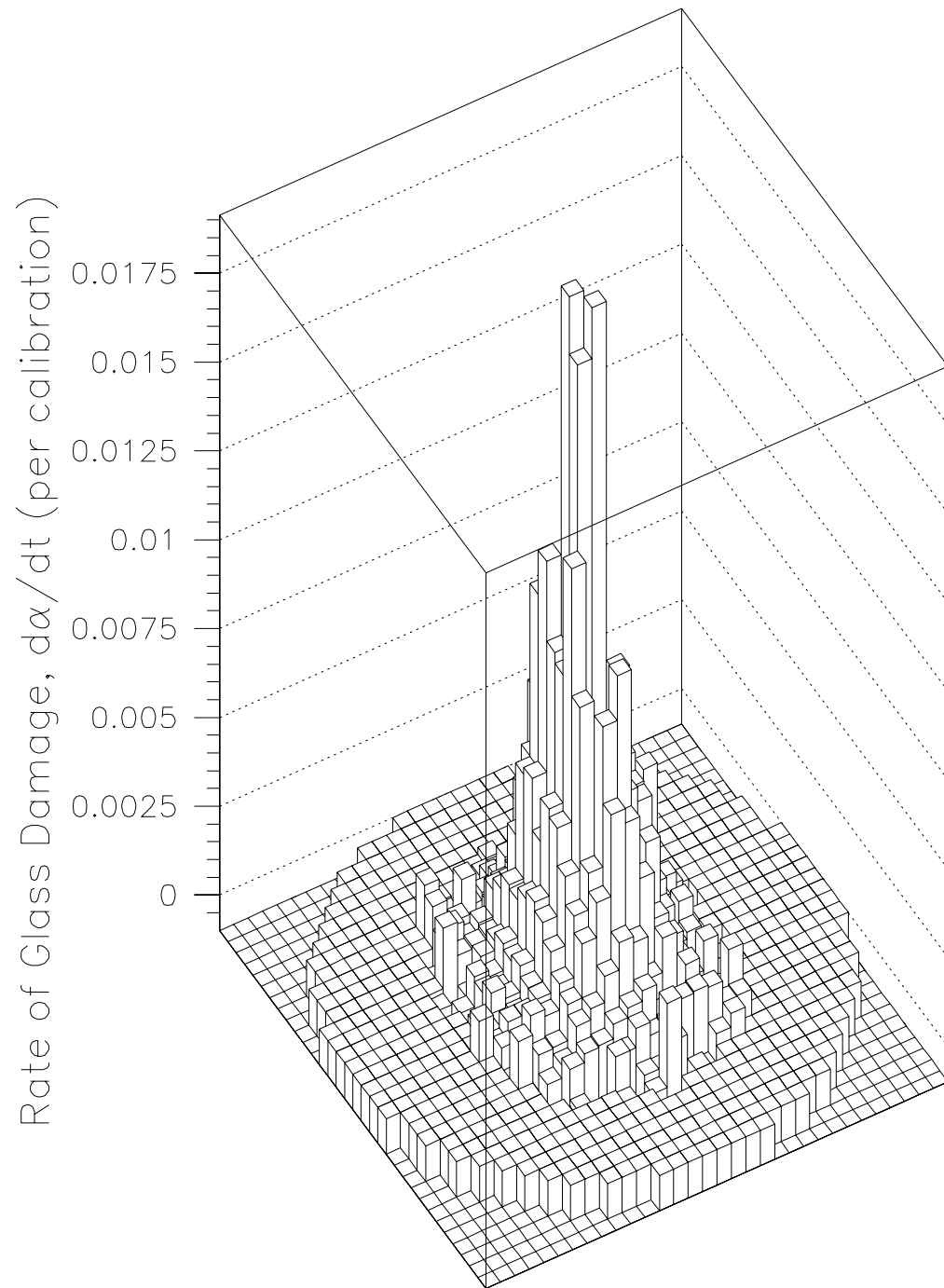
Figure 32. The rate of increase of the absorption coefficient for each lead-glass block, taken from reference [1]

showers in the pipe blocks, a special algorithm must be used since not all 9 blocks are available for position information. This section describes both the standard algorithm as well as the special algorithm used for the pipe blocks. Within these two categories of blocks, the algorithm itself does not depend specifically on which particular block in the array is the central block.

### 5.7.1 Standard Algorithm

To simplify the standard algorithm the two dimensions (x,y) are assumed to be independent and the same method is used for each dimension. Figure 33 shows the array of blocks used with the energy in each block labeled. The three columns of energy are the energies $a+d+g$, $b+e+h$, and $c+f+i$. By looking at the ratio of the energy of the center column and the larger energy sum of the two side columns we determine how far along in the (x) direction the shower was centered. The column with less energy is ignored in the standard position algorithm. The ratio of the row energy sums are used in the same way to determine the (y) position.

| a | b | c | Column Energies: |
|---|---|---|---|
|   |   |   | a+d+g, b+e+h, c+f+i |
| d | e | f | Row energies: |
|   |   |   | a+b+c, d+e+f, g+h+i |
| g | h | i | y → x |
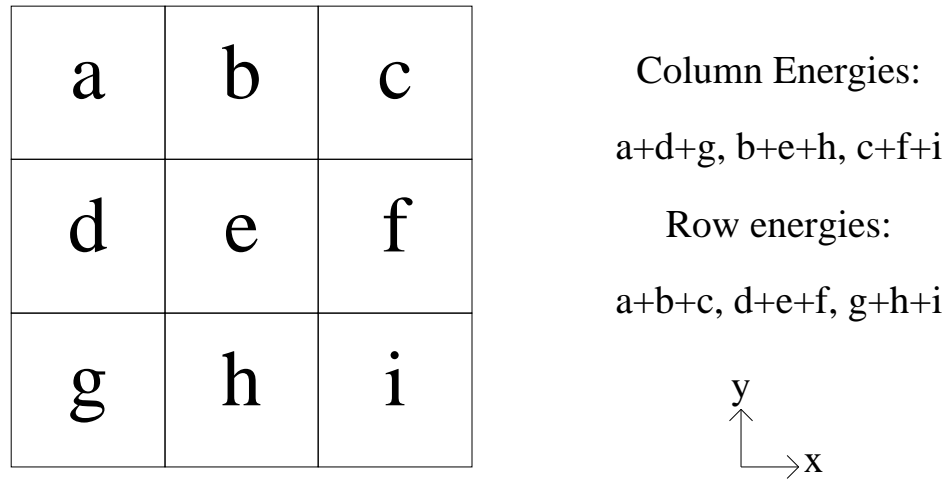
Figure 33. Definitions of column and row energies used for standard position algorithm

To determine the position as a function of the ratio of column energies, a look-up table was generated using a sample of electrons which were uniformly distributed along the front face of a block. (Recall that once the calibration was complete, any block which is not adjacent to the beam-pipes or the outer edges can be treated equivalently). For this sample of electrons the distance between the center of the block and the center of the cluster, x, can be expressed as a function of r, the maximum ratio of the column energies in the following way:

$$x(r) = \frac{b}{2} \frac{\int_0^r N(r')dr'}{\int_0^1 N(r')dr'},$$

where $N(r)$ is the number of events with energy fraction $r$, and $b$ is the width of a block. Rather than using an integral we sum between 276 equal fractions of r between about 4% and 100%. Figure 34 shows the lookup table that was used in two sections. To determine the position using a lookup table the program simply determines the energy fraction in the lookup table closest to the actual ratio, and extrapolates linearly to the actual ratio. The energy ratio was changing very quickly near the edge between the two energy columns, as is shown by the difference in slopes between the first and second plots in figure 34. Since the ratio is changing the most rapidly near the edge between the two blocks, the position resolution will evidently be the best in that region. Figure 35 shows the difference between the reconstructed cluster position and the track position of electrons extrapolated to the lead glass, in units of block width (b) as well as calculated $\sigma$. Although on average the position resolution for electrons is about $3\,mm$ in the lead-glass, from the above discussion it is obvious that the resolution is significantly improved closer to the edge of a block. Figure 36 shows the position resolution as a function of how far along the block length the shower started. So, given that the average photon cluster separation in $K_L \to \pi^+ \pi^- \pi^0$ decays is about $50\,cm$ the position resolution of approximately $3\,mm$ for each direction, for each photon, contributes about $\sqrt{8} \times \frac{0.3}{50}\%$, or $1.7\%$ absolute uncertainty (or $2.3\,MeV/c^2$) in the $\pi^0$ mass resolution.

## 5.7.2 Pipe Block Algorithm

When a photon or electron hits one of the pipe blocks, as shown in Figure 37, the cluster geometry is very different from the one shown in figure 33. In particular, there are two different kinds of geometries, shown in figure 37. shows these two geometries. For showers that start in blocks that are labeled $a$, there is only one block missing from the $3 \times 3$ array. From symmetry one can see that again, the two directions can be treated similarly, similar to the case for "normal" blocks. For showers that start in blocks that are labeled $b$, there are two blocks missing from the $3 \times 3$ array and the two different directions are not symmetric and the position determination becomes more complicated.

**Corner Pipe Blocks**

We shall first consider the situation when only one block is missing from the nominal $3 \times 3$ array. By transforming the coordinate system on any of the blocks labeled $a$ in figure 37
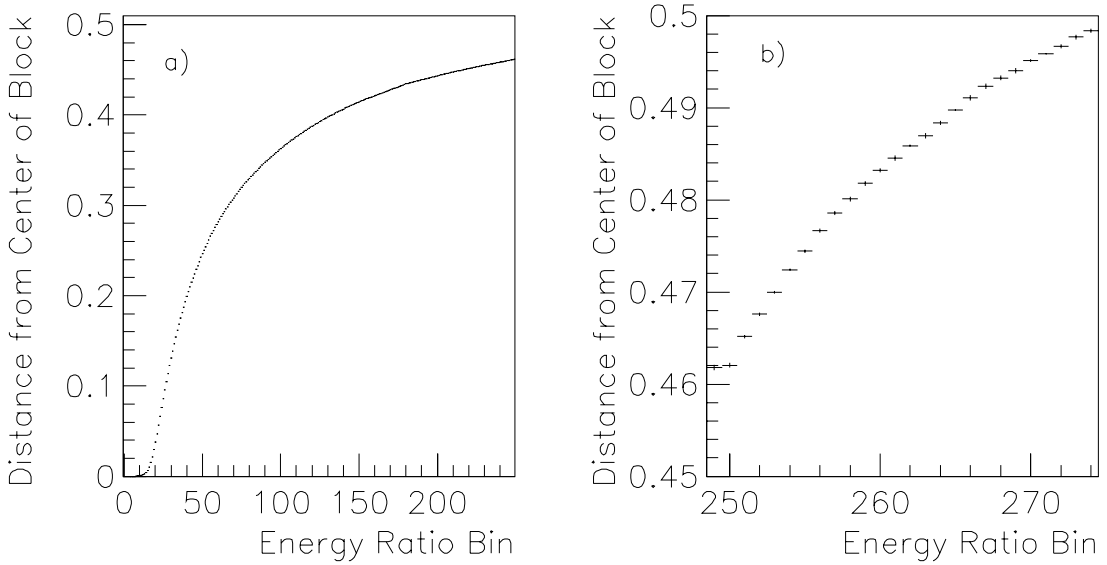


Figure 34. Two plots of the lookup table used for standard position algorithm, where figure (a) spans most of the block and figure (b) shows the region near the block edge where the position resolution is best. The lookup table gives the distance from center of block as a function of the ratio of column (or row) energies
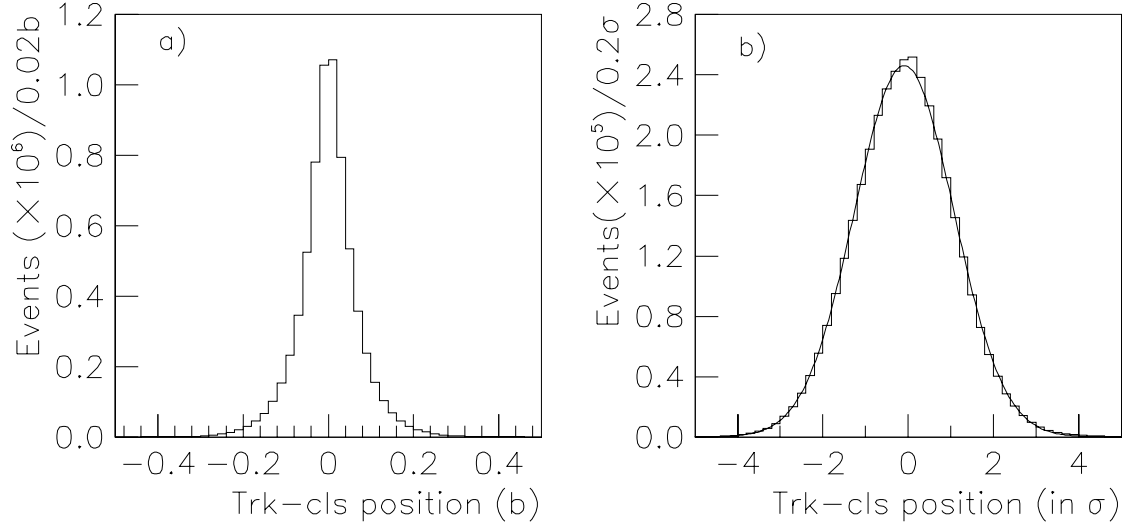
Figure 35. Difference between extrapolated track and cluster position for the standard position algorithm, measured in units of block-width, "b", (figure a), and expected position resolution, $\sigma$ (figure b). The fit of the $\sigma$ distribution to a Gaussian is also shown.
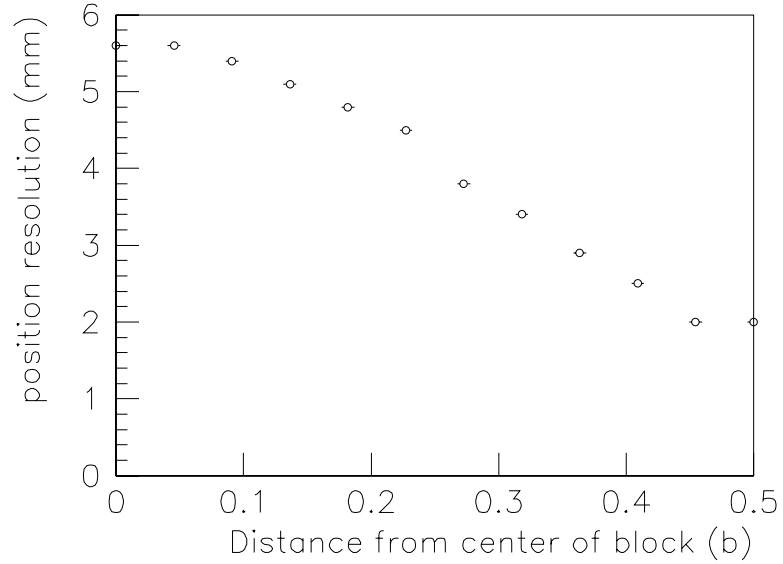


Figure 36. Lead-Glass position resolution as a function of the distance from center of block

one arrives at the block configuration "*a*" in figure 38. As one can see from the relevant variables, if one defines (x=0,y=0) as the center of the block, then events with positive x or positive y coordinates will be reconstructed the same way as was done in the normal algorithm. It is unlikely that the shower will deposit more energy in the two blocks in the column or row farther away than in the three blocks closer to the shower center. To determine the position if the shower is closer to the missing block, a lookup table was

|   |   |   |   |
|---|---|---|---|
| a | b | b | a |
| b |   |   | b |
| b |   |   | b |
| a | b | b | a |
| a | b | b | a |
| b |   |   | b |
| b |   |   | b |
| a | b | b | a |

a:
one block missing
from 3x3 array

b:
two blocks missing
from 3x3 array

Figure 37. Pipe block configuration and definition of special geometry

formed by calculating the average ratio of (a+b)/(b+e) or (h+i)/(e+f) as shown in figure 38 as a function of distance from the center of the block. It was assumed that the ratio (a+d)/(b+e) was independent of the (y) position of the shower, and likewise, (h+i)/(e+f) was independent of the (x) position of the shower. Figure 39 shows the difference between the extrapolated track position and the cluster position (the track-cluster difference) and the average difference as a function of where the track points to in the block. Note that the RMS on the track-cluster difference is still reasonably small, namely $4.4\,mm$.

**Side Pipe Blocks**

A new algorithm is necessary when there are two blocks missing from the standard cluster array, as in blocks labeled "$b$" in figure 37. The energy ratios that are used for the lookup
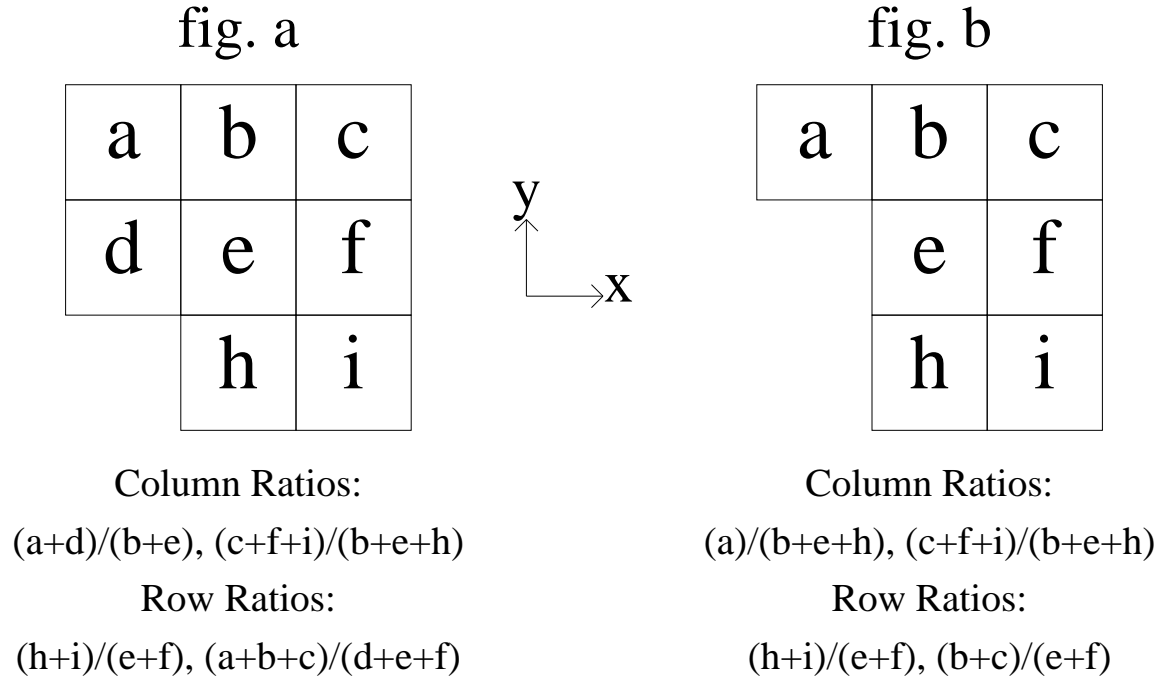


Figure 38. The two configurations of pipe block clusters corresponding to type "a" and type "b" blocks as defined in the previous figure, and the definitions of the energy and column energy ratios used in the pipe block position algorithms
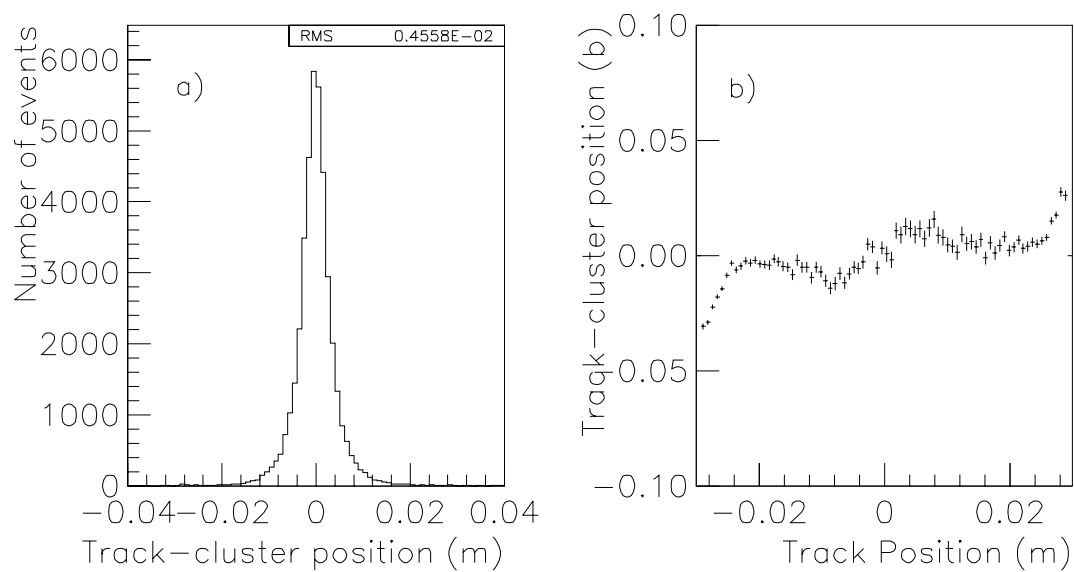
Figure 39. The distribution of the difference between extrapolated track position and cluster position for calibration electrons (figure a) and as a function of incident track position for electrons arriving in type "a" blocks (figure b) Ideally, figure b should be flat.
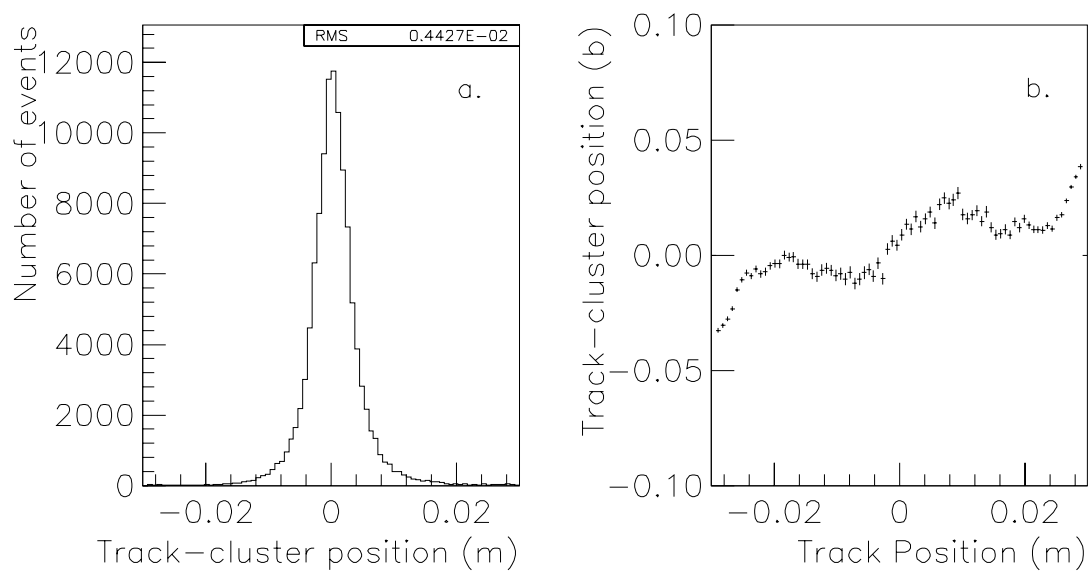
Figure 40. (a) The distribution of the difference between the extrapolated track (y) position and cluster (y) position for calibration electrons, and (b) this same difference as a function of incident track position for electrons arriving in type "b" blocks. Ideally, figure b should be flat as a function of track position

tables in this case are also shown in figure 37. Note the similarity between the row ratios used for determining the (y) direction when there are two blocks missing and the ratios used in either direction when there is only one block missing and the shower is close to the missing block. Because of this similarity, the same lookup table is used. The resulting track-cluster distributions in this direction are shown in figure 40, and the resulting RMS on the track-cluster difference is again about $4\,mm$.

The lookup tables that determine the (x) direction are more complicated. First of all, one only has one out of the normal three blocks of energy in the numerator of the column ratio. The amount of energy left in that one block (block "a" in figure 37b) is strongly dependent on both the x and y coordinates of the incident shower. Therefore, a two-dimensional lookup table for this energy ratio is calculated. By using the y position found with the other row ratios first, one then looks in the appropriate row of the 2 dimensional look-up table. Finally, one then compares the (x) position found in this way with the (x) position found by using the ratio of energies (c+f+i)/(b+e+h) in figure 38. The resulting track-cluster distribution is found in figure 41 and the resulting position resolution in the half of the block closest to the missing blocks is about $6\,mm$. The position resolution on the other half of the block is of course much better, and a weighted average was used to combine these two x position measurements. Again, position resolutions obtained in this way are sufficiently good so that they don't contribute substantially to the $\pi^0$ mass resolution, which is about $12\,MeV/c^2$ when one photon is in a pipe block and the other is at least four blocks away from the beam-holes.

## Run Dependent Corrections to Position Algorithm

To avoid having to re-make position algorithm tables for these blocks for each calibration, the look-up tables were calibrated during an early run when the radiation damage was small, and hence the C-light corrections were small. Then for later runs, C-light corrections were made to the energy in each block before forming the ratios of the energies used in the position algorithm. The C-light correction that was used assumed that the photon entered the block at the front of the block. Strictly speaking, this is not true for secondary particles in the shower which deposit energy in neighboring blocks, because they enter the block in
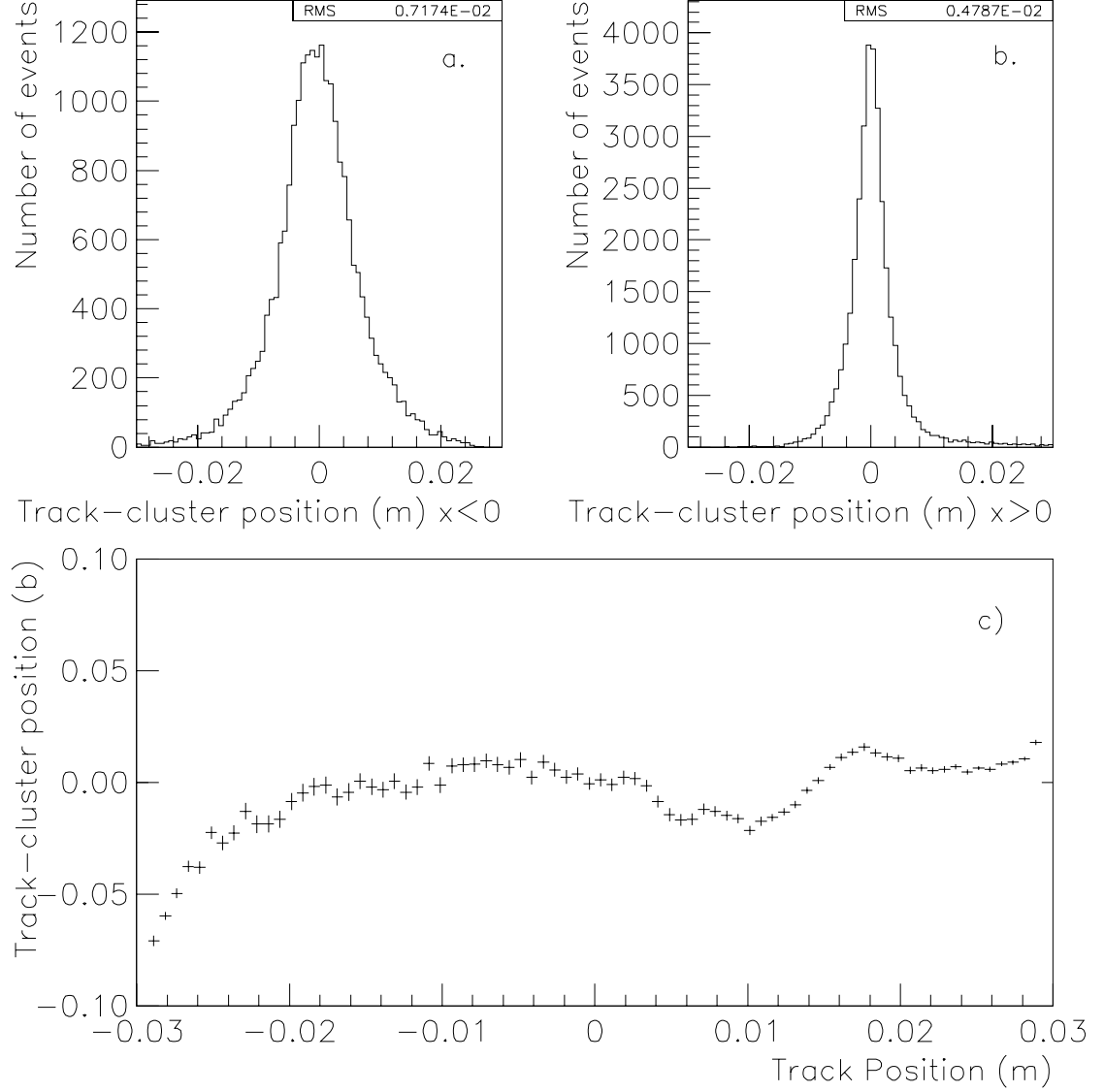
Figure 41. The distributions of the difference between the extrapolated track (x) position and the cluster (x) position for calibration electrons as a function of incident track position for electrons arriving in type "b" blocks. $x < 0$ (figure a) corresponds to the half of the block closest to the beam-hole, and $x > 0$ (figure b) corresponds to the other half. Figure c is this same difference as a function of track position

question downstream of the front face of the array. Furthermore, the $\alpha$'s measured for each block were not necessarily constant for the entire length of the block.

Empirically, however, the simple C-light correction made adequately eliminated any run-dependence in the position algorithm. Figure 42 shows the difference between the electron track and the electron cluster position for the case where two blocks are missing. Although the position resolution degrades somewhat as the energy resolution deteriorates, there is no systematic shift as a function of the calibration. The worst dependence is in the (x) direction as defined above in the inner half of the block, but even there the structure in the plot of the track-cluster position vs. track position never varies by more than a tenth of a block or $6\,mm$, which is $\sim 1\sigma$ for the position resolution in that region of the block.

## 5.8    Pipe Block Energy Algorithm

For showers that start more than half of a block width away from the inner edge of the array the amount of energy lost down the beam-holes is small, less than a few per cent, and can be accounted for with small corrections. Similarly, if there is only one block missing from the $3 \times 3$ array then the energy lost is also small. However, if the cluster has two blocks missing from the array and has been determined to be within a half a block width of the beam-pipe, a position-dependent fraction of the measured energy is added to the cluster energy to account for this energy loss. This procedure was needed for both electrons and photons, and hence must take the calculated cluster position as input. This section describes the energy reconstruction algorithm developed for photons.

The lookup table for the energy reconstruction was made by considering electron calibration data for electrons that were pointed at the pipe blocks of type "b". For showers in these blocks which are closest to the beam-hole, $E/p$ has a strong dependance on (x). In light of the fact that the position resolution in the (x) direction for these blocks is about $6\,mm$, the energy/momentum ratio was computed in 10 bins across the half of the block closest to the hole, or in bins approximately $3\,mm$ wide in (x). To account for the small changes in $E/p$ as a function of (y), each x bin was split into 10 y bins, or bins approximately $6\,mm$ across in (y). So, for every electron whose cluster was reconstructed to be
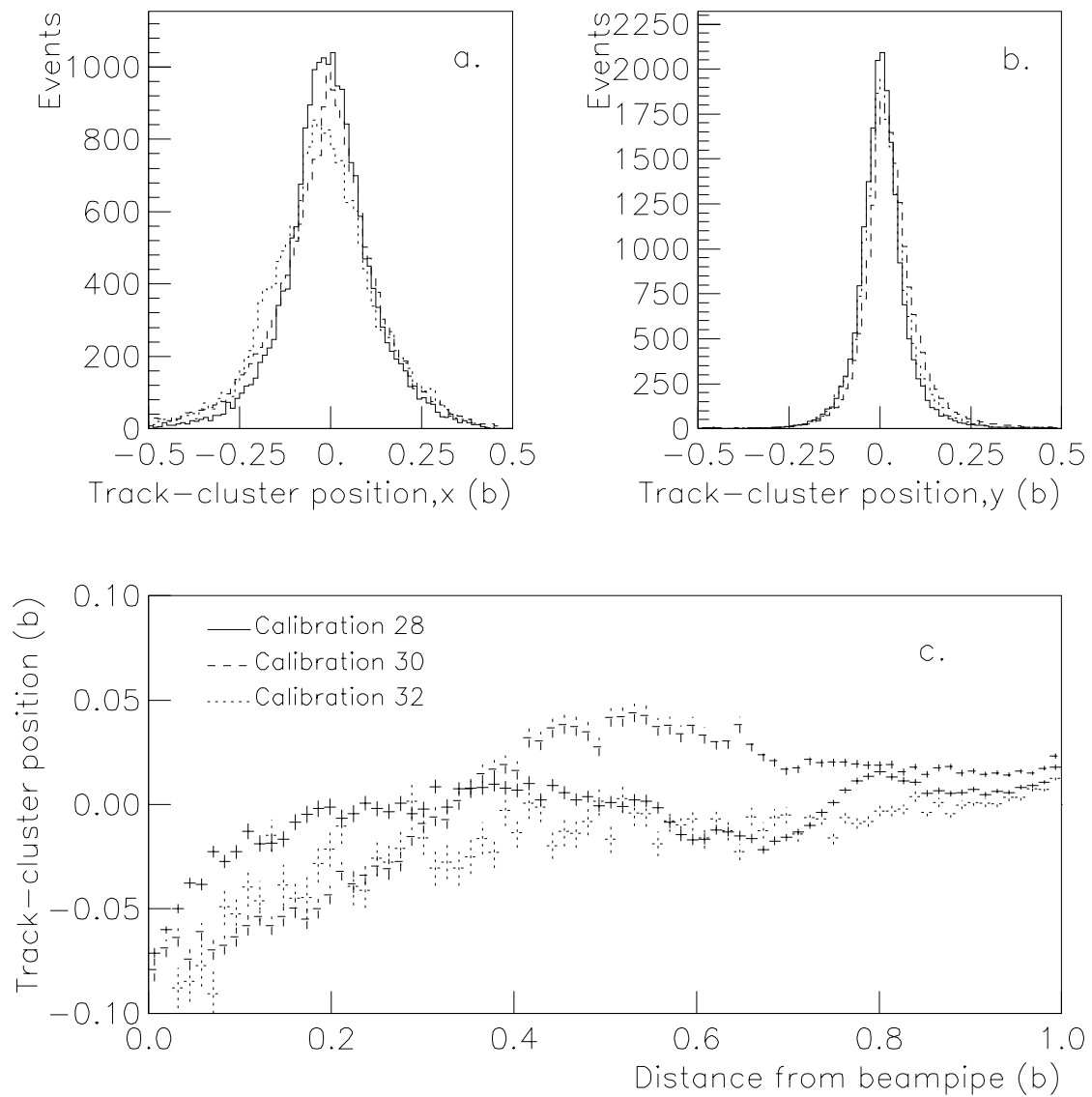
Figure 42. The distributions of track-cluster differences for type "b" blocks for three different calibrations, in both the (x) direction in the worst part of the block (figure a), and the (y) direction for the pipe blocks, (figure b), and as a function of the track distance from the beam-pipe (figure c). The length "b" is one block length

within a half a block of the pipe blocks, its $E/p$ went into the calculation of the energy lookup table.

To make the table, each of the 100 different $E/p$ distributions were fit to a Gaussian, ignoring the tails of the distributions. The peaks of the Gaussian distributions became the scale factors one would use to make the mean $E/p$ equal to 1.0 in each bin. The $\sigma$'s of these distributions were also recorded and used as a measure of the energy resolution. While the energy resolution in any non-pipe-block is roughly constant across the block, for the pipe blocks the energy resolution changed dramatically with position. Figure 43 shows the results of the fits of the $E/p$ distributions for calibration electrons whose clusters were calculated to be in a particular row in the center of a pipe block.

## 5.9    Results for Photons

The primary purpose of the position and energy algorithms has been to optimize the photon response of the calorimeter in a region which, because of the Lorentz boost of the decaying
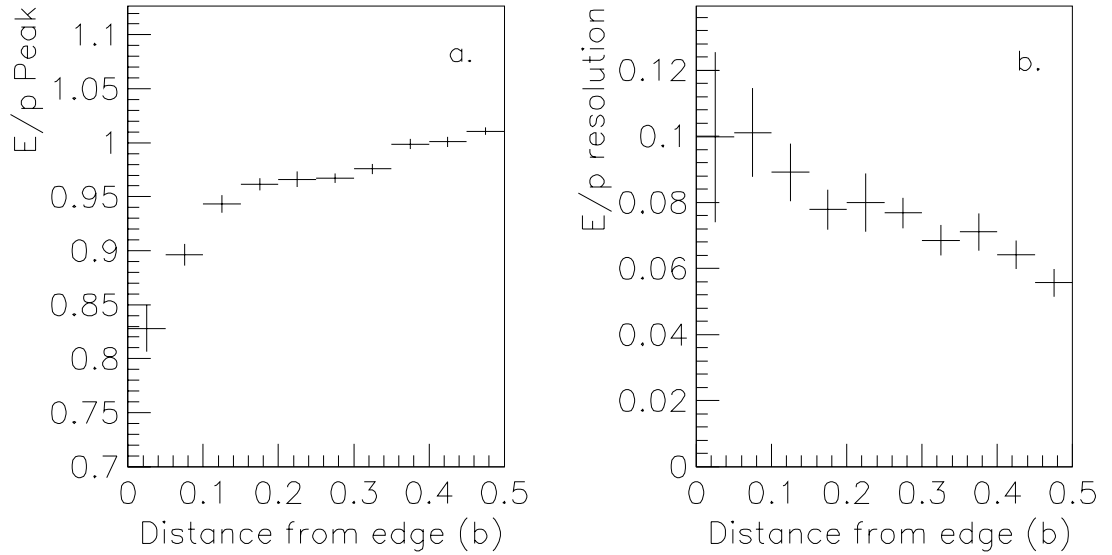


Figure 43.    Average $E/p$ for calibration electrons as a function of position from beam-pipe, and Gaussian $\sigma$'s of the $E/p$ distributions for blocks adjacent to the beam-hole. The length unit "b" is the width of one block

$K_L$'s, constituted a large fraction of the photon acceptance. To check the algorithms we looked at a sample of $K_L \to \pi^+\pi^-\pi^0$ decays found in the minimum bias trigger, described in section 4.1.2. By making cuts described in chapters 8 and 10 a sample of about $50,000$ $K_L \to \pi^+\pi^-\pi^0$ decays remained. Figure 44 shows the difference between $M_{\gamma\gamma}$ and the nominal $\pi^0$ mass for both data and Monte Carlo events which have no photons in the inner half of the pipe blocks. Although the means of the two distributions differ by roughly a per cent due to the modeling of photon showers in the calorimeter, the shape of the $\pi^0$ mass distribution is reproduced in the Monte Carlo. The nominal $\pi^0$ mass resolution is about $6.0\,MeV/c^2$, or about 4.4%. Figure 44 shows how the $\pi^0$ mass resolution depends on the innermost ring that was hit by a photon in the decay. The deterioration of the photon energy resolution is correlated with the deterioration of the glass due to radiation damage, as is the case with electrons.

Before correcting for the energy loss in the beam-holes, the reconstructed $M_{\gamma\gamma}$ in
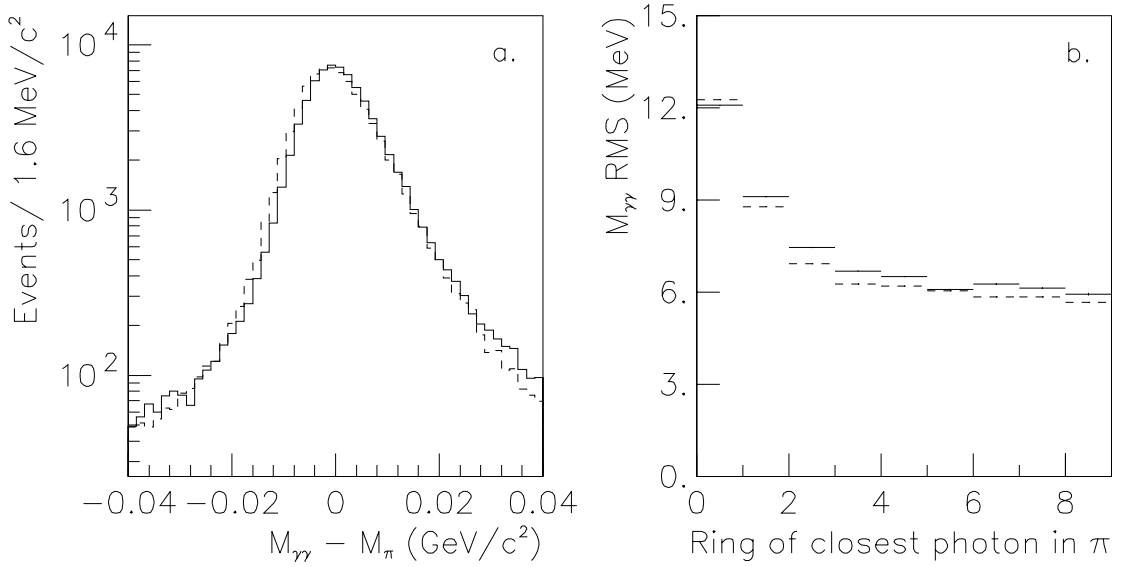


Figure 44. The $M_{\gamma\gamma}-M_{\pi^0}$ distribution for $K_L \to \pi^+\pi^-\pi^0$ events which have no photons in the pipe blocks (figure a), and the fluctuations (RMS) on the $M_{\gamma\gamma}-M_{\pi^0}$ distributions as a function of ring number (figure b), where a ring number is the number of blocks between the photon closest to the beam-hole, where the other photon was in at least the fourth ring. Ring number 0 consists of the pipe blocks.
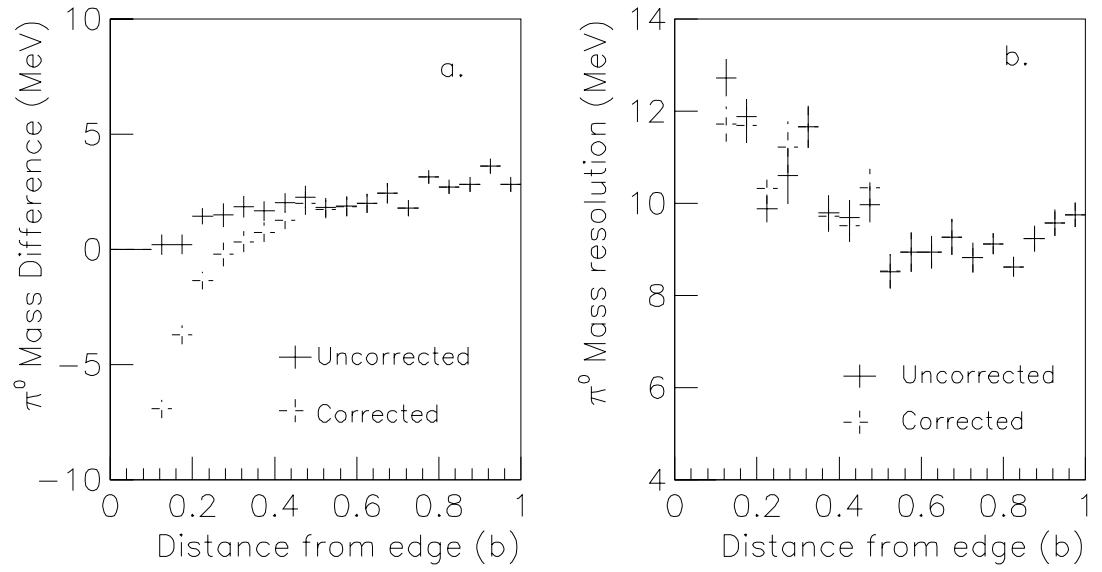
Figure 45. Average $M_{\gamma\gamma}-M_{\pi^0}$ (figure a) and Gaussian sigmas (figure b) of the $M_{\gamma\gamma}-M_{\pi^0}$ distributions for $K_L \to \pi^+\pi^-\pi^0$ events where one photon is in a type "b" block and the other photon is at least three blocks away from the beam-hole. The results of applying the energy correction for pipe block clusters is also shown.

$K_L \to \pi^+\pi^-\pi^0$ decays depends strongly on the position of the photon, for photons which are in the inner half of the pipe blocks. After incorporating the energy algorithm, however, the reconstructed $\pi^0$ mass no longer depends as much on the reconstructed position of the photon cluster, as can be seen in figure 45.

Even with these energy corrections applied to the pipe blocks, the energy resolution of those blocks is drastically worse than the rest of the calorimeter, due to radiation damage. The best (albeit the most difficult) way to combat this loss of resolution due to radiation damage would be to use a calorimeter of much more radiation-hard material. The next section describes efforts done by E799 to test new materials for just that purpose.

## 5.10    A Study of Barium Flouride Hole Calorimeters

"It's not easy being green" —*Kermit the Frog*

When E799 was first proposed, the $K_L \to \pi^0 e^+ e^-$ acceptance was to be increased by instrumenting the beam-holes of the lead-glass with new electromagnetic calorimeters. Constructing these detectors provided the opportunity to study new materials for large scale calorimeter use. These new materials, which were not available when the lead-glass calorimeter was originally built, supposedly combine the properties of fast signal response, good energy resolution, and radiation hardness. E799 constructed two small calorimeters to be placed behind the beam-holes of the lead-glass; one was made of Lead Flouride, ($PbF_2$), and the other was made of Barium Flouride ($BaF_2$). We describe here the construction and testing of the $BaF_2$ calorimeter.

### 5.10.1    Physical Characteristics of Barium Flouride

Barium Flouride ($BaF_2$) is a scintillator which has promising applications as a high energy physics calorimeter material. The scintillation light has an extremely fast rise-time and a decay time of $550\,psec$. The scintillation light spectrum peaks at $190\,nm$, in the very ultraviolet region. There are also two slow components to the scintillation light which peak at $310\,nm$ and have a decay times of 430 and $620\,nsec$. [19]. The crystal, at $4.88\,g/cm^3$ is

also very dense and has a radiation length of only $2.05\,cm$ [19], compared to the $3.21\,cm$ radiation length of lead-glass.

The property that makes this material viable for calorimeters is that the crystal itself is transparent to light at the scintillation light frequency. However, many materials, including normal glass, are not. UV transparency must be verified for any material which is to be optically coupled to the crystals. The high index of refraction of $BaF_2$ (1.8 at UV wavelengths) and the fact that it is very hard and therefore easily polished ensures that total internal reflection is an efficient means for light propagation through the crystal.

Another property of $BaF_2$ is that both the scintillation and optical properties are expected to be stable even after large doses of radiation, which was the primary motivation for using this material as a beam-hole calorimeter. References [20] and [21] describe radiation damage tests done on small samples of $BaF_2$.

### 5.10.2  Design Specifications for Calorimeter

The goal of this study was to see if $BaF_2$ could be used to make a calorimeter with an energy resolution of about 1% and survive in the E799 beam-holes. As is shown in figure 24 the fluctuations on energy leakage out the back of the E799 18.7 radiation length lead-glass calorimeter, for high energy showers, is about 1.25%. To determine the number of radiation lengths required for these fluctuations to be below 1% in $BaF_2$ we ran an EGS Monte Carlo of $BaF_2$. It was shown in this Monte Carlo that for a $BaF_2$ calorimeter which was 25 radiation lengths long the fluctuations on the energy depositions are less than 1% at all energies studied, up to $50\,GeV$. Since the radiation length of $BaF_2$ is $2.05\,cm$, this means the calorimeter had to be about $50\,cm$ long. Unfortunately at the time of construction $BaF_2$ crystal manufacturers could not grow crystals that long, so instead two crystals of $3.6\,cm \times 3.6\,cm \times 25\,cm$, were glued end to end and wrapped as a single crystal for this test. The crystals were manufactured by Optovac.

As was obvious from the discussion of absorption coefficients in the previous section, the flatter the scintillation light response as a function of distance from the phototube, the better the energy resolution, because longitudinal shower fluctuations contribute less to the fluctuations on the amount of light reaching the PMT. Since unlike Čerenkov light,

scintillation light tends to be emitted uniformly over $4\pi$, absorption effects are less impor-
tant, but surface reflection is very important. While Čerenkov light is emitted in a cone
of energy and only travels towards the phototube, scintillation light emitted away from the
phototube can reflect off wrapping on the back face of the crystal and can arrive at the
phototube. Absorption coefficient effects then become "second order" effects, since for any
position along the crystal there is a large fraction of light which travels at least one crystal
length. EGS Monte Carlo shows, for a given calorimeter size and various energies, that if
the light response was flat to 5% over the entire crystal (corresponding to an $\alpha$ of 0.2%
per radiation length) then the resolution would be as good as if the response were perfectly
flat. Figure 46 shows the EGS prediction for the resolution for several different energies for
a 3block $\times$ 3block $\times$ 25 radiation length array of $BaF_2$, where the cross section of a block
was a square $3.6\,cm$ long on a side. For this study the transmission was assumed to be a
linear function of the distance from the phototube, and a fractional loss of 5% is effectively
an alpha of $5\%/25X_0$ or an $\alpha$ of 0.2% per radiation length.
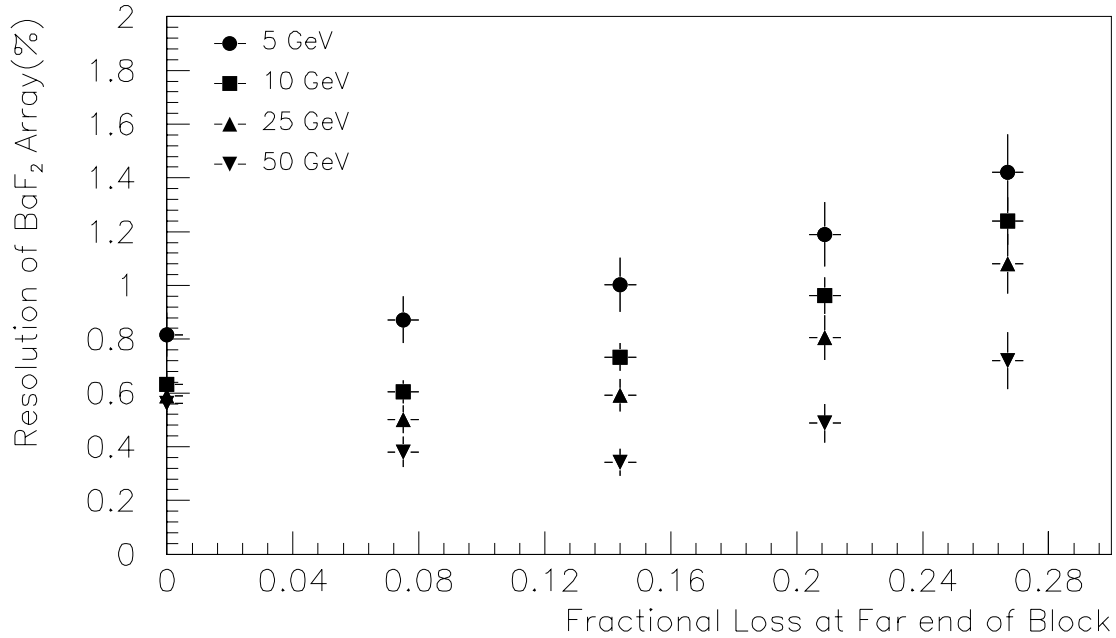


Figure 46. EGS-Predicted resolution for a $BaF_2$ array as a function of crystal response

### 5.10.3    Gluing and Wrapping Procedure

In order for the light from one crystal to pass un-absorbed and un-reflected into the next crystal the joint itself had to be transparent to ultraviolet light and if possible, have an index of refraction close to that of $BaF_2$. The glue joint between two crystals was made with Wacker Chemie Silguard 601 epoxy and was cured while the two crystals were clamped together in such a way that their edges were aligned. Unfortunately there was some bowing in the joints, and when they were eventually stacked this bowing had to be taken into account. The angle between one crystal and the one it was glued to was as much as $6\,mrad$. Care was taken that there be no air or defects in the glue joints, and the glue itself was tested in a photo-spectrometer to ensure that it would be transparent at ultraviolet wavelengths.

When the crystal surface was wrapped with $5\,mil$ Teflon tape, the scintillation light escaping the crystal was diffusely reflected off the Teflon and sent back into the crystal to eventually be internally reflected to the PMT. However, if the crystal surface was wrapped with mylar, light could escape the crystal and would not reach the phototube. Thus, by wrapping different areas of the crystal with different materials one could tune the overall response of the crystal. For example, if there was a large drop in light across the glue joint, one could wrap the side farther away from the glue joint with Teflon and leave the side close to the phototube wrapped only with mylar. Although the overall signal would be smaller, the crystal response would at least be flat. Since at the relevant photon energies in E799 photo-statistics contribute less than 1% to the energy resolution in $BaF_2$, this slight loss in overall light signal was unimportant. A pair of crystals with no light drop across the glue joint (perhaps because the joint itself was thinner) could be wrapped with Teflon along the entire length of the pair of crystals. Each pair of crystals were tuned individually to flatten the response.

Once the crystals were glued and wrapped with Teflon tape and mylar they were tested in the laboratory using a $^{137}$Cs ($662\,keV\,\gamma$ ray) source and a high gain (10 stage) phototube, Hamamatsu R1802. Using a multichannel analyzer (MCA) hooked up to the phototube, each crystal was tested by moving the $^{137}$Cs source along the length of the crystal and finding the photo-peak of the $662\,KeV$ line of $^{137}$Cs. At this energy the photo-peak of $BaF_2$

had an RMS width of about 30%, and at the voltage setting used in the lab the peak was about 200 counts on the MCA. By using photons of this energy the energy deposition was ensured to be contained in the crystal and relatively localized to where the source itself was placed.

If the energy resolution at this energy ($660\,keV$) was primarily due to photostatistics, then the width observed in the laboratory corresponds to $\sim 40$ photoelectrons per MeV. This is significantly below the light output observed previously in other $BaF_2$ crystals (light outputs between 300 and 500 photoelectrons per MeV are standard [26][27]). However, even with such a low number of photoelectrons per MeV, photostatistics will only contribute a resolution of 0.5% per $GeV$, which is over a factor of four better than the lead-glass (or a factor of sixteen more light!).

Figure 47 shows the light response for different wrappings of a single pair of crystals. The signals in the MCA were normalized. Notice that when the entire crystal was wrapped the drop in the response was 35%, and that was eventually reduced to a drop of only 5%, which was within the design specifications. All nine pairs of crystals were tuned in this way. Table 10 is a listing of all nine pairs of crystals, showing how close to collinear each pair was glued, and how flat the responses were across all $50\,cm$ of crystal.

## 5.10.4   Beam-line Testing with Muons

Once the crystals were glued, wrapped, and tested with the $^{137}$Cs source, they were transported to the E799 beam-line, where they were stacked into a $3 \times 3$ array and held in place with clamps. The phototubes were pressed to a cookie made of silicon gel (Wacker Chemie Silgel) which was in turn pressed against the crystal, a mounting which was identical to the mounting in the laboratory. The PMT's used were 6 stage Hamamatsu $R4480$ tubes with a lower gain than those used previously in the laboratory. While the lower gain was ideal for the high energy electromagnetic showers expected in the calorimeter and for a fast response time, to test the crystal response with muons going sideways through the crystals one needed to use ($\times 10$) amplifiers before the analog signals were sent to ADC's. To test the crystals, they were initially placed with their long axes perpendicular to the beam. By triggering on the combination of B and C counters which were directly in front of the
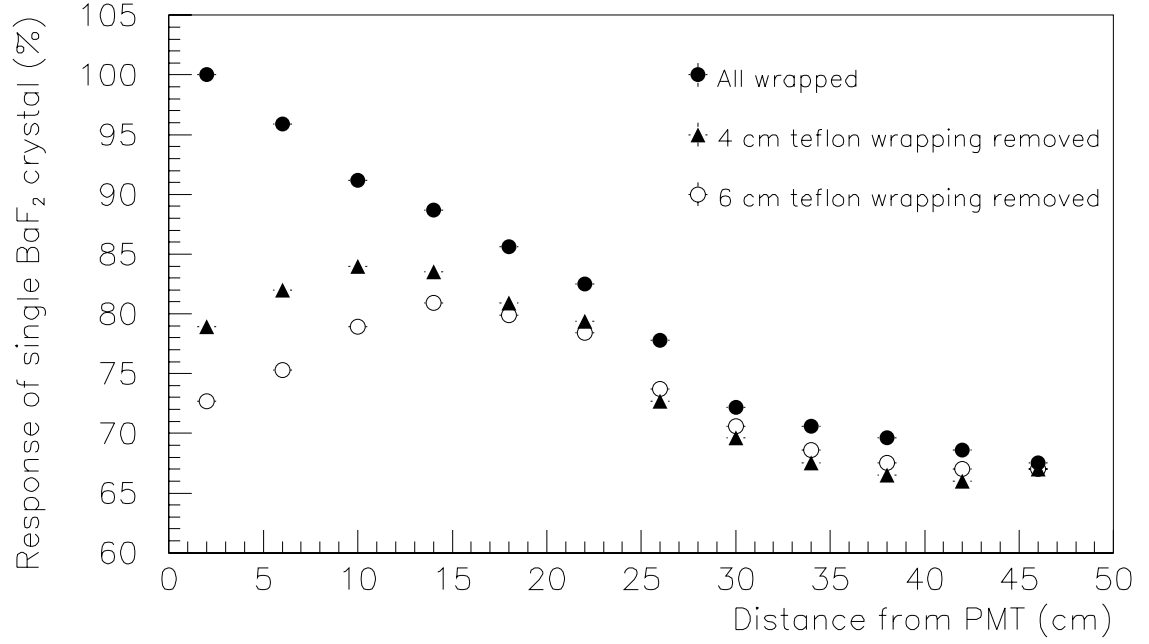
Figure 47. Response of a pair of crystals as a function of source distance from the phototube for different wrappings. The region where the teflon was removed was the end close to the phototube.

Table 10. Gluing and Wrapping Results of BaF$_2$ Crystals

| Crystal Pair | Deviation from Straight | Deviation from Flat Response |
|---|---|---|
| 1 | $2\,mrad$ | 4% |
| 2 | $2\,mrad$ | 6% |
| 3 | $0.8\,mrad$ | 5% |
| 4 | $< 0.4\,mrad$ | 3% |
| 5 | $< 0.4\,mrad$ | 3% |
| 6 | $2\,mrad$ | 6% |
| 7 | $6\,mrad$ | 7% |
| 8 | $3\,mrad$ | 5% |
| 9 | $2\,mrad$ | 3% |

crystals and the muon trigger bank behind the muon filter we were able to study the signal of muons going sideways through each of the crystals. Figure 48 shows the observed ADC distributions for three of the nine crystals.

Figure 49 shows the response for muons as a function of the distance the muon crossed the crystal from the PMT. Although the responses are worse than the responses seen in the laboratory, because of slight differences in coupling to the phototube or damage in transit to the glue joints, most are still within acceptable values. The worst two pairs of crystals have effective $\alpha$'s of about 1%. Recall that for the lead-glass array the $\alpha$'s ranged from 4% to 17%.

### 5.10.5    Electron Calibration of $BaF_2$

During Calibration 27 (see table 9) the $BaF_2$ calorimeter was mounted behind one of the beam-holes of the lead-glass calorimeter. Figure 50 shows the mechanical support for the $BaF_2$ array. The crystals were mounted behind the beam-holes in such a way that the front
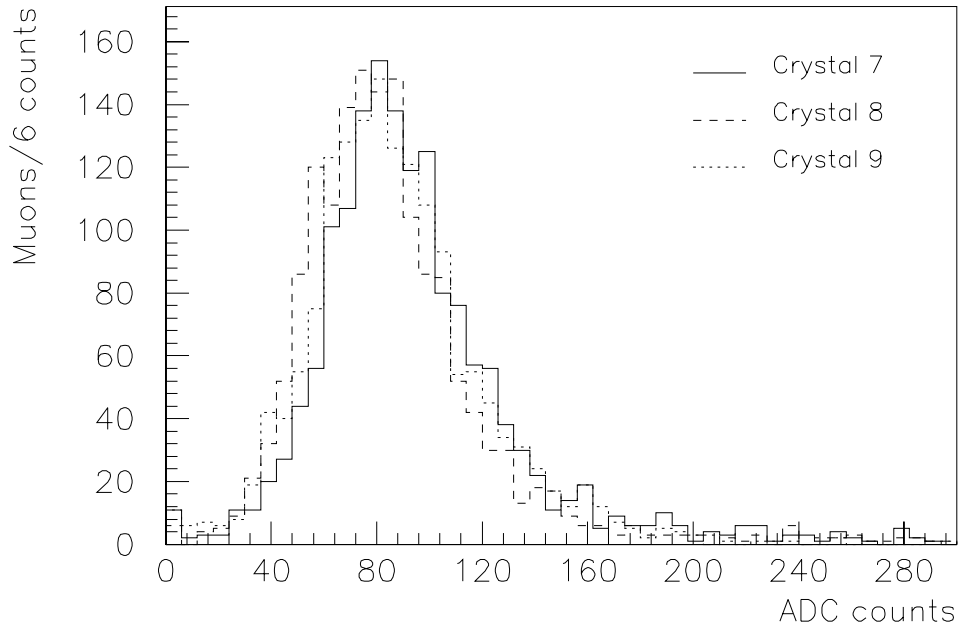
Figure 48. Muon signals in three out of nine $BaF_2$ crystals
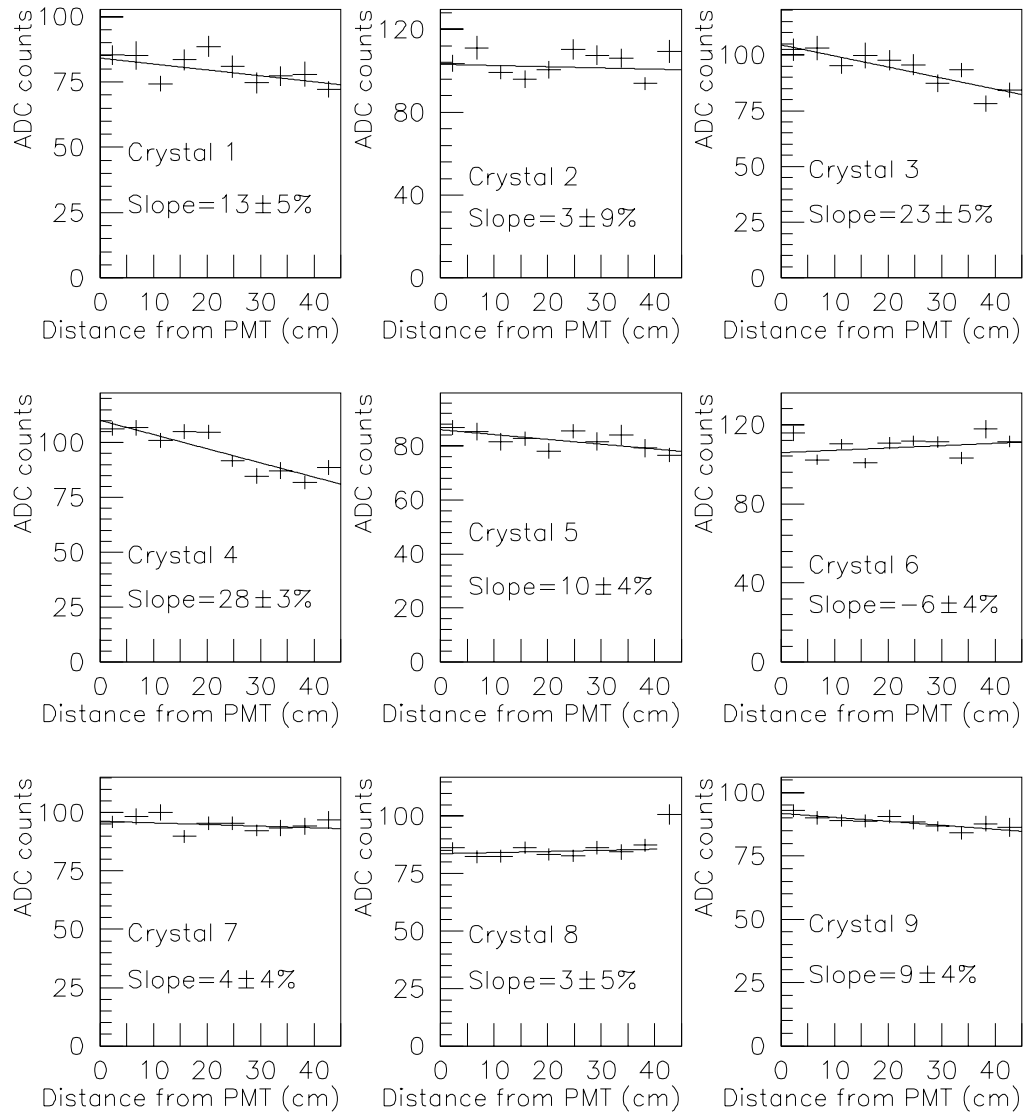
Figure 49. Response for Muons Crossing BaF$_2$ crystals as a function of distance from the PMT
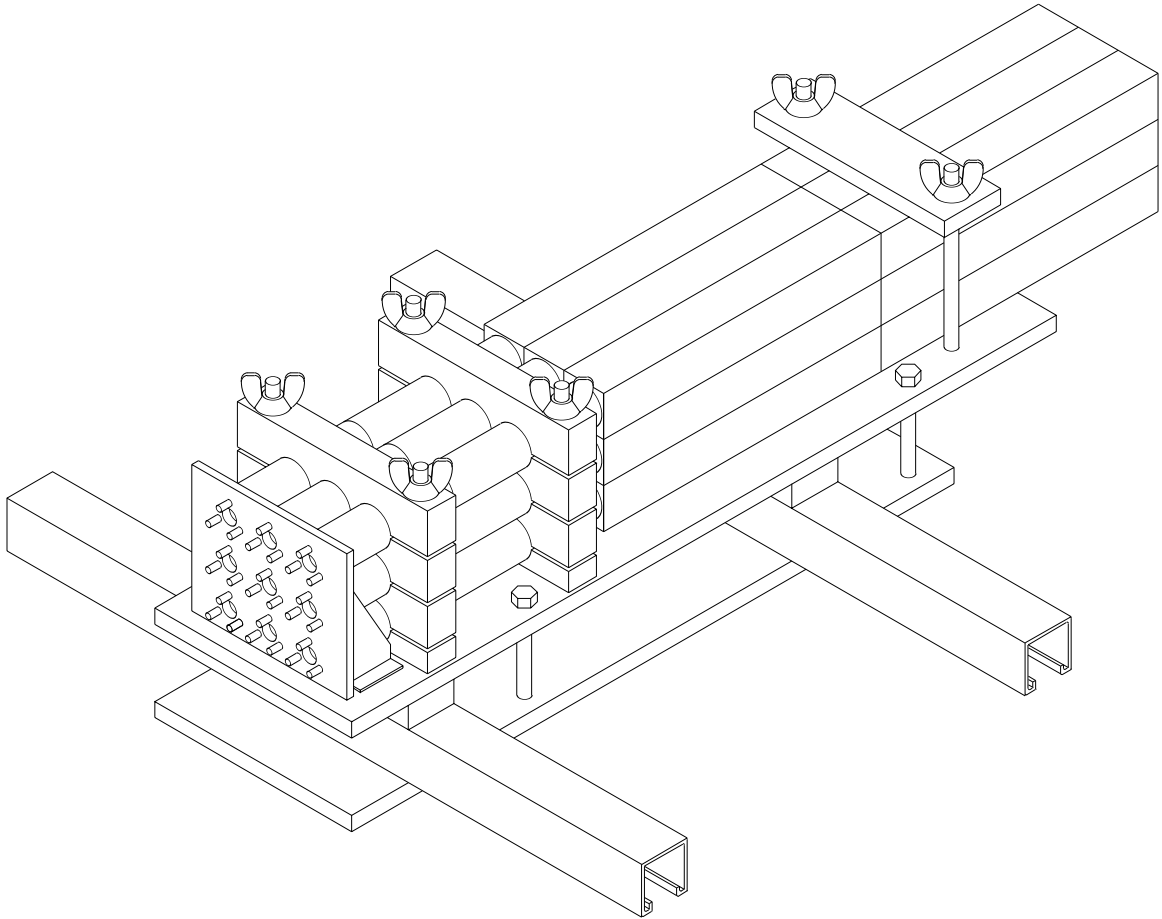
Figure 50. Mechanical Support for the BaF$_2$ Calorimeter

face of the BaF$_2$ crystals are a few centimeters from the back face of the lead-glass blocks. Originally the beam-hole calorimeters were to be placed directly inside the beam-holes of the lead-glass rather than behind them, but GEANT studies showed that the hadron shower splash into the inner lead-glass blocks from the beam hitting the calorimeter would be too large and therefore render those lead-glass blocks useless.

The calibration data was taken at lower intensity than normal electron calibration runs to reduce accidental activity in the beam-hole detectors, but there was still a large amount of energy from the beam impinging on the crystals. The trigger was the same as that for the regular lead-glass calibration. The voltages on the crystals were set very low and the pre-amplifiers were removed to account for the extra energy that was expected in the crystals, given that the electrons expected ranged in energies from $3\,GeV$ to $60\,GeV$. The pedestals were studied online and were determined to have an RMS of about seven ADC counts (or $\sim 0.35$ picocoulombs) for all nine crystals while the beam was hitting the calorimeter.

**Gain Balancing**

In order to optimize the calorimeter resolution the gains of each of the nine crystals had to be matched. To do this the signal for electrons hitting each of the nine blocks of BaF$_2$ had to be measured. Figure 51 shows the resulting number of ADC counts per $GeV$ of energy for electrons hitting the inner $2\,cm \times 2\,cm$ of each block for all nine blocks. Since the BaF$_2$ calorimeter was behind and offset from the beam-hole the illuminations on the different blocks were slightly different. If one fits the peaks of the distributions in figure 51 to Gaussian distributions, the resolutions for the crystals range between 5 and 7%. Of course, for a large calorimeter one will sum up energies of several crystals and so the resolution will improve dramatically. In the next section we discuss the process of fine-tuning the gains and the determination of the total calorimeter resolution for electrons which hit the central block of the calorimeter.

**Fine Tuning of the Gains**

To determine the ultimate resolution of a large BaF$_2$ electromagnetic calorimeter, we next considered only events which had electrons pointing into the middle $2.8\,cm \times 2.8\,cm$ of the
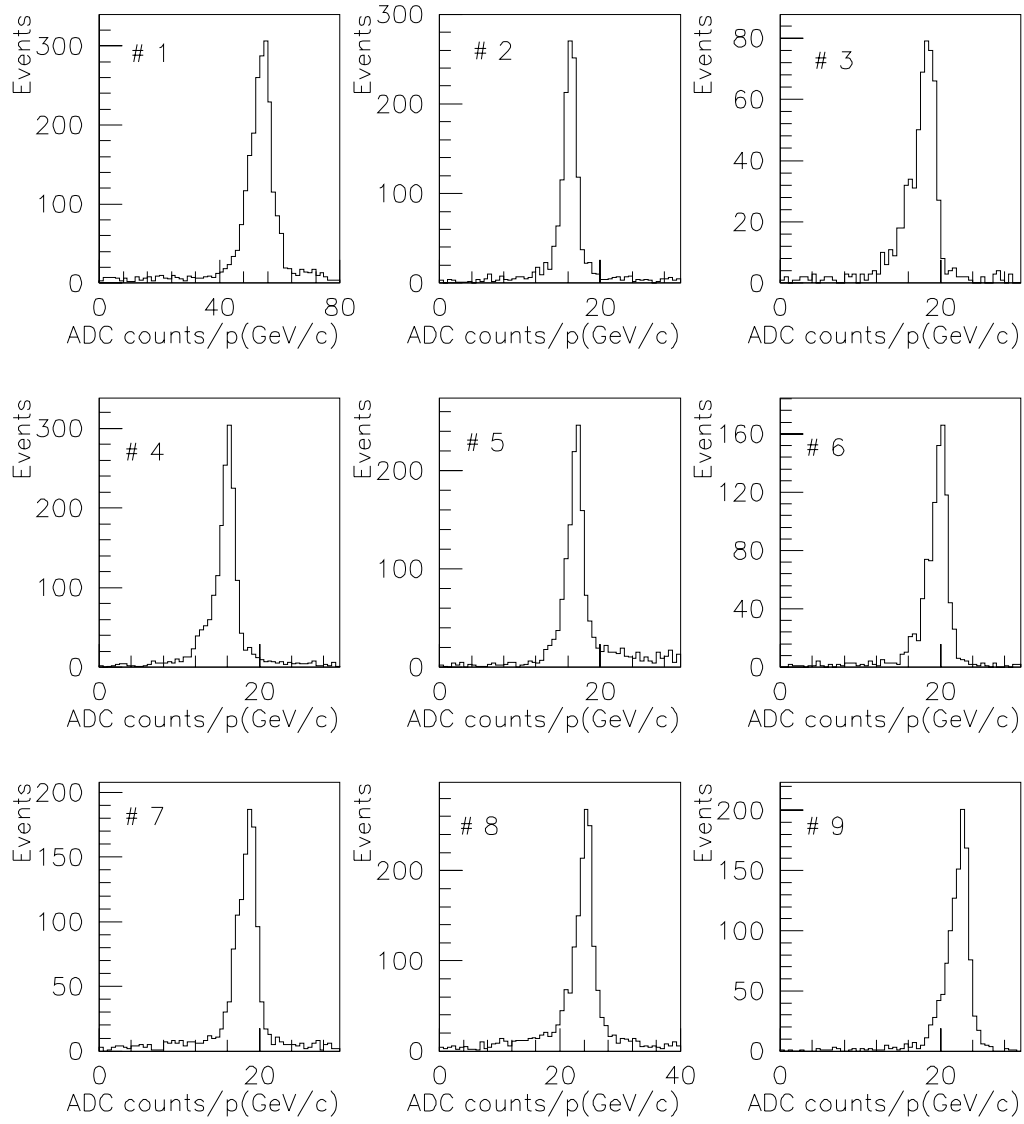
Figure 51. ADC counts divided by momentum for all 9 pairs of BaF$_2$ crystals, for electrons hitting the inner $4\,cm^2$ of each crystal

central block. Cuts were made on this sample to reduce accidental activity. For example, the other electron in the event was required to arrive at least two glass blocks away from the beam-holes, and the fraction of energy in each of the neighboring $BaF_2$ blocks was required to be less than 25% of the total energy. Since electromagnetic showers of the crystal are very collimated, and considering that showers were required to be in the inner $4\,cm^2$ of the crystal, this cut does not bias the signal.

To fine-tune the gains we minimize the following quantity:

$$\chi^2 = \sum_{\text{allevents}} \left[ 1 - \frac{\sum_{i=1}^{9} G_i ADC_i}{p} \right]^2$$

where $ADC_i$ is the number of ADC counts for the $i^{th}$ block, $G_i$ is the gain (in GeV/c per ADC count), a rough estimate of which was obtained in the previous gain-balancing step, and $p$ is the electron momentum (in GeV/c). By setting the derivative of this quantity with respect to each $G_i$ equal to zero, the equation becomes:

$$\begin{aligned}
\frac{d\chi^2}{dG_i} &= 2 \sum_{\text{allevents}} \sum_{j=1}^{9} (1 - \frac{G_j ADC_j}{p}) \frac{ADC_i}{p} \\
&= 0
\end{aligned}$$

Re-casting this equation in the form of a matrix equation, we get:

$$\sum_{\text{allevents}} \left[ \frac{ADC_j ADC_i}{p^2} \right] G_j = \sum_{\text{allevents}} \frac{ADC_i}{p}$$

By inverting the matrix multiplying $G_j$ one can solve for the gains and the resulting resolution will be at a minimum. The resulting distribution of the measured $E/p$ for $BaF_2$ is shown in figure 52. The high-side tail is due to accidental activity that was below the threshold of the cuts mentioned above. For this sample of electrons the electron energy resolution of the peak is $1.33 \pm 0.1\%$

The resolution itself has several contributions, and is not limited by the inherent resolution of the calorimeter itself. First of all, when measuring an energy resolution of a fraction of a per cent, the momentum resolution contribution to the width of $E/p$ becomes important. For an average electron energy of $45\,GeV$ the momentum resolution of the chamber system (see section 3.2.2) is 0.6%. Second of all, the gains were set so low that unfortunately

the 7 ADC count pedestal rms seen on the sum of the 9 crystals corresponds to a 0.35 $GeV$ smear in the resolution. Finally, there is the resolution due to shower fluctuations, which the EGS program predicts to be 0.5% for a $BaF_2$ calorimeter of this size. When adding these quantities in quadrature the average predicted resolution is 1.2%, which is consistent with the observed resolution.

### 5.10.6 Radiation Damage of $BaF_2$

After this calibration, the normal experiment configuration with a high rate neutral hadron beam was tested. When the experiment ran with calorimeters in the beam-holes, the accidental activity in the detectors behind the calorimeters increased dramatically due to neutron and kaon interactions in the calorimeters. A large fraction of otherwise good events were vetoed due to this activity. Table 11 shows the ratio of singles rates for various counters in the detector with and without the hole calorimeters in place. Because of the increased accidental activity the calorimeters were removed after only a week of running. All of
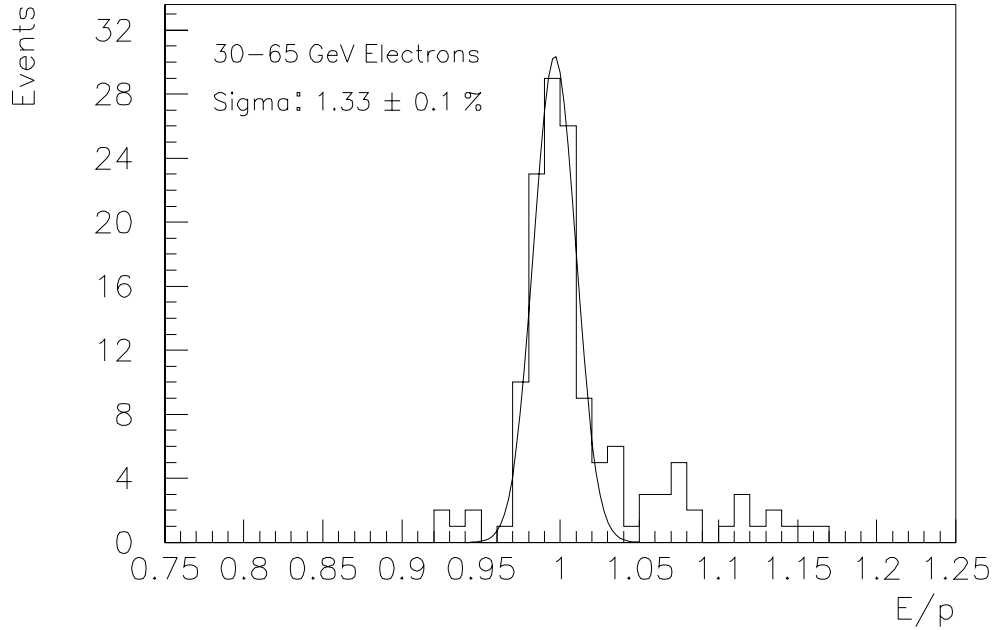


Figure 52. Distribution of $E/p$ for clean events entering center crystal

Table 11. Comparison of Singles Rates with and without Beam-hole Calorimeters

| Trigger Source | Without $BaF_2$ | With $BaF_2$ | Ratio |
|---|---|---|---|
| 1B | 46.6M | 70.9M | 1.5 |
| 2B | 12.3M | 15.4M | 1.25 |
| $E_{Thi}$ | 0.555M | 0.613M | 1.1 |
| Mu1 | 32.3M | 107M | 3.0 |
| $BA_3$ | 54.6M | 36.0M | 0.66 |

the physics which is discussed in the remainder of this thesis is from data taken after the beam-hole calorimeters were removed from the beam.

During that week, the crystals saw on the order of $50\,Krad$ of radiation, which, according to the literature [20] [21], is harmless to small crystals of $BaF_2$. In reference [20] the authors tested crystal disks which were $22\,mm$ in diameter and $6\,mm$ thick with a dose of $13\,Mrad$. The authors determined that the scintillation properties were not altered and the 0.5% loss in transmission measured was within the systematical uncertainty in the measurement. Unfortunately, in order to make predictions on large pieces of $BaF_2$ the accuracy with which one measures light loss across a small piece is considerably less than 0.5%. Furthermore, loss of light can be due to deterioration of surface quality, loss of scintillation efficiency, or increased absorption of scintillation light. These effects are impossible to separate if one is only testing a small piece of $BaF_2$ and can only make light measurements with 0.5% accuracy.

Once these $BaF_2$ crystals were removed from the beam they were again placed perpendicular to the beam behind the lead-glass, and the amplifiers were re-installed. Once again the response of the crystals as a function of distance from the phototube was studied with muons. Figure 53 shows the response of four of the nine crystals after irradiation, normalized to the response before irradiation by using the bin closest to the phototube. As a reminder of how flat the response was before irradiation, the responses from fig. 49 for

the same crystals are also shown on the same scale. The crystals are no longer useful for high resolution calorimetry.

Upon removal of the blocks from the beam-line it was discovered that the blocks themselves were green in certain regions. The crystals were not evenly discolored, nor were the darker sides correlated with respect to which way they were oriented in the beam-line. If the discoloration was simply from the radiation damage of the crystal itself one might expect more discoloration downstream rather than upstream due to hadronic shower development in the crystal. However, if the discoloration was due to impurities in the crystal, it would
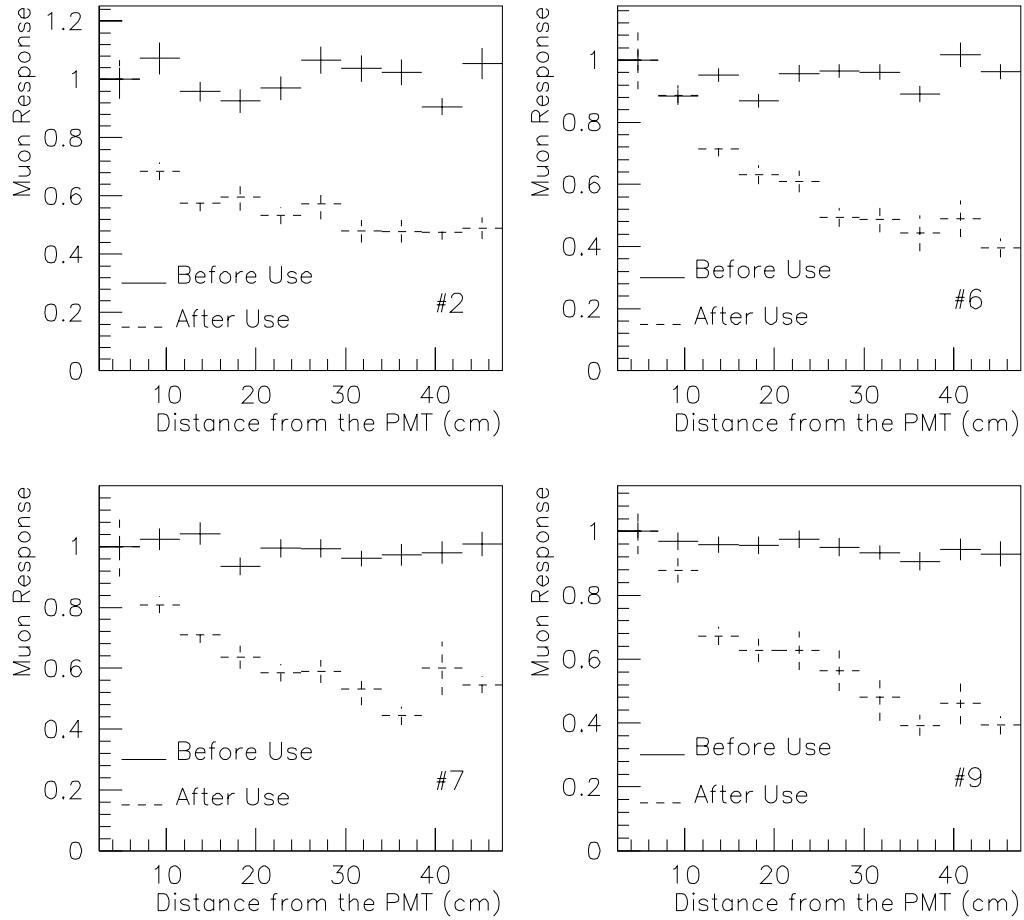


Figure 53. Normalized Response for Muons Crossing BaF$_2$ crystals as a function of distance from the PMT, both before and after irradiation

likely be located at one end of the crystal. For example, if the crystals were grown vertically, the impurities might be expected to rise to the top or fall to the bottom as the crystal was being grown. At any rate, much work needs to be done before one can claim that large crystals of $BaF_2$ are as radiation hard as is necessary for high flux environments found in high energy physics experiments.

Still another potential problem caused by radiation was that many barium nuclei were broken up by the large flux of neutrons, and then the unstable products of these interactions decayed by emitting $\gamma$ rays. In this way the $BaF_2$ crystals became radioactive. When looking at a crystal with a NaI crystal designed for $keV$ energies, there were several lines which were identified. Figure 54 shows the resulting photon spectrum of one $BaF_2$ crystal. Several of the more intense lines have been identified as being from radioactive elements near the atomic weight of Ba. In future experiments, this low-level activity must be accounted for and subtracted if the crystals themselves are to see a high neutron flux.
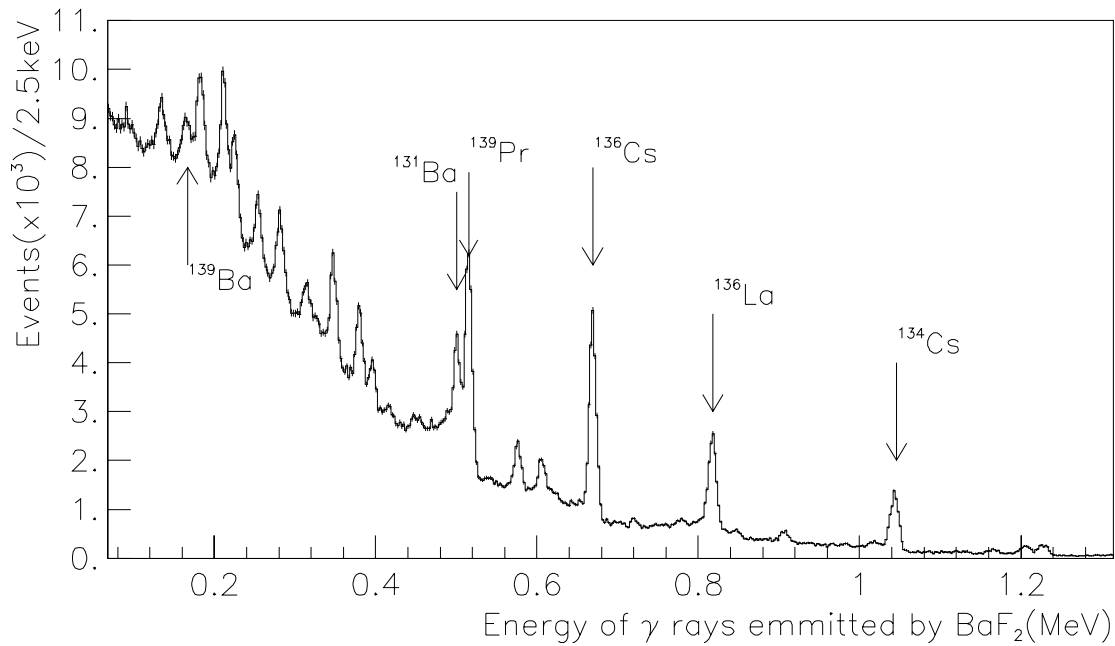


Figure 54. Photon Spectrum of Irradiated $BaF_2$

### 5.10.7   Conclusions on $BaF_2$ Calorimetry

Although the experiment was unable to do physics with the hole calorimeters in place, much was learned about $BaF_2$ as a result of this study. The two most important issues which were learned were that $BaF_2$ can be glued and wrapped in such a way to create a calorimeter with extremely good ($\sim 1\%$) resolution, and secondly, that much work needs to be done on both the issue of $BaF_2$ purity and related radiation damage tests before a large-scale radiation hard $BaF_2$ calorimeter can be constructed.

# CHAPTER 6

# CALIBRATION OF THE MUON SYSTEM

"You load 16 tons, what do you get?" —*Merle Travis*

## 6.1 Overview

To accurately measure the acceptance for the decay $K_L \to \pi^0 \mu^+ \mu^-$ the muon response of the detector must be well-understood. The detector components that comprise the muon system are the hadron shower veto (MU1), the steel hadron filter, and the muon trigger bank (MU3). Since in the $\pi^0 \mu^+ \mu^-$ analysis the normalization mode does not have muons, there was no requirement on either of those scintillator banks, and so the absolute efficiencies of both MU1 and MU3 do not affect the normalization mode and will not cancel in the ratio of signal to normalization acceptances.

To calibrate MU1 and MU3 we used data from special runs taken at several points during the experiment which contain a pure flux of muons on the detector. To ensure that the particles in the detector for these runs were muons, we required that the primary beam hit a beam stop located 1420 feet upstream of the E799 target. The only particles which passed through the 36.8 interaction length beam stop to reach the detector were muons. Table 12 is a listing of all of the muon calibration runs that were taken, and the fraction of the data that used the calibration constants determined in that calibration. In particular, the efficiencies for the muon trigger counters were measured as a function of the calibration, and then used in the Monte Carlo simulation. Since MU1 required a large data

Table 12. Muon System Calibrations in E799

| Date | Calibration | Events | Fraction of Two-Muon Data |
|-------|-------------|--------|---------------------------|
| 11/5  | 1 | 1.0 M | 15% |
| 11/13 | 2 | 1.0 M | 25% |
| 12/4  | 3 | 4.8 M | 18% |
| 12/5  | 4 | 2.2 M | 20% |
| 12/17 | 5 | 1.3 M | 22% |

set for calibration, it was only calibrated once using muons from the longest calibration run, Calibration 3. The same gains were then used throughout the entire run.

The trigger requirement for the calibration muons was that there be at least one B-bank counter and one C-bank counter hit in each event. In software, exactly one track in each of the (x) and (y) views was required, and that track was required to point to both a B-bank and C-bank counter that had fired. This provided us with a clean sample of muons which could be used to determine the efficiencies of the muon trigger plane and the hadron shower veto, and were also used to measure the muon response in the lead-glass calorimeter. The accidental activity in the detector for these runs is very different from the activity in the detector during normal physics data-taking. So, while this data was useful for calibrating the muon response in various aparati, the effects of accidental activity in the same detectors needed to be considered separately. This chapter will describe the measurements necessary to calculate the muon trigger plane efficiency and the hadron shower veto efficiency; how those measurements were used in the Monte Carlo simulation of the detector is described in chapter 7.

## 6.2 Multiple Scattering in the Muon Steel

As described in section 3.2.6, downstream of the calorimeter there was a wall of lead bricks 0.7 nuclear interaction lengths long followed by a steel hadron filter 20 interaction lengths long. The total number of interaction lengths the muons pass through after having their

positions measured in the chamber system is $22.4\lambda_0$. A muon's RMS scattering angle with respect to an arbitrary plane, $\theta$, is given by the following equation [18]:

$$\theta_{plane}^{RMS} = \frac{13.6\,MeV}{\beta cp}\sqrt{\frac{x}{\lambda_0}}\left[1 + 0.038\ln\frac{x}{\lambda_0}\right]$$

where $\beta$, or v/c, is $\approx 1$ for muons at these energies. $p$, the momentum, ranges from 7 to $70\,GeV/c$ and is on average about $10\,GeV/c$, and $x/\lambda_0$ is the number of radiation lengths that the particle traverses. The $\theta_{plane}^{RMS}$ prediction is good to 11% for $x/\lambda_0$ values between .001 and 100 [18]. So, $\theta_{plane}^{RMS}$ ranges from 1.9 to $19\,mrad$, and given that the chambers are $12.5\,m$ from the muon trigger bank this means that the RMS muon deflection ranges between 1.4 to $14\,cm$ in a single direction. Because the muons can be deflected by such a large amount the $\pi^0\mu^+\mu^-$ analysis does not require the muon tracks to extrapolate to a particular counter, only to the muon trigger bank itself. Another effect due to multiple scattering is that sometime muons which extrapolate to the muon trigger plane will scatter so much that it will not hit the counters at all by the time they reach the (z) position of the trigger plane. Finally, the muon trigger requirement was that two non-adjacent counters in the muon trigger bank fire. The efficiency of the muon trigger bank must be measured in such a way as to include each of these effects in the Monte Carlo.

## 6.3   Muon Trigger Plane

As mentioned in the detector section, the muon trigger plane used in this analysis consisted of 16 non-overlapping counters which measured $9\,cm \times 1.2\,m$ each. The counters were made of plastic scintillator with phototubes at the bottom of each counter. Figure 55 shows the 16 active regions of the counters, as well as the 128 regions whose efficiencies are measured separately. By looking at high-energy muons passing through the center of the muon trigger bank array we determine the overall muon efficiency of the bank alone to be about 98%, where the small inefficiency is due primarily to the spaces between the different counters. There is also a $\sim 5\%$ chance that a single muon can fire more than one trigger plane due to either multiple scattering in the trigger bank itself, or a delta ray produced when the muon exits the muon filter. These effects were small and were not included in the Monte Carlo.

### 6.3.1 Efficiency

The analog signal in the individual muon trigger counter was discriminated, and the resulting digital signal was used in the trigger. Because of light absorption or leakage in the counters, the signal from a muon passing through the counter close to the phototube is larger than the signal from a muon passing through far away from the phototube. Depending on the discriminator level, this may result in a lower efficiency for the far end of the counters. Figure 56 is a plot of the efficiency of each counter in the array as a function of where the extrapolated muon position is, for all muons above $7\,GeV/c$. The four different plots in figure 56 represent four different regions in (y). By looking at a single counter for all four views one can see that the phototube is closest to the counters in the $4^{th}$ region as marked in the plot. The rounded edges of these efficiencies are due to multiple scattering in the steel
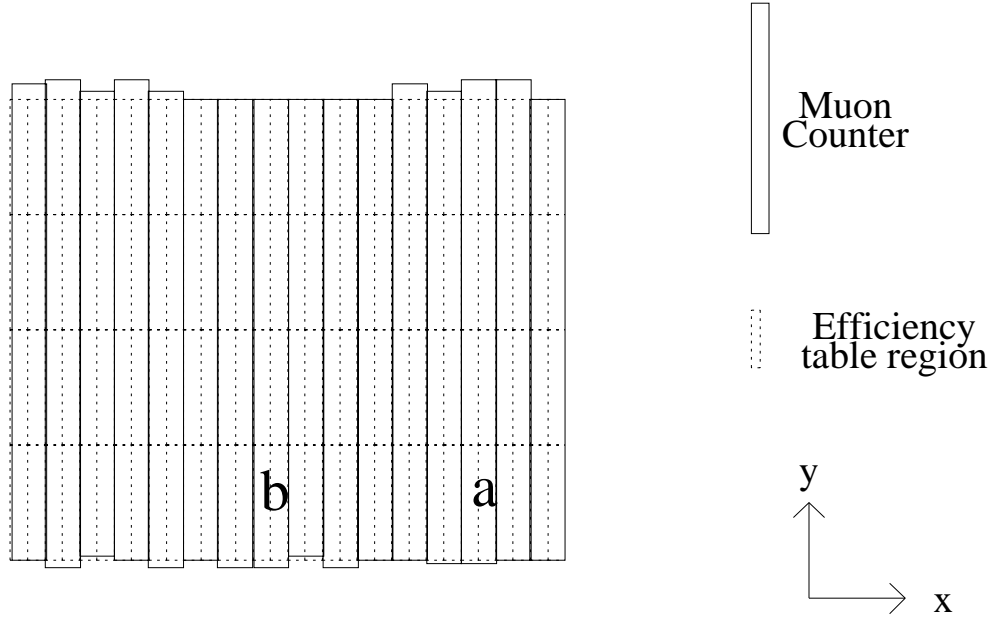


Figure 55. The 16 counters that comprise the muon trigger plane, and the 128 regions whose efficiencies are calculated as a function of momentum.
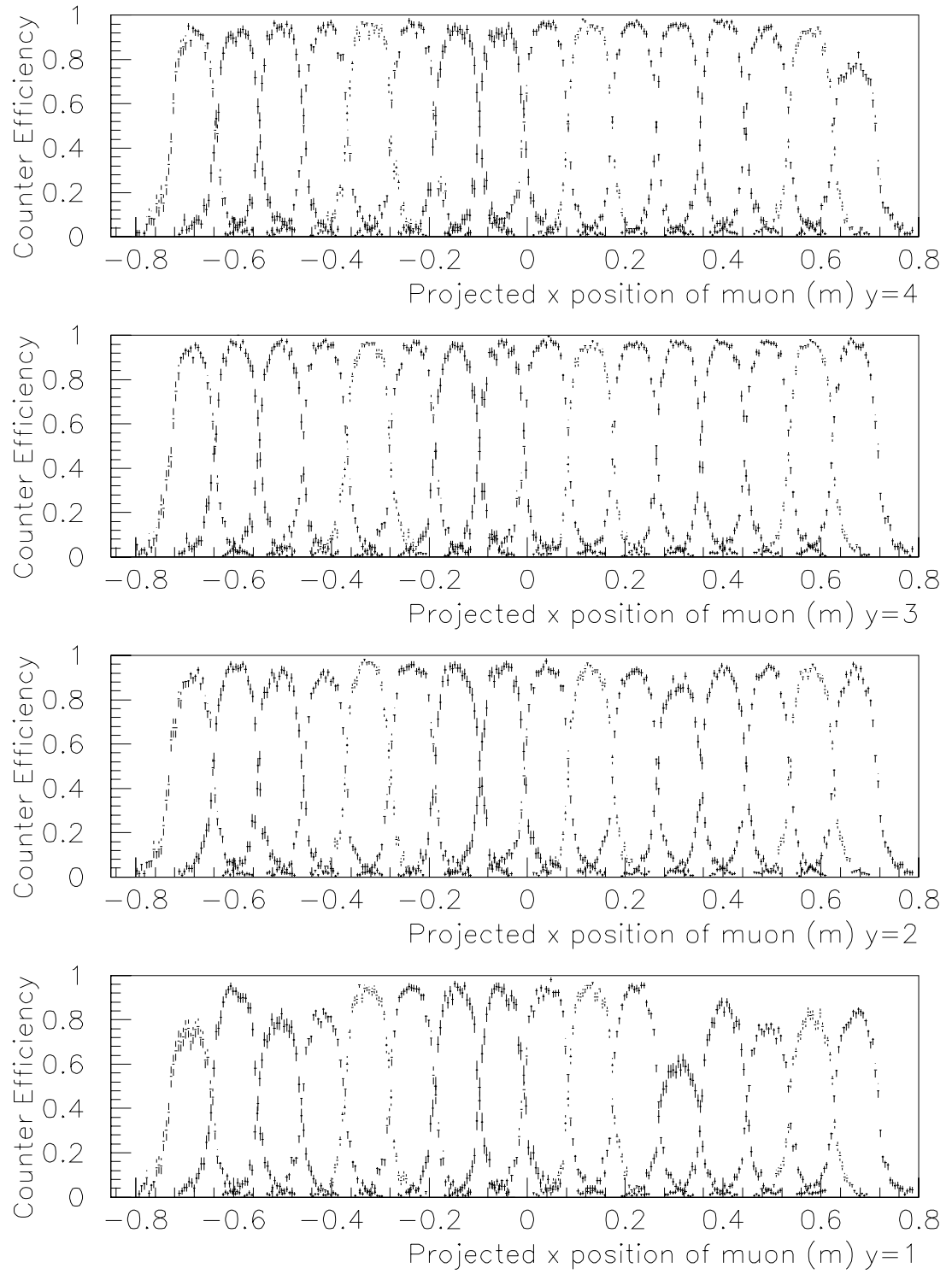
Figure 56. The efficiencies of all 16 counters as a function of (x) for four different (y) regions, where (y=4) region is closest to the phototubes.

hadron filter. Note that the counters themselves are so narrow and multiple scattering so large, that for a significant fraction of the bank, the regions that two adjacent counters are sensitive to overlap, even though the counters themselves do not overlap. For this reason we measure the efficiency of the entire bank as a single unit as a function of extrapolated (x) and (y) position, rather than measure the efficiency of each counter individually.

The efficiencies shown in plot 56 were calculated for all muons with momenta above $7\,GeV$, but in fact, because of multiple scattering these efficiencies should be measured as a function of momentum as well as (x) and (y). Furthermore, any measurement of what has been called "counter efficiency" is really the effect of both the counter efficiency and the multiple scattering combined. The efficiencies are defined as the fraction of events which have ANY muon trigger counter fired for a track extrapolating into a given region in x and y, for four different momentum bins–namely, $7 - 14\,GeV/c$, $14 - 21\,GeV/c$, $21 - 28\,GeV/c$, and above $28\,GeV/c$. The regions at the edges of the bank of counters are typically lower because of multiple scattering, as expected, light absorption tends to lower the efficiency at the edge of the counters far away from the phototube.
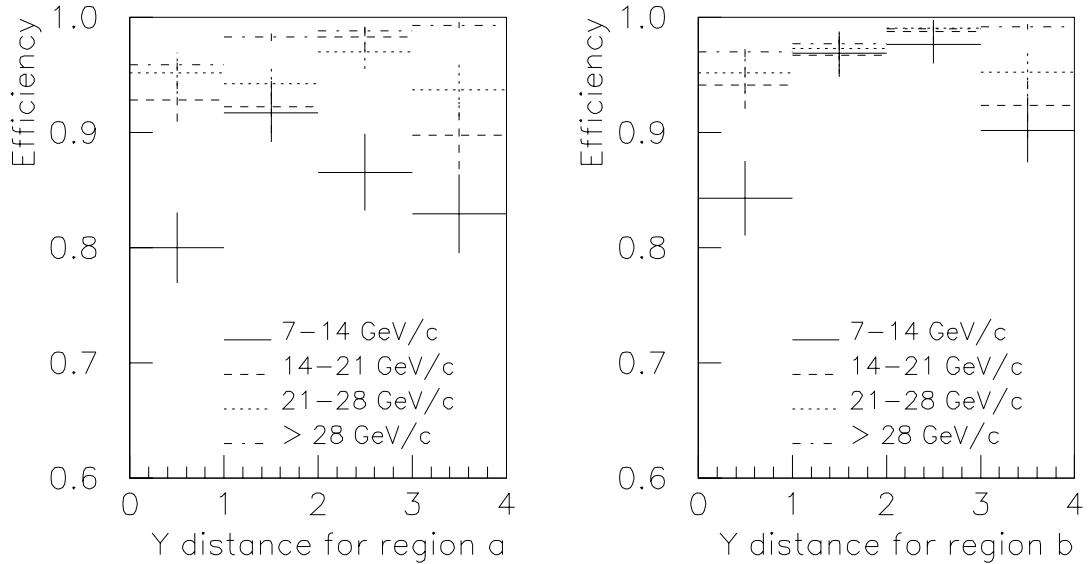


Figure 57. The efficiencies of all 16 counters as a function of (x) for four different (y) regions.

Figure 57 shows the measured efficiency for a given run region as a function of the (y) position for two different (x) positions, one position two counters from the edge of the array (region "a" in figure 55) and one position closer to the center (region "b" figure 55). The four different efficiency functions in the same plots show the efficiencies for the different momentum regions. For counters closer to the edge of the array the efficiencies change more dramatically as a function of momentum, whereas for counters closer to the middle the efficiencies are closer to constant. This is because even if the muon pointed near the center of the counter were to scatter through a large angle it would still most likely get to a counter somewhere in the array.

## 6.4   Hadron Shower Veto

The other detector calibrated with the beam-dump muons is the Hadron Shower Veto (MU1). The counter orientations are shown in figure 58, as are the relative sizes of the MU1 bank and the muon trigger plane. In total there were about 42 radiation lengths and 2.5 nuclear interaction lengths of material before this veto. Ideally electromagnetic showers would deposit very little energy outside the lead, yet hadronic showers will often produce a large signal in these counters. The strategy was to gain balance all 45 counters by tuning the phototube voltages so that the signal for a minimum ionizing particle would be roughly the same in all counters, and then veto on the analog sum of all the counters. The veto threshold would then be set at some small number of minimum ionizing showers. This veto was included in any trigger not looking for charged pions in the final state. Although there were no counters in the beam-holes (see fig.58) the counters were still rather noisy—from looking at accidental data one can see that the veto was on 18% of the time. About $\sim 1\%$ of this activity was due to muons from the target reaching MU1, and less than 1% was due to actual $K_L$ decays. The remainder of the MU1 activity was due to beam halo (from beam particles scattering off collimators or the B and C banks) and shower particles from the Back Anti reaching MU1.

Unfortunately, the MU1 counters were not all gain balanced, and although the discriminated signal for the veto was read out into the data stream, along with the ADC counts in

all the counters (each having a gate of $30\,nsec$), the analog sum from which the veto was formed was not recorded. This made calibration somewhat complicated, as is described in the following section. In particular, for each counter, we needed both the muon response of a given counter, and the relative gain of that counter in the analog energy sum.

### 6.4.1  Muon response

In general, there are two different effects which contribute to the signal of a muon going through a thin piece of scintillator. First of all, the distribution of a minimum ionizing particle's energy deposition, a Landau distribution, can be described as a sharp peak with a long tail. Figure 59 a. shows a Landau distribution with arbitrary energy units. The width of the peak depends on the thickness of the material. The sharp rise is due to the minimum
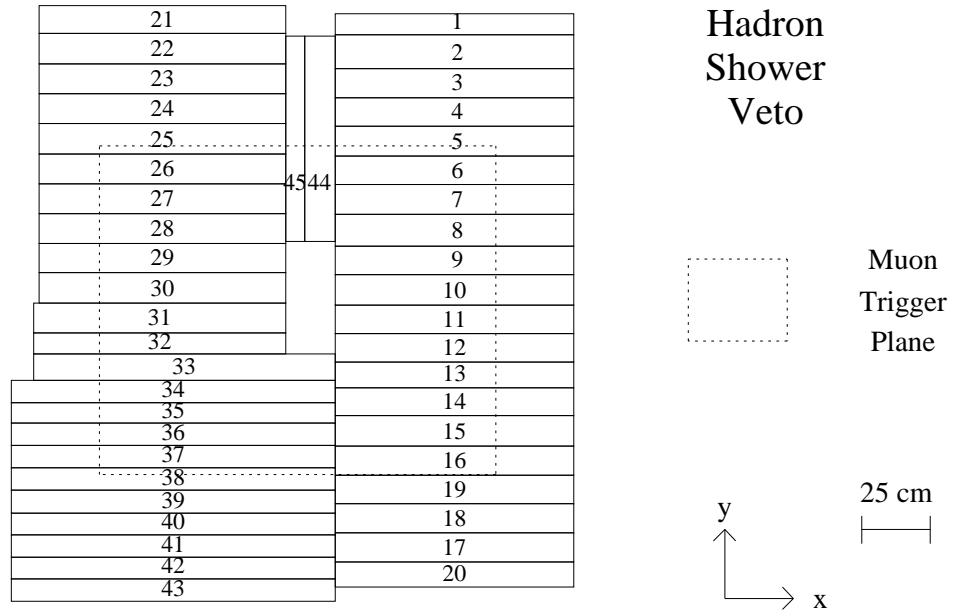


Figure 58.  The 45 counters which comprise MU1 and the relative size of the muon trigger plane.

amount of scatters that occur when a muon traverses a short length of scintillator, and the long tail is due to events where a muon scatters many times before exiting the short length of scintillator, or hard scatters that produce $\delta$-rays. Another effect which needs to be included is the photo-statistical smearing due to the finite number of photo-electrons emitted by the plastic scintillator.

Figure 59 b. shows the muon response for counter numbered 10 in figure 58. Before determining how to best represent the muon signal in the counters it is necessary to take into account still another effect, namely, the absorption of scintillation light as it traverses the counter. If one measures the Muon signal for a given counter and then fits the distributions as a function of distance from the phototube, one can see a definite dependance of the signal on this distance. To keep the number of parameters used to quantify a given counter to a minimum, we divide the signal that goes to a given counter by the average signal in that "distance" region, where distance is defined as the distance between where the muon hit and the phototube. Figure 60 shows the average signal (in ADC counts) as a function of the distance from the phototube for a few counters.
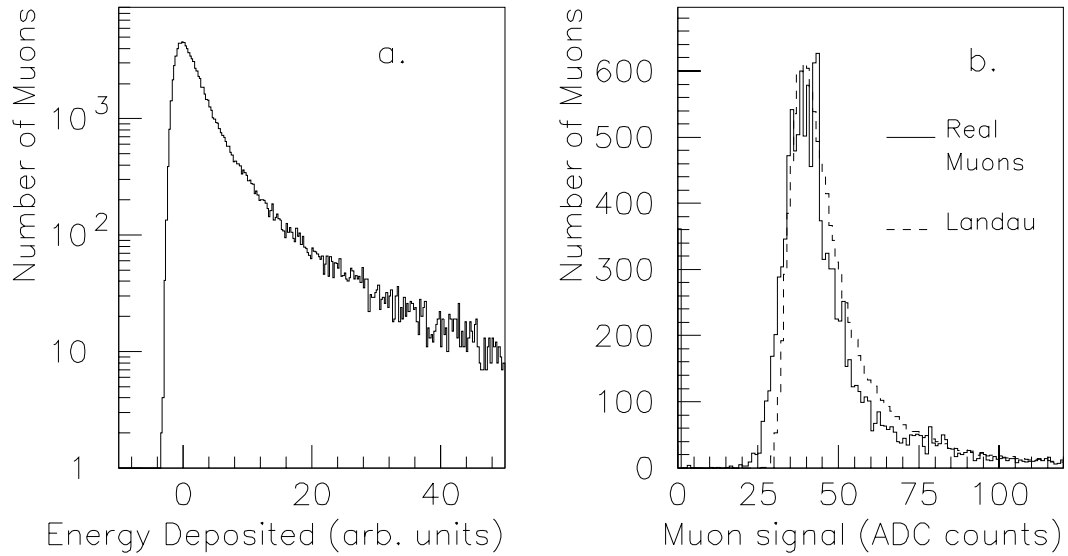


Figure 59. a. Landau distribution for muons through a thin layer b. the response for counter 10 (in ADC counts) for single muons.

Once the average signal size as a function of distance from the PMT is known, one can divide out by this factor and fit the remaining distribution to some combination of a Landau distribution convolved with a Gaussian distribution. As an approximation, however, we simply fit the normalized distribution to a "running Gaussian", which was also used in the lead-glass energy response fits (see reference [1]). It is a function of the following parameterization:

$$f(x) = e^{\left[ -\frac{1}{2} \left( \frac{x-x_0}{\sigma + a(x-x_0)} \right)^2 \right]}$$

where $a$ is a measure of how non-Gaussian the tails of the distribution are. A large positive $a$ would signal the presence of a tail on the high side of the distribution, and a large negative $a$ would signal the presence of a tail on the low side of the distribution. In general this function describes the normalized muon responses quite well. Figure 61 shows the resulting normalized distributions as well as the running Gaussian fits to those distributions for a few counters. Although the fits are not perfect, there are far fewer parameters to fit for than in a general Landau and Gaussian fit, and the fits are fairly stable. The difference between the
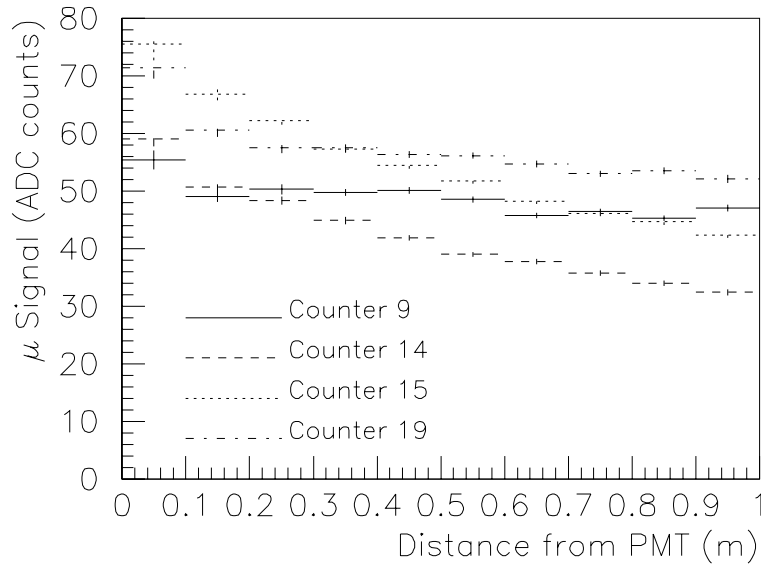


Figure 60. The average muon response of a few hadron veto counters as a function of distance from PMT

fit and the actual distribution is not important as long as the overall single-muon efficiency for MU1 is correctly predicted.

## 6.4.2   Counter Threshold

Once the response of each counter has been determined the threshold for each counter must be measured. If we had recorded the ADC'd sum of the trigger ADC counts then once the counts in the maximum counter had been calculated one could simply assume that the remaining counters had a negligible amount of energy in them due to the real muon in the event. Then if there were an overall threshold and width the Monte Carlo could simply determine what the threshold is for this event and decide whether or not that signal was above threshold. As this sum was not recorded, individual thresholds and threshold widths had to be measured for each of the 45 counters. The only information recorded was the ADC value for each counter, and we can extrapolate for each event where the muon hit
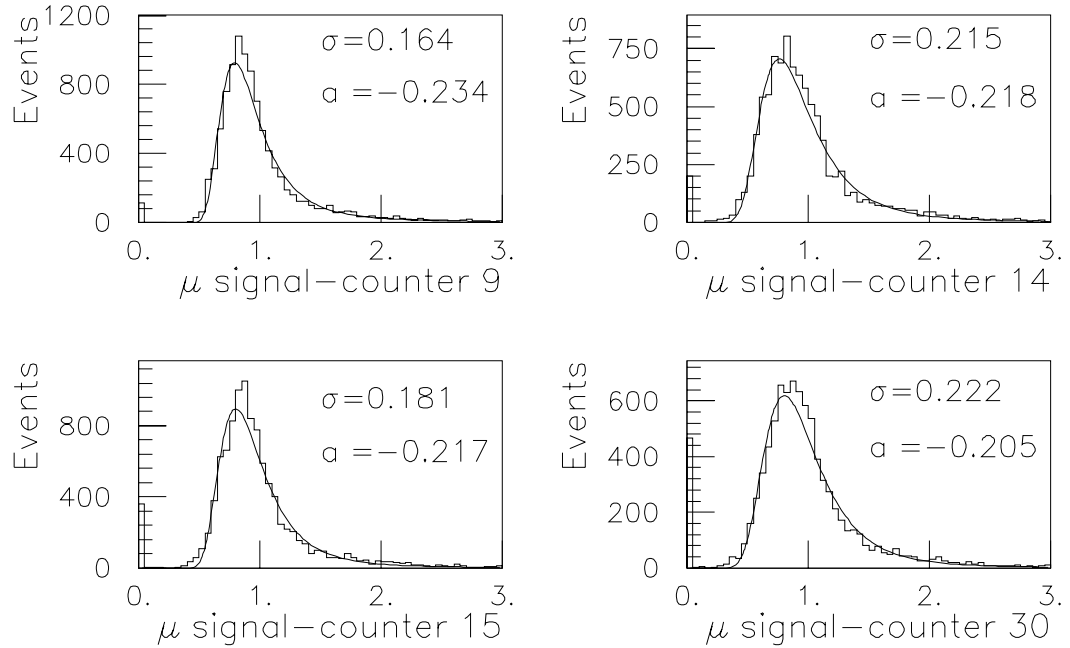


Figure 61. The normalized muon response of a few hadron veto counters and the resulting fits to a "running Gaussian".

the array. To avoid accidental energy being added to the analog sum when measuring the thresholds for the counters, the events used in these measurements were required to have the muon pointing to the counter with the highest number of ADC counts in it, and also that no other counter have more than 25% of the highest counter's ADC counts. This removes 37% of the beam-dump muon data but leaves enough statistics to measure most of the thresholds.

To measure a threshold we first plot of the fraction of time the MU1 veto is on as a function of the number of ADC counts in a given muon counter (referred to as "Plot A"). In the ideal world of course this would be a step function, with the step at the threshold. However, there is a Gaussian spread due to noise and varying counter timing, which results in a smearing of the step function. To determine the threshold we calculate the derivative of Plot A (referred to al "Plot B"). By fitting Plot B to a Gaussian one can determine the threshold and threshold width for each counter, given adequate statistics for plot A. For some counters the gain was very low and there were very few events where the counter the muon was pointing to was actually the counter with the highest number of ADC counts. Figure 62 shows both Plot A and Plot B, for a representative sample of four different counters in the bank, and also shows the fit of plot B to a Gaussian for these counters. Overall, there were 40 counters whose thresholds could be determined in this way. The errors on the thresholds and their widths ranged from 5% to 10%. The remaining five counters with low statistics were in a seldom-hit region of the array and were therefore ignored.

## 6.5   Conclusion

Using the methods outlined in this chapter the single-muon efficiencies of both the MU1 and the MU3 scintillator banks were measured to $\sim 1\%$. The overall efficiencies of these banks for two muons are crucial for estimating the $\pi^0 \mu^+ \mu^-$ acceptance, because this acceptance enters directly into the single event sensitivity of the experiment. The following chapter describes how the single-muon efficiencies are included in the Monte Carlo to correctly estimate the overall dimuon acceptance.
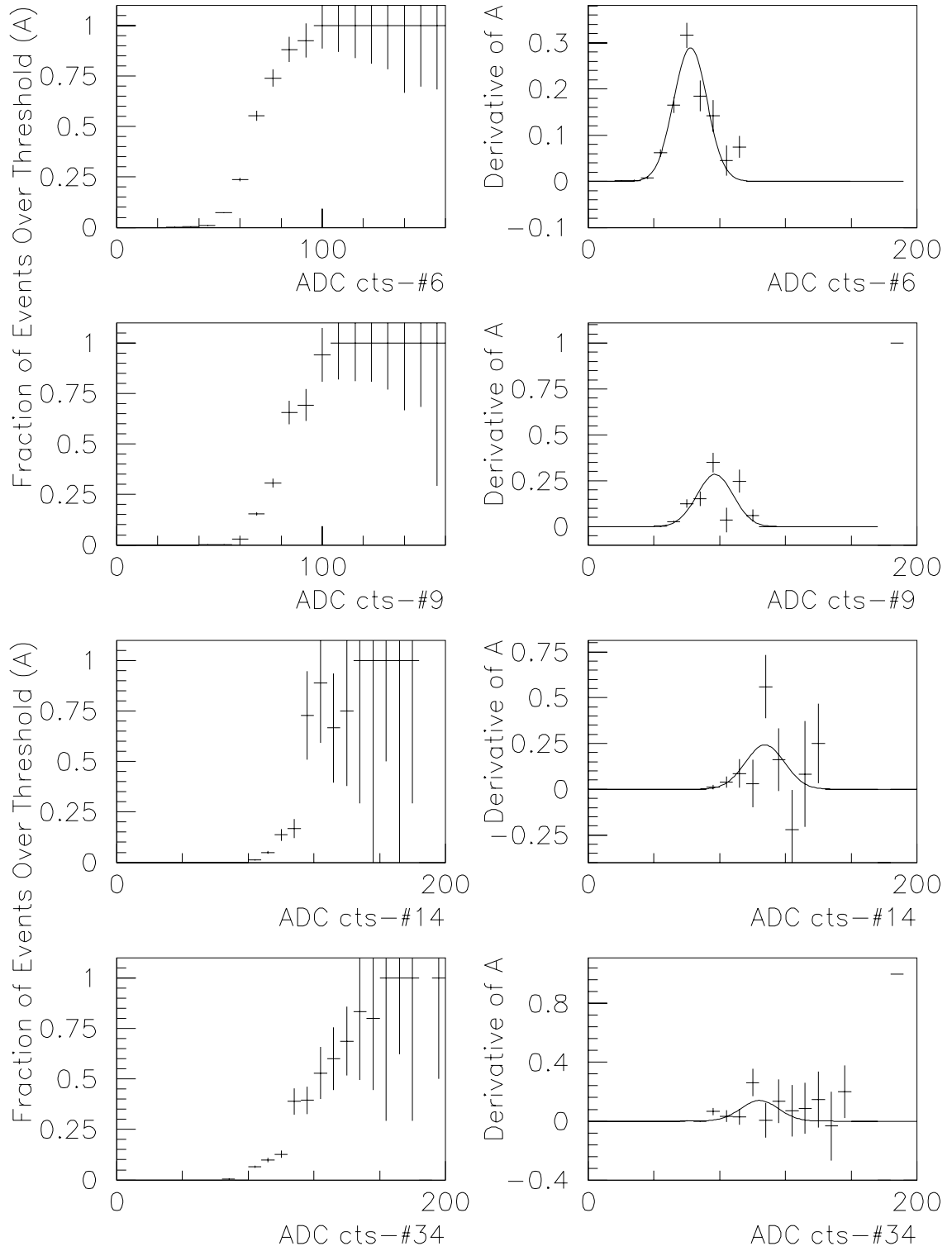
Figure 62. The fraction of events over the MU1 threshold and its derivative, as a function of the number of ADC counts counters 6, 9, 14, and 34

# CHAPTER 7

# DETECTOR SIMULATION

*"Comme c'est curieux! comme c'est bizarre! et quelle coïncidence" —Ionesco,*
*La cantatrice chauve*

To accurately measure a branching ratio in this experiment, the ratio of signal to normalization decay acceptances must be determined. This analyses use a detector simulation (Monte Carlo) that generates events as output that have the same format as real data events. This "Monte Carlo" (MC) data is then analyzed with the same analysis code that will be described in chapters 8, 9 and 10, and after all the cuts are made, an overall acceptance can be calculated for each mode. The Monte Carlo is also extremely useful for simulating possible backgrounds to the signal mode. By looking at these backgrounds cuts to remove them can be designed. from the signal. Finally, if necessary, the Monte Carlo can be used to predict the number of background events expected in the signal region. This chapter describes the detector simulation and how the Monte Carlo events are generated.

## 7.1   Event Generation

### 7.1.1   $K_L$ Beam

A Monte Carlo sample of $K_L$'s is generated with the energy spectrum shown in figure 7, as measured in E731 [4]. The $K_L$ beam is generated with an appropriate range of production angles (given the incident proton beam direction) and corresponding energies, and then traced through the collimators described in section 3.1. The collimator positions can be determined by looking at the illumination of the various apertures by events consistent with a high-statistics decay, such as $K_L \to \pi^0 \pi^0 \pi^0, \pi^0 \to e^+ e^- \gamma$ (see reference [1]). If a generated $K_L$ hits a collimator then the event is lost and the event generator starts from

the beginning. Typically about 83% of the events generated are lost due to collimation, but of course those events would not have reached the fiducial decay volume of the experiment and are therefore not included in the acceptance calculation.

Once the kaon passes the collimators then the decay position is selected, as long as it is allowed to decay within the specified decay volume of the detector, between $90\,m$ and $160\,m$ from the target. The probability of a $K_L$ decaying depends on its lifetime and energy. The $K_L$'s are also only generated in a specified momentum range. In the $K_L \to \pi^0 \mu^+ \mu^-$ analysis the given decay momentum limits are between $20\,GeV/c$ and $220\,GeV/c$. For the $K_L \to \pi^0 e^+ e^-$ analysis there was a higher minimum calorimeter energy requirement in the trigger and therefore the given decay momentum limits were reduced to between $35\,GeV/c$ and $220\,GeV/c$.

## 7.1.2  $K_L$ Decays

Once the decay vertex has been chosen a specific decay can occur, and the decay products are traced through the detector. As was mentioned earlier, the signal and normalization decays must be generated to determine the ratio of acceptances, but there are also a number of background decays which are studied in the Monte Carlo. In this section all of these decays and how they were generated are discussed.

### $K_L \to \pi^0 \ell^+ \ell^-$ Decays

For a general three body decay there are twelve variables which must be determined— three components of momentum and one energy for each decay product. There are three constraints from the fact that each decay particle's four-vector squared must equal the square of the particle's invariant mass. Four more constraints are that the energy and each component of momentum be conserved. Finally, a random direction for one of the decay particles must be chosen (this gives three more constraints). After these ten constraints are satisfied there are only two remaining free parameters. The kinematically allowed range of these two variables define the available phase space. One choice of two phase space variables are the energies of the two leptons. The Monte Carlo decides two energies of the leptons randomly within the available phase space, and then from this the neutral pion's energy is

also determined, as well as the relative angles between the three different particles. After the energies and angles are determined then the decay is boosted into the lab frame of reference. This procedure is used for generating each of the decays $K_L \to \pi^0 e^+ e^-$, $K_L \to \pi^0 \mu^+ \mu^-$, and $K_L \to \pi^+ \pi^- \pi^0$ in the Monte Carlo. Figure 63 shows the resulting $M_{e^+e^-}$ spectrum for the decay $K_L \to \pi^0 e^+ e^-$.

**Dalitz Decays**

Dalitz decays are important to the $K_L \to \pi^0 e^+ e^-$ analysis because they constitute both the normalization modes considered, and two of the important backgrounds. The decays that are relevant are the decays $K_L \to e^+ e^- \gamma$ and $\pi^0 \to e^+ e^- \gamma$, where the $\pi^0$ comes from the decay $K_L \to \pi^0 \pi^0$. In both decays there is an intermediate virtual photon which then converts to an electron-positron pair. The fact that the intermediate state is a vector boson changes the nature of the decay and therefore the decay rate does not populate phase space evenly. The differential rate for Dalitz decays with respect to the square of the $e^+ e^-$ invariant mass, $M_{e^+e^-}{}^2$ , ignoring radiative corrections, has been calculated by Kroll and
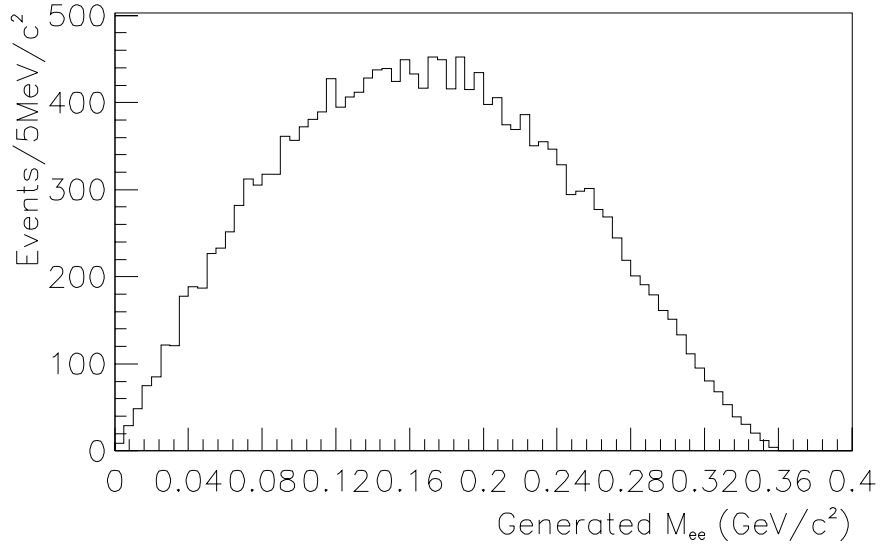


Figure 63. The generated $M_{e^+e^-}$ spectrum for a $K_L \to \pi^0 e^+ e^-$ Monte Carlo that equally populates the available phase space

Wada to be [62]

$$\begin{aligned}
\frac{d\rho}{dx} &= \frac{2\alpha_{\mathrm{EM}}}{3\pi}\frac{1}{x}(1-x)^3\left(1+\frac{r}{2x}\right)\sqrt{1-\frac{r}{x}}, \text{where} \\
x &= (m_{ee}/m_p)^2, \text{and} \\
r &= (2m_e/m_p)^2
\end{aligned}$$

and where $m_p$ is the parent decay particle, in this case either the kaon or the pion.

Internal structure in the kaon or the pion will lead to a slight difference in the predicted decay rate as a function of $M_{e^+e^-}$ from what is expected from a vector interaction. This difference is referred to as the "form factor". In the case of the pion form factor, this slight change is parameterized in the following way:

$$\frac{d\rho}{dx} = \frac{d\rho_{\mathrm{QED}}}{dx} \times |F(x)|^2.$$

where

$$F(x) \approx (1 + ax).$$

and "a" is the form factor for the pion. In the case of the kaon form factor, there are different predictions from both the quark model and vector meson dominance models, both of which predict a slightly higher decay rate at high $x$. Figure 64 shows the Kroll-Wada spectrum for pions (figure a) and kaons (figure b), and in both plots the spectrum with the form factor included is indicated by a dotted line. Note that in both cases the $e^+e^-$ invariant mass spectrum is sharply peaked at low invariant mass. In the case of the kaon spectrum the form factor plotted is the one predicted by the quark model, as shown in reference [64]. Other predictions are listed in this paper as well, but the quark model agrees best with the data. The kaon form factor does not affect this measurement since the uncertainty in the overall branching ratio of the decay is larger than the uncertainty in the size of the Kaon form factor. In the case of the pion form factor the two graphs are barely distinguishable.

**Radiative Dalitz Decays**

The radiative Dalitz decay differs from the Dalitz decay in that bremsstrahlung photons from either of the two electrons can interfere constructively. This interference is particularly

important when the photons are emitted far from the electron axis, which is precisely the region where the background to $K_L \to \pi^0 e^+ e^-$ arises. The expected amount of background from the decay $K_L \to e^+ e^- \gamma \gamma$ depends on various kinematic cuts in the analysis, most importantly, the two-photon invariant mass ($M_{\gamma\gamma}$) cut. Figure 65 shows the $M_{\gamma\gamma}$ and the $M_{e^+e^-}$ generated distributions, based on calculations by Greenlee [63].

**Semi-Leptonic Decays**

The semi-leptonic decay $K_L \to \pi^{\pm} e^{\mp} \nu$ (called the "$K_{e3}$ decay") was the most significant background in the search for the decay $K_L \to \pi^0 e^+ e^-$. The radiative decay $K_L \to \pi^{\pm} e^{\mp} \nu \gamma$ was also included in the standard $K_{e3}$ simulation. In the non-radiative $K_{e3}$ event generation the decay is first generated over flat phase space, and then its generation probability is weighted by the semi-leptonic matrix element. The $K_{e3}$ decay is a pure vector form with a linear $q^2$ interaction [65], where $q^2$ is the momentum transfer squared between the kaon and the pion.

The radiative decay generation is more complicated, and a discussion of the decay
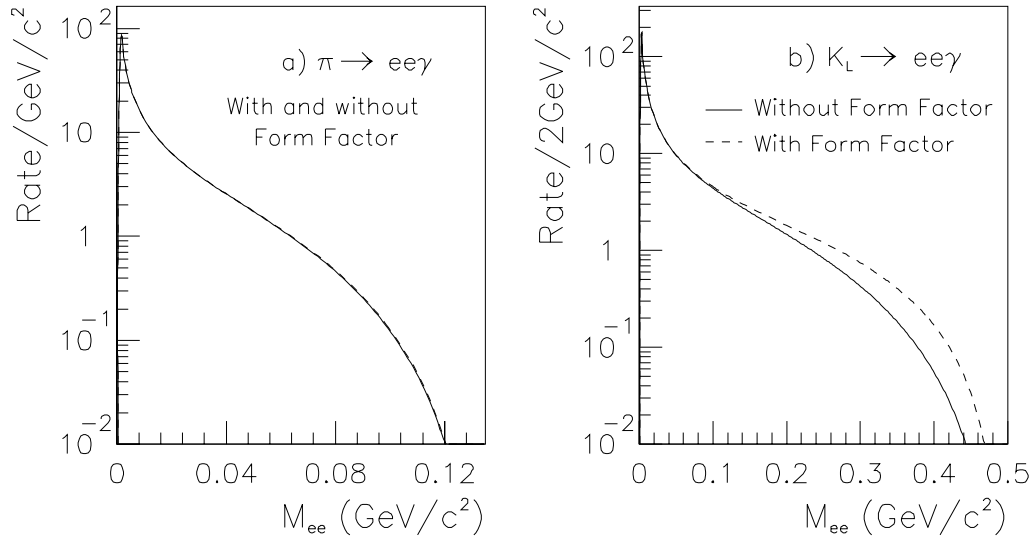


Figure 64. The Kroll-Wada $M_{e^+e^-}$ spectrum for both (figure a) $\pi^0 \to e^+ e^- \gamma$ and (figure b) $K_L \to e^+ e^- \gamma$ decays, and the effect of including a form factor in the decay

and relevant matrix element calculation can be found in reference [67]. The decay itself is generated in two separate chains—first the kaon decays to the neutrino and the $\pi e \gamma$ system, then the $\pi e \gamma$ system decays, with a minimum photon energy of $1\,MeV$ in the kaon center of mass frame. The invariant masses of the $\pi e$ system and the $e\gamma$ system are then generated with a $1/\text{mass}^2$ dependance. The angles between all the particles are chosen and the radiative $K_{e3}$ matrix element is used in the weighting.

### 7.1.3   Particle Propagation

Once the decay particles have been generated in the $K_L$ center of mass frame, they are boosted to the lab frame and propagated through the detector. If particles extrapolate to regions outside various detector apertures that define the decay volume, then the event is rejected and a new decay is generated. For example, if a charged particle hits any of the photon vetoes listed in section 3.2.1, or goes outside those vetoes, the event was rejected. Table 13 shows the fraction of events lost due to various apertures in the detector, for both
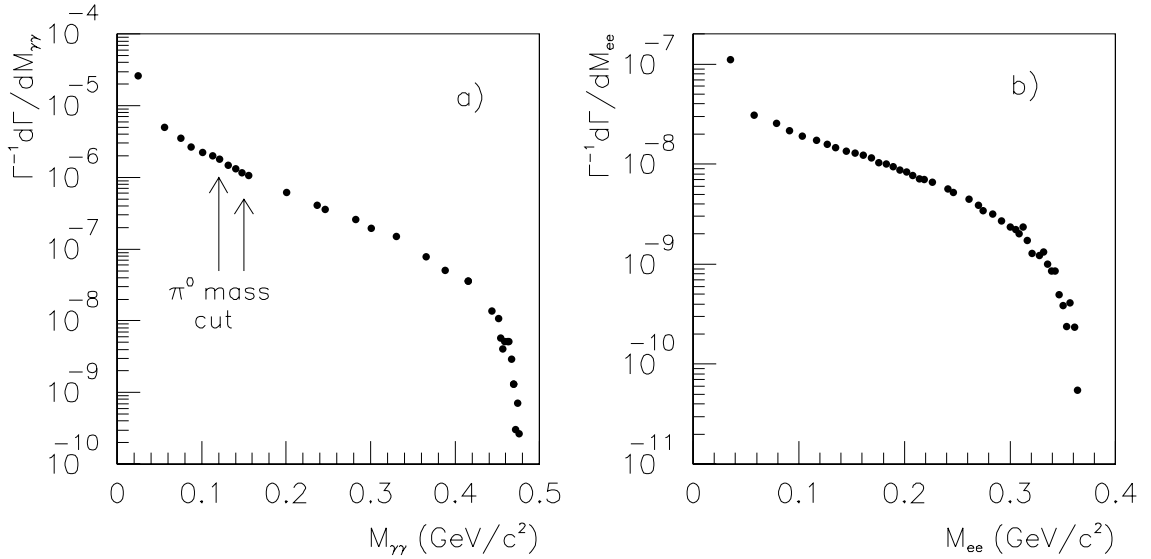


Figure 65. The two-photon and two-electron invariant mass spectra ($M_{\gamma\gamma}$ and $M_{e^+e^-}$, respectively) for radiative $K_L$ Dalitz decays, taken from reference [63]

Table 13. $K_L \to \pi^0 e^+ e^-$ Acceptance Losses due to Detector Apertures

| Aperture | Fractional Loss | |
|---|---|---|
| | $K_L \to \pi^0 e^+ e^-$ MC | $K_L \to e^+ e^- \gamma$ MC |
| PA | 29.5% | 23.3% |
| VA9 | 0.8% | 0.5% |
| VA0 | 3.5% | 2.6% |
| VA1 | 0.9% | 0.6% |
| VA2 | 2.0% | 1.3% |
| DRA | 3.7% | 2.6% |
| VA3 | 1.1% | 0.7% |
| VA4 | 2.2% | 1.6% |
| Vacuum Window | 0.01% | 0.02% |
| Spectrometer and Calorimeter | 1.3% | 2.0% |
| Total Loss | 45% | 35.2% |

$K_L \to \pi^0 e^+ e^-$ and $K_L \to e^+ e^- \gamma$ Monte Carlo. The small differences in the fractional losses of acceptance are due to the very different $M_{e^+ e^-}$ spectra.

As charged particles traverse material in the detector, they may undergo multiple scattering and bremsstrahlung, and this is included in the Monte Carlo. The multiple scattering angle which is included is only the Gaussian shape of the scattering, and not the tails of that distribution, which are caused by $\delta$-rays. The effect of not including these tails can be seen in figure 80. If a particle emits a bremsstrahlung photon, then that photon is also propagated through the detector.

Another effect which is not included in the Monte Carlo is electron or photons undergoing electromagnetic showers in any detector other than the calorimeter. This can cause problems in the photon vetoes, since they are 6 radiation lengths each, but the effects for these analyses

were negligible. The one problem this could create is when one is trying to determine the acceptance for a decay mode where one of the photons is lost, for example, background to $\pi^0 e^+ e^-$ from the decay $K_L \to \pi^0 \pi^0$, $\pi^0 \to e^+ e^- \gamma$. But as can be seen in the plot 112, this background level has been correctly predicted at the level of statistics necessary.

Photons with energy above $0.1\,GeV$ are allowed to convert with the appropriate conversion probability, given the number of radiation lengths in the detector element the photon is traversing. Once photons convert the electron and positron pair are propagated through the remainder of the detector. The energies of the electron-positron pair are chosen as $\epsilon E_\gamma$ and $(1 - \epsilon)E_\gamma$, where $E_\gamma$ is the energy of the photon which has converted. The probability of an electron of energy $\epsilon E$ being emitted, $P(\epsilon)$, is given by the Bethe-Heitler formula [10]:

$$P(\epsilon) \approx \epsilon^2 + (1 - \epsilon)^2 + \epsilon(1 - \epsilon)\left(\frac{2}{3} - a\right), \tag{7.1}$$

where $a$ is a constant of the material, ($\approx 0.0297$ for the lead-glass).

## 7.1.4 Allowances for Lost Particles

An important issue in the simulation is the following: how many particles are allowed to be lost in inactive regions of the detector before the event is rejected in the Monte Carlo? One might claim that if one is generating a signal decay, then as soon as a final state particle is lost in an inactive region of the detector then the event should be discarded. However, consider the case in any decay containing at least one photon in the final state where one photon is lost in an inactive region of the detector but a cluster of accidental energy makes up that lost photon. This could conceivably become a signal event, hence one needs to include this effect in the Monte Carlo. In fact the acceptances for both the $K_L \to \pi^0 e^+ e^-$ mode and the $K_L \to e^+ e^- \gamma$ mode both increase by about 5% when the Monte Carlo allows for one lost particle. The ratio between the two acceptances remains the same and hence the sensitivity would remain the same. In order to correctly normalize backgrounds, especially those which arise from one missing particle, we also allowed one particle to be lost for each background decay mode generated.

## 7.2 Detector Simulation

Once it is determined that the decay products have reached active parts of the detector, the response of that active region was simulated for each particle, then the accidental activity was added, then the trigger was checked, and then if the event passes the trigger, it was written to an output data file. By going from geometrically accepting the event to writing the event there is a 38.7% loss in the $K_L \rightarrow \pi^0 e^+ e^-$ sample from trigger effects alone. If accidental activity is included in the same Monte Carlo, only 15.3% of the events which are geometrically accepted pass the trigger, so it is important to understand where these large losses originate.

### 7.2.1 Calorimeter Simulation

One of the most important detectors to correctly simulate is the lead-glass calorimeter. In chapter 5 the model of electromagnetic showers and light collection given by the EGS Monte Carlo [11] is described. In contrast, there is no simulation either of hadronic showers or of minimum ionizing signals in the lead glass. Since a minimum ionizing particle deposits a signal roughly equivalent to $700\,MeV$ in the lead-glass that amount of energy is simply added to the block hit by the muon or pion. Because of this inadequacy, effects seen in the data due to hadron showers are not simulated, as will be discussed in later sections. In the remainder of this section we will describe the simulation of the lead-glass for electrons and photons.

**Energy Deposition**

The first thing to determine when a Monte Carlo electron of a given energy hits the calorimeter is how much light will be collected at the back of the phototube. As described in chapter 5, the amount of light depends on the energy of the electromagnetic particle hitting the block, the absorption coefficient of the lead-glass block, and the length of the block itself. For electrons the length of the block is the total length of the block, while for photons, the effective block length is the total length of the block minus the conversion depth of the photon.

There are two different effects which can change the response of a block from a standard Gaussian distribution. The first is simply the fact that electrons which shower closer to the phototube have less light absorbed before the light gets to the phototube, which results in a high-side tail on the normal (Gaussian) response. However, electrons which shower closer to the phototube also are more likely to have energy leaking out the back of the array, which of course results in a low-side tail on the normal response. The two effects tend to cancel for a certain range of absorption coefficients and shower depths, but in most cases either a high side or low side tail in the cluster energy distribution is present. This tail was parameterized by what was called an "asymmetric Gaussian", and is of the form

$$f(x) = exp\left[-\frac{1}{2}\left(\frac{x - x_0}{\sigma - A(x - x_0)}\right)^2\right],$$

where $A$ is a measure of how non-Gaussian the tails of the distribution are. If $A$ is negative then the Gaussian has a high-side tail, and if $A$ is positive then the Gaussian has a low-side tail. Figure 66 shows the difference between a normal Gaussian distribution and this "asymmetric Gaussian", for both a high-side and a low-side tail. From this parameterization
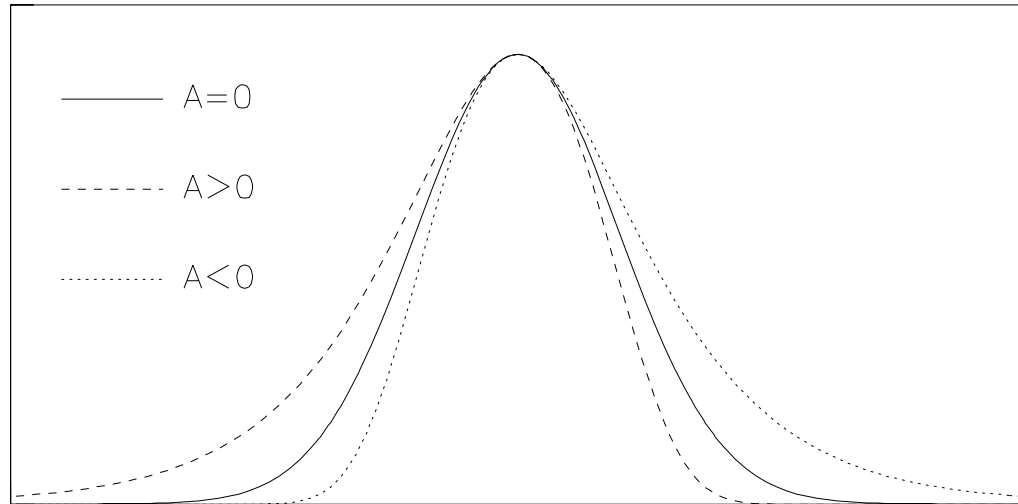


Figure 66. "Asymmetrical Gaussian" functional form

the fluctuations on the amount of light eventually reaching the back of the lead-glass block could be simulated. Reference [1] includes plots describing both $A$ and $\sigma$ as functions of $\alpha$, block length, and energy.

Once the amount of light at the phototube was determined, the smearing due to photo-statistics (which was discussed in section 5.4.2) was added. The shower was then ready to be converted into a cluster of lead-glass block energies—for this step a cluster library containing real electron clusters from the E731 electron calibration runs was used. The cluster from the cluster library determined the relative fractions of energy which were deposited in each of the 9 blocks in the $3 \times 3$ array; these energies were then translated into ADC counts using the measured gains of each block.

**Photon Simulation**

Once the procedure for simulating electrons in the calorimeter has been determined, the procedure for photons is straightforward. The position along the block length that the photon converts to two electrons is chosen, given that the effective radiation length for photons is $\frac{9}{7}$ that of a radiation length for electrons. The energies of the electron-positron pair are chosen, using the Bethe-Heitler formula (equation 7.1).

For photons, the energies from two clusters were added together, on top of each other. This procedure resulted in reasonably accurate photon energy resolution, as can be seen in plots of $M_{\gamma\gamma}$ for $K_L \to \pi^+ \pi^- \pi^0$ data and Monte Carlo events. Figure 67 shows $M_{\gamma\gamma}$ from these events where the photon farthest from the beam-pipes arrived outside the third ring of glass blocks, as a function of where the photon closer to the beam-pipes arrived. Although the means of the distributions are displaced a fraction of a per cent due to residual problems in the photon modeling, the overall shapes of the distributions are similar.

**$E_{Thi}$ Simulation**

Another important aspect of the calorimeter which needed to be correctly simulated was the $E_{Thi}$ trigger. Nominally the trigger was set to $55\,GeV$, but because of gain variations in the adders this threshold was sometimes lower. Rather than cut well above the threshold and lose acceptance, the Adder gains and thresholds were measured and included in the
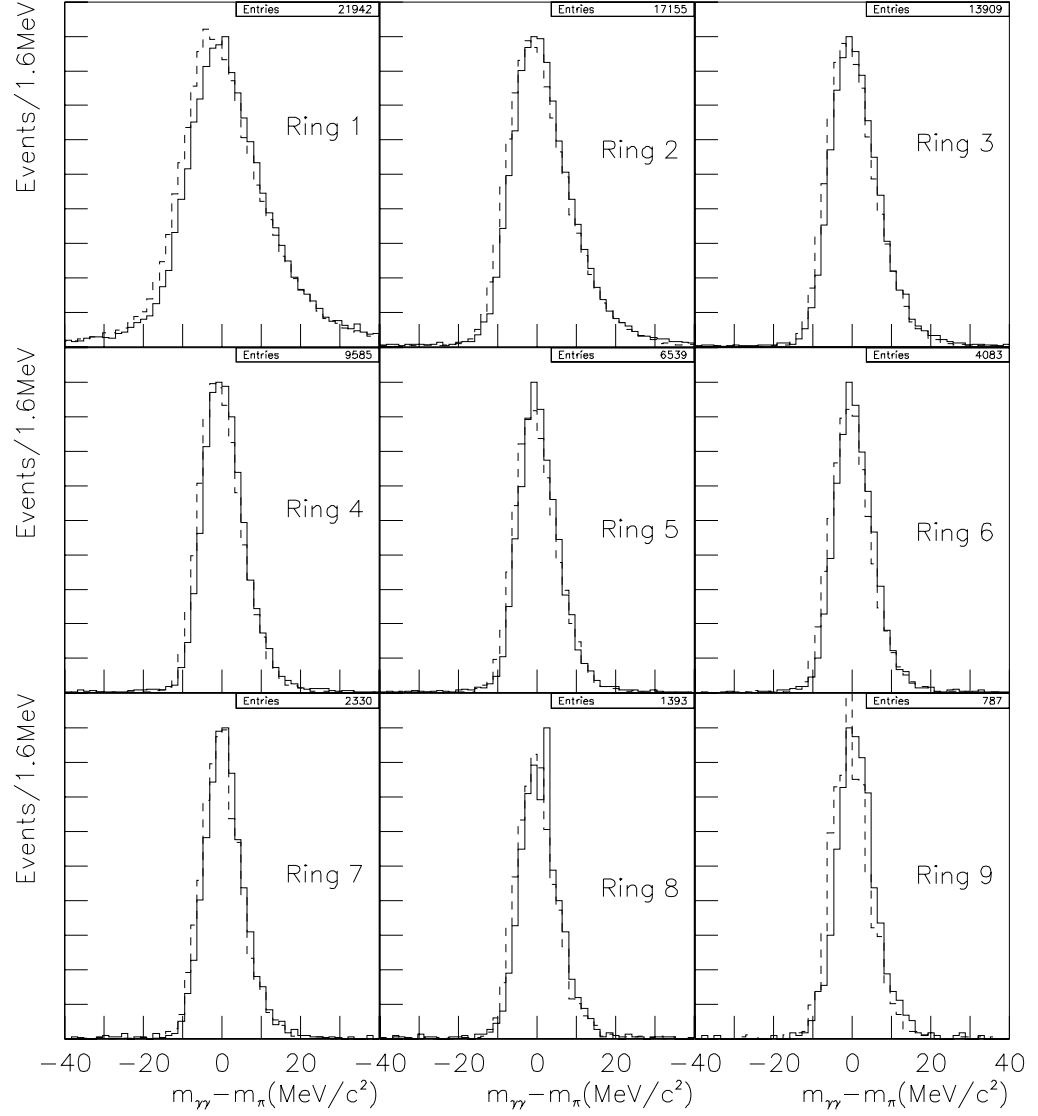
Figure 67. The difference between $M_{\gamma\gamma}$ and the $\pi^0$ mass for $K_L \to \pi^+\pi^-\pi^0$ events for different rings in lead-glass. The events are classified in the following way: the photon farthest from the beam-holes is at least 4 blocks from the holes, and the "ring" definition is then the number of blocks away from the beam-holes the other photon arrived. (The pipe blocks are "ring 1"). The solid histograms are the data and the dashed histograms are the $\pi^+\pi^-\pi^0$ Monte Carlo.

Monte Carlo [1]. By looking at the total energy spectrum for an electromagnetic decay in both both data and Monte Carlo events the $E_{Thi}$ simulation can be checked. Figure 68 shows the energy spectrum for $K_L \rightarrow \pi^0 \pi^0 \pi^0$, $\pi^0 \rightarrow e^+ e^- \gamma$ events in both the data and the Monte Carlo [1], and the nominal $E_{Thi}$ threshold. The agreement is good, even below the $E_{Thi}$ threshold.

**Hardware Cluster Finder Simulation**

The last aspect of the lead-glass which needs to be properly simulated is the Hardware Cluster Finder. Because of varying voltages on the phototubes, the cluster threshold is not necessarily independent of where the cluster arrives at the glass. Furthermore, during the last 38% of the run a few of the blocks failed to act as inputs to the HCF. For the last 13% of the run the HCF threshold mysteriously jumped from around $2.4\,GeV$ to $3.2\,GeV$. This caused a significant loss in acceptance and needed to be included in the Monte Carlo. The HCF block thresholds themselves were measured using $K_L \rightarrow \pi^0 \pi^0 \pi^0, \pi^0 \rightarrow e^+ e^- \gamma$ events in the data, which were a plentiful source of low-energy photons (see reference [1]). The agreement between data and Monte Carlo for the minimum photon energy distribution of $K_L \rightarrow \pi^+ \pi^- \pi^0$ events shows the accuracy with which the HCF threshold has been simulated. Figure 69 shows this distribution for both the $\pi^+ \pi^- \pi^0$ data and the $\pi^+ \pi^- \pi^0$ Monte Carlo simulation, where the photons in the decay were required to be selected by the HCF.

## 7.2.2 Drift Chamber Simulation

Based on the measured efficiency and position resolution of each of the wires in the drift chambers and the resulting time-to-distance relation (as discussed in section 3.2.2 and reference [1]), for each charged particle passing through the chambers a number of hits and times on the appropriate sense wires could be generated. The same tracking algorithms in the analysis could then be applied to both the data and the Monte Carlo. One effect that is ignored in the Monte Carlo is the presence of $\delta$ rays in the chambers. $\delta$-rays emanating from a charged particle sometimes travel at high speeds towards the sense wires in the drift chambers and cause early hits on the wires. This results in a mis-measurement of where the incident particle crossed the plane of the wires, and can sometimes cause extra hits on
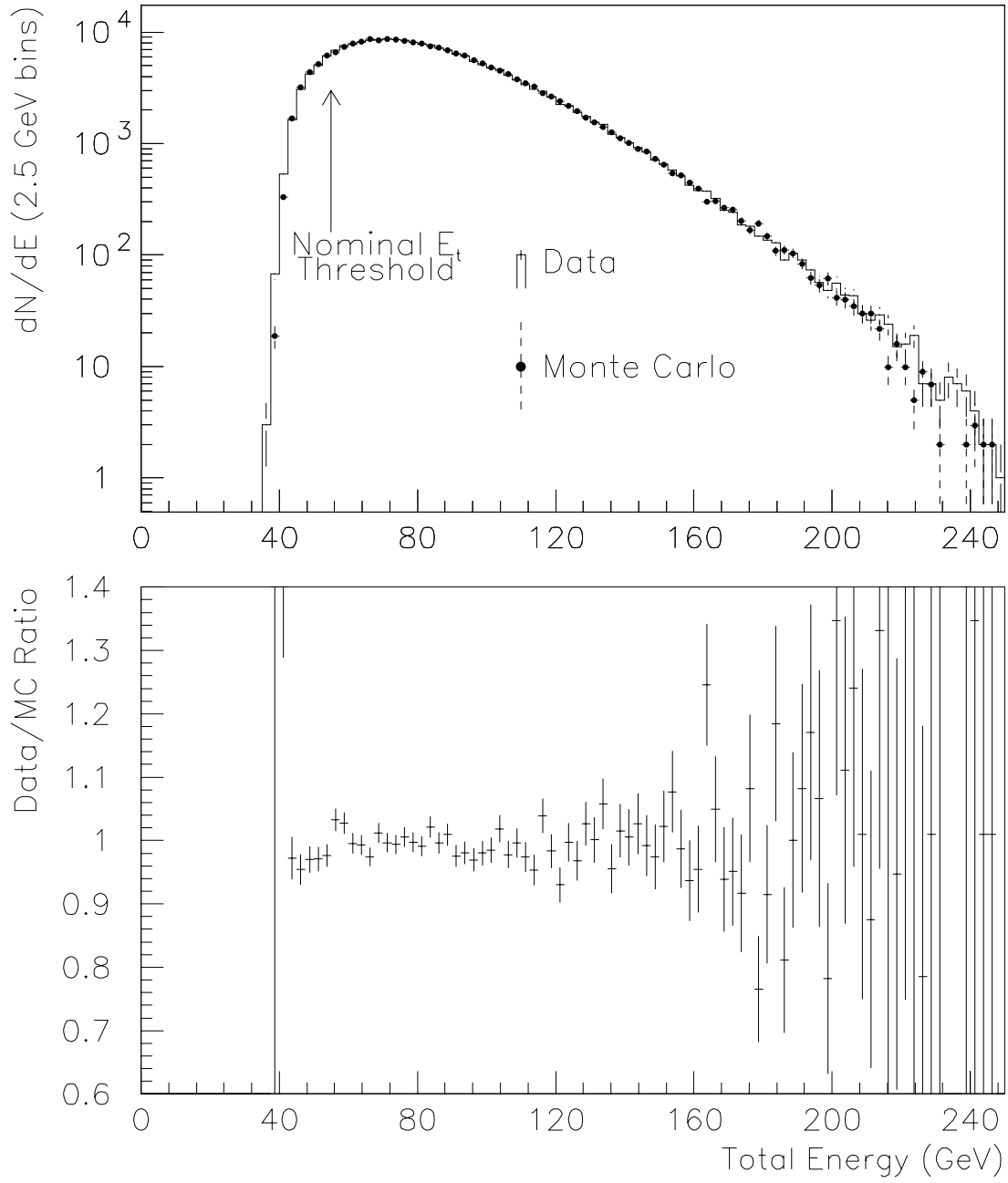
Figure 68. The total energy distributions for $K_L \to \pi^0\pi^0\pi^0$, $\pi^0 \to e^+e^-\gamma$ events, in both the data and the Monte Carlo, and the ratio of the two distributions. The nominal $E_{Thi}$ threshold is also shown.

adjoining wires, but does not significantly effect the momentum resolution of the spectrometer Because of this inadequacy in the Monte Carlo there were no cuts on track hits and only loose cuts on tracking variables.

In general, the momentum scale and resolution were well-simulated in the Monte Carlo, even without $\delta$-ray effects. The simulation of the drift chamber is best tested by reconstructing a decay containing only charged particles in the final state, such as the $K_L \to \pi^+ \pi^-$ decay, which can be found in the minimum bias data. Figure 70 shows the two-pion invariant mass for $K_L \to \pi^+ \pi^-$ decays, in both the data and Monte Carlo. The peaks of the two reconstructed mass distributions differ by 0.03%, and the difference in the widths of the two peaks is equivalent to an additional 0.26% smearing which is not included in the
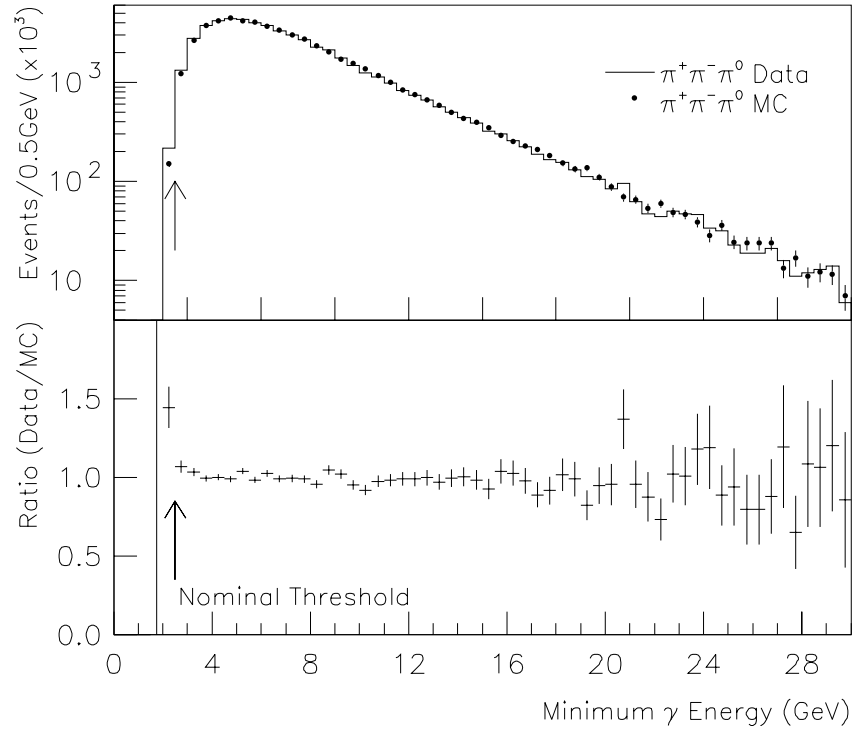


Figure 69. The minimum photon energy distributions for $K_L \to \pi^+ \pi^- \pi^0$ events, in both the data and the Monte Carlo, and the ratio between the two distributions. The nominal HCF threshold is also shown.

Monte Carlo. The effect of these discrepancies on signal acceptance was checked and was found to be negligible (see table 25).

### 7.2.3  Hadron Shower Veto Simulation

Chapter 6 describes the muon calibration of the hadron shower veto. The parameters which could be measured with single muons were the overall response of each counter in the hadron shower veto, the threshold for each counter, and the width of the threshold. The overall response was determined by fitting the ADC distributions for each counter in the scintillator bank.
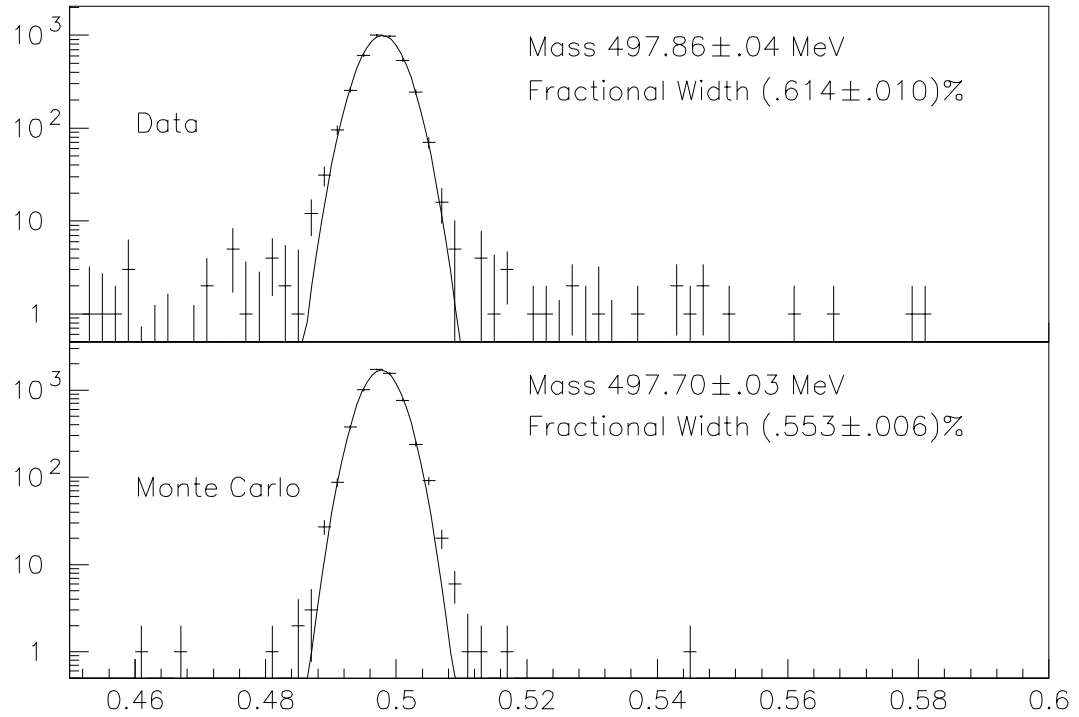


Figure 70. $m_{\pi\pi}$ for candidate $K_L \to \pi^+\pi^-$ decays in data and Monte Carlo

## Counter Response

After measuring the muon response of the Hadron Shower Veto, as described in chapter 6, the scintillator bank can be simulated in the Monte Carlo. One effect that has not been taken into account can be seen in figure 61. There are a few events where there was no energy deposited in the counter, even though the muon extrapolates to the counter. This is because muons may scatter before they hit the counter, or the edge of the counter is not very well determined, which is often the case for counters far away from the beam-holes where statistics were low. So, to compute the signal in MU1 due to real muons the Monte Carlo uses the position that the muon extrapolates and generates a distribution with the appropriate weighting. As a measure of how well this method works we compare the overall distribution of ADC counts in the counters that the muon has hit and the generated distribution of ADC counts in those same counters. Figure 71 shows these two distributions for real muons and the simulated response for the same set of muons. The events at zero in the simulated distribution correspond to events where the muon points outside of MU1. As mentioned earlier, the events at zero in the real ADC distribution correspond to events where the muon has scattered and does not hit MU1. The difference between the distributions is noticeable but not significant because, as will be shown later, the predicted rejection factor is correct.

## Simulation of Trigger

The prescription to predict the fraction of time that the MU1 veto was on for single muons is as follows: from the signal calculated for a given MU1 counter one determines the threshold for that event for that counter (given a Gaussian distribution of the actual threshold) and then divide the signal by the threshold. If the signal is greater than 1, then the event would have been vetoed. In the case of two muons, one simply adds the two fractions, and if the sum of the fractions is greater than one, then that event is vetoed. As a general check of the simulation, we compare the occupance of the MU1 veto (the fraction of events for which the MU1 veto is on) in the data to the Monte Carlo prediction. Figure 72 shows the overall occupance of MU1 veto as a function of the ADC signal of the highest counter. Although the

two distributions are not exactly the same, in particular for a given occupancy the number of generated ADC counts is about 5 ADC counts lower than the number of ADC counts in the data, this is compensated by the fact that the generated distribution of ADC counts is also slightly low (see figure 71). Overall, for these events the fraction of time that MU1 is off is about $(89.1 \pm 0.1)\%$ of the time. The predicted fraction of time that the veto is off is $(88.8 \pm 0.1)\%$ of the time. As mentioned earlier, these thresholds were determined during the longest beam-dump muon run, Calibration 3. The other muon runs didn't contain nearly as much data, and so rather than re-calibrate MU1 each time (as was done with the muon trigger bank) we simply compared the real to simulated MU1 occupancy and determined a systematic error based on the difference between the two occupancies. Still a
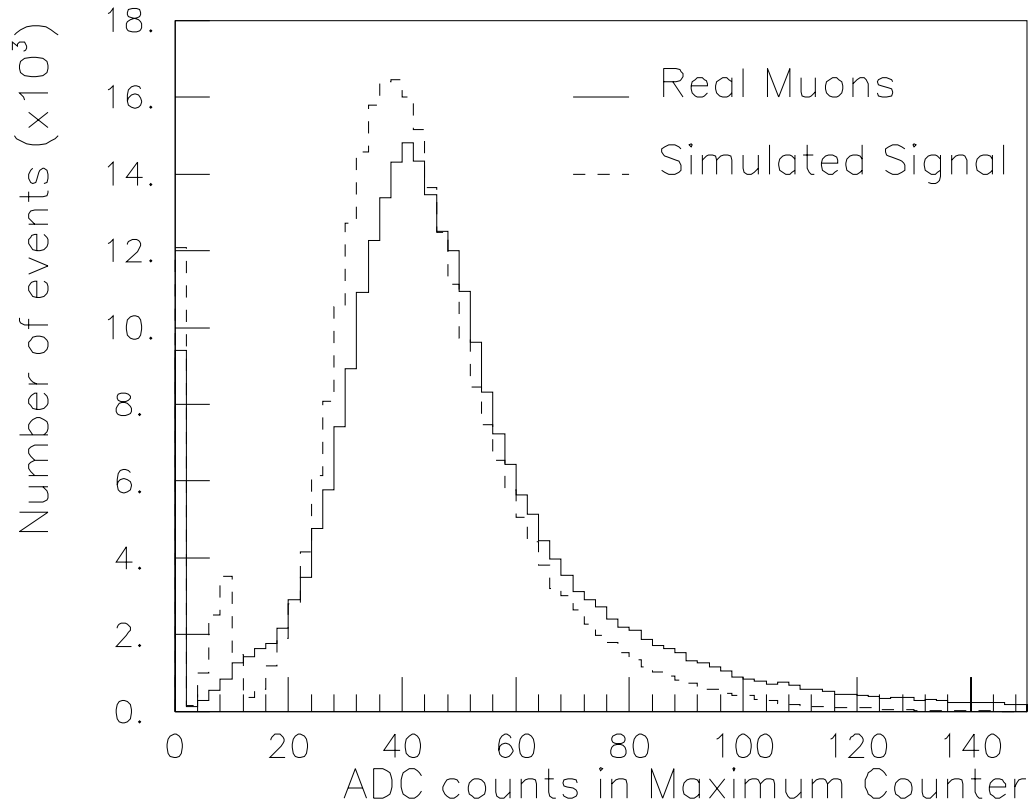
Figure 71. The ADC distribution for real and simulated muons in the hadron veto counters

more stringent check was performed by looking at the real and predicted MU1 efficiency for several different sets of calibration run data, using the same gains and thresholds measured from the data from Calibration 3. We set a limit on the error induced by only using one set of MU1 gains and thresholds for the entire run. This study is described in section 11.3.3.

The most important parameter of this simulation has yet to be measured. The signal mode, $K_L \to \pi^0 \mu^+ \mu^-$, contains two muons, but only the MU1 occupancy for single muons has been checked. The efficiency for two muons is not simply the square of the efficiency for one muon since the signals in MU1 are added, then discriminated. To check the dimuon simulation a sample of events containing two verified muons was needed. Unfortunately, there was no trigger for events of this type during the calibration runs and so to obtain such a sample all the muon calibration runs were scanned for clean events with two muons in the same event.

After requiring the muons to hit two separate counters and making the same requirement as in the case of single muons that the maximum counter is one that was hit by a muon and that there not be much activity in any counters that were not hit, there were only 51 events
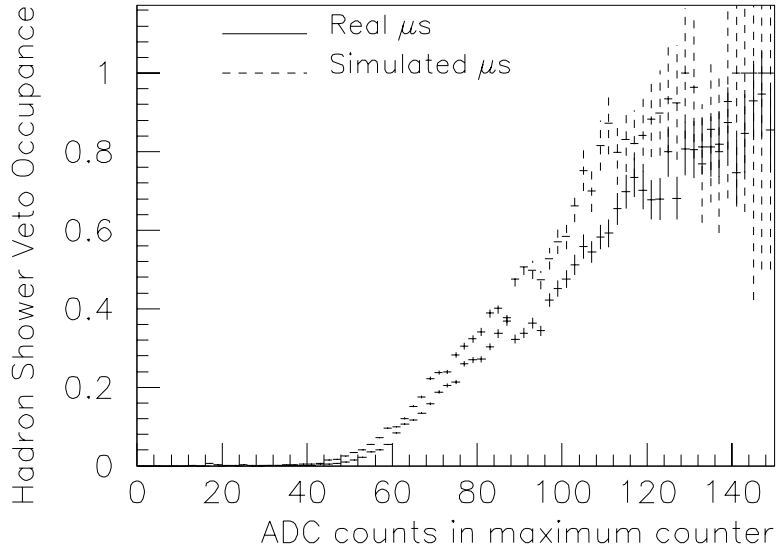


Figure 72. The occupance of the MU1 veto, as a function of the number of ADC counts in all counters

remaining. After running the simulation on those events with the above prescription, the Monte Carlo predicts that MU1 should have fired 15 times, and in fact, the actual hadron shower did veto 15 events in that sample. The di-muon efficiency (without any accidental activity added) is therefore $(70.5 \pm 6.4)\%$.

### 7.2.4 Muon Trigger Plane Simulation

If a muon hit the lead-glass, the extrapolated position of the muon at the plane of the muon trigger bank was determined. The probability that a muon fires some counter in the trigger bank is weighted by the efficiency of that extrapolated position and muon momentum. To determine which counter fires, the muon is multiply scattered through the filter, and whichever counter it arrives at, that is the one that fires. If the muon scatters out of the steel, the scattering routine is run again until the muon hits some counter in the array. In this way the effect of multiple scattering is taken into account for both the efficiencies and which counter in the trigger bank fires. Accidental activity can also help satisfy the muon trigger, but since this was not present in the calibration data it can safely be added from the accidental trigger data.

## 7.3 Accidental Activity

There is a significant amount of accidental activity in the detector, and this must also be added on an event-by-event basis. Accidental activity can be due to electronic noise, or to particles due to the beam scattering and hitting active parts of the detector. For example, given that the probability of a bucket containing a $K_L$ in the detector is 0.05 [1], and the kaon to neutron ratio in the experiment is about 1/6, and because of the bucket structure not all buckets are not equally populated, a bucket which already has a kaon decaying in it (i.e. a real event) has a 90% chance of containing another kaon or neutron in the same bucket. Of course the vast majority of these extra particles will pass through the beam-holes of the calorimeter and will be deposited in the hadron filter without interacting, but those that scatter may leave signals. The effects from this accidental activity are included in the simulation by adding random data events which are correlated with beam activity to the

base Monte Carlo events. The trigger which accepted these random events was discussed in section 4.2.1, and in section 8.7 the specific ways in which accidental activity can contribute backgrounds to the signal will be discussed. In this section we discuss how this activity is added to the Monte Carlo event and how it affects the acceptance for the various signal modes.

### 7.3.1   Overlay of Accidental Signals

This addition of accidental activity occurred after the decay was generated and the final state particles were traced through the detector. The ADC's for both the non-glass and lead-glass signals were overlaid, the latches for all of the trigger bits were overlaid, and finally, the drift chamber hits were overlaid. Each one of these signals can interfere with the detection of the decay itself, and overall, the addition of accidental activity reduced the signal Monte Carlo acceptance by $\sim 50\%$. In other words, the single event sensitivity was degraded by a factor of two due to this activity. In the next section we discuss the various ways in which this occured.

### 7.3.2   Signal Acceptance Loss

In general, there are two ways in which accidental activity can reduce the signal acceptance. First of all, there can be small amounts of energy which add to the given signal and cause the event to fall outside the kinematic windows allowed. This is most obvious in the case of the lead-glass calorimeter. Added energy in the photon clusters could result in a calculated $M_{\gamma\gamma}$ which was above the $M_{\gamma\gamma}$ mass cut.

A second way signal acceptance can be lost is when various trigger elements which may have been in veto in the trigger are above the veto threshold in the accidental event. The latter effect accounts for the largest loss in acceptance. Figure 73 shows the occupancy for three different latches which were in veto for both $K_L \to \pi^0 \ell^+ \ell^-$ triggers. For example, the MU1 veto rejects hadron showers, including a neutron showers in the lead-glass. This is probably the noisiest bank of counters and is for 18% of accidental events. The "Photon Veto Occupancy", the occupancy of any one of the photon vetoes VA9, VA0-VA4, or LGA, is 14% for accidental events. Finally, the Back Anti Veto which rejects events with electro-
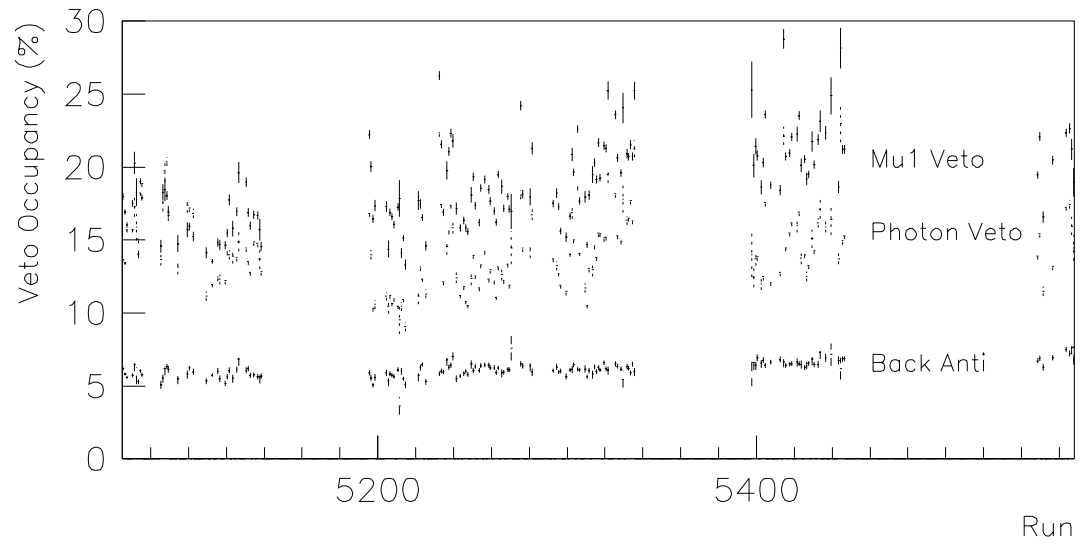
Figure 73. The occupancy of the MU1 veto, a combination of Photon Vetoes, and the Back Anti Veto as a function of run number

magnetic particles which went through the beam holes in the calorimeter was on in 6% of the accidental events.

### 7.3.3  Accidental Activity in the Hadron Shower Veto

When the generated decay contained one or more muons and the MU1 trigger source was in veto, accidental activity in the Hadron Shower Veto needed to be accounted for in a different procedure than the standard Monte Carlo simulation. While in the standard simulation a given trigger bit is simply the "or" of the bit in the base decay event and the bit in the accidental event, this does not account for those events where the base event has almost the amount of energy in the counter required to fire a given latch, and then the small amount of accidental activity pushes the signal over the trigger bit threshold. In this case either contribution is not enough by itself to set the latch, but when added together they are above the threshold. Since the MU1 threshold was low ($\sim 2.5 muons$), the muon activity and the accidental activity must be summed together before determining whether or not the event was vetoed.

Since the data consists only of the ADC counts for accidental events and not the sum that was discriminated, one cannot add up the ADC counts in each counter in the accidental event to the real muon signal in each counter and use the thresholds as determined above. By studying the dependance of the MU1 occupancy on the sum of accidental ADC counts in all counters in $K_L \rightarrow \pi^+ \pi^- \pi^0$ Monte Carlo events which have passed all other analysis cuts, one can parameterize the accidental threshold and width. The functional dependance is shown in figure 74 a. Notice that the veto occupancy is never 1.0, unlike the occupancy for real muons. This is due to the fact that some of the accidental signal arrives after the gate for the MU1 latch has been closed. By taking the derivative of the occupancy function (fig. 74 b.) and fitting it to a Gaussian the overall threshold and width for accidental activity can be determined, and then that parameterization is used to calculate for each event the fraction of the veto that is "used up" by the accidental activity. To check this we look at the resulting predicted occupancy of the MU1 as a function of the total accidental ADC counts in the event. Since the Occupancy never goes to 1.0, however, a Gaussian shape for the threshold will not accurately mock-up the shape.
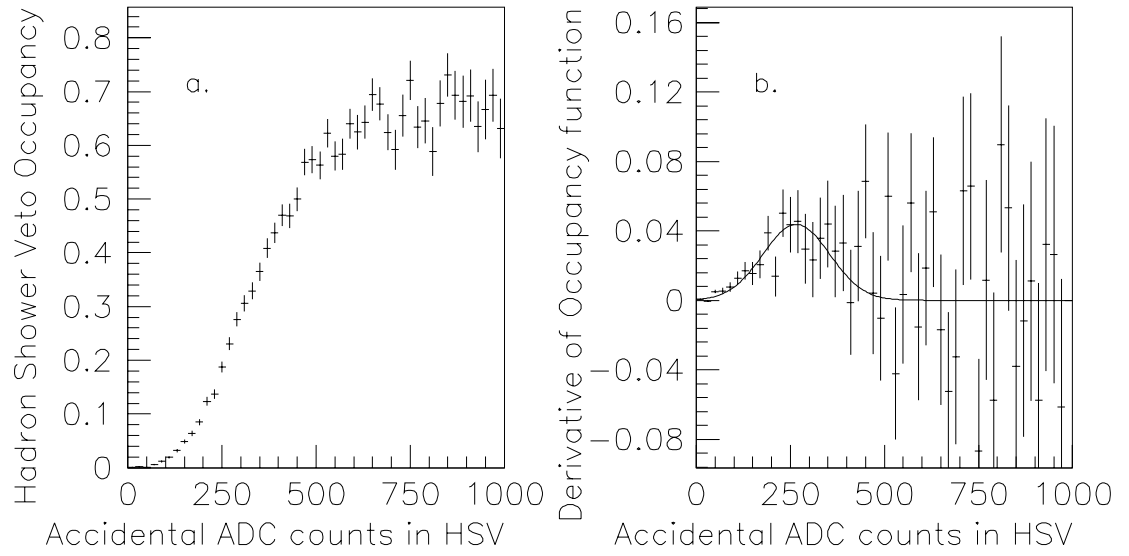
Figure 74. a.The occupance of MU1 for $K_L \rightarrow \pi^+\pi^-\pi^0$ Monte Carlo events, as a function of the total number of accidental ADC counts in all counters b. The derivative of plot a.

After trying various functions to parameterize the threshold, we determined the threshold shape to be two Gaussians: the center of both Gaussians was at 380 ADC counts, and the low side had a width of 125 ADC counts, and the high side had a width of 850 ADC counts. By calculating an accidental threshold for each event with this threshold distribution, the Monte Carlo could then determine whether or not MU1 would have vetoed that event. Figure 75(a.) shows the real and predicted occupancy of MU1 as a function of total accidental ADC counts. This is shown on a logarithmic plot to accentuate the region where most events lie, that is, at low total accidental counts. The distribution of accidental counts in the $K_L \rightarrow \pi^+\pi^-\pi^0$ Monte Carlo has a mean of 121.1 counts and is shown in figure 75(b).

## 7.4 Conclusion

After all the relevant decays have been simulated (both signal and background processes) the Monte Carlo events written to tape can be analyzed in almost precisely the same way as the data. In the following three chapters the analyses themselves are described.
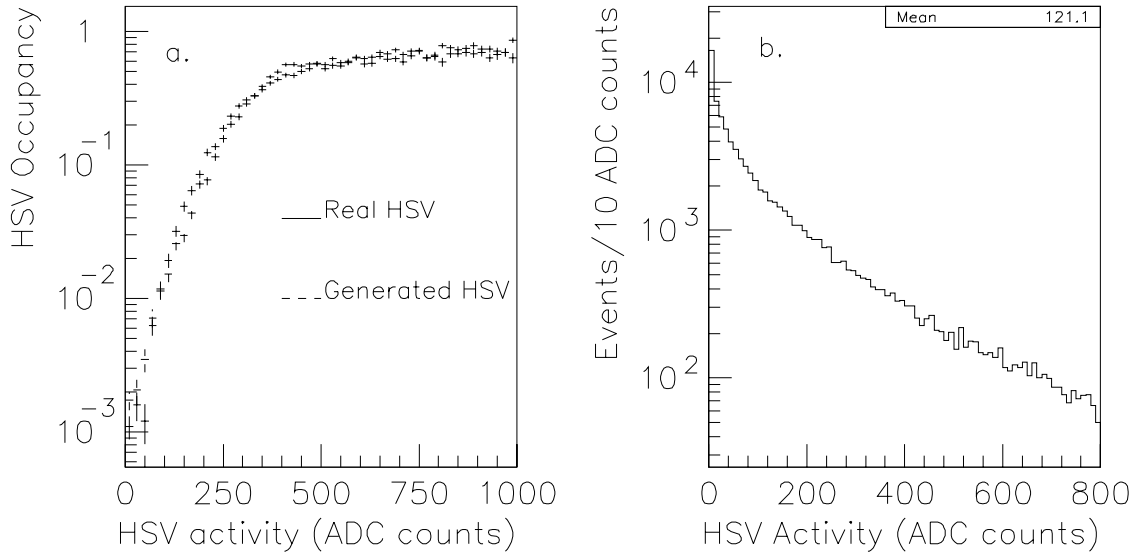


Figure 75. (a.) The occupance of the actual and generated MU1 as a function of the total number of accidental ADC counts in all counters (b.) The distribution of accidental ADC counts, both for $K_L \rightarrow \pi^+\pi^-\pi^0$ Monte Carlo events

# CHAPTER 8

# Event Reconstruction

This chapter outlines the method used to identify the signal decays. The photon selection is very similar for all the analyses, since they all contain photons from $\pi^0$ decays in the final state; differences arise in the lepton selection. Once all of the final state particles have been identified and their four-vectors determined an event could potentially be a signal if the invariant mass of the final particles is consistent with the $K_L$ mass. Kinematic reconstruction is described, as are cuts made to ensure the particles are well-measured by requiring the decay to be within the fiducial region of the detector.

## 8.1 Lepton Selection

The signal for a charged particle traversing the spectrometer is several hits on different wires in the drift chambers, as described in section 3.2.2. The hits are grouped together to make segments, and the segments are grouped to make tracks. In the (y) view, since there is no bend expected in the particle's trajectory, the entire track is found at once. The tracks in the (x) direction get matched to tracks in the (y) direction by using the cluster positions in the calorimeter. Since the signals in the calorimeter are different for electrons and muons, two different algorithms were employed to find clusters of energy in the glass.

### 8.1.1 Cluster Finding

To find a cluster in the lead-glass the analysis program loops over a certain number of blocks (called the seeds) and finds which block in the neighborhood of the seed has the largest amount of energy. For the two-electron analysis, the Hardware Cluster Finder (HCF) provided the seeds that were used to find clusters. However, in the dimuon analysis

all blocks were possible seeds, since a muon, being a minimum ionizing particle, typically leaves a signal well below the HCF threshold. This method of clustering was called the "software cluster finder", in contrast to the HCF. The software cluster was any $3 \times 3$ array of blocks whose summed energy was above $500\,MeV$ and contained a local maximum. This threshold was low enough so that muons could be associated with clusters. Some of these clusters may have also been selected by the HCF, but the HCF information was ignored. This cluster finding procedure was also used for the normalization mode, $K_L \to \pi^+ \pi^- \pi^0$. By using this looser definition for a cluster in the dimuon analysis there is less dependence on muon or charged pion signals in the lead-glass.

## 8.1.2   Electron Tracking

For electrons, the method of matching the segments to form tracks is simplified by the fact that at trigger level the electrons were expected to make lead-glass clusters selected by the Hardware Cluster Finder (HCF). After the segments have been selected, different (x) segments are matched with (y) segments to see which combination extrapolates closest to the clusters in the glass. For 78% of the crunch events two (x) and (y) tracks can be matched to two clusters to within a total distance of $5\,cm$. Of that data, 54% has only one combination where the (x) and (y) track extrapolations at the glass are close to the hardware cluster. For the other 46% one must consider the difference between the extrapolated track and cluster positions for both combinations of matching clusters to tracks. The matching algorithm chooses the combination whose track-cluster position difference is smallest. Eventually, the upstream and downstream (x) track segments are matched by requiring both segments to meet when extrapolated to the plane of the magnet. Figure 76 shows the distribution of (x) and (y) tracks for both the electron crunch data and the $\pi^0 e^+ e^-$ Monte Carlo. The crunch required that there be at least one (y) track and at least two (x) tracks, which kept 33% of the data. Eventually the analysis required that only those events with two (x) tracks and two (y) tracks be kept.

### 8.1.3 Muon Tracking

The muon tracking is done the same way as the electron tracking, only for this analysis all clusters found by the software cluster finder were used, and only one track was required to point to a cluster. The requirement that there be exactly 2 (x) tracks and 2 (y) tracks keeps 69% of the dimuon crunch data, and 95% of the $\pi^0\mu^+\mu^-$ Monte Carlo acceptance. Figure 77 shows the distribution of (x) vs (y) tracks of the dimuon data (figure a) and the $\pi^0 e^+ e^-$ Monte Carlo (figure b).

### 8.1.4 Track Quality Cuts

Once the hits are grouped to form segments, the four space points (or three, depending on how many hits for a given track there are) are fit to a straight line. The residuals of the fit for all space points are added in quadrature, and a cut is made on the resulting sum, which
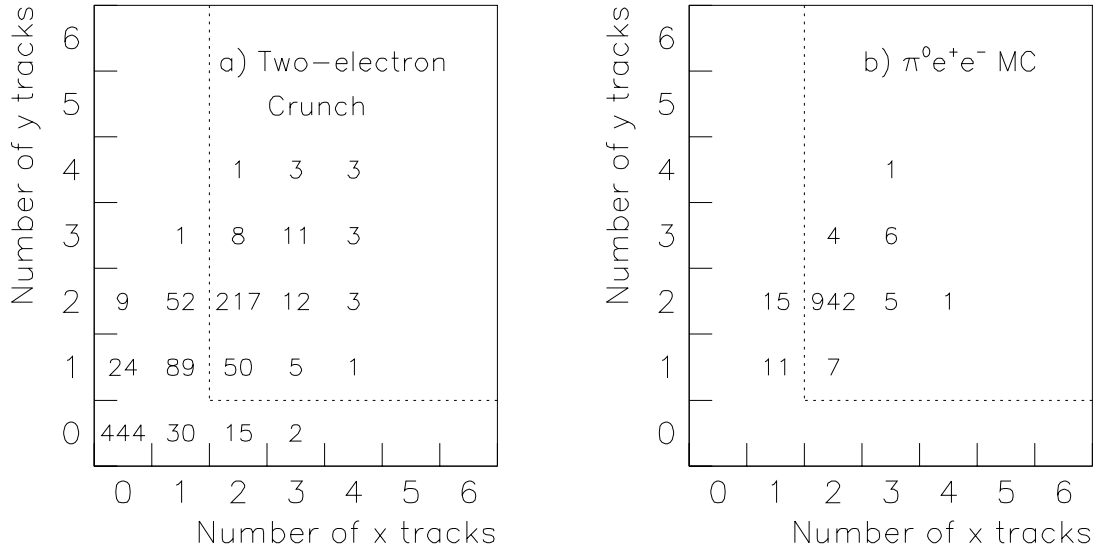
Figure 76. The number of x vs y tracks in (a) the two electron crunch and (b) the $\pi^0 e^+ e^-$ Monte Carlo, where both plots have been normalized to 1000 events. The dotted lines represent the cuts in the crunch analysis. The large peak at zero x and y tracks in the crunch data (a) is caused by the requirement that the tracks point to hardware clusters. The Monte Carlo data (b) have already passed the tracking requirements at trigger level.

is in a sense a $\chi^2$ for each segment. Since the single hit resolution of each chamber is about $100\,\mu m$, or $10^{-4}\,m$, the mean $\chi^2$ for each segment is $\sim 4 \times 10^{-8} m^2$. Figure 78 shows the upstream (x) segment $\chi^2$ distributions and the cuts made on the data for both electrons and muons. In the $\pi^0 \mu^+ \mu^-$ analysis there was a cut requiring the entire (y) track $\chi^2$ to be less than $6 \times 10^{-7}$. In fact there may be small fringe fields in the magnet in the (x) direction which might cause bending in the (y) direction, and these fields were not included in the Monte Carlo. The rejection from this cut was small in both the data and the Monte Carlo samples, however, and this inadequacy in the Monte Carlo induces a negligible systematic error in the acceptance determination.

Another tracking variable which is checked is the offset at the plane of the magnet between where the upstream and downstream tracks extrapolate. If a charged pion decays in the chamber system and the $\nu$ carries off a substantial fraction of the pion energy, for example, this variable could be large. Figure 79 shows an example of how these two extrapolations can miss each other when a charged pion decays.
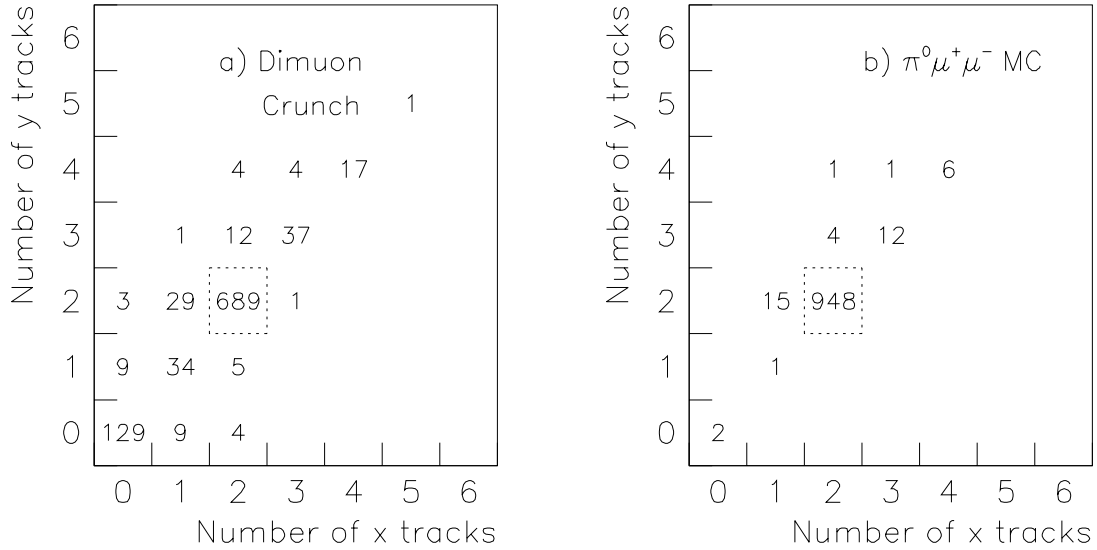


Figure 77. The number of x vs y tracks in (a) the dimuon crunch and (b) the $\pi^0 \mu^+ \mu^-$ Monte Carlo, where both plots have been normalized to 1000 events. The dotted lines represent the cuts in the crunch analysis.

Figure 80 shows the offset at the magnet for both $\pi^0\mu^+\mu^-$ candidates and the $\pi^0\mu^+\mu^-$ Monte Carlo. The width of the distribution is reproduced by the Monte Carlo but the tails in the data are primarily due to $\delta$-rays, which are not in the simulation, and from pion decay, which of course would not occur in a $K_L \to \pi^0\mu^+\mu^-$ decay. The offset resolution, $\sigma_{\text{offset}}$, given the chamber resolution and the material in the spectrometer, is:

$$\sigma_{\text{offset}} = \left(250 + \frac{2700}{p(\,GeV/c)}\right) \times 10^{-6}\, m$$

where $p$ is momentum of the track in question, measured in $GeV/c$. The cut on the separation at the magnet $3\sigma$ in the $\pi^0\mu^+\mu^-$ analysis, where backgrounds from charged pion decays are important, and $6\sigma$ for the $\pi^0 e^+ e^-$ analysis. Table 14 lists all of the tracking variables which were checked in the analyses, the values of the final cuts, and the efficiencies for the signal data and Monte Carlo events.
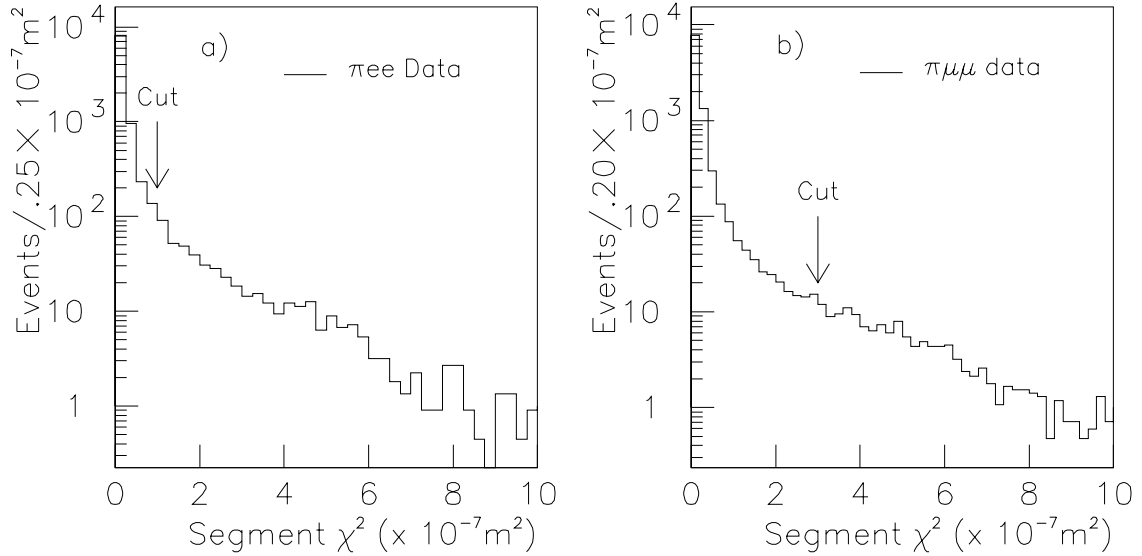


Figure 78. The segment $\chi^2$ distributions for both dimuon and two-electron data, for x segments
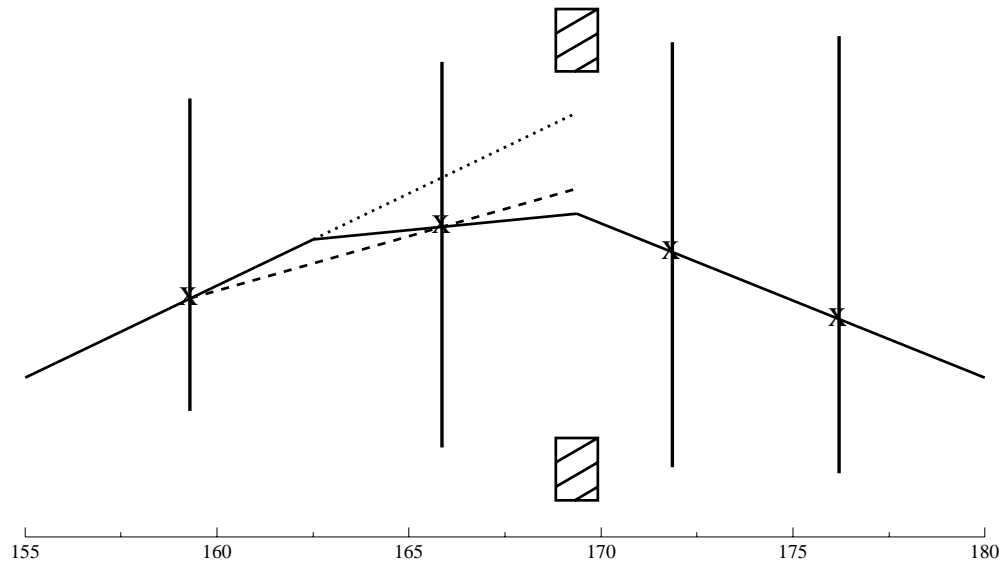
Figure 79. The difference from upstream and downstream extrapolations to the magnet plane when a charged pion decays in the chamber system. The x's represent hits in the chambers, the solid line is where the charged pion actually goes, the dashed line is the wrong upstream extrapolation. The kink in the charged pion's trajectory is caused by the neutrino in the decay taking away some of the pion's energy
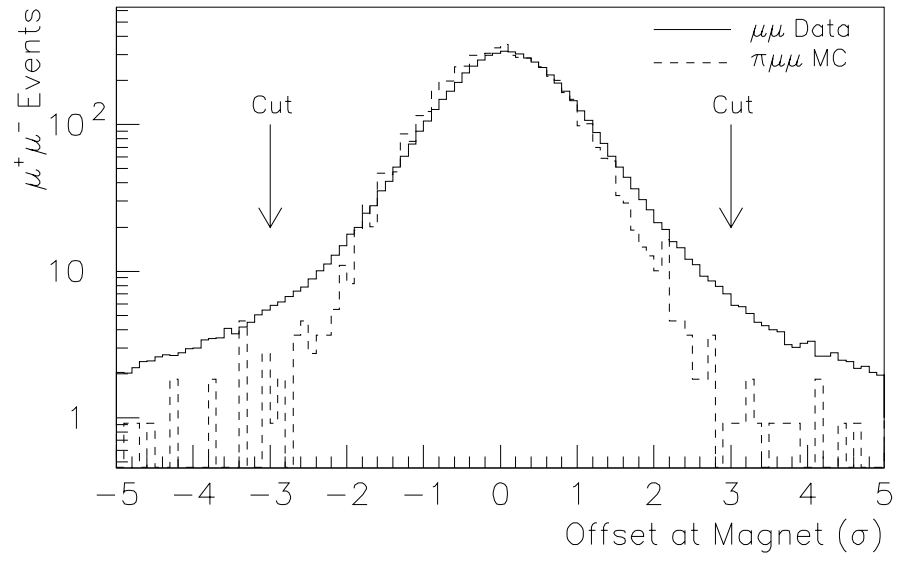
Figure 80. The offset at the magnet of the upstream - downstream segments for both dimuon and $K_L \to \pi^0 \mu^+ \mu^-$ Monte Carlo

Table 14. Tracking Cuts

| | $K_L \to \pi^0 e^+ e^-$ analysis | | | $K_L \to \pi^0 \mu^+ \mu^-$ analysis | | |
|---|---|---|---|---|---|---|
| | | Fraction Kept | | | Fraction Kept | |
| Tracking Variable | Cut | Data | MC | Cut | Data | MC |
| All $\chi^2_{segment}$'s | $1 \times 10^{-7}$ | 90 | 99 | $3 \times 10^{-7}$ | 89 | 99 |
| Offset at Magnet | $6\sigma$ | 98.5 | 99.8 | $3\sigma$ | 96.8 | 99.9 |

### 8.1.5    Vertex Selection

Once the tracks have been selected the next step is to determine if they originated from a common vertex in the decay region. There are two different variables that are computed—the distance of closest approach ($D_{CA}$) of the two tracks, and a vertex $\chi^2$ ($\chi^2_{vtx}$).

$D_{CA}$ is formed by looking at the track segments upstream of the magnet as they were originally selected and then extrapolating back to the (z) position where the tracks come closest to intersecting. The resolution on $D_{CA}$ can be expressed the following way:

$$\sigma_{D_{CA}} = 0.245 \times 10^{-4} + 0.0085 \left( \frac{1}{p_1(\,GeV/c)}^2 + \frac{1}{p_2(GeV/c)}^2 \right) m$$

where $p_1$ and $p_2$ are the momentum of the two tracks in the events, measured in $GeV/c$. The constant term in the resolution function is from multiple scattering in the chamber system, and the momentum-dependent term is due to the position resolution of the drift chambers.

$\chi^2_{vtx}$ is formed by re-fitting the upstream slopes and intercepts of the tracks with the constraint that the two tracks come from a common vertex. Figure 81 shows the distributions of this variable for both samples of $K_L \to \pi^0 \ell^+ \ell^-$ candidates and Monte Carlos. Table 15 shows the values of the cuts for the vertex quality variables.

## 8.2    Particle Identification

After the vertex is found, the tracks are checked to see if their signals in the rest of the detector are consistent with an electron or a muon signal. Although the HCF requirement

Table 15. Vertex Quality Cuts

| Vertex Quality Variable | $K_L \to \pi^0 e^+ e^-$ analysis | | | $K_L \to \pi^0 \mu^+ \mu^-$ analysis | | |
| | | Fraction Kept | | | Fraction Kept | |
| | Cut | Data | MC | Cut | Data | MC |
|---|---|---|---|---|---|---|
| $\chi^2_{vertex}$ | 15.0 | 98.8% | 98.8% | 10.0 | 66.1% | 96.7% |
| $D_{\mathrm{CA}}$ | $6\sigma$ | 95.6% | 99.8% | $6\sigma$ | 82.6% | 99.5% |

inherent in the two-electron trigger is one consistency check, there are much tighter require-
ments which can be made. This section describes the lepton identification cuts made in
both of the $\pi^0 \ell^+ \ell^-$ analyses.

## 8.2.1 Muon Identification

On all lead-glass clusters associated with muon tracks, we required the cluster energy to
be below $3\,GeV$. For muons which pointed to the pipe-blocks, a $6\,GeV$ cut was made at
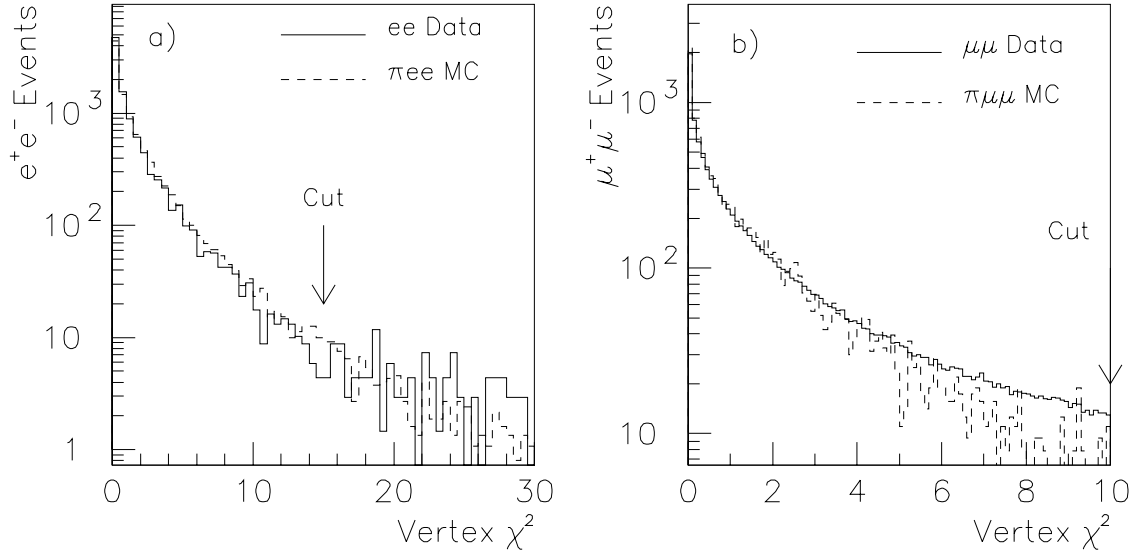


Figure 81. $\chi^2_{vtx}$ for both $K_L \to \pi^0 \ell^+ \ell^-$ candidates and $K_L \to \pi^0 \ell^+ \ell^-$ Monte Carlos

the crunch level. A looser cut was made in the pipe blocks because there was significantly more accidental energy there and because the absorption effects were larger. Since a muon deposits energy evenly along its trajectory it will deposit just as much energy close to the phototube as it will far away from the phototube. This means that the muon signal , when translated to $GeV$, will be larger in blocks with high $\alpha$'s than in blocks with low $\alpha$'s. This cut removed contamination from electrons and pions, both of which can shower in the blocks and leave a sizeable signal. Figure 82 shows the cluster energies for tracks from three samples: muons from the muon calibration runs, which have no hadron contamination and little accidental activity in the glass, events from the dimuon crunch, and finally, charged pions from well-identified $K_L \rightarrow \pi^+ \pi^- \pi^0$ events. The final muon identification cut made selects 44% of the data events while keeping 99% of the $\pi^0 \mu^+ \mu^-$ acceptance.

For 25% of the data events and 16% of the $\pi^0 \mu^+ \mu^-$ Monte Carlo events, one of the muons is not associated with a cluster. There are two processes that contribute to this effect. The first occurs when a muon arrives in a block with a very low absorption coefficient. For
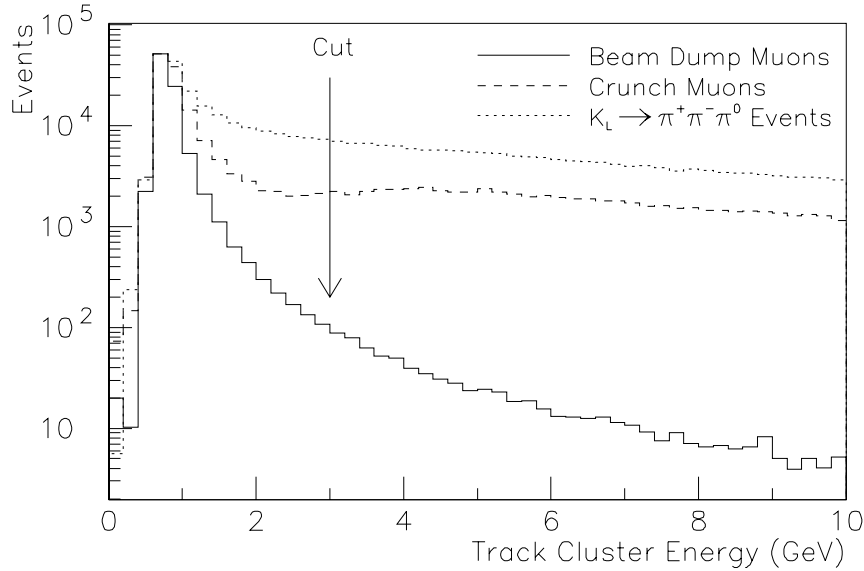


Figure 82. Track cluster energy for three samples: from calibration runs, from the dimuon crunch sample, and verified charged pions from $\pi^+ \pi^- \pi^0$ decays. The long tails on the last two samples are due to pion showers and accidental activity in the lead-glass.

this block, the reconstructed energy may be slightly less than the "software cluster finder" threshold. The second process occurs when a muon arrives very close to a large cluster of energy in the glass, and its energy deposition is confused with the nearby cluster. To ensure that tracks without associated clusters are not masked by a neighboring cluster, a cut was made requiring the sum of the energies in the two blocks closest to where the muon hit the glass to be less than $3\,GeV$ or $5\,GeV$ for regular and pipe blocks, respectively. This cut kept 84% of the data while keeping 97% of the $\pi^0\mu^+\mu^-$ acceptance.

Finally, in order for a muon to be energetic enough to cross the hadron filter it has to have at least $5\,GeV/c$ in momentum. We rejected events with muons with momentum less than $7\,GeV/c$, well away from this threshold. The cut kept 90% of the $\pi^0\mu^+\mu^-$ data, and 99% of the acceptance.

## 8.2.2 Electron Identification

Since an electron is expected to leave all of its energy in the calorimeter, much more stringent energy requirements are made in the $\pi^0 e^+ e^-$ analysis. At the crunch level, the electron cluster energy was required to match the track momentum to within 35%, and for electrons which extrapolated to the pipe blocks, no $E/p$ cut was made. Figure 83 shows the ratio of cluster energy to track momentum ($E/p$) for each electron that was matched to a cluster not in the pipe blocks in the two electron crunch. The structure in this plot is due primarily to three kinds of decays. The peak where both tracks have an $E/p$ of about 1 is from real two-electron events, primarily photon conversions at the vacuum window. The ridges in the plots where one track has an $E/p$ peaked at 1 and the other track has a broad range of $E/p$'s is due to $K_{e3}$ decays. Finally, the region where both $E/p$'s are low is from $K_L \rightarrow \pi^+\pi^-\pi^0$ decays. After the lead-glass calibrations were complete, $E/p$ for all electron clusters was required to be within 15% of unity, which for undamaged blocks in the calorimeter was a $3\sigma$ cut. Figure 84 shows $E/p$ for electrons from the $\pi^0 e^+ e^-$ candidate events, as well as where the final cuts were made.
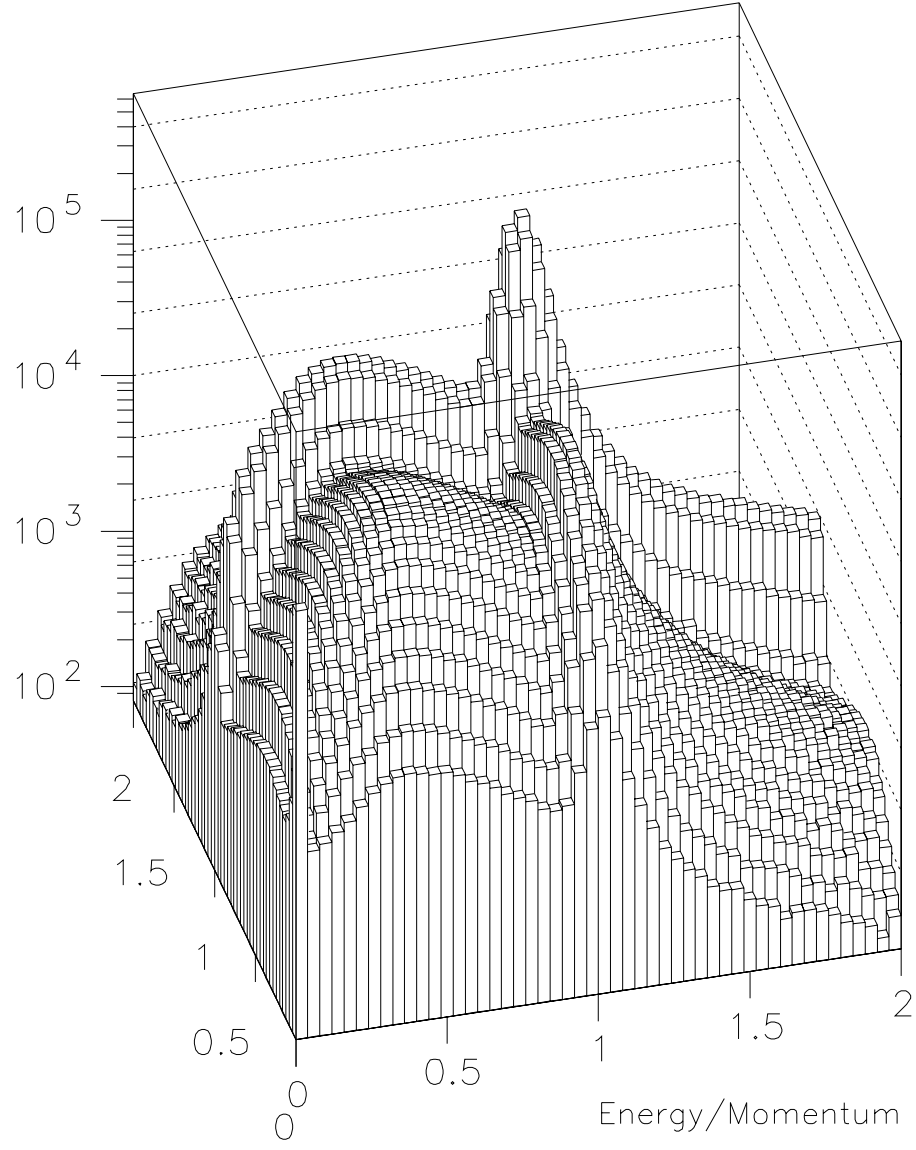
Figure 83. The distribution of $E/p$ for both the tracks in the event for all crunch data

## 8.3 Photon Selection

Once all the clusters in the calorimeter which can be identified with tracks have been determined, the remaining clusters, called "extra clusters", are photon candidates. In both analyses the photons were required to make clusters selected by the Hardware Cluster Finder.

### 8.3.1 Two-electron Data

As was mentioned in Chapter 4, the two-electron trigger accepted events with 4,6,7, and 8 hardware clusters for most of the run. The Dalitz trigger, which was prescaled usually by 14, accepted only events with 3 or 5 clusters in the lead glass. Figure 85 shows the distribution of hardware clusters in the two electron crunch data. The three and five cluster data, which contained the normalization decays, made up 17% of the crunch output data, and the four cluster data made up 52% of the data. The data with more than five clusters was used for rare pion decay searches and was used for the analyses described in reference [1].
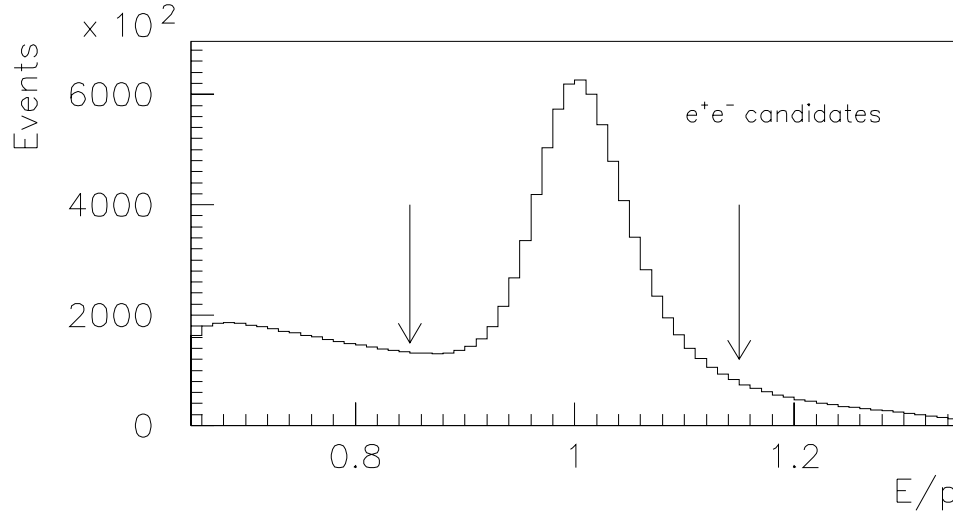
Figure 84. The quantity $E/p$ for electrons from the crunch The cuts eventually made in the analysis are shown, as well as the flat background corresponding to charged pions showering in the calorimeter.

### 8.3.2   Di-muon Data

At the crunch level, the analysis saved events with at least one extra hardware cluster (29%
of the raw data), and the minimum bias analysis saved events with at least two hardware
clusters (8.3% of the raw data). The $\pi^0\mu^+\mu^-$ and $\pi^+\pi^-\pi^0$ analyses require exactly two extra
hardware clusters selected by the HCF, and any extra clusters not selected by the HCF were
ignored. The dimuon data not used for the $\pi^0\mu^+\mu^-$ analysis was saved for other analyses,
such as the search for the decay $K_L \rightarrow \mu^+\mu^-\gamma$. The two-photon data comprised 28% of the
remaining dimuon crunch output, and 82% of the remaining minimum bias crunch output.
Figure 86 shows the distribution of extra clusters selected by the Hardware Cluster Finder
for both the dimuon candidates after loose muon identification cuts had been made, and
for minimum bias events which contained the $K_L \rightarrow \pi^+\pi^-\pi^0$ normalization sample.
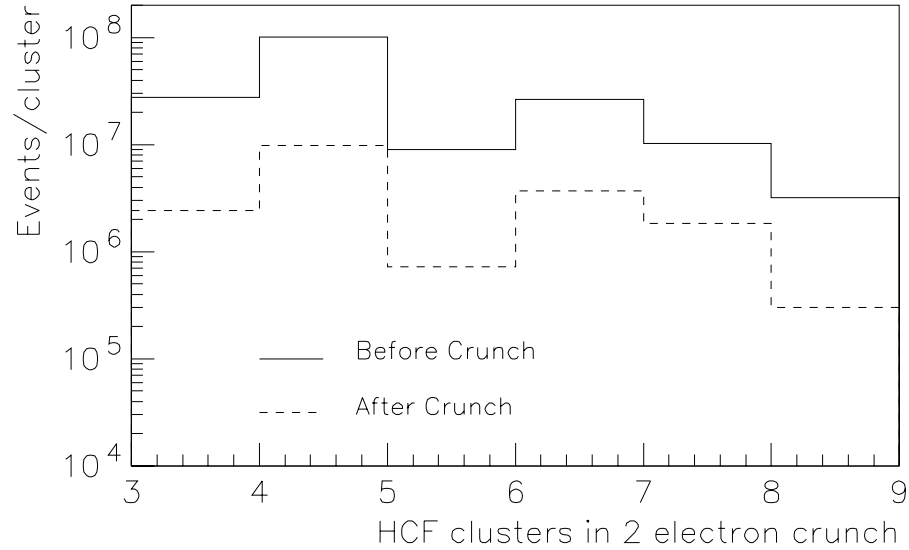


Figure 85. The distribution of hardware clusters for the crunch data

## 8.4    Event Reconstruction

### 8.4.1    Invariant Mass and $P_t^2$ of Event

The invariant mass of the decay is computed by summing the four-vectors of the two leptons and two photons, given the measurements of the lepton momenta and the photon energies and positions, and assuming the appropriate invariant mass for each particle. The resulting invariant mass distributions for both searches can be found in figure 87. By adding up the three-momenta of all four decay particles and projecting into the plane perpendicular to the initial parent $K_L$ direction calculated from the decay vertex and the target position, one can also compute the $P_t^2$ of the decay. Figure 87 shows the $P_t^2$ distribution. If a $K_L$ scatters before decaying, for example off the edge of the beam-pipe, or if all the final state particles have not been measured, then the $P_t^2$ of that event will be large.

The large bumps in both mass spectra in the data are due to $K_L \rightarrow \pi^+ \pi^- \pi^0$ decays. If the invariant masses are recalculated such that the track is assigned the invariant mass
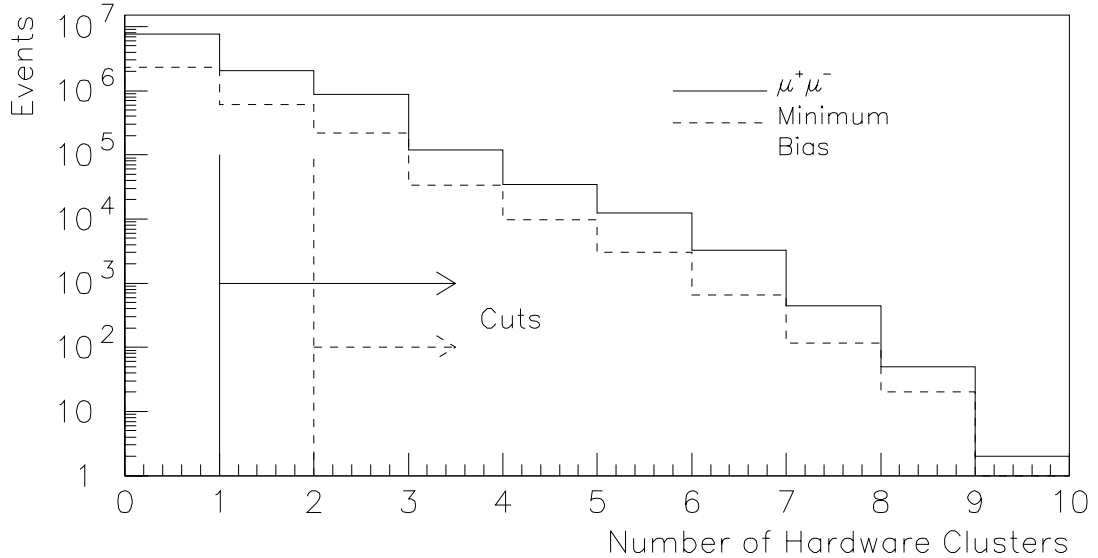


Figure 86. The distributions of extra clusters selected by the hardware cluster finder for both the raw dimuon data and minimum bias data. The cuts made in the crunch are shown
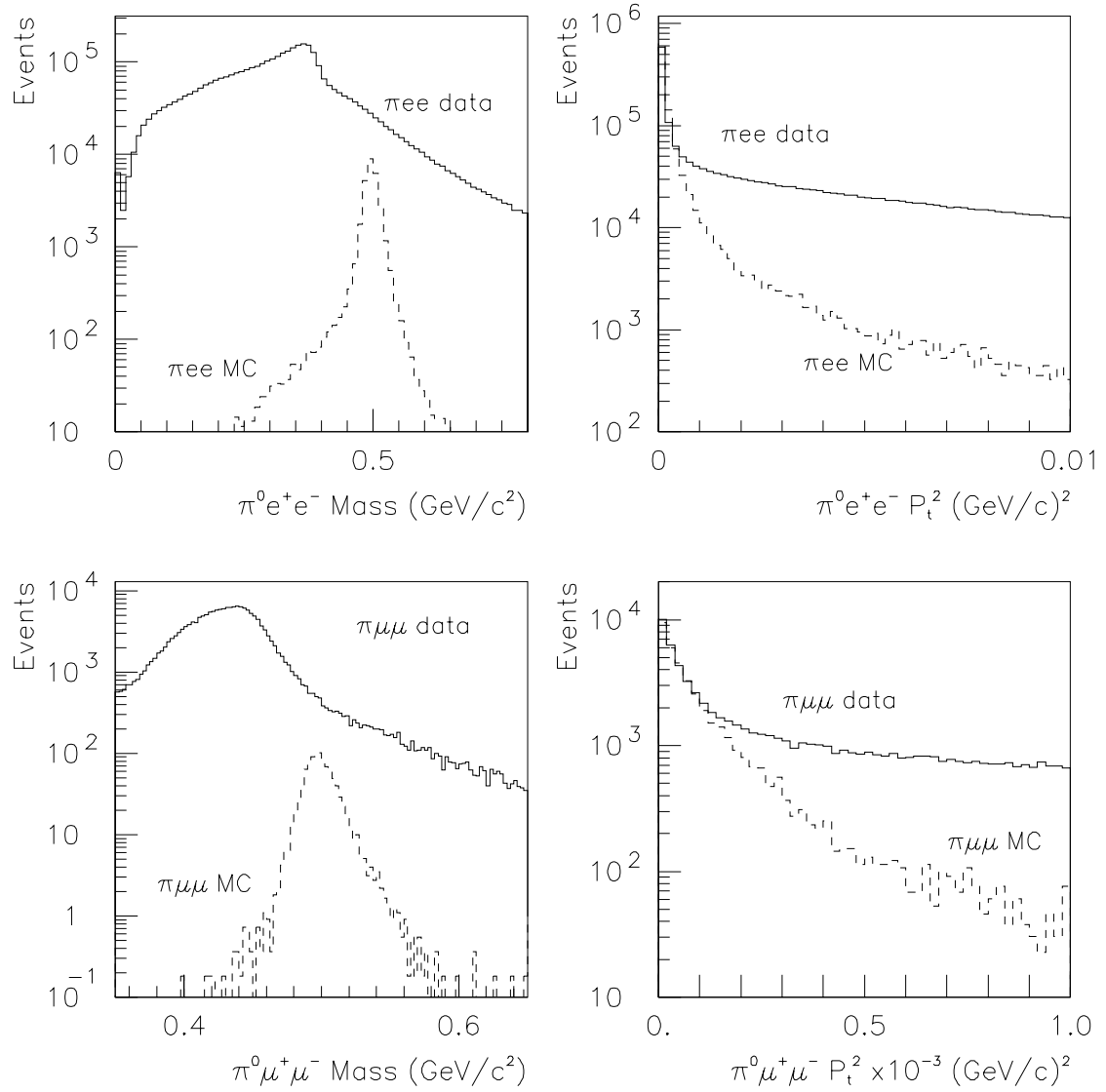
Figure 87. The distributions of total mass (figures a & c) and $P_t^2$ (figures b & c) in the $\pi^0 e^+ e^-$ and $\pi^0 \mu^+ \mu^-$ Data and Monte Carlo after finding two tracks from a vertex and two extra photon candidates

of a charged pion instead of an electron or muon, it is even more clear that many of the events which are selected by either trigger are due to the decay $K_L \to \pi^+ \pi^- \pi^0$, as is shown in figure 88.

Since the photon momentum is correct regardless of the invariant mass of the track, and the momentum of the track is what is used to determine the lepton four-vector, the total $P_t^2$ of an event is independent of the mass assumed for the charged track. Therefore, backgrounds in which all the final particles are measured but misidentified will still have low $P_t^2$, for example the background from the decay $K_L \to \pi^+ \pi^- \pi^0$.

### 8.4.2 Two photon Invariant Mass

Another kinematic handle that exists for the $\pi^0 \ell^+ \ell^-$ signal is the two-photon invariant mass ($M_{\gamma\gamma}$). If one assumes that the photons from the decay come from the track vertex, $M_{\gamma\gamma}$ is simply:

$$M_{\gamma\gamma}^2 = \frac{E_1 E_2 r_{12}^2}{z^2} \tag{8.1}$$
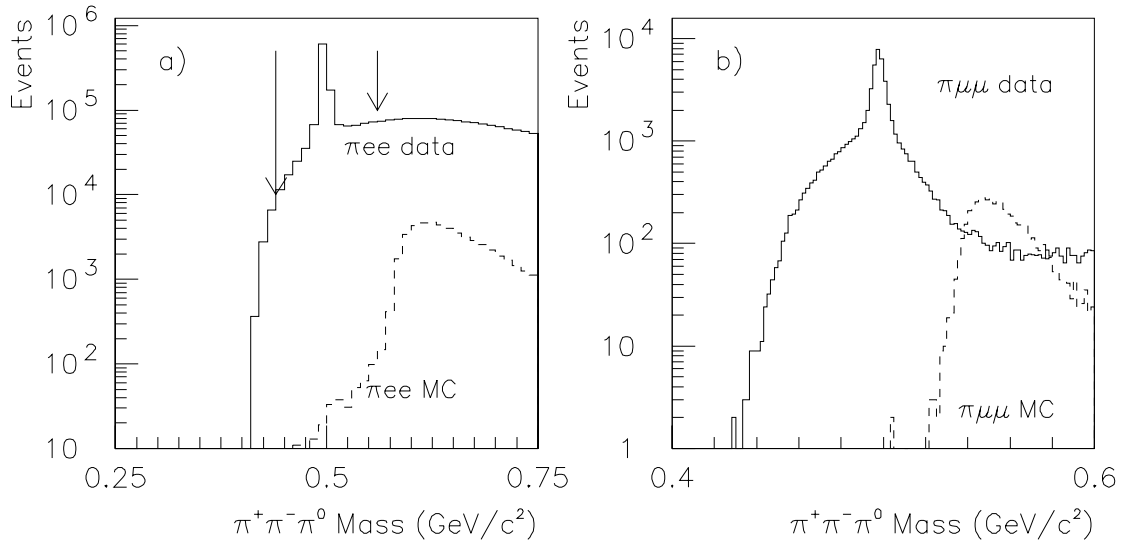


Figure 88. The distribution of the $\pi^+ \pi^- \pi^0$ invariant mass for both the $\pi^0 e^+ e^-$ (figure a) and $\pi^0 \mu^+ \mu^-$ (figure b) candidates

where $E_{1,2}$ are the photon energies, $r_{12}$ is the distance between the photons at the lead-glass, and $z$ is the distance between the lead-glass and the track vertex.

Figure 89 shows a plot of the $M_{\gamma\gamma}$ distribution for the electron data that passed the two-electron crunch. Once events consistent with $K_L \to \pi^+\pi^-\pi^0$ decays have been removed the remaining data set has an almost flat $M_{\gamma\gamma}$ distribution near the $\pi^0$ mass. The cut eventually made on the $\pi^0 e^+ e^-$ candidates is that the $M_{\gamma\gamma}$ mass be within $15\,MeV/c^2$ of the nominal $\pi^0$ mass, a $2.5\sigma$ cut in the undamaged regions of the lead-glass.

In the $\pi^0\mu^+\mu^-$ analysis events with real $\pi^0$'s are selected by cutting on a $\chi^2$ for the hypothesis that the two photons were emitted by a $\pi^0$ decaying at the track vertex. Since the dominant contribution to the $M_{\gamma\gamma}$ width is from the energy resolution of the two photons, the $\chi^2$ only uses the photon energies and resolutions for photons of that energy. Define the $\chi^2_{\pi^0}$ in the following way:

$$\chi^2_{\pi^0} = \left[\frac{E_1 - E_{1c}}{\sigma(E_1)}\right]^2 + \left[\frac{E_2 - E_{2c}}{\sigma(E_2)}\right]^2 \tag{8.2}$$
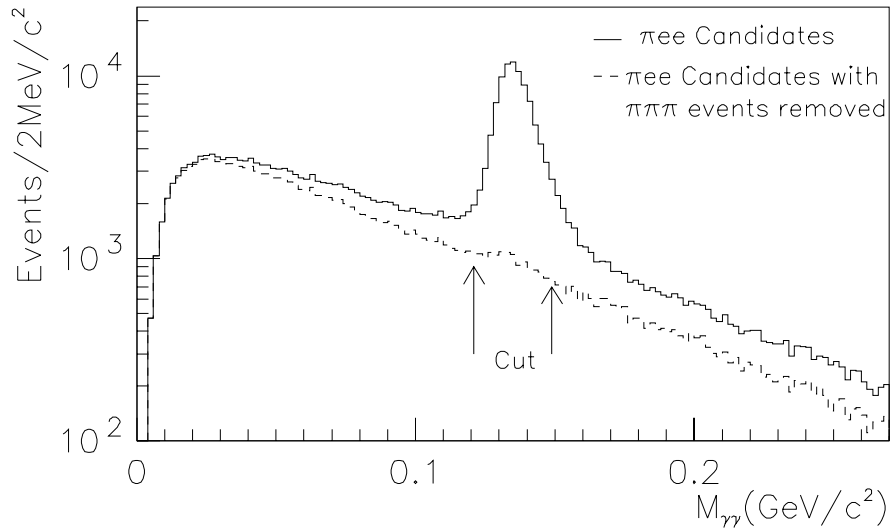


Figure 89. The $M_{\gamma\gamma}$ distribution for $\pi^0 e^+ e^-$ candidates. The solid histogram represents all of the events analyzed, and the dashed line histogram represents same distribution but for events that, when the tracks are given the charged pion mass, have total invariant mass at least $60\,MeV/c^2$ from the $K_L$ mass

where $E_{1c}$ and $E_{2c}$ are the energies which result in $M_{\gamma\gamma}$ exactly equal to the $\pi^0$ mass and

$$\left.\frac{d\chi^2_{\pi^0}}{dE_1}\right|_{E_1=E_{1c},E_2=E_{2c}} = 0 \text{ and } \left.\frac{d\chi^2_{\pi^0}}{dE_2}\right|_{E_1=E_{1c},E_2=E_{2c}} = 0 \qquad (8.3)$$

Cutting on $M_{\gamma\gamma}$ this way takes into account different energy resolutions in the different parts of the glass. Such a sophisticated treatment is probably unnecessary, however, because any uncertainty in the cut roughly cancels when the same cut is made in both the signal and the normalization modes. This cut was only used in the $\pi^0\mu^+\mu^-$ analysis for historical reasons. Figure 90 shows the $\chi^2_{\pi^0}$ distribution in the $\pi^0\mu^+\mu^-$ data, both with and without the $\pi^+\pi^-\pi^0$ contamination. The cut in the analysis which will eventually be made is $\chi^2_{\pi^0} < 8$ for two degrees of freedom.

### 8.4.3 Photon Energy Constraint

Once the event has been identified as having a neutral $\pi^0$ in the decay, the energies of the two photons are constrained such that $M_{\gamma\gamma}$ is exactly equal to the $\pi^0$ mass, and the $\chi^2_{\pi^0}$ is
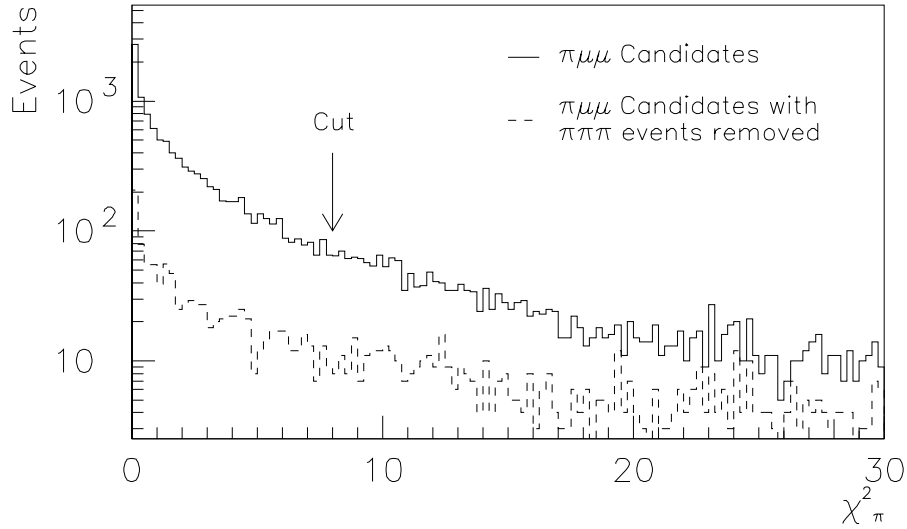


Figure 90. The $\chi^2_{\pi^0}$ distribution for $\pi^0\mu^+\mu^-$ candidates. The solid histogram represents all of the events analyzed, and the dashed line histogram represents same distribution but for events that, when the tracks are given the charged pion mass, have total invariant mass at least $30\,MeV/c^2$ from the $K_L$ mass
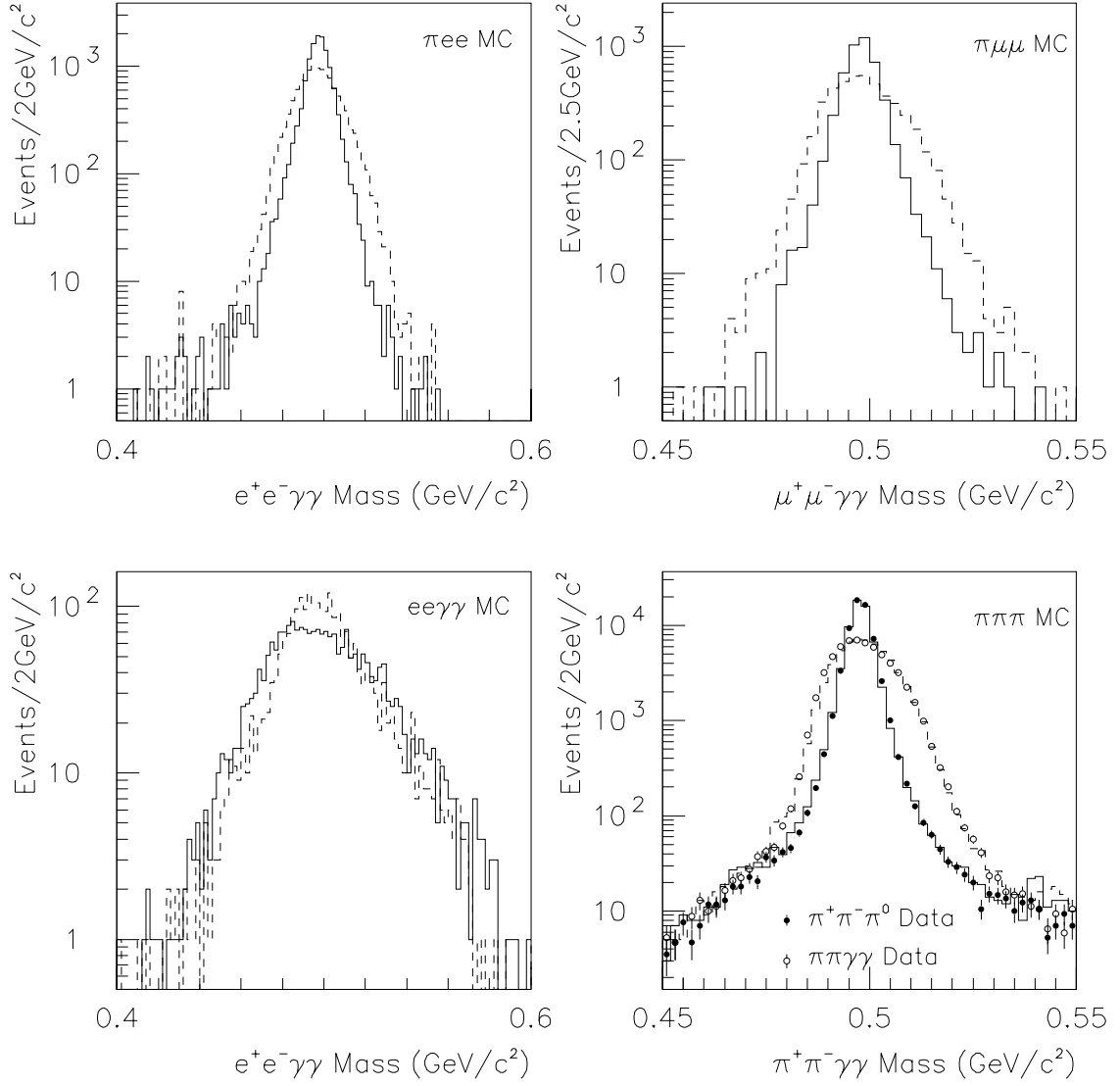
Figure 91. The total invariant mass distributions for $\pi^0 e^+ e^-$, $\pi^0 \mu^+ \mu^-$, $e^+ e^- \gamma\gamma$, and $\pi^+ \pi^- \pi^0$ Monte Carlo, and $\pi^+ \pi^- \pi^0$ Data. The solid histograms show the mass calculated by constraining $M_{\gamma\gamma}$ to be $M_{\pi^0}$ and the dotted histograms show the mass calculated without that constraint

minimized. This has the effect of improving the $K_L$ mass resolution for decays with real $\pi^0$'s in them and allows for tighter final mass cuts. This also degrades the mass resolution for backgrounds which do not contain real pions, for example, $K_L \to e^+e^-\gamma\gamma$. Figure 91 shows the mass distributions for several samples: the two signal Monte Carlos, the $K_L \to e^+e^-\gamma\gamma$ Monte Carlo, and the $K_L \to \pi^+\pi^-\pi^0$ data and Monte Carlo. From the $\pi^+\pi^-\pi^0$ samples it is clear that this narrowing of the mass distribution due to the photon energy constraint is well simulated in the Monte Carlo.

### 8.4.4 Four photon Invariant Mass

To reconstruct decays of the type $K_L \to \pi^0\pi^0$, $\pi^0 \to e^+e^-\gamma$, a different method of event reconstruction was used. Since for these decays the $e^+e^-$ pair has a low invariant mass $(M_{e^+e^-})$, the electron and positron are emitted with a very small opening angle. When there is a small opening angle between the pair, the resolution of the (z)-position of the vertex is worse, which in turn degrades the resolution on the photon four-vectors, which ultimately degrades the total mass resolution. Figure 92 shows the calculated fractional error on the distance between the (z) position of the vertex and the (z) position of the lead-glass, as a function of $M_{e^+e^-}$. Clearly for events with $M_{e^+e^-}$ less than $20\,MeV/c^2$ the (z) position resolution is much larger than the typical photon energy resolution ($\sim 4.5\%$ in undamaged regions of the glass).

To more efficiently reconstruct $K_L \to \pi^0\pi^0$, $\pi^0 \to e^+e^-\gamma$ decays the $e^+e^-$ pair's energy is summed and is treated as a photon. Then, the three real photons in the decay and the fourth $e^+e^-$-pair "photon" in the decay are treated equally. For each pair of photons $i$ and $j$, the (z) position as measured from the lead-glass for that pairing, $z_{ij}$, can be calculated, assuming they came from a $\pi^0$ decay. $z_{ij}$ is obtained using the following equation:

$$z_{ij}^2 = \frac{E_i E_j r_{ij}^2}{m_\pi^2}, \tag{8.4}$$

where $E_{i,j}$ are the $i^{th}$ and $j^{th}$ photon energies, $r_{ij}$ is the separation between the two photons at the lead-glass, and $m_\pi$ is the neutral pion mass. To reconstruct a decay of the type $K_L \to \pi^0\pi^0$, the (z) positions for the two correct pairs of photons should be consistent. To

check this, a pairing $\chi^2$ can be formed, defined in the following way:

$$\chi^2 = \frac{(z_{ij} - z_{kl})^2}{\sigma^2_{z_{ij}} + \sigma^2_{z_{kl}}} \tag{8.5}$$

where $i, j, k$, and $l$ are the three photons and the $e^+e^-$ pair.

Once the best pairing, or the one with the lowest $\chi^2$, has been determined, the vertex position of the event is then the weighted average of the two "pair" vertices for the best pairing. Then, the total invariant mass of the event is simply

$$m^2_{\pi\pi} = \sum_{i=1,4} \sum_{j>i} \frac{E_i E_j r_{ij}^2}{z^2} \tag{8.6}$$

where again, $z$ is measured as the distance from the vertex to the calorimeter. If an event is not from a $K_L \to \pi^0\pi^0$ decay, then the pairing method will determine a (z) position with a very large $\chi^2$. The $\chi^2$ was required to be less than 40, the total invariant mass had to be within $100\,MeV/c^2$ of the $K_L$ mass, and the reconstructed (z) position of the pairing had to be upstream of the first drift chamber. Only 52% of the $\pi^0\pi^0$ candidates in normalization
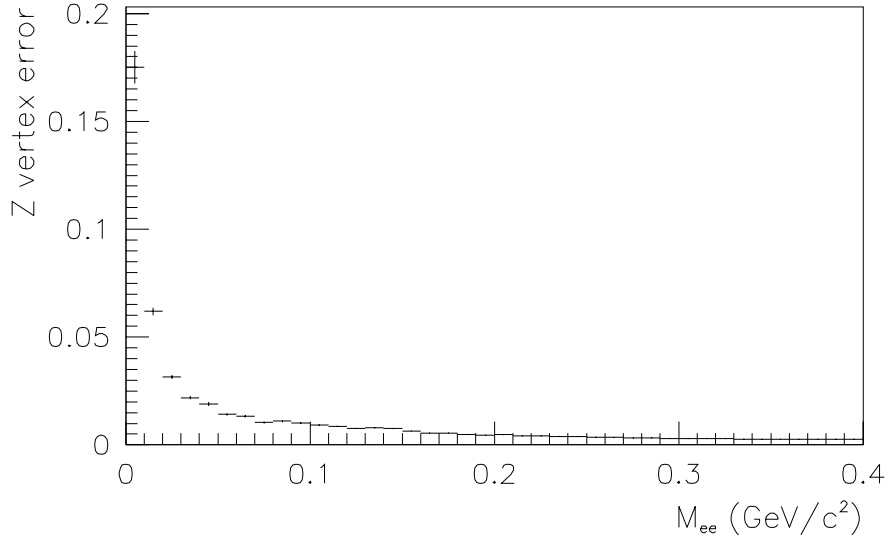


Figure 92. The calculated error on the (z) position of the track vertex as a function of the invariant mass of the $e^+e^-$ pair

data passed these cuts, while 96% of the $\pi^0\pi^0$, $\pi^0 \to e^+e^-\gamma$ Monte Carlo events survived. Figure 93 shows the pairing $\chi^2$ distributions of those events that passed in both the data and the $\pi^0\pi^0$, $\pi^0 \to e^+e^-\gamma$ Monte Carlo.

Figure 94 shows the mass resolution using the standard method of finding the vertex and the pairing method of finding the vertex position, for both the $K_L \to \pi^0\pi^0$, $\pi^0 \to e^+e^-\gamma$ data and Monte Carlo, after the loose cuts described above have been made. For both sets of events the mass resolution obtained by the pairing method outlined above is improved by a factor of 2.5.

To make the $K_L \to \pi^0\pi^0$, $\pi^0 \to e^+e^-\gamma$ events which were used for normalization more similar to the signal decay in spite of the different reconstruction technique, as well as to remove background arising from photon conversions, there was a minimum $M_{e^+e^-}$ requirement in the $\pi^0\pi^0$, $\pi^0 \to e^+e^-\gamma$ sample at $15\,MeV/c^2$, and the (z) positions of the vertices for the track vertex and the vertex determined by the pairing method had to agree to within $2.5\sigma$. Ultimately, the mass had to be within $25\,MeV/c^2$ of the $K_L$ mass (a $2.5\sigma$ cut), and the pairing $\chi^2$ had to be less than 10. Together these cuts kept 5.1% of candidate data
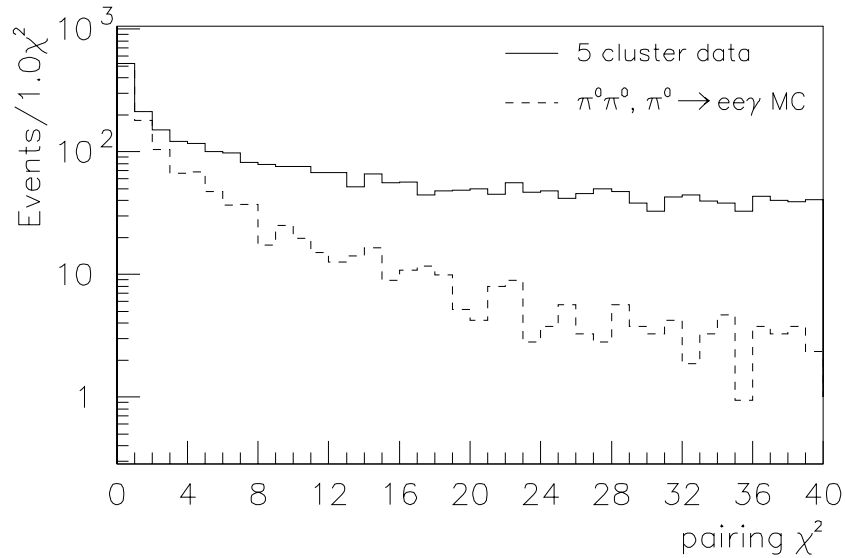


Figure 93. The pairing $\chi^2$ distributions for $K_L \to \pi^0\pi^0$, $\pi^0 \to e^+e^-\gamma$ data and Monte Carlo events, normalized to the first bin.
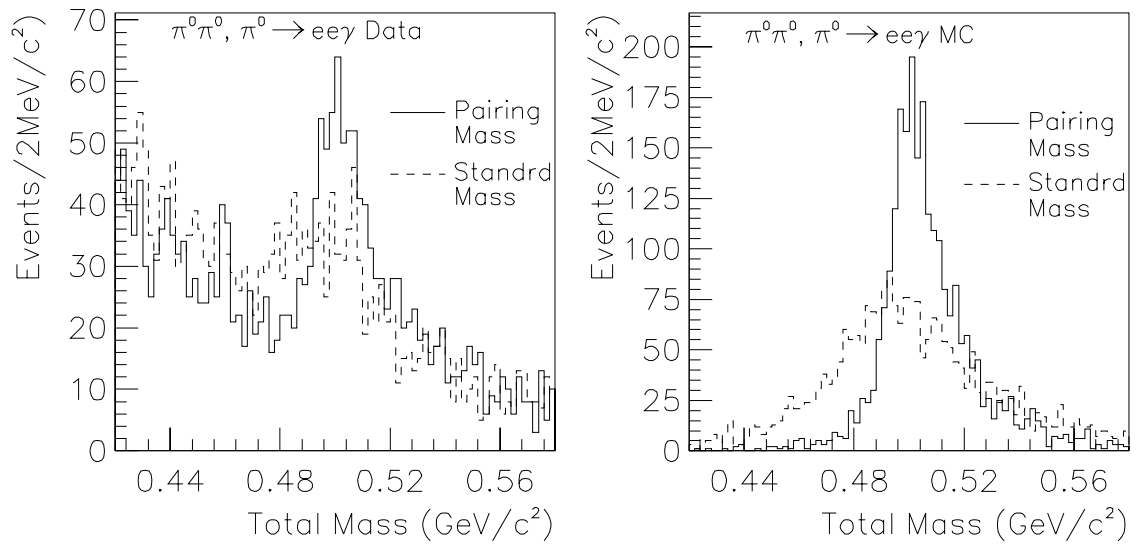
Figure 94. The mass distributions for $K_L \rightarrow \pi^0\pi^0$, $\pi^0 \rightarrow e^+e^-\gamma$ data and Monte Carlo, using two different reconstruction methods. The standard reconstruction uses the z vertex as determined by the two-track vertex, and the pairing reconstruction uses the z vertex which is determined by the best pairing of photons in the decay to make $\pi^0$'s

events events and 40.1% of the $\pi^0\pi^0$, $\pi^0 \to e^+e^-\gamma$ acceptance, where most of that loss in the Monte Carlo was due to the $M_{e^+e^-}$ cut. In the remainder of this document, when the mass of $\pi^0\pi^0$, $\pi^0 \to e^+e^-\gamma$ events is mentioned, the mass is assumed to be the one obtained by the pairing method.

## 8.5  Detector Cuts

The following section discusses the cuts made in both analyses made to keep the event in parts of the detector that were well-understood, as well as the cuts which verified that the particles from the decay satisfied the trigger.

### 8.5.1  Photon Fiducial Cuts

Events with photon candidates less than $6\,mm$ from the beam-pipes were rejected. To illustrate the understanding of the photon acceptance as a function of photon position at the glass, figure 95 shows the photon x and y distributions for $K_L \to \pi^+\pi^-\pi^0$ data and Monte Carlo after all cuts.

Another fiducial cut rejected photons which extrapolate to the iron ring described in chapter 3. This iron ring was not included in the Monte Carlo and hence there were discrepancies between data and Monte Carlo in the glass illumination near the edge of the ring. Figure 96 shows a plot of the distance between the origin in the (x-y) plane and the photon positions extrapolated to the (z) location of the iron ring, for $K_L \to \pi^+\pi^-\pi^0$ decays in both the Monte Carlo and the data. The cut in both analyses at $0.835\,m$ ensures that the photons are well away from that aperture.

### 8.5.2  Tracking Fiducial Cuts

As was done with the photons, there was a cut to remove events which had tracks which extrapolated to within $6\,mm$ of the beam-pipes. These events were cut out in both the $K_L \to \pi^0\mu^+\mu^-$ and $K_L \to \pi^0 e^+e^-$ analysis because particle identification was poorest in that region.

There was a cut on the (z) position of the vertex to reject events which decayed upstream of $90\,m$ and downstream of the vacuum window, which was at $160\,m$. Figure 97 shows the (z) vertex distribution for the normalization sample $K_L \to \pi^+\pi^-\pi^0$. Although there are discrepancies in far upstream regions of the detector, in most of the detector, the acceptance as a function of the (z) position of the vertex is well simulated.

A cut was made in the $\pi^0\mu^+\mu^-$ analysis to remove events where there were two tracks pointing to the pipe blocks. This cut was made because the particle identification there was substantially worse than in the rest of the detector. Figure 98 shows the distribution of number of tracks pointing to the pipe blocks for both $\pi^0\mu^+\mu^-$ (figure a) and $\pi^+\pi^-\pi^0$ (figure b) data and Monte Carlo simulations. In the $K_L \to \pi^+\pi^-\pi^0$ sample, both the data
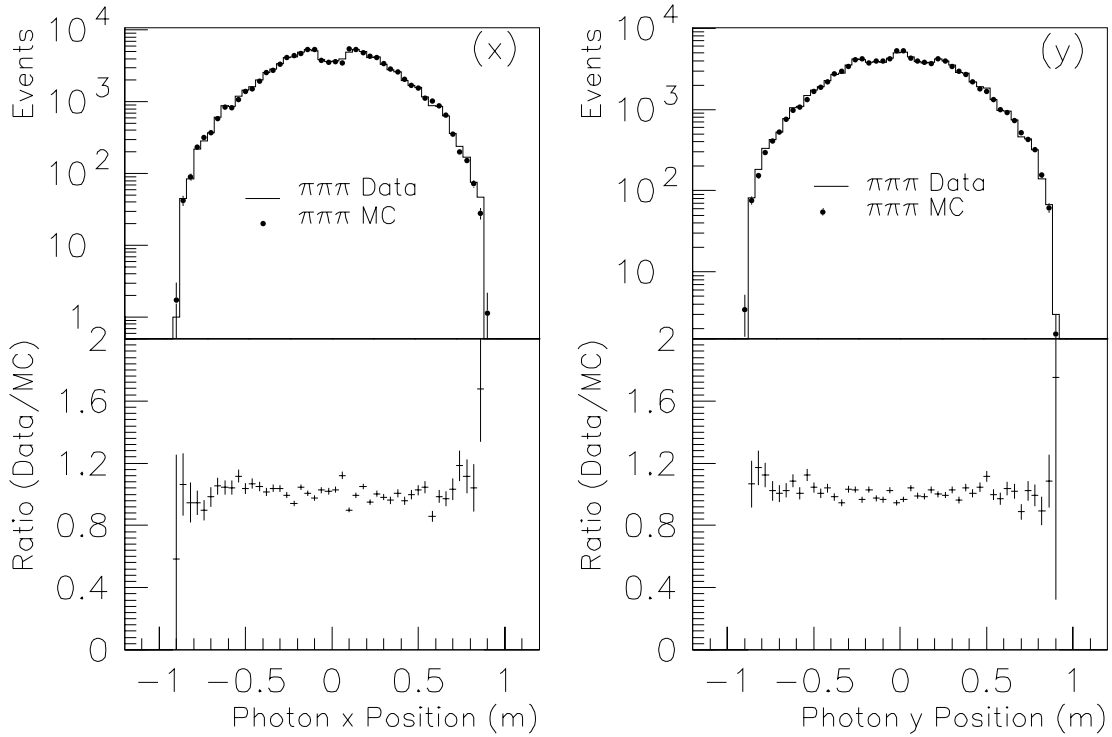
Figure 95. The distributions x and y positions of photons for both $K_L \to \pi^+\pi^-\pi^0$ data and Monte Carlo, and the ratio of the two distributions
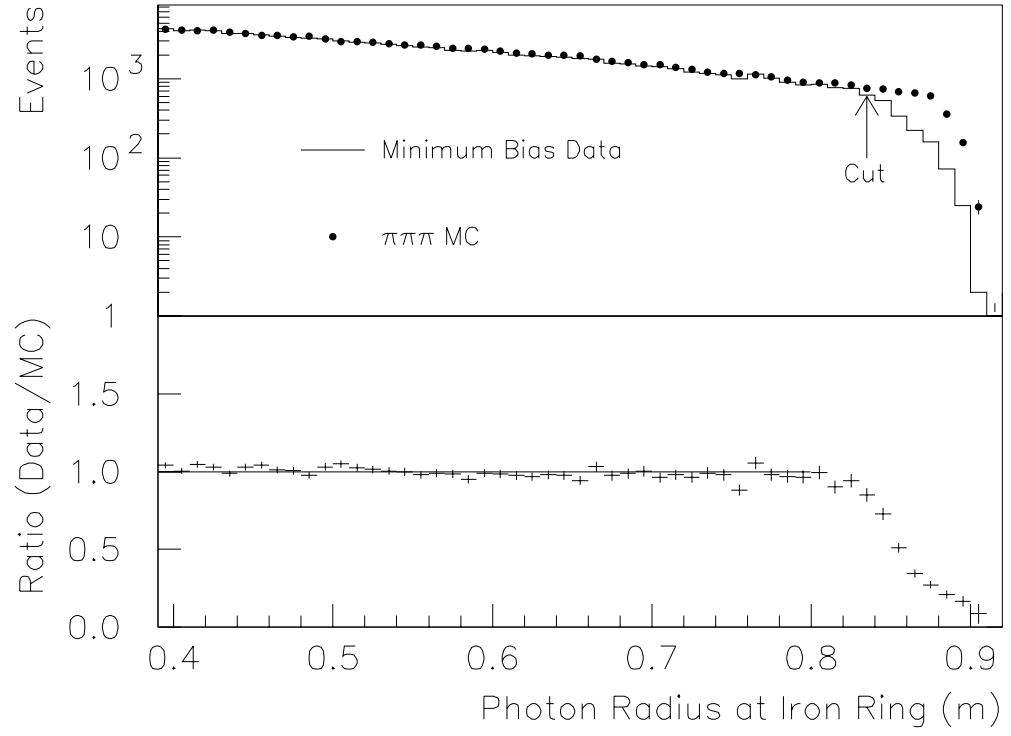
Figure 96. The distributions of the photon radius at the (z) position of the iron ring for both $K_L \to \pi^+\pi^-\pi^0$ data and Monte Carlo

and Monte Carlo distributions agree, while in the $K_L \to \pi^0 \mu^+ \mu^-$ sample there is a clear excess in the data for two tracks entering the pipe blocks.

There was a cut in the $\pi^0 \mu^+ \mu^-$ analysis to remove events in which one of the two tracks in the event went through one of the beam-holes of the calorimeter, and a cut requiring the two muons to extrapolate to the muon trigger plane. Figure 99 shows the understanding of the acceptance as a function of track position for charged pions at the lead-glass. The discrepancy between data and Monte Carlo is small.

### 8.5.3 Trigger Verification Cuts

To reduce the effects of accidental activity on signal acceptance each event was checked to ensure that the charged particles from the drift chamber tracks fired the trigger, and not
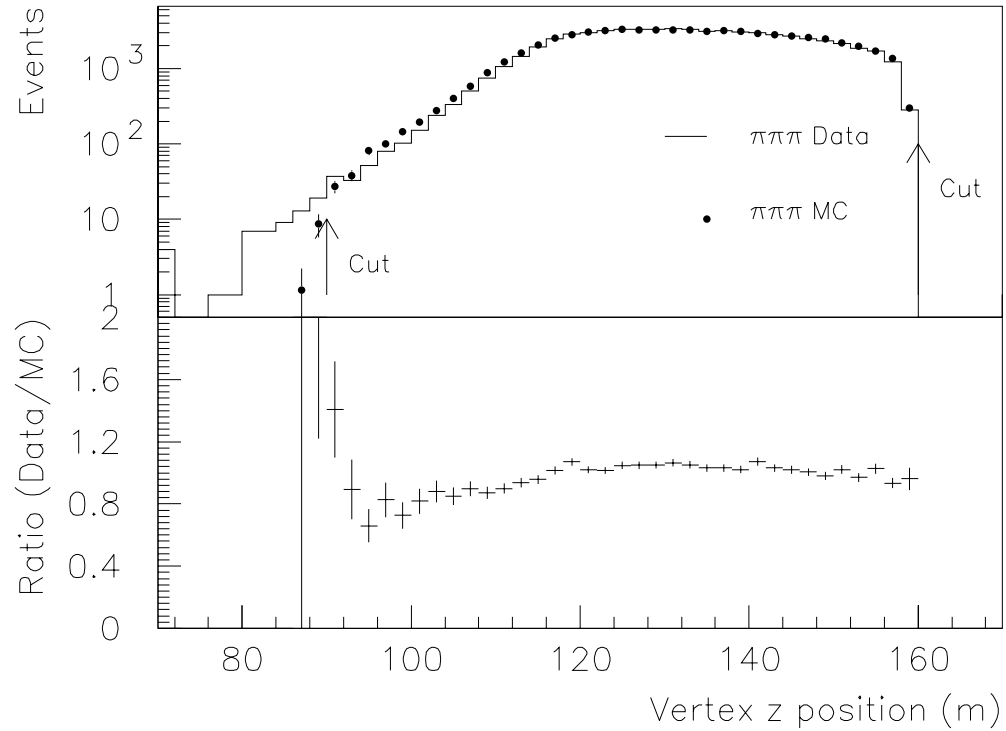


Figure 97. The distributions of the the (z) positions of decays for both $K_L \to \pi^+ \pi^- \pi^0$ data and Monte Carlo. The discrepancy between data and Monte Carlo is most likely due to the fact that no attempt was made to cut away from the beam-pipe apertures.

accidental activity. At least two of the B and C counters that fired had to be the ones to which the charged particles extrapolated. Also, the drift chamber hits from the two charged particle tracks in the event were required to satisfy the track processor trigger.

### 8.5.4   Summary of Cuts

Table 16 is a listing of the cuts that were discussed in this chapter, as well as the cut efficiencies for both data and Monte Carlo events.

## 8.6   Background Processes

Figure 100 shows the distribution of total mass versus $P_t^2$ after the cuts listed in table 16 have been made but before applying any of the background-specific cuts. From this plot it is clear that there are still sizeable backgrounds in both analyses. In table 17 the various decays of the $K_L$ particle are listed and the searches to which they provide backgrounds are indicated.
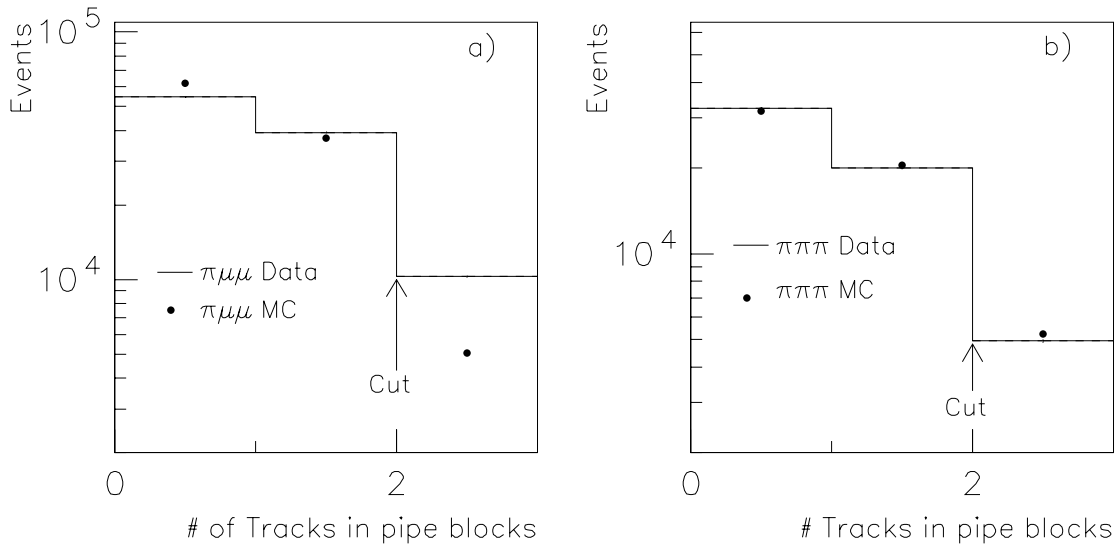


Figure 98. The number of tracks which point to the pipe blocks for both $\pi^0\mu^+\mu^-$ (figure (a)) and $\pi^+\pi^-\pi^0$ (figure (b)) data and Monte Carlo
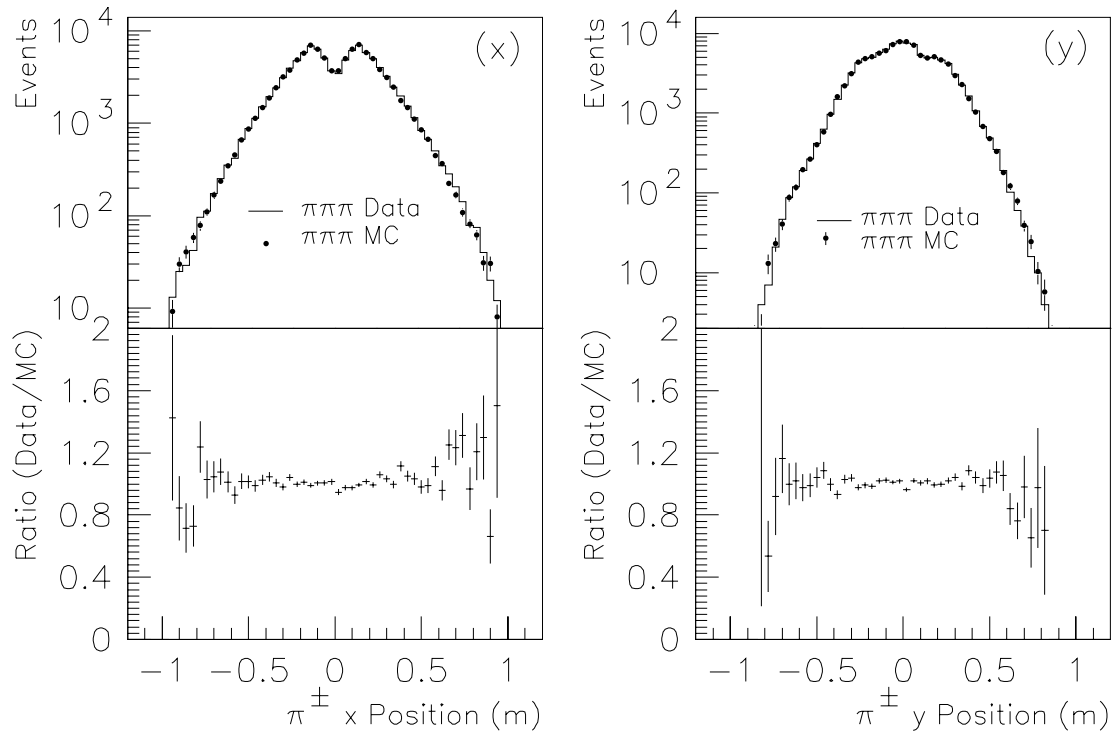
Figure 99. The distributions of the the x and y positions of charged pions for both $K_L \to \pi^+\pi^-\pi^0$ data and Monte Carlo, and the ratio of the two distributions

Table 16. Particle Identification Cuts. The cuts that were made in each of the crunches are indicated

| | $\pi^0 e^+ e^-$ | | $\pi^0 \mu^+ \mu^-$ | | $\pi^+ \pi^- \pi^0$ | |
|---|---|---|---|---|---|---|
| | Fraction Kept | | | | | |
| Cut | Data | MC | Data | MC | Data | MC |
| Number of x and y tracks* (crunch) | .33 | .94 | .69 | 0.93 | .51 | .92 |
| Tracks Matched in x and y*(crunch) | .78 | 1.0 | .95 | 0.99 | .95 | .97 |
| Crunch Level Tracking Cuts | - | - | .88 | - | .88 | - |
| Track and Vertex Quality Cuts | .89 | .99 | .48 | .95 | .85 | .89 |
| Muon Cluster Energy* (crunch) | - | - | .51 | - | - | - |
| Muon Cluster Energy | - | - | .87 | .99 | - | - |
| Muon Block Energy Cut | - | - | .84 | .97 | - | - |
| $\mu$ Momentum$> 7\,GeV/c$ | - | - | .90 | .99 | | |
| $E/p$ for electrons* (crunch) | .42 | .98 | - | - | - | - |
| $E/p$ for electrons* (final) | .53 | .95 | - | - | - | - |
| Number of Photon Clusters (crunch) | - | - | .29 | - | .79 | - |
| Exactly 2 extra clusters | .52 | .99 | .28 | .76 | .82 | .76 |
| Crunch Reduction | .11 | | .083 | | .034 | |
| Track Processor Verified | .999 | .978 | .884 | .970 | .906 | .970 |
| 2B2C Trigger Verified | .942 | .965 | .916 | .957 | .927 | .934 |
| No photons in Inner Block | .719 | .975 | .903 | .981 | .913 | .965 |
| No photons in Iron Ring | .987 | .980 | .985 | .979 | .988 | .972 |
| No tracks near or in beam-hole | .966 | .992 | .576 | .835 | .828 | .849 |
| $90m <$zvertex$< 160m$ | .997 | 1.00 | .999 | .999 | .999 | 1.00 |
| NOT 2 tracks in pipe blocks | - | - | .894 | .950 | .912 | .909 |
| Muon trigger bank extrapolation | - | - | .859 | .959 | .850 | .853 |

Table 17. Possible Backgrounds

| Decay | Branching Ratio | $K_L \to \pi^0 e^+ e^-$ | $K_L \to \pi^0 \mu^+ \mu^-$ |
|---|---|---|---|
| $K_L \to \pi^\pm e^\mp \nu$ | $0.387 \pm 0.005$ | yes | |
| $K_L \to \pi^\pm \mu^\mp \nu$ | $0.270 \pm 0.004$ | | yes |
| $K_L \to \pi^0 \pi^0 \pi^0, \pi^0 \to e^+ e^- \gamma$ | $0.216 \pm 0.008$ | yes | |
| $K_L \to \pi^+ \pi^- \pi^0$ | $0.124 \pm 0.002$ | yes | yes |
| $K_L \to \pi^0 \pi^0, \pi^0 \to e^+ e^- \gamma$ | $(9.09 \pm 0.35) \times 10^{-4}$ | yes | |
| $K_L \to \pi^0 \pi^\pm e^\mp \nu$ | $(6.2 \pm 2.0) \times 10^{-5}$ | yes | |
| $K_L \to e^+ e^- \gamma$ | $(9.1 \pm 0.5) \times 10^{-6}$ | yes | |
| $K_L \to e^+ e^- \gamma \gamma$ | $(6.6 \pm 3.2) \times 10^{-7}$ | yes | |
| $\Lambda \to p^+ \pi^-$ | | | yes |
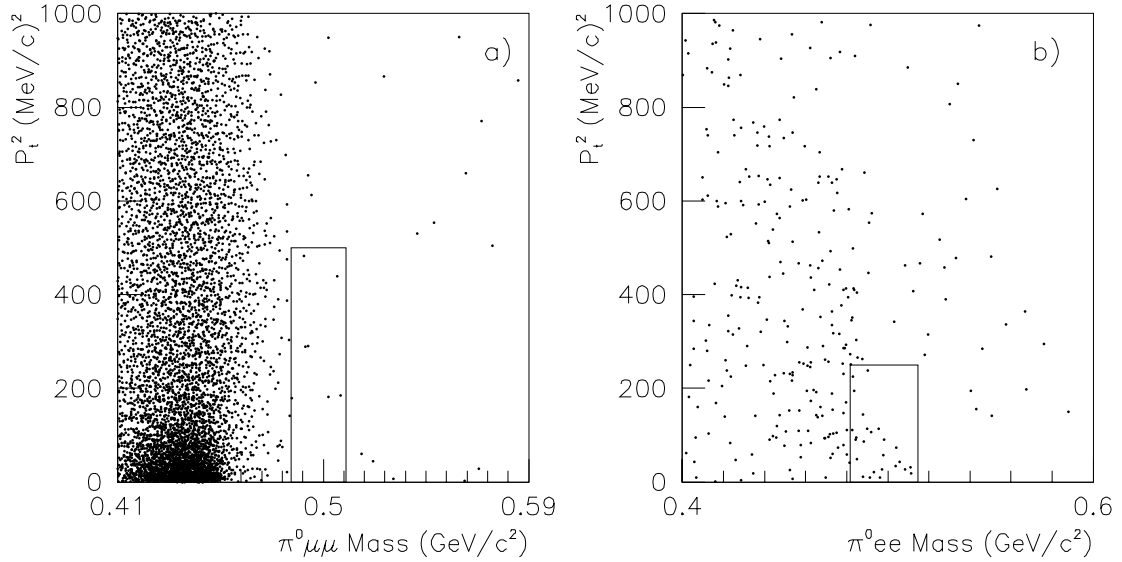


Figure 100. The mass versus $P_t^2$ distributions for both the $\pi^0 e^+ e^-$ (figure (a)) and $\pi^0 \mu^+ \mu^-$ (figure (b)) candidates after detector cuts and the relevant $\pi^0$ mass cut, and the final signal box chosen for each analysis

There are many more backgrounds which are important to the $K_L \to \pi^0 e^+ e^-$ search than are important to the $K_L \to \pi^0 \mu^+ \mu^-$ search. This is because there are more decays with electrons in the final state, and also because the electron/pion discrimination of the detector is significantly worse than the muon/pion discrimination. One might wonder how a two-body final state decay, such as $K_L \to \pi^{\pm} e^{\mp} \nu$ or $\Lambda \to p^+ \pi^-$ could possibly contribute a background to a four-body final state decay. The next section describes how this could (and most emphatically did!) occur.

## 8.7    Beam-Related Activity

Neutrons from the beam could scatter off the collimators, the absorber, or the B and C scintillator banks and shower in active regions of the detector. Muons from other targets upstream of the E799 target could enter the decay volume and satisfy part or all of the muon trigger bank requirement. Photons from another $K_L$ decay (for example, $K_L \to \pi^0 \pi^0 \pi^0$) could arrive in the same bucket as a decay producing two charged particles. Finally, the decay $\Lambda \to p^+ \pi^-$ is also a source of charged particles which could pass either muon or electron identification cuts. In this section we will describe the various ways in which accidental activity introduces backgrounds to the signal decay.

### 8.7.1    Accidental Photon Clusters

When neutrons from the beam scattered and hit the lead-glass, they could produce hadronic showers. The energy deposited in the blocks could then pass all the photon candidate cuts and hence be indistinguishable from real photons from a $K_L$ decay. Most of these neutrons do not arrive at the lead-glass at the same time as the products from the real decay. Furthermore, these neutron-induced showers may have different transverse profiles that electromagnetic showers. Figure 101 shows the distribution of the number of extra HCF-selected clusters in accidental events. 2.6% of the accidental events have two extra clusters which make photon candidates.

The calorimeter illumination is quite different, depending on whether the photons are due to accidental clusters or clusters from real decays. Although in both cases the lead-glass
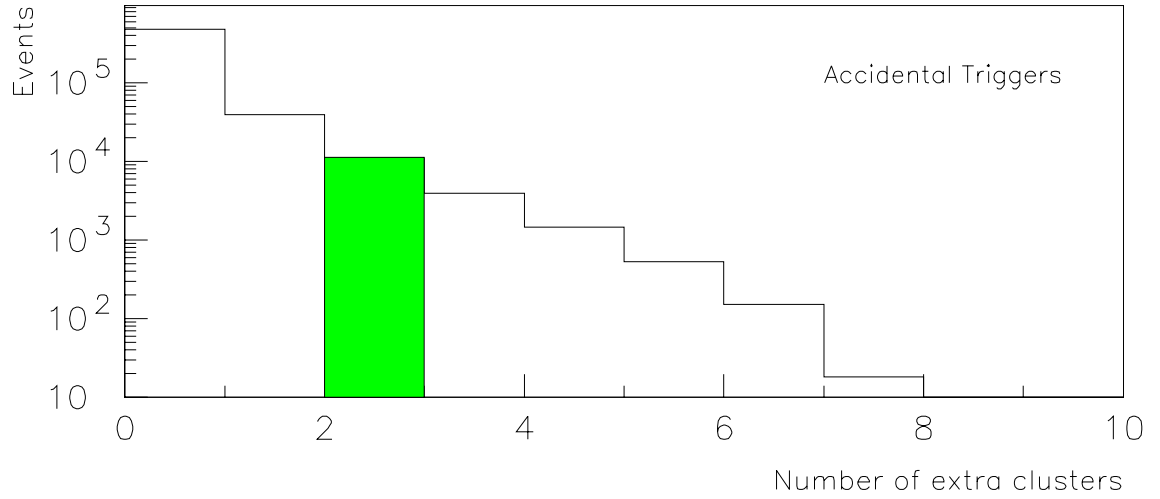
Figure 101. The number of extra clusters in accidental events. The most serious background is due to events with two extra clusters, which are the shaded events in the plot.
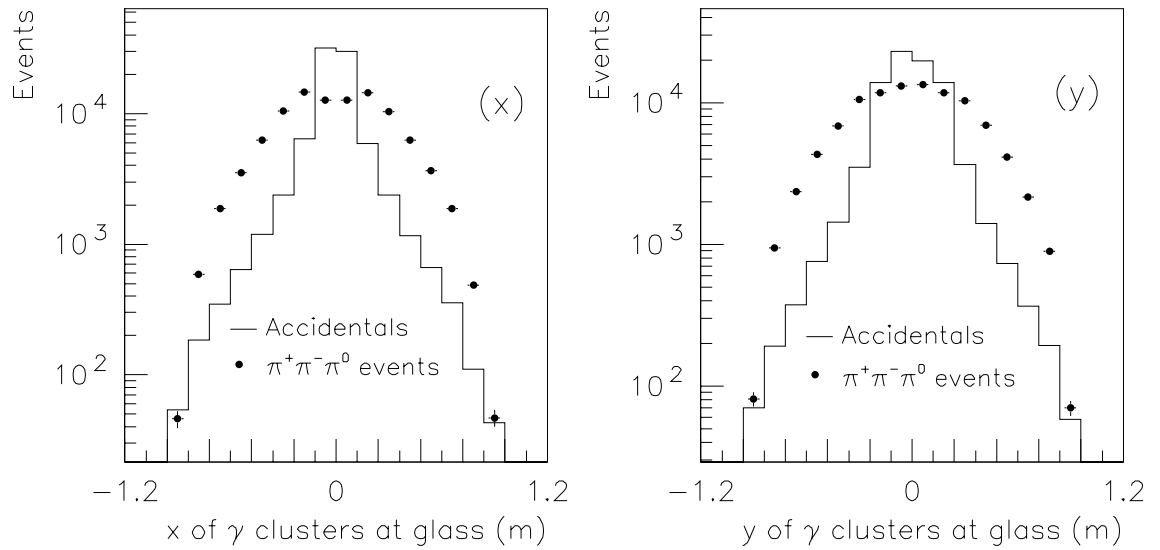


Figure 102. The x and y distributions of extra clusters for both accidental and $\pi^+\pi^-\pi^0$ events.

illumination is peaked in the center of the array, the accidental clusters are much more likely to be close to the beam-holes. Figure 102 shows the (x) and (y) distributions of the extra hardware clusters in both accidental events and verified $K_L \to \pi^+\pi^-\pi^0$ events.

## 8.7.2    Accidental Muon Candidates

About 3% of accidental events have tracks in them which are likely to be muons from the target or beam dump. These tracks do not cause significant background to the search for $K_L \to \pi^0 e^+ e^-$, but can be a problem in the $\pi^0\mu^+\mu^-$ analysis when in coincidence with a proton or pion from lambda decay. Figure 103 shows the distribution of the numbers of tracks for accidental events.   The distribution of lead-glass cluster energy for these tracks shows that they are predominantly muons. Figure 104 shows both the track cluster energy (figure a) and the number of latches in the muon trigger bank (Mu3) which have fired (figure b) for accidental events. 7.3% of the accidental events have one or more Mu3 scintillator counter fired, and 0.6% of accidental events satisfied the dimuon trigger bank requirement.
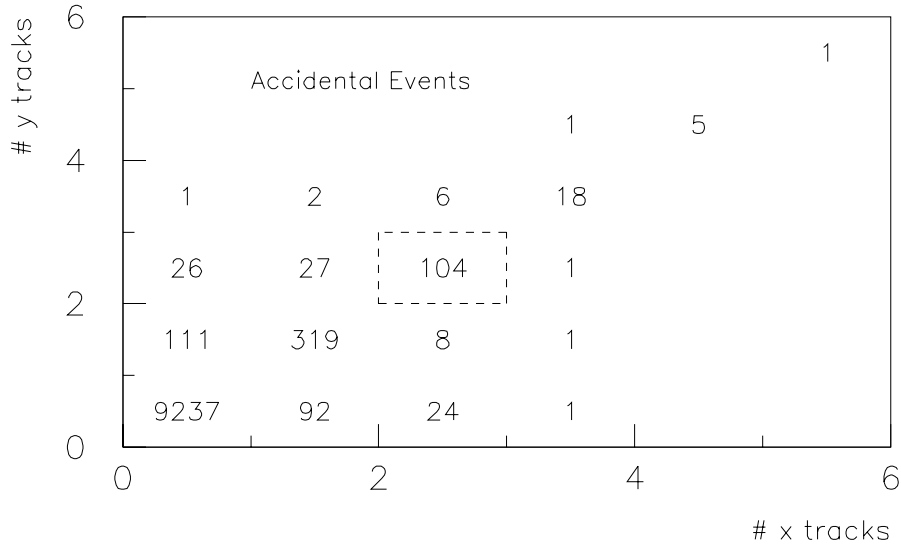


Figure 103.  The number of x view and y view tracks for accidental events, where the distribution is normalized to 10000 events.
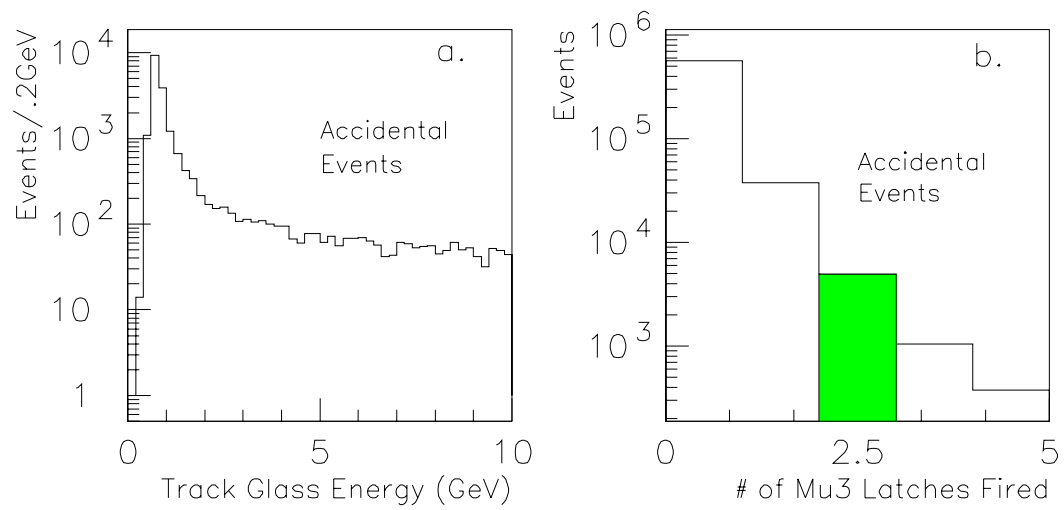
Figure 104. Signs of muons in accidental events: (a.) The track cluster energy distribution (b.) The distribution of the number of MU3 latches fired

## 8.8    Particle Misidentification

Hadrons being misidentified as leptons is another serious source of background for both analyses. When a hadron hits the lead-glass it can either initiate a hadronic shower, or it can pass through as a minimum ionizing particle. The lead glass itself is 1.6 nuclear interaction lengths, so if one assumes the interaction cross section for a high energy charged pion is roughly $\frac{2}{3}$ that of a nucleon, the probability of a hadron passing through without showering in the glass is $\sim 65\%$. The difference between a hadronic shower and the electromagnetic shower, however, is that the energy distributions are very different. This means that the absorption will affect hadronic showers differently from electromagnetic showers. The result is that the calculated energy for hadronic showers can be very different from the actual energy deposited, since the calorimeter was calibrated with electromagnetic showers.

### 8.8.1    Electron-Hadron Discrimination

Because of the large signal that a showering pion can leave in the lead-glass, electron/pion discrimination at trigger level is low. If a pion showers in the glass it often leaves enough energy to make a cluster selected by the hardware cluster finder. From looking at fully reconstructed $\pi^+\pi^-\pi^0$ decays the probability of a pion making a cluster in the glass which will be selected by the HCF is 44%.

As a measure of the overall $2\pi^\pm/2e^\pm$ discrimination at trigger level, the fraction of $K_L \to \pi^+\pi^-\pi^0$ decays from the minimum bias sample which pass the two electron trigger, namely, the pions produce hardware clusters in the glass and do not fire the hadron shower veto or the Back Anti counter, is $5.5 \pm 0.1\%$. Much of that rejection comes from the hadron shower veto, which is on for 77% of the $K_L \to \pi^+\pi^-\pi^0$ decays in the minimum bias sample, and is on for 18% of the accidental triggers.

A more stringent electron identification cut is the requirement that the energy of each cluster associated with a track match the track momentum $(E/p)$. Figure 105 shows the $E/p$ for charged pions from the sample of fully reconstructed $K_L \to \pi^+\pi^-\pi^0$ decays from the minimum bias sample. For pions which have already made an HCF-selected cluster in the lead-glass, the probability of that cluster passing the final $E/p$ cut is 8.4%.
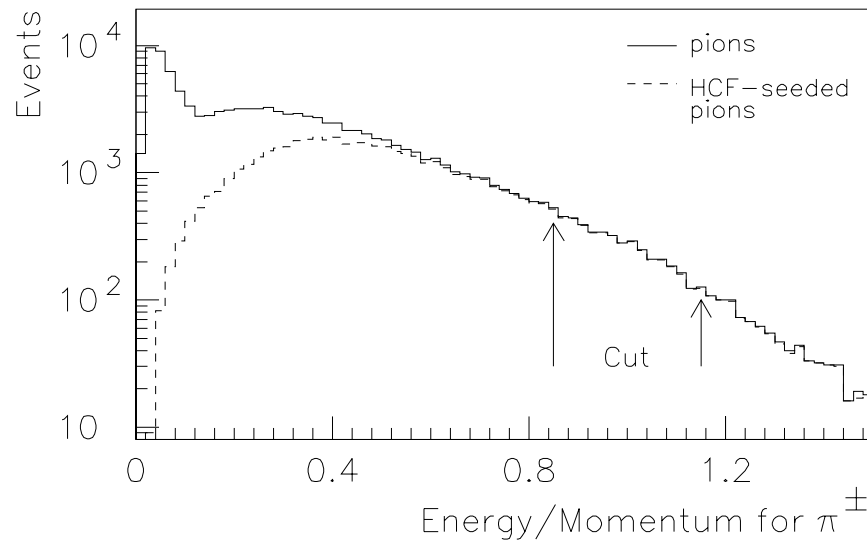
Figure 105. The Cluster Energy/Track Momentum for pions from $K_L \rightarrow \pi^+\pi^-\pi^0$ decays. The distributions shown are for all pions, and for pions which make clusters selected by the HCF

## 8.8.2 Muon-Hadron Discrimination

For the hadrons which do not shower, or shower very late in the glass, there is the possibility that they will leave a little enough energy in the glass to render it indistinguishable from a muon passing through the glass. Figure 106 shows the distribution of cluster energies for pions associated with clusters above $0.5\,GeV$ in the lead-glass. There is also the possibility that the hadron shower would not fire the hadron shower veto, and the products from the hadronic shower in the muon steel could reach the muon trigger bank. Figure 107 shows the extent to which this effect (called "punch through") is a problem. Figure 107 is the distribution of the number of latches in the muon trigger bank for good $K_L \rightarrow \pi^+\pi^-\pi^0$ decays, in both the data and Monte Carlo. The Monte Carlo includes accidental muons but not hadronic shower punch-through. Still another possibility is that a pion will decay to a muon and fire the trigger bank. The pion decay probability is about 3% per pion at typical $K_L \rightarrow \pi^+\pi^-\pi^0$ energies.

From looking at this distribution we set a limit on the probability of muons from hadron
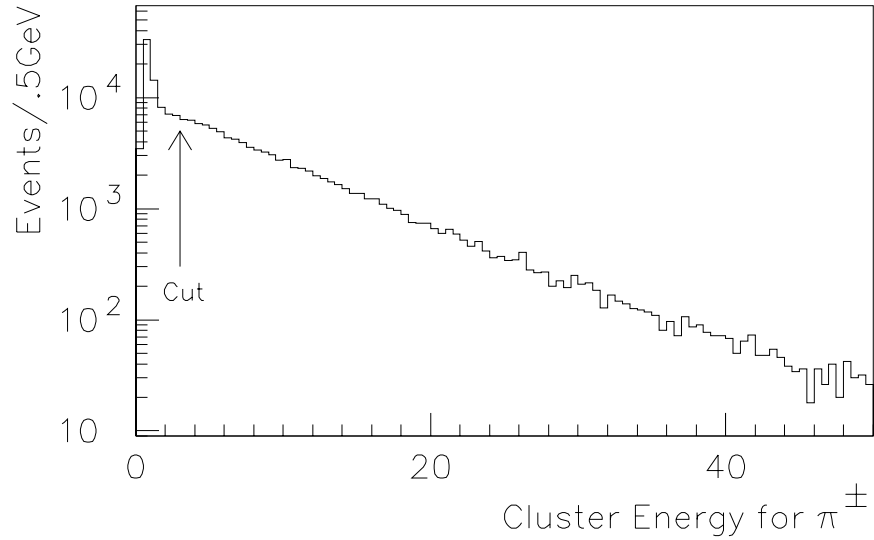


Figure 106. The Cluster Energy for verified charged pions from $K_L \rightarrow \pi^+\pi^-\pi^0$ decays

showers triggering the muon trigger bank. Given the excess above the first bin we determine the probability for punch-through is determined to be $(8.7 \pm 1.3)\%$ per pion.

The fraction of $K_L \to \pi^+\pi^-\pi^0$ events which pass the dimuon trigger is $(0.46 \pm 0.02)\%$, and of those events, only $(3.1 \pm 1.2)\%$ pass the cluster energy cut. Overall the probability of a pion passing both of those cuts is $1.2\%$ per pion.
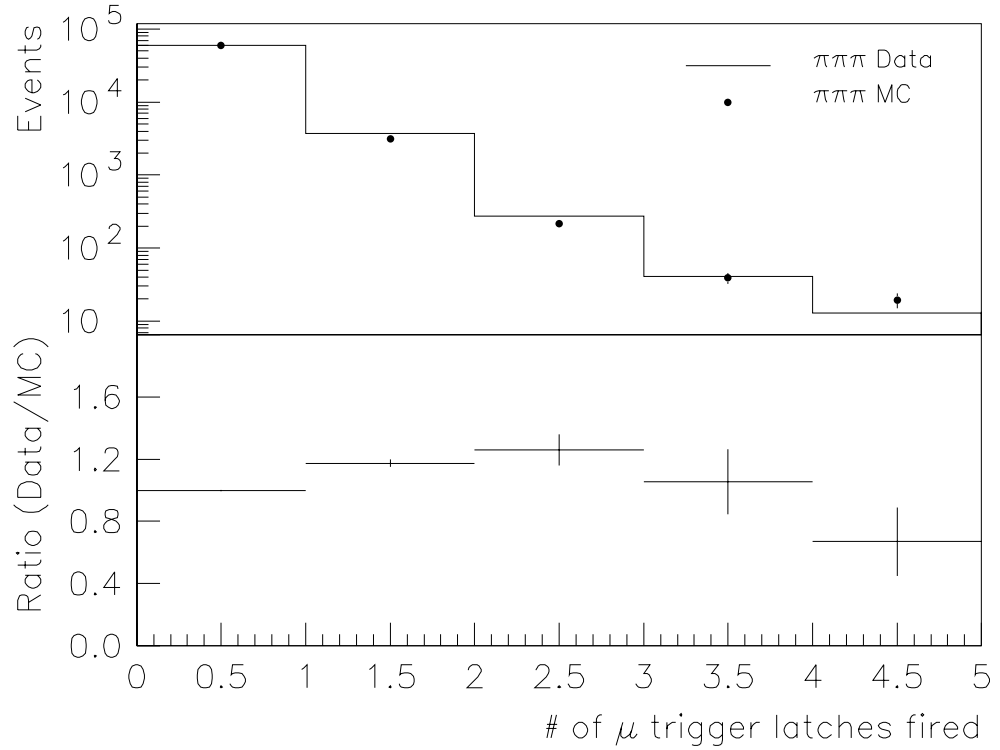


Figure 107. The number of muon trigger bank latches which fired in both data and Monte Carlo for $K_L \to \pi^+\pi^-\pi^0$ decays

# CHAPTER 9

# BACKGROUNDS TO $K_L \to \pi^0 e^+ e^-$

## 9.1 Introduction

After all of the cuts in the previous chapter were made on the data set there were still substantial backgrounds to the $K_L \to \pi^0 e^+ e^-$ search. The high flux of $K_L$'s and the large amount of accidental activity result in backgrounds which threaten to swamp the signal region. This chapter describes the most important backgrounds to the search for the decay $K_L \to \pi^0 e^+ e^-$ and how each background is removed in the analysis. The final section compares the expected number of events in the data to the predicted background level.

## 9.2 Remaining Backgrounds

Although there are many $K_L$ process which may satisfy the $\pi^0 e^+ e^-$ trigger and get written to tape, there are only a few which can be reconstructed as real $\pi^0 e^+ e^-$ decays. In this section only those decays which can result in reconstructed masses within $100\,MeV$ of the $K_L$ mass will be discussed.

### $K_L \to \pi^+ \pi^- \pi^0$ Background

After making the cuts described in the previous chapter, the decay which accounts for much of the remaining data is the $K_L \to \pi^+ \pi^- \pi^0$ decay. The possibility of misidentifying a pion as an electron is large enough that given the enormous branching ratio of the decay $K_L \to \pi^+ \pi^- \pi^0$ the vast majority of events with real $\pi^0$'s in them were of this type.

$K_L \rightarrow \pi^0 \pi^0$

Although this decay occurs at a very low level, namely $(9.09 \pm 0.35) \times 10^{-4}$, it can give rise to two possible sources of background. The first such source occurs when one of the $\pi^0$'s decays to $e^+ e^-$, in which case the final state particles are the same and the two photons come from a neutral $\pi^0$ decay. The branching ratio for $\pi^0 \rightarrow e^+ e^-$, which was measured by E799 and described in great detail in [1], is

$$BR(\pi^0 \rightarrow e^+ e^-, (\frac{m_{ee}}{m_{\pi^0}})^2 > 0.95) = (7.6^{+3.9}_{-2.8}(stat) \pm 0.5(syst)) \times 10^{-8},$$

and therefore this process becomes important at the $1.4 \times 10^{-10}$ level. For this analysis a background at this level was unobservable, but at the standard model levels of $10^{-12}$ this background will need to be removed by an $e^+ e^-$ invariant mass cut above the $\pi^0$ mass.

A more relevant $\pi^0$ decay which contributed a significant background in this search is the decay $\pi^0 \rightarrow e^+ e^- \gamma$, which occurs with a branching ratio of 1.20%. Given this branching ratio and the fact that there are two neutral pions in the decay the overall branching ratio for this process is $2.15 \times 10^{-5}$. To understand this background and to decide the best method to remove it a $K_L \rightarrow \pi^0 \pi^0$, $\pi^0 \rightarrow e^+ e^- \gamma$ Monte Carlo Simulation was used. There are several ways that the decay $K_L \rightarrow \pi^0 \pi^0$, $\pi^0 \rightarrow e^+ e^- \gamma$ can fake a $K_L \rightarrow \pi^0 e^+ e^-$ decay: an extra photon can be lost, an extra photon can be emitted which is so low in energy that it will not fire the online hardware cluster finder, or one of the photons in the decay can arrive too close to another photon or electron to be distinguished as a separate cluster. If a photon overlaps at the glass with another shower in the decay, the total $K_L$ mass and $P_t^2$ will be preserved and the event is likely to pass the corresponding cuts on those variables.

$K_L \rightarrow e^+ e^- \gamma$

The decay $K_L \rightarrow e^+ e^- \gamma$ contributes a background in a variety of ways, which are distinguished by the source of the extra photon which must accompany the decay. This extra photon can come about through the process of bremsstrahlung, or it can simply be due to an accidental cluster of energy in the lead-glass. In the case of bremsstrahlung photons, the process can either take place internally, in the actual decay, or externally, namely, in the detector. The internal Bremsstrahlung process is described in section 7.1.2. As is the

case with the decay $K_L \to \pi^0 \pi^0$, $\pi^0 \to e^+ e^- \gamma$ where two photons overlap at the lead-glass such that all the final state particles are measured, when a $K_L$ Dalitz decay is accompanied by a bremsstrahlung photon the total $K_L$ mass and $P_t^2$ are likely to be preserved, and will appear in the signal region. On the other hand, if a $K_L$ Dalitz decay is accompanied by a photon from accidental activity, the extra energy in the photon is likely to push the total invariant mass of the event to be higher than the nominal $K_L$ mass.

$$K_L \to \pi^\pm e^\mp \nu + \gamma\gamma$$

The most significant background by far in the search for $K_L \to \pi^0 e^+ e^-$ is the $K_{e3}$ decay accompanied by two extra photons. As in the case for the $K_L$ Dalitz decay background, the extra photons can be due to either bremsstrahlung or accidental activity, or a combination of the two. Yet another possible source of photon candidates is isolated clusters of energy resulting from the charged pion showering in the lead-glass. The background from this decay is roughly flat over the mass and $P_t^2$ region of interest.

## 9.3 Total Mass and $P_t^2$ cuts

There are many decays which can be selected by the trigger but are completely irrelevant to the search because they reconstruct to have total masses well below that of the $K_L$ mass. The only decays relevant to this analysis are those which have a total invariant $e^+ e^- \gamma\gamma$ mass near the $K_L$ mass. By removing events with invariant masses more than $100\,MeV/c^2$ away from the nominal $K_L$ mass, as well as those events with a higher $P_t^2$ than $5000\,(MeV/c)^2$, 95% of the data is rejected, while 95% of the $\pi^0 e^+ e^-$ Monte Carlo acceptance is retained. These cuts can be compared with the final mass and $P_t^2$ cuts of $\pm 16.5\,MeV/c^2$ and $250\,(MeV/c)^2$, respectively. Figure 108 shows the $e^+ e^- \gamma\gamma$ mass distribution for all the events surviving the two-electron crunch, and the loose cuts that are made before proceeding with the rest of the analysis.

## 9.4 Particle Identification Cuts

To maximize the particle identification capabilities of the lead-glass calorimeter, there were tight cuts made on the clusters of energy in the calorimeter. Although these cuts resulted in decrease of acceptance for the signal mode, they were critical for removing backgrounds from hadronic events or fused photons.

### 9.4.1 Fusion Cuts

In general, electromagnetic showers in the lead-glass calorimeter tend to be much more collimated than hadronic showers. By cutting on the transverse profile of the clusters in the lead-glass one can remove a large fraction of hadronic showers which contaminate the $\pi^0 e^+ e^-$ data. There are three cuts made on the transverse shower profile, based on three different parameters describing of the energy distribution. These cuts were originally designed to remove events with fused clusters, or clusters too close together to be distinguishable.
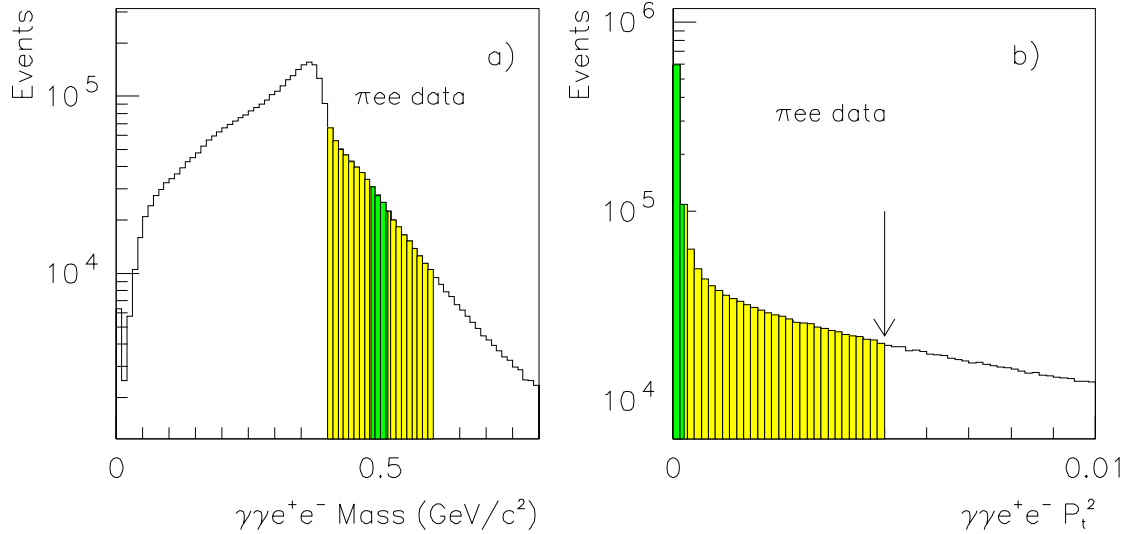


Figure 108. The $e^+ e^- \gamma\gamma$ mass and $P_t^2$ for all events surviving the two-electron crunch. The lightly shaded areas show the first loose cuts, and the darker areas show the final tight analysis cuts. The large shoulder in the mass and the peak at low $P_t^2$ are both due to the presence of $K_L \rightarrow \pi^+ \pi^- \pi^0$ decays.

The simplest way to categorize these categories are by the kind of fusions they are designed to remove. The categories are: side fusions, corner fusions, and fusions resulting from clusters in the next ring of blocks outside the $3 \times 3$ array. Figure 109 shows the variables used for these cuts.

To remove events with low energy clusters less than three blocks away from existing clusters, the analysis checks the 16 blocks which constitute the $5 \times 5$ ring outside of the nominal $3 \times 3$ ring of a cluster (figure 109). Of those 16 blocks, the side-fusion cut sums the energies in two adjacent blocks which were below the HCF threshold. If that sum is greater than $0.8\,GeV$ then the event is rejected. This is the first fusion cut made and is the most powerful cut for removing hadronic showers.

The next two fusion cuts are made on the distribution of energy within the $3 \times 3$ array

| x | x | x | x | x |
|---|---|---|---|---|
| x | a | b | c | x |
| x | d | e | f | x |
| x | g | h | i | x |
| x | x | x | x | x |

Total Cluster Energy:E
E=a+b+c+d+e+f+g+h+i
Central Block of Cluster: e

Side Fusion:
Maximum sum of
2 adjacent x blocks

Row or Column Fusion:
(a+b+c)/E and (g+h+i)/E
(a+d+g)/E and (c+f+i)/E

Corner Fusion:
d/a,b/a,b/c,f/c,etc.

Figure 109. The variables which are used in determining if a given cluster is actually fused with another

of the cluster. The first aspect of the cluster profile that is checked is the ratio of energies of the columns and rows of a given cluster. The column and row ratios are the same as those used in the position algorithm (and are described in figure 33) for the lead-glass. Although only the larger of the two ratios is used to determine the cluster position, there is a fusion cut which checks the smaller of the two ratios as well. If the smaller ratio is too large to be consistent with a shower in the position determined by the larger ratio, the event is rejected. Finally, if the energy in one of the corners of the $3 \times 3$ array is more than twice that of one of the neighboring blocks in the array (see figure 109), then the event is rejected.

As a measure of how well these cuts remove events due to accidental photon candidates, figure 110a shows the rejection for the various fusion cuts for three different samples of data: the $K_L \to \pi^0 e^+ e^-$ candidates in the data after the events consistent with $K_L \to \pi^+ \pi^- \pi^0$ decays have been removed, the $K_L \to \pi^0 e^+ e^-$ Monte Carlo simulation, and finally, the extra clusters which have been selected by the HCF in the accidental trigger. The fusion cuts keep only 53% of the photon candidate clusters in both the $\pi^0 e^+ e^-$ data and the accidental data, while keeping 85% of the $\pi^0 \pi^0$, $\pi^0 \to e^+ e^- \gamma$ background Monte Carlo events and 92% of the $\pi^0 e^+ e^-$ Monte Carlo clusters. The fact that the rejection factors are about the same between the real data and the accidental data indicates that the most likely source of extra photon candidates is indeed accidental activity, and is primarily hadronic in nature. Figure 110b shows the rejection of the fusion cuts for a well-simulated high-statistics decay, namely $K_L \to \pi^0 \pi^0 \pi^0$, $\pi^0 \to e^+ e^- \gamma$. The signal efficiency of each fusion cut is higher in the Monte Carlo than in the data, but the overall discrepancy is on the order of 5% [1]. This is due to misunderstanding in the radiation damage modeling, in particular in the highly damaged blocks near the center of the lead-glass array. The discrepancy is less important for photons from $\pi^0 e^+ e^-$ decay because they are less likely to be in the center of the array where blocks were the most damaged.

## 9.4.2 Adder Energy Cuts

A cut was made to remove events with in-time clusters which were too low to be selected by the HCF but were consistent with being from the parent $K_L$ decay because they arrived simultaneously with the higher energy clusters. To find these kinds of events all the energies

in the blocks corresponding to each Adder are summed, not including the Adders which are associated with the $3 \times 3$ array of the above-threshold clusters in the event. The in-time requirement is made by only considering Adders for which the amount of energy in the glass blocks ADC's (which have a gate of $100\,nsec$) is within $40\%$ of the energy in the Adder (which has a gate of $30\,nsec$). The number of ADC counts in these Adders is required to be less than 120 counts. This corresponds to an energy cut of approximately $0.8\,GeV$, or more if the blocks were in the center in the array where the gains were lower. This cut was most effective for removing events where there was either a low energy bremsstrahlung photon or an extra photon, say, from a $K_L \to \pi^0\pi^0$, $\pi^0 \to e^+e^-\gamma$ decay where one of the photons was below the HCF threshold.
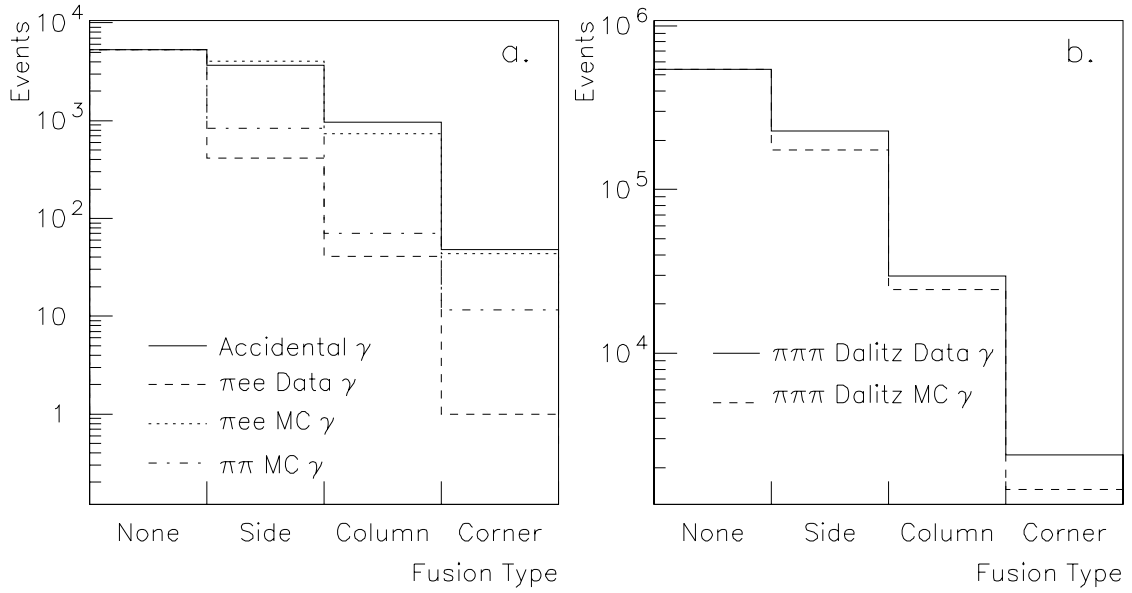


Figure 110. a. The fusion cut efficiencies for the photon clusters in three different data samples: $K_L \to \pi^0 e^+ e^-$ data, Monte Carlo, $K_L \to \pi^0\pi^0$, $\pi^0 \to e^+e^-\gamma$ background Monte Carlo, and accidental triggers. b. The fusion cut efficiencies for the photon clusters in $\pi^0\pi^0\pi^0$, $\pi^0 \to e^+e^-\gamma$ events in both the data and Monte Carlo. All distributions in each plot are normalized to the first bin.

## 9.5 $K_L \to \pi^0 e^+ e^-$ Background Cuts

There are four cuts made on the $K_L \to \pi^0 e^+ e^-$ sample which were specifically designed to remove the backgrounds listed in section 9.2. Since some cuts remove more than one background, these backgrounds will be listed with each cut.

### 9.5.1 $K_L \to \pi^+ \pi^- \pi^0$ Invariant Mass Cut

Figure 111 shows the invariant mass of the event with the assumption that the tracks are due to charged pions for both the $K_L \to \pi^0 e^+ e^-$ data and Monte Carlo. Since this cut was made before the cut on $M_{\gamma\gamma}$, the photon energies were not constrained before the total $\pi^+ \pi^- \pi^0$ mass of the event was computed. A cut is made in the $K_L \to \pi^0 e^+ e^-$ analysis to remove events whose reconstructed invariant $\pi^+ \pi^- \pi^0$ mass is within $60\,MeV$ of the $K_L$ mass. This cut removes about 1% of the $K_L \to \pi^0 e^+ e^-$ signal acceptance, 22% of the $\pi^0 e^+ e^-$ data, and safely eliminates any $\pi^+ \pi^- \pi^0$ background.
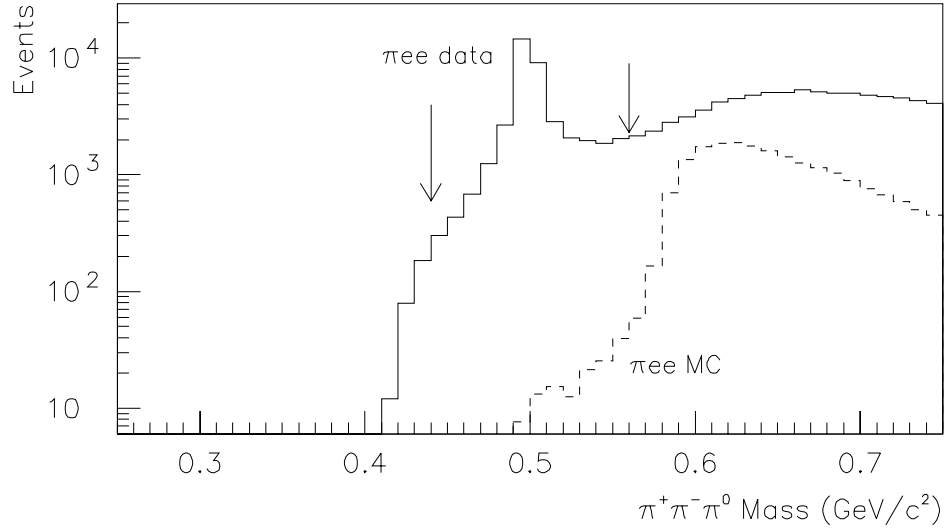


Figure 111. The $\pi^+ \pi^- \pi^0$ invariant mass distribution for both $\pi^0 e^+ e^-$ candidates in the data and the $\pi^0 e^+ e^-$ Monte Carlo. The arrows indicate the cut made in the analysis.

### 9.5.2 Electron Pair Invariant Mass Cut

To remove backgrounds from photon conversions and Dalitz decays of either the $K_L$ or the $\pi^0$, a cut was made on invariant $e^+e^-$ mass ($M_{e^+e^-}$) in the event. In Dalitz decays the $M_{e^+e^-}$ spectrum is steeply falling, and of course for $e^+e^-$ pairs resulting from photon conversions $M_{e^+e^-}$ is near zero. Figure 112 shows the $M_{e^+e^-}$ distribution for both $K_L \to \pi^0\pi^0$, $\pi^0 \to e^+e^-\gamma$ background and $K_L \to e^+e^-\gamma$ background, the prediction of the spectrum for the data events (absolutely normalized). The data events, are dominated by the $K_L \to \pi^\pm e^\mp \nu$ decays at high $M_{e^+e^-}$ and are also shown in figure 112. Finally, the $M_{e^+e^-}$ distribution for the $K_L \to \pi^0 e^+e^-$ Monte Carlo is shown, where a flat phase space Monte Carlo was used. Different decay models may produce different $M_{e^+e^-}$ distributions, as is described in section 11.3.5.

### 9.5.3 Bremsstrahlung Cut

Since Bremsstrahlung photons are emitted preferentially along the direction of flight of the electron [18], one can check to see if real photons in the decay are consistent with being Bremsstrahlung photons emitted upstream of the magnet. This is done by comparing the extrapolated position at the glass of a track upstream of the magnet, and the position of real photons in the event. Figure 113 shows a schematic picture of an electron emitting a bremsstrahlung photon before bending at the plane of the magnet. The "brem distance" is defined as the minimum distance between a real photon in the decay and the extrapolated position of an upstream track. If the "brem distance" of an event is less than one lead-glass block width ($5.82\,cm$), the event is rejected. Figure 114 shows the distribution of this variable for the background Monte Carlos, the $K_L \to \pi^0 e^+e^-$ candidates, and the $K_L \to \pi^0 e^+e^-$ Monte Carlo. The $K_L \to e^+e^-\gamma$ background prediction is absolutely normalized, and the $K_L \to \pi^\pm e^\mp \nu$ background prediction is normalized to the $P_t^2$ sidebands. The cut at one block width is also shown on the plots. While this cut gets rid of 33% of the $K_L \to e^+e^-\gamma$ background and 19% of the $K_L \to \pi^\pm e^\mp \nu$ background, it only removes 2.2% of the $K_L \to \pi^0 e^+e^-$ signal Monte Carlo.
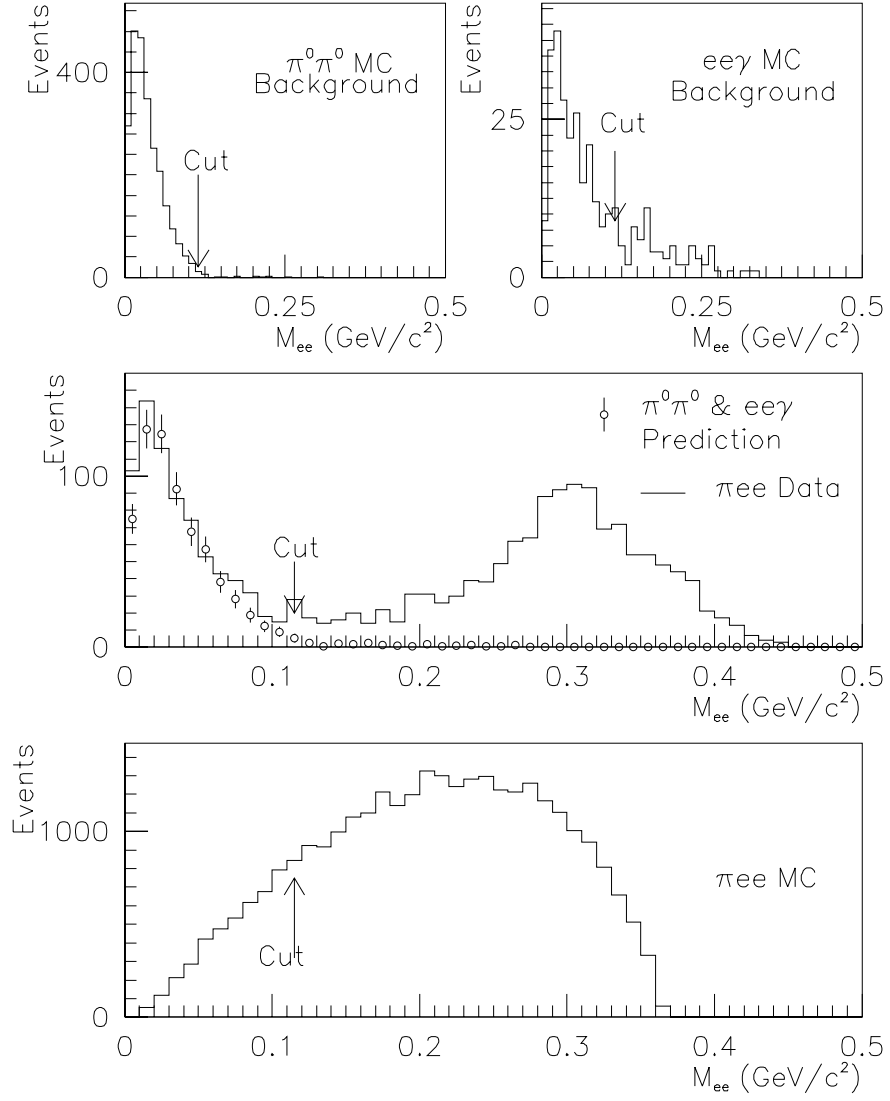
Figure 112. The $M_{e^+e^-}$ distributions for $\pi^0\pi^0$, $\pi^0 \to e^+e^-\gamma$ and $K_L \to e^+e^-\gamma$ background Monte Carlo, the distribution in the data, the prediction in the Monte Carlo, and finally the $M_{e^+e^-}$ distribution for the $K_L \to \pi^0 e^+e^-$ Monte Carlo.
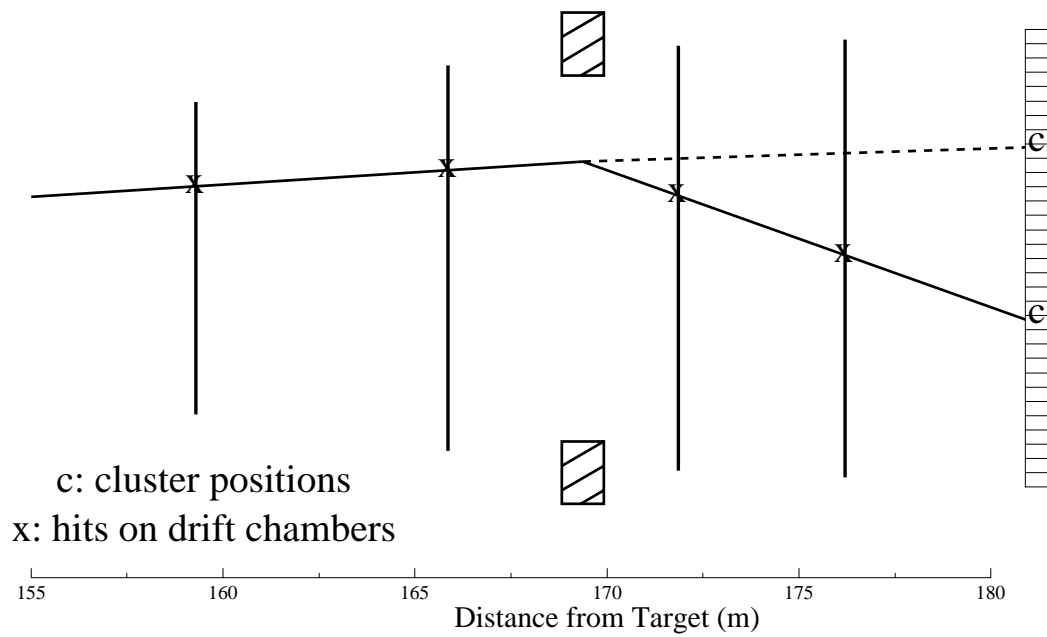
Figure 113. An example of an electron emitting a Bremsstrahlung photon before bending at the plane of the magnet.
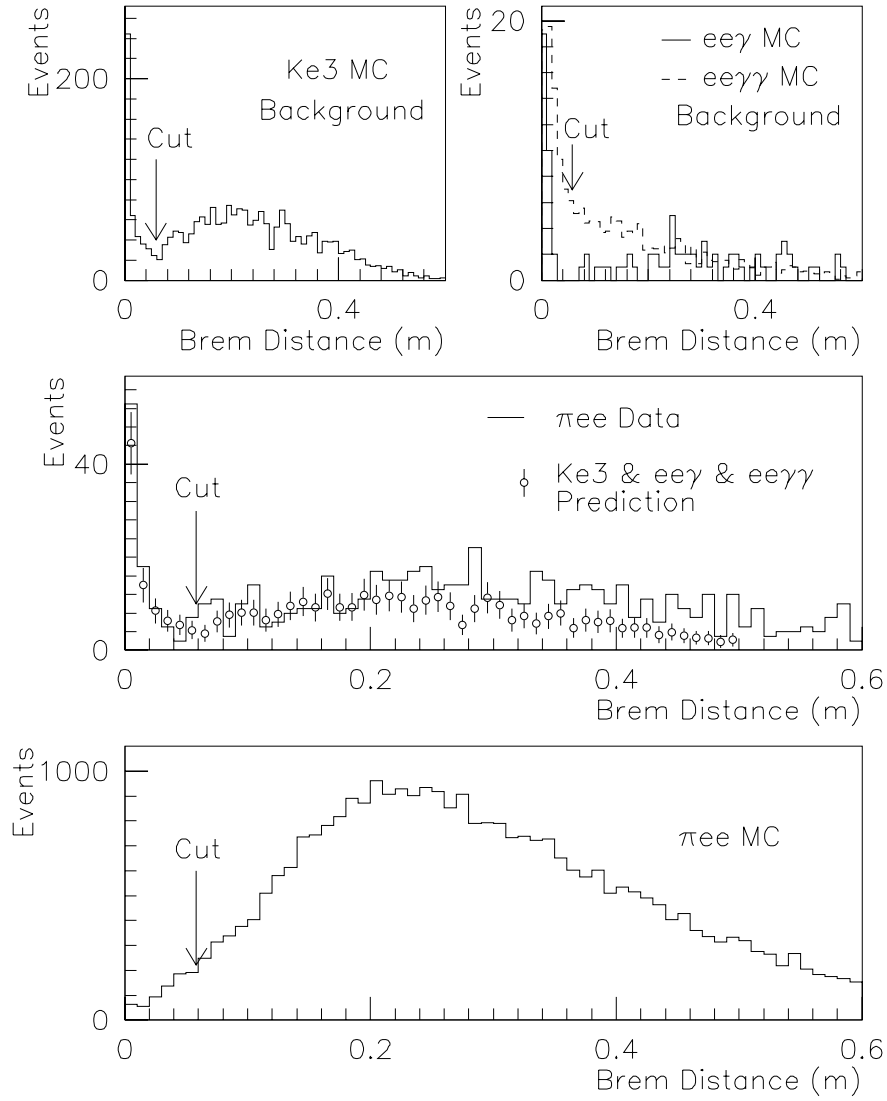
Figure 114. The Brem distance contribution for four samples: $K_L \to e^+e^-\gamma$ background Monte Carlo, $K_L \to \pi^\pm e^\mp \nu$ background Monte Carlo, $K_L \to \pi^0 e^+e^-$ candidates, and $K_L \to \pi^0 e^+e^-$ Monte Carlo.

### 9.5.4   Product of sums of cosines

Due to the high rate of accidental activity in the detector, $K_{e3}$ decays contributed significantly more background to this search than to previous searches using this detector, and a new strategy for removing them was necessary. To remove decays in coincidence with two accidental photons, the analysis took advantage of the fact that accidental photons tend to be near the beam-holes of the lead-glass, and thus do not contribute much transverse momentum to the decay. In order for a $K_{e3}$ decay to pass the transverse momentum cut, the $\pi e$ pair has to have low transverse momentum as well; in other words, the $\pi e$ pair contains most of the parent $K_L$ energy and the $\nu$ carries off almost none. As a result, the pion and electron are emitted preferentially back-to-back in the $K_L$ rest frame.

This configuration implies a very specific relation among the angles between a photon in the decay and each charged particle. For each photon we define a quantity $\Sigma_{cos}^i$:

$$\Sigma_{cos}^i \equiv cos\alpha^i + cos\beta^i$$

where $\alpha^i$ and $\beta^i$ are the angles between the $i^{th}$ photon and each electron candidate in the center-of-mass frame of that photon and the two electron candidates. Figure 115 shows two different $e^+e^-$ pair-photon configurations, one where the two tracks are almost back-to-back, as in a $K_{e3}$ decay with an accidental photon, and one where the two tracks have a small opening angle, as in a Dalitz-type decay. For $K_{e3}$ decays where the electron and pion are back-to-back $\Sigma_{cos}^i$ is near 0. For decays where the tracks have a small opening angle, i.e. Dalitz decays, $\Sigma_{cos}^i$ is near $-2$.

To illustrate the distributions of this variable: in the case where there is only one photon in the decay, consider the problem of removing a $K_{e3}$ background from a sample of Dalitz decays. In this case the $K_{e3}$ background arises from the presence of only one accidental photon in coincidence with a $K_{e3}$ decay. Figure 116 shows the distribution of this variable for both $K_L \rightarrow e^+e^-\gamma$ and $K_L \rightarrow \pi^\pm e^\mp \nu$ Monte Carlo, and then the prediction from both of these Monte Carlos and the actual distribution in the data. In the search for normalization events of the type $K_L \rightarrow e^+e^-\gamma$, there was a cut requiring $cos\alpha + \cos\beta$ to be less than $-0.5$. This removes 92% of the $K_L \rightarrow \pi^\pm e^\mp \nu$ background, while only removing 4% of the $K_L \rightarrow e^+e^-\gamma$ acceptance.
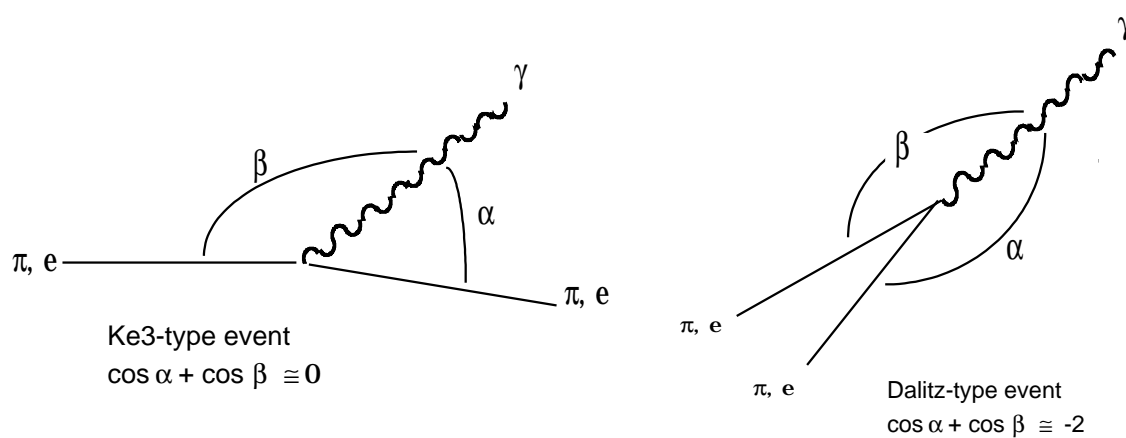
Figure 115. Two different configurations in the center of mass of two tracks and one photon in an event: a "$K_{e3}$ configuration", and a "Dalitz configuration"
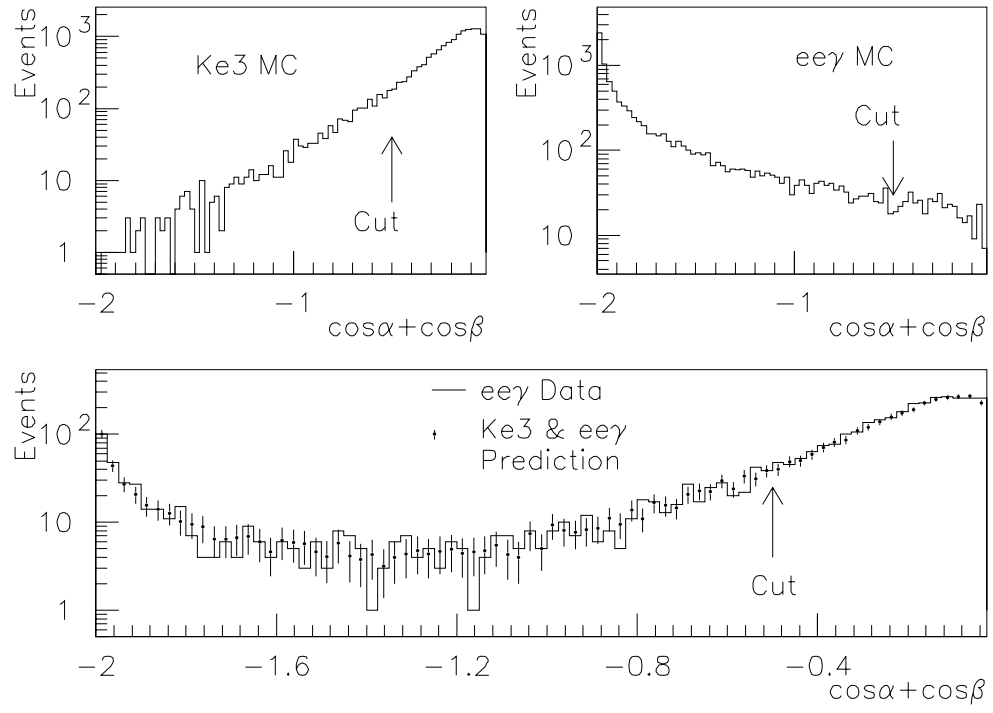
Figure 116. The $\cos\alpha + \cos\beta$ distributions for both $K_L \to e^+e^-\gamma$ and $K_L \to \pi^\pm e^\mp \nu$ Monte Carlos, and the distribution actually found in the data with the background MC predictions added.

In the case where one is looking for the decay $K_L \rightarrow \pi^0 e^+ e^-$, since there are two photons in the decay, one wants to remove backgrounds where both $\Sigma_{cos}^i$'s are small. Thus, the product $\Sigma_{cos}^1 \times \Sigma_{cos}^2$ is required to be above 0.05. This cut, when made after the bremsstrahlung cut, decreases the $K_L \rightarrow \pi^0 e^+ e^-$ acceptance by 15% while removing 35% of the remaining $K_{e3}$ background. Figure 117 shows $\Sigma_{cos}^1 \times \Sigma_{cos}^2$ for the $K_{e3}$ and $\pi^0 \pi^0$, $\pi^0 \rightarrow e^+ e^- \gamma$ Monte Carlos, the data, and finally the $K_L \rightarrow \pi^0 e^+ e^-$ Monte Carlo. The $\pi^0 \pi^0$, $\pi^0 \rightarrow e^+ e^- \gamma$ Monte Carlo is absolutely normalized, and the $K_{e3}$ Monte Carlo is normalized using sidebands in the transverse momentum squared ($P_t^2$). The peak in the data at $\Sigma_{cos}^1 \times \Sigma_{cos}^2 = 4$ signals the presence of $K_L \rightarrow \pi^0 \pi_D^0$ events, which are removed by the cut on $M_{ee}$. The $K_{e3}$ decays, which dominate the data, have a low $\Sigma_{cos}^1 \times \Sigma_{cos}^2$, and the $K_L \rightarrow \pi^0 e^+ e^-$ decays populate a broader region of the allowed range.

## 9.6    Efficiencies of $K_L \rightarrow \pi^0 e^+ e^-$ Analysis Cuts

Table 18 is a listing of the analysis cuts listed above, and the efficiencies for the signal, the various backgrounds, and the data sample itself. Since hadronic showers are not simulated in the Monte Carlo, the efficiencies of some of the cuts on the $K_L \rightarrow \pi^{\pm} e^{\mp} \nu$ acceptance have been estimated by studying pions from $K_L \rightarrow \pi^+ \pi^- \pi^0$ decays in the data.

## 9.7    Remaining $K_L \rightarrow \pi^0 e^+ e^-$ Candidates

Once all the analysis cuts have been made the remaining task for this analysis is to see if the number of $\pi^0 e^+ e^-$ candidates left in the data agree with with backgrounds predicted, or if there is some excess which could signal the presence of the decay $K_L \rightarrow \pi^0 e^+ e^-$. This section describes the background levels expected for the most significant backgrounds, and how those levels were predicted. Given the number of $K_L$ particles which were determined to have decayed in the decay volume of the experiment, N, the number of times the data statistics are represented by a given Monte Carlo data set can be expressed as:

$$N = \frac{F_{K_L} B(\text{Background})}{N_{\text{generated}}}$$
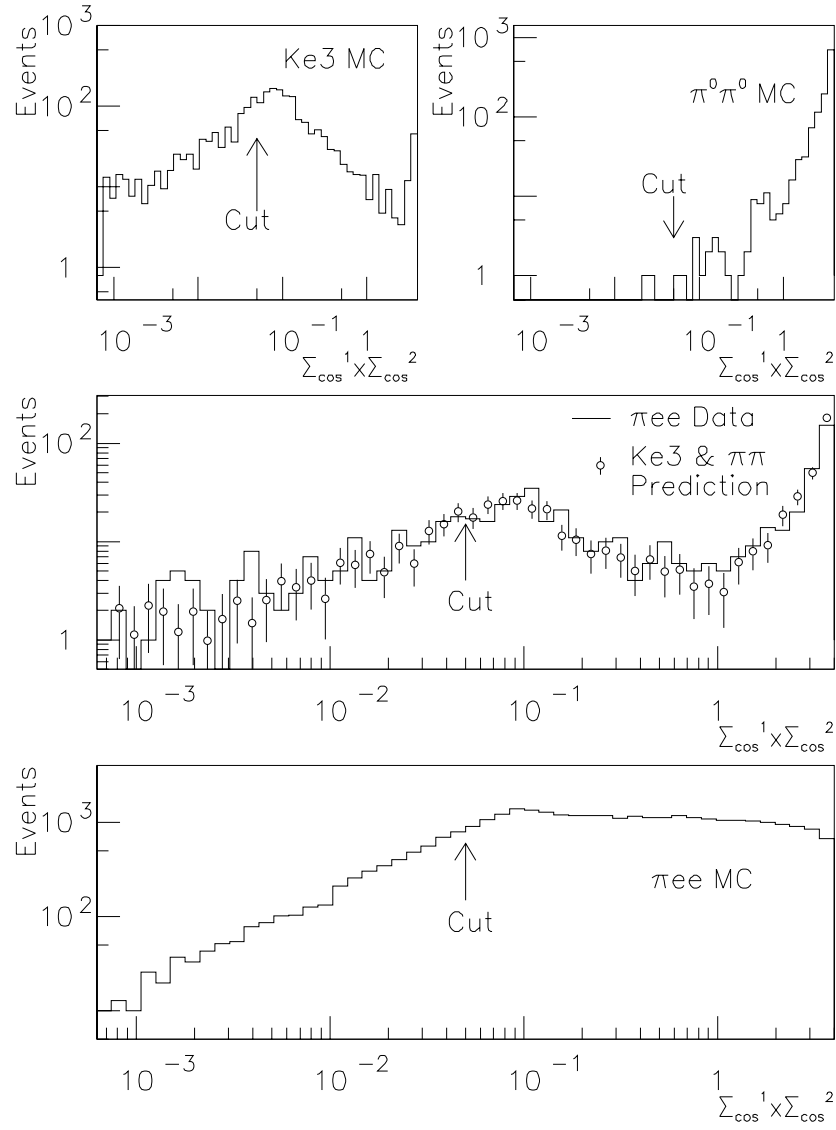
Figure 117. The $\Sigma_{cos}^{1} \times \Sigma_{cos}^{2}$ distributions for four samples: $\pi^{\pm}e^{\mp}\nu$ and $\pi^{0}\pi^{0}\pi^{0} \to e^{+}e^{-}\gamma$ background, $\pi^{0}e^{+}e^{-}$ candidates, and $\pi^{0}e^{+}e^{-}$ Monte Carlo.

Table 18. Efficiencies (in percentages) of $K_L \rightarrow \pi^0 e^+ e^-$ Analysis Cuts for both signal and background Monte Carlos, and for the data itself. A $\sqrt{}^*$ indicates that the cut has been slightly modified due to the different number of photons in the final state

| Analysis Cut | $\pi^0 e^+ e^-$ Data | $\pi^0 e^+ e^-$ MC | $\pi^0 \pi_D^0$ MC | $\pi^\pm e^\mp \nu$ MC | Background $e^+ e^- \gamma$ MC | $e^+ e^- \gamma\gamma$ MC | $e^+ e^- \gamma$ Signal Cut? |
|---|---|---|---|---|---|---|---|
| 21 Loose Mass and $P_t^2$ cuts | 5 | 95 | 34 | 10 | 69 | 80 | $\sqrt{}^*$ |
| $\pi^+\pi^-\pi^0$ Invariant Mass | 78 | 99 | 64 | 99 | 84 | 70 | - |
| Fusion Cuts | 15 | 75 | 65 | 13 | 56 | 65 | $\sqrt{}$ |
| Adder Energy | 79 | 98 | 73 | 90 | 95 | 97 | $\sqrt{}$ |
| $85\% < E/p < 115\%$ | 81 | 95 | 94 | 5 | 95 | 94 | $\sqrt{}$ |
| $\pi^0$ Mass $\pm 15\,MeV$ | 11 | 89 | 50 | 5 | 16 | 14 | - |
| $e^+ e^-$ Invariant Mass(only) | 86 | 87 | 1 | 99 | 30 | 25 | - |
| $\Sigma^1_{cos} \times \Sigma^2_{cos}$ and Brem(only) | 39 | 79 | 99 | 25 | 52 | 50 | $\sqrt{}^*$ |
| $P_t^2 < 1000\,(MeV/c)^2$ | 32 | 99 | 73 | 22 | 75 | 84 | $\sqrt{}$ |
| Final Mass and $P_t^2$ | 0 | 90 | 40 | 6 | $< 8$ | 43 | $\sqrt{}^*$ |
| Total Acceptance | | 0.38 | $4.1 \times 10^{-4}$ | $9.5 \times 10^{-8}$ | $4.1 \times 10^{-4}$ | $2.6 \times 10^{-3}$ | |

where $F_{K_L}$ is the $K_L$ flux, B(Background) is the branching ratio for that background process, and N is the number of events generated by the Monte Carlo. The four most significant backgrounds to the $K_L \to \pi^0 e^+ e^-$ search are (in increasing importance) the background arising from $K_L \to e^+ e^- \gamma$ decays, $K_L \to \pi^0 \pi^0$, $\pi^0 \to e^+ e^- \gamma$ decays, $K_L \to e^+ e^- \gamma \gamma$ decays, and most importantly, the background from $K_{e3}$ decays. Figure 118 shows the four most significant backgrounds to the $K_L \to \pi^0 e^+ e^-$ search, where each plot shows several times the data statistics.

### 9.7.1 Two-electron Backgrounds

To predict the number of background events expected from backgrounds which include two electrons in the final state, one simply uses the $K_L$ flux as measured in the $K_L \to e^+ e^- \gamma$ sample. Since the flux determined by the $K_L \to e^+ e^- \gamma$ normalization sample agrees with the flux determined by the $K_L \to \pi^0 \pi^0$, $\pi^0 \to e^+ e^- \gamma$ sample, the differences in acceptance based on the different kinematics of background decays is accounted for in the Monte Carlo.

### 9.7.2 Semi-leptonic Backgrounds

Since the Monte Carlo does not include hadronic showers it is difficult to determine accurately the efficiencies of the various electron identification cuts on charged pions. Without these efficiencies the Kaon flux, as measured by the number of $K_L \to e^+ e^- \gamma$ and $K_L \to \pi^0 \pi^0$, $\pi^0 \to e^+ e^- \gamma$ candidates, cannot be used to predict the rate of $K_{e3}$ background level. Another way to determine the $K_{e3}$ background level in the $\pi^0 e^+ e^-$ search might be to consider how many $K_{e3}$ events arise after electron identification cuts are made in the $K_L \to e^+ e^- \gamma$ sample. From Figure 116 it is clear that there is a large sample of $K_{e3}$ events in the $e^+ e^- \gamma$ sample before the $\Sigma_{cos}$ cut. One could compute a special "$K_{e3}$ Flux" which has folded into it the average efficiency of the electron identification cuts as applied to that particular sample of charged pions. This sample, however, cannot be used because there is the possibility that a pion could shower in the lead-glass and create an extra cluster which could pass all the photon identification cuts. These sorts of events will not be predicted by this method.
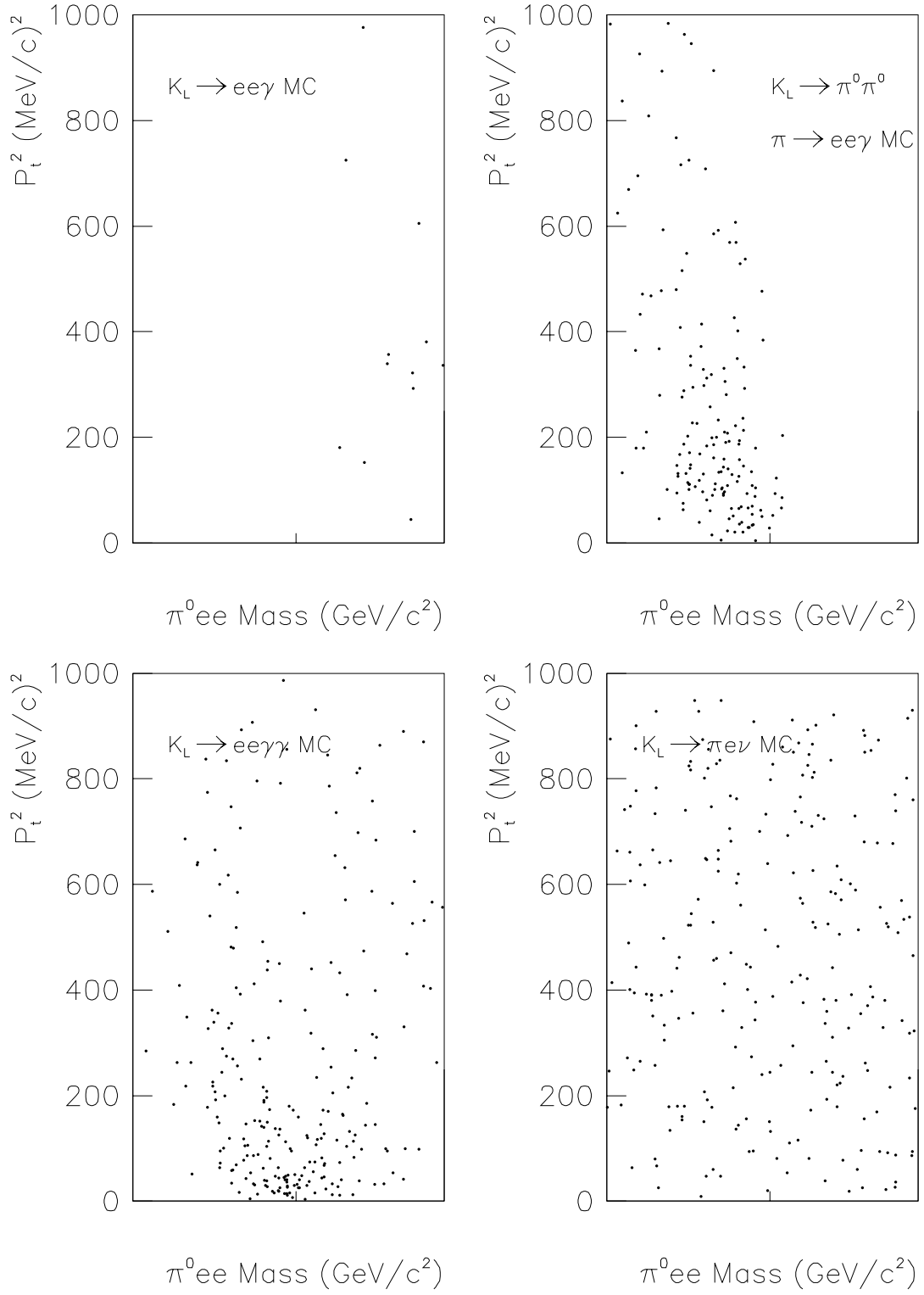
Figure 118. The final mass versus $P_t^2$ distributions for the four most significant backgrounds to the $K_L \to \pi^0 e^+ e^-$ search after all analysis cuts other than mass and $P_t^2$ were made

To accurately predict the number of $K_{e3}$ background events expected in the final $\pi^0 e^+ e^-$ sample a sideband of the $\pi^0 e^+ e^-$ data was considered. After all the cuts listed above have been made on the data, the backgrounds from other decays are predicted to be negligible. Since the $K_{e3}$ background is expected to be roughly flat in $P_t^2$, by considering a sideband in $P_t^2$ which was four times the size of the final plot, then one could expect to predict the number of events in the final plot with roughly twice as good an error as the statistical error on the expected background. Figure 119 shows the different regions relevant to the $K_{e3}$ normalization procedure. The most darkly shaded region represents the signal region, and is where the background ultimately needs to be predicted. The most lightly shaded region is the "final plot" region. By normalizing the $K_{e3}$ Monte Carlo to the number of events in the most lightly shaded region in that plot, namely $1000\,(MeV/c)^2 < P_t^2 < 5000\,(MeV/c)^2$ and $450\,MeV/c^2 < M_{\pi ee} < 550\,MeV/c^2$, one can predict the number of events expected in both the final plot and the signal region, and use the number of events seen in the final plot as a cross-check of the Monte Carlo prediction. Any statistically significant excess in the signal region would be evidence for the decay $K_L \to \pi^0 e^+ e^-$.
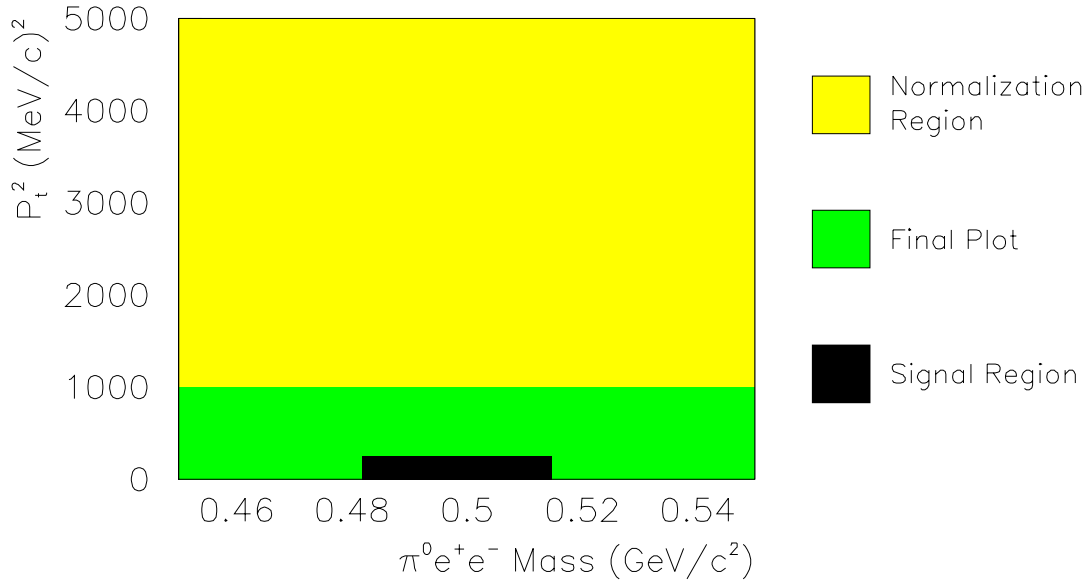


Figure 119. The definition of the $K_{e3}$ Normalization sideband region

When all the analysis cuts are made on the $\pi^0 e^+ e^-$ candidates except for the $\Sigma_{cos}^1 \times \Sigma_{cos}^2$ cut, there are 200 events remaining in the normalization region, as defined in figure 119. By looking at various kinematic quantities and comparing with the $K_{e3}$ Monte Carlo it is clear that these events are due to $K_{e3}$ decays. Most importantly the $\Sigma_{cos}^1 \times \Sigma_{cos}^2$ distributions between the sideband events in both the data and the Monte Carlo agree and thus unambiguously signal the presence of $K_{e3}$ decays. Figure 120 shows the $\Sigma_{cos}^1 \times \Sigma_{cos}^2$ distributions for both the data and the $K_{e3}$ Monte Carlo for the events in the normalization region. The Monte Carlo statistics is about six times the data statistics.

Using this normalization scheme, the $K_{e3}$ Monte Carlo predicts $28.5 \pm 2.9$ events in the final plot region (including the signal region), and $1.8 \pm 0.5$ events in the actual signal box.

## 9.8 Final $K_L \rightarrow \pi^0 e^+ e^-$ signal

Table 19 lists the four most important backgrounds that arise in the search for the decay $K_L \rightarrow \pi^0 e^+ e^-$, and the number of events expected in the final plot as well as in the signal
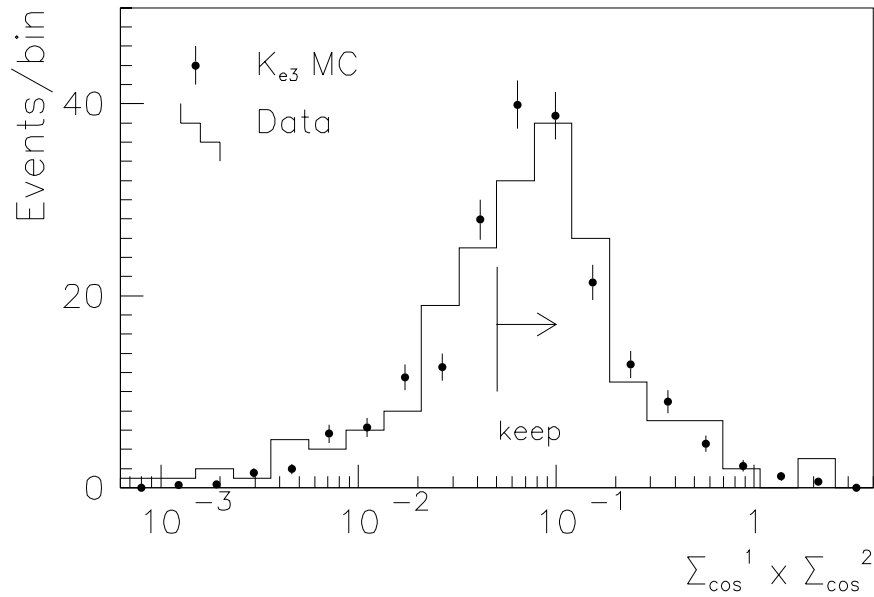


Figure 120. The $\Sigma_{cos}^1 \times \Sigma_{cos}^2$ distributions for data and Monte Carlo for events in the $K_{e3}$ Normalization sideband region

Table 19. $K_L \to \pi^0 e^+ e^-$ Expected Backgrounds

| | Number of Events Expected | |
| --- | --- | --- |
| Background | Final Plot | Signal Region |
| $K_L \to e^+ e^- \gamma$ | $2.9 \pm 0.8$ | $< 0.2$ |
| $K_L \to \pi^0 \pi^0$, $\pi^0 \to e^+ e^- \gamma$ | $1.3 \pm 0.1$ | $0.3 \pm 0.05$ |
| $K_L \to e^+ e^- \gamma \gamma$ | $< 2$ | $< 1$ |
| $K_L \to \pi^{\pm} e^{\mp} \nu$ | $28 \pm 2$ | $1.8 \pm 0.5$ |
| Total | $32 \pm 2.1$ | $2.1 \pm 0.5$ |

region. After all cuts have been made on the final sample there are 25 remaining events in the final plot, and 0 events in the final signal region. This is in reasonable agreement with the background prediction of $32 \pm 2$ events in the final plot and $2.1 \pm 0.5$ events in the signal region, most of which are $K_{e3}$ decays. The chance of 2.1 events fluctuating to 0 events in the signal region is 12%. Although this probability is low, it can be seen by the prediction of the number of events in the final plot that the overall estimates are slightly higher than what is actually seen in the data. Figure 121 shows the mass versus the $P_t^2$ of the remaining 25 events, as well as the signal region, for both the remaining candidates and the $K_L \to \pi^0 e^+ e^-$ Monte Carlo.

## 9.9   $\pi^0 e^+ e^-$ Normalization Events

After all cuts were made on the three and five cluster events, there were 255 events of the type $K_L \to e^+ e^- \gamma$ and 194 events of the type $K_L \to \pi^0 \pi^0$, $\pi^0 \to e^+ e^- \gamma$. Since some of the five-cluster data was collected in the two-electron trigger and all of the three-cluster data was collected in the Dalitz trigger, the prescales of the two samples differed drastically for part of the run. Table 20 lists the three different parts of the run for which the prescale
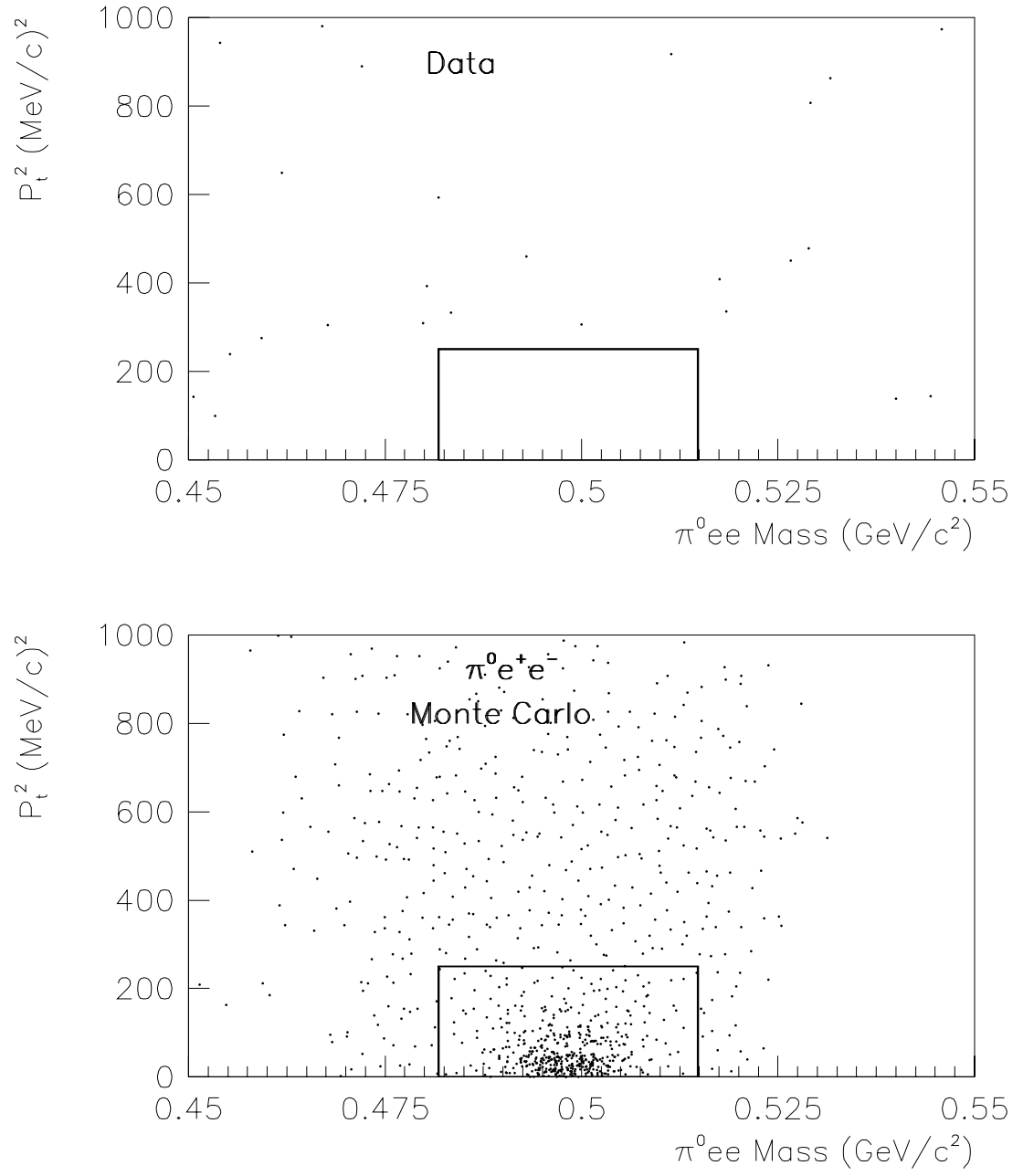
Figure 121. The final mass and $P_t^2$ for all $\pi^0 e^+ e^-$ events remaining in both the data and the $\pi^0 e^+ e^-$ Monte Carlo after all cuts

Table 20. $\pi^0 e^+ e^-$ Normalization Events as Function of Time

| Date | $\pi^0 \pi^0$  $\pi^0 \to e^+ e^- \gamma$ | | $e^+ e^- \gamma$ | |
|------|----------|--------|----------|--------|
| | Prescale | Events | Prescale | Events |
| 10/13-10/19 | $\infty$ | 0 | 1 | 113 |
| 10/19-10/19 | 16 | 27 | 16 | 12 |
| 11/9-1/9 | 14 | 228 | 14 | 69 |

on the two normalization samples varied, the prescales themselves, and the number of normalization events (in each mode) which were collected.

Figure 122 shows the final mass distributions for both normalization samples. The sidebands of the $\pi^0 \pi^0$, $\pi^0 \to e^+ e^- \gamma$ distribution indicate that there is some background under the $K_L$ mass peak, which is most likely due to the decay $K_L \to \pi^0 \pi^0 \pi^0$, $\pi^0 \to e^+ e^- \gamma$, where some combination of photons overlapped or otherwise escaped detection. Although cuts could be placed on the photon veto signal to reduce this background, they were not made because this decay did not represent a serious background to the signal mode, because of the $M_{e^+ e^-}$ cut. The total background estimated under the $K_L$ mass peak in the $\pi^0 \pi^0$, $\pi^0 \to e^+ e^- \gamma$ signal is 4.4%, and this background is assumed to be constant as a function of time.

Upon careful examination of the $\pi^0 \pi^0$, $\pi^0 \to e^+ e^- \gamma$ mass plot it is clear that the mean of the distribution is approximately $6\,MeV/c^2$ or 1% higher than the nominal $K_L$ mass, in both the data and the Monte Carlo events. This effect is due to accidental activity and can be seen in the change of the $E/p$ distributions between calibration electrons, which have negligible accidental activity, and electrons in the $K_L \to \pi^0 \pi^0 \pi^0$, $\pi^0 \to e^+ e^- \gamma$ sample (see reference [1]). For the $\pi^0 e^+ e^-$ Monte Carlo events and the $e^+ e^- \gamma$ data and Monte Carlo events the mass distributions are peaked at the nominal $K_L$ mass because more of the mass information is located in the leptons, and the momentum measurements in the spectrometer are much less dependent on accidental activity than the energy measurements in the lead-glass. The final mass cuts are therefore different for the two normalization samples, but as
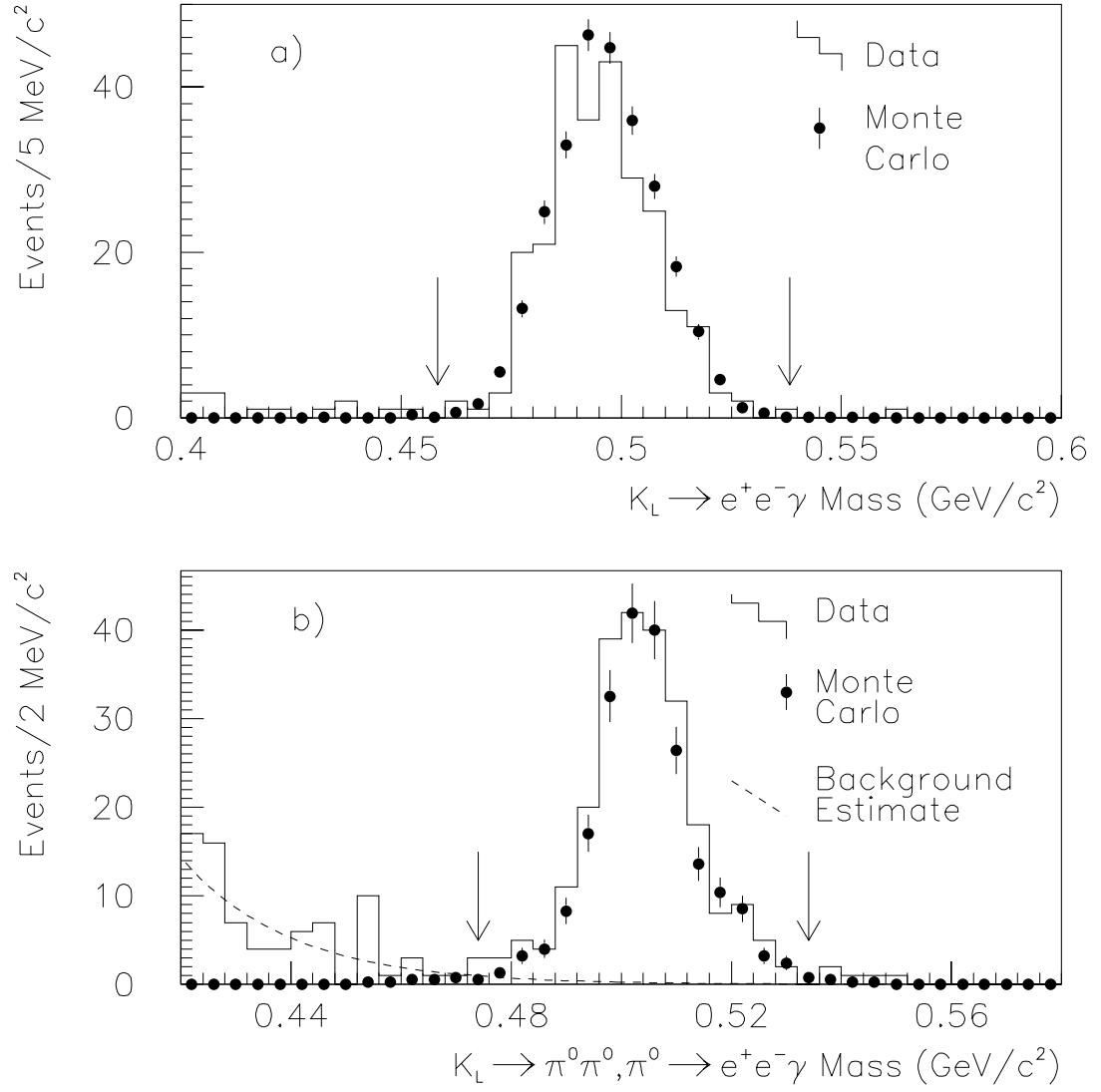
Figure 122. The final mass distributions for the normalization decays $K_L \to e^+e^-\gamma$ and $K_L \to \pi^0\pi^0$, $\pi^0 \to e^+e^-\gamma$ after all cuts besides the mass cut were made. The arrows indicate the final mass cuts for each sample. The dashed line in the $\pi^0\pi^0$, $\pi^0 \to e^+e^-\gamma$ sample indicates the fit to the background used in the $K_L$ flux measurement

is shown by figure 122, they are both loose enough to include 99% of the signal. The final mass cut for the $K_L \to e^+ e^- \gamma$ events is $40\,MeV/c^2$ around the nominal $K_L$ mass, which is a $3.4\sigma$ cut. Events in the $\pi^0 \pi^0$, $\pi^0 \to e^+ e^- \gamma$ sample within $30\,MeV/c^2$ of the peak mass of the $\pi^0 \pi^0$, $\pi^0 \to e^+ e^- \gamma$ distribution $(504\,MeV/c^2)$ were accepted.

## 9.10   Conclusion

At this point it has been determined that there is no evidence for the signal $K_L \to \pi^0 e^+ e^-$. The remaining task is to calculate the branching ratio limit that can be set using the normalization events which have been found and the ratio of acceptances between the signal and normalization mode. The upper limit on the $K_L \to \pi^0 e^+ e^-$ branching ratio depends on the systematic errors as well, and in chapter 11 the various sources of error in both the $\pi^0 e^+ e^-$ and $\pi^0 \mu^+ \mu^-$ searches will be discussed. The following chapter describes the backgrounds which interfere with the search for the decay $K_L \to \pi^0 \mu^+ \mu^-$ and how they are removed. While it is clear from considering figure 121 that much improvement on background rejection must occur before improvements in $\pi^0 e^+ e^-$ sensitivity can be made, the $\pi^0 \mu^+ \mu^-$ search is much less fraught with backgrounds.

# CHAPTER 10

# BACKGROUNDS TO

# $K_L \to \pi^0 \mu^+ \mu^-$

## 10.1 Introduction

Compared to the backgrounds seen in the search for $K_L \to \pi^0 e^+ e^-$, the backgrounds to the search for $K_L \to \pi^0 \mu^+ \mu^-$ are fewer in number and simpler to remove. We will now discuss the few backgrounds which were seen in this search, as well as mention a few which could become important in future searches.

### 10.1.1 $K_L \to \pi^+ \pi^- \pi^0$

The vast majority of events which are written to tape as dimuon triggers are consistent with being from $K_L \to \pi^+ \pi^- \pi^0$ decays where the pions were misidentified as muons or the pions decayed to muons before arriving at the calorimeter. In general these decays reconstruct to a lower mass than a real $\pi^0 \mu^+ \mu^-$ decay, but with low $P_t^2$.

### 10.1.2 $K_L \to \pi^\pm \mu^\mp \nu$

Although the branching ratio for $K_L \to \pi^\pm \mu^\mp \nu$ is approximately as large as that of the $K_L \to \pi^\pm e^\mp \nu$ decay, it poses a much less serious threat to the $K_L \to \pi^0 \mu^+ \mu^-$ search than did the decay $K_L \to \pi^\pm e^\mp \nu$ to $K_L \to \pi^0 e^+ e^-$. This is because the overall pion/muon discrimination was roughly a factor of two better than the pion/electron discrimination. But as in the case of $K_L \to \pi^\pm e^\mp \nu$, this decay occurs as a background when it occurs in co-

214

incidence with two accidental photons. The resulting background is again roughly flat in invariant mass and $P_t^2$.

### 10.1.3  $\Lambda \to p^+ \pi^-$

While the beam contained $K_L$ particles and neutrons, there were also a significant number of $\Lambda$ particles. When a $\Lambda$ particle decays to a proton or a pion one or both of the particles could conceivably pass all of the muon trigger requirements. When the $\Lambda \to p^+ \pi^-$ decay is accompanied by two accidental photons which happen to have the right invariant mass, the decay contributes background. These events are particularly dangerous because as was mentioned before, accidental photons tend not to add much transverse momentum to the decay, and since the decay $\Lambda \to p^+ \pi^-$ is a two-body decay all of the momentum is conserved. Therefore, background from this decay tends to have very low $P_t^2$.

### 10.1.4  $K_L \to \mu^+ \mu^- \gamma$

Prior to this experiment, only one event of the type $K_L \to \mu^+ \mu^- \gamma$ had been seen [18]. The dimuon trigger in E799 is perfectly suited to accept this decay, and in fact a preliminary result has been announced with $\sim 150$ such events. This decay could contribute a background if it came in coincidence with an accidental cluster of low energy, or if one of the muons emitted (either internally or externally) a Bremsstrahlung photon. Although this background is too low to interfere with this search, it could prove dangerous at levels where the standard model predicts the decay $K_L \to \pi^0 \mu^+ \mu^-$, as discussed in section 1.5.4.

## 10.2  $K_L \to \pi^0 \mu^+ \mu^-$ Accidental Activity Cuts

One dominant cause of events passing the di-muon trigger was increased accidental activity in the muon trigger bank. Since it is correlated with activity in other detector elements, there were additional cuts made on the $K_L \to \pi^0 \mu^+ \mu^-$ sample to reduce the number of events with unreasonably high levels of accidental activity.

## 10.2.1   Adder Ratio Cut

One measure of the accidental activity in the lead-glass is the ratio of energy which arrives in the first $30\,nsec$ to the total energy arriving in the calorimeter blocks, whose ADC gates are open for $100\,nsec$. There was a cut requiring the amount of energy in all the adders summed together to be at least 70% of the total energy in all of the lead-glass blocks. Figure 123 shows the distribution of this ratio for the Accidental events (which are added to the Monte Carlo) and the $K_L \rightarrow \pi^0 \mu^+ \mu^-$ data, after the cluster energy cuts on the muons have been made on the latter sample. The width of the adder ratio peak is 4.0% in the $\pi^0 \mu^+ \mu^-$ data and is due to different gains in the various lead-glass blocks. Reference [1] describes the adder simulation and calibration in detail.

## 10.2.2   B and C Latch Cut

There was a cut on the $K_L \rightarrow \pi^0 \mu^+ \mu^-$ sample requiring that there be less than 12 counters in the B and C banks which fired. In fact the B and C counter distributions between data
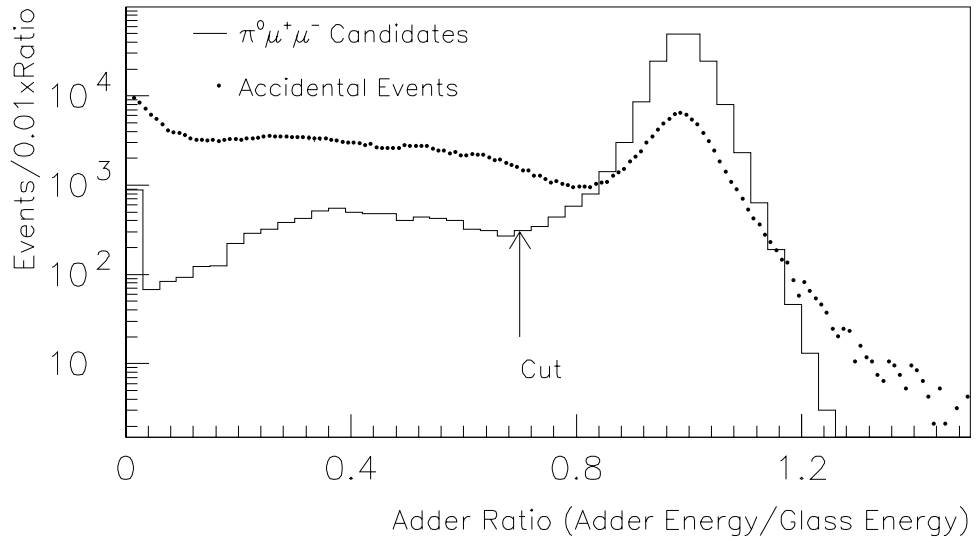


Figure 123.   The ratio of the Adder energy to the total Calorimeter energy for both Accidental events and $K_L \rightarrow \pi^0 \mu^+ \mu^-$ data after muon energy cluster cuts were made

and Monte Carlo did not agree well, as is shown in figure 124, but the cut was loose enough that the discrepancy between data and Monte Carlo was less than 1%. The discrepancy between data and Monte Carlo has several contributions. One possibility is that accidental activity in the B and C banks didn't get mocked up properly in the Monte Carlo. Another known problem is that when particles hit the lead-glass the shower particles sometimes leave the glass in the opposite direction and then hit the scintillator planes (referred to as "splash-back"). This is especially true of the pions when they shower, and this is not in the Monte Carlo simulation. Since the charged pion distribution is in general less peaked in the center of the detector than the the accidental activity distribution, one can look at the illumination of counters which have particles pointing to them and see if at least the illumination is the same, even if in the data a larger fraction of counters which have particles pointing near them fire (due to splash-back). Figure 125 shows the distribution of B and C counters which were hit in both $\pi^+\pi^-\pi^0$ data and Monte Carlo where either a photon or a pion was pointing to the given counter. In the case of photons, they were required to point to within $2\,cm$ of a counter that fired, and in the case of charged pions, they were required
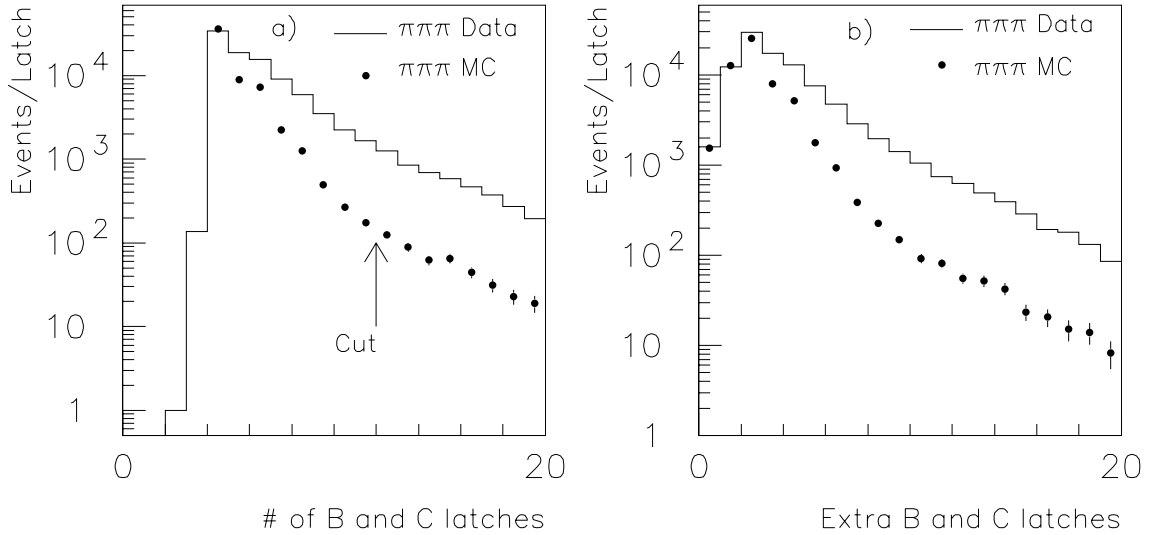
Figure 124. The number of latches in the B and C counters which fired in both $\pi^0\mu^+\mu^-$ and $\pi^+\pi^-\pi^0$ samples, data and Monte Carlo
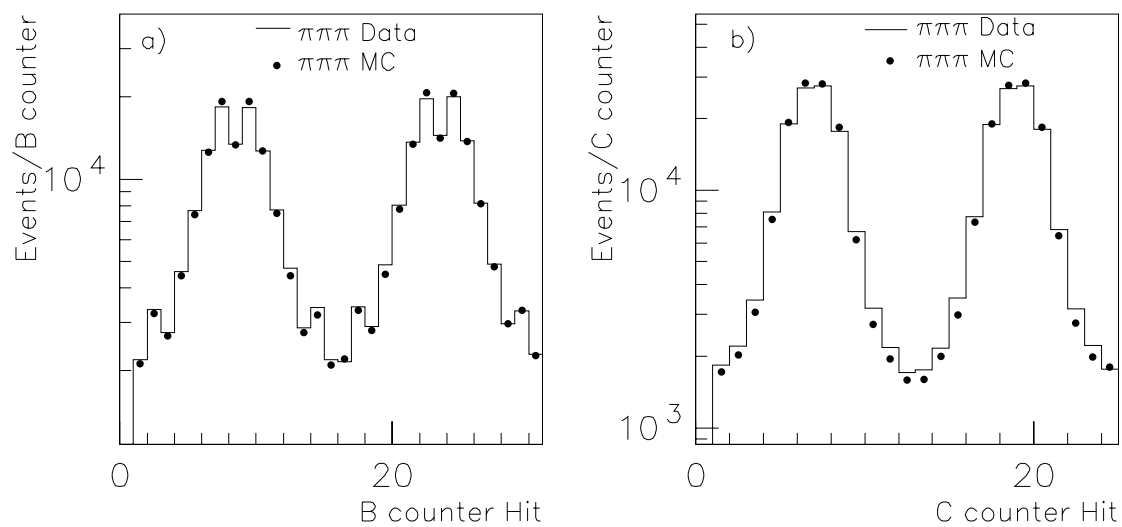
Figure 125. The B and C counter illuminations for counters which fired which had decay particles pointing towards them in both $K_L \rightarrow \pi^+\pi^-\pi^0$ data and Monte Carlo

to point to within $2\,mm$ of a counter that fired. The discrepancy between data and Monte Carlo indicates the level at which splash-back changes the counter occupancy. Since there is not much disagreement between the two illuminations, and splash-back is expected to roughly preserve the illumination, and accounts for about 16% of the counters hit in the data.

## 10.3  $K_L \to \pi^0 \mu^+ \mu^-$ Background-Specific Cuts

### 10.3.1  Lambda Kinematics

One way to remove events from $\Lambda$ decay is by reconstructing the invariant mass of the two charged tracks assuming the track with higher momentum corresponds to a proton (or antiproton) and the other is a pion. Figure 126 is a plot of the $p\pi$ invariant mass distributions for both the data and the $K_L \to \pi^0 \mu^+ \mu^-$ Monte Carlo; the peak at $1.115\,GeV$ is clearly visible in the data distribution. By cutting out events with reconstructed $p\pi$ invariant mass within $10\,MeV/c^2$ of the $\Lambda$ mass all events of this type are removed.

As a measure of how well this cut is simulated we can compare the $p\pi$ invariant mass distribution for $K_L \to \pi^+ \pi^- \pi^0$ events in both the data and the Monte Carlo. Figure 127 shows this distribution for both samples and also the ratio between the two samples. Clearly the acceptance as a function of invariant $p\pi$ mass is well enough understood to allow this cut.

### 10.3.2  Maximum Momentum Cut

When a $\Lambda$ particle decays in the fiducial decay volume of the E799 detector, it has on average a much higher energy than a $K_L$ decaying at the same point. This is because the lifetime of the $\Lambda$ particle is $2.632 \times 10^{-10}\,sec$ or $7.9\,cm$, while that of the $K_L$ is $5.17 \times 10^{-8}\,sec$, or $15.5\,m$, and the $\Lambda$'s need a high boost to travel $90\,m$ to reach the decay volume. The products from the $\Lambda$ decay, particularly the proton, will on average be higher in energy than the decay products from $K_L$ decays. By cutting out events which have tracks of momenta greater than $70\,GeV$, events with protons from $\Lambda$ decays are removed. Figure 128 shows the momentum distribution for $\pi^0 \mu^+ \mu^-$ candidate events in the data and the Monte Carlo,
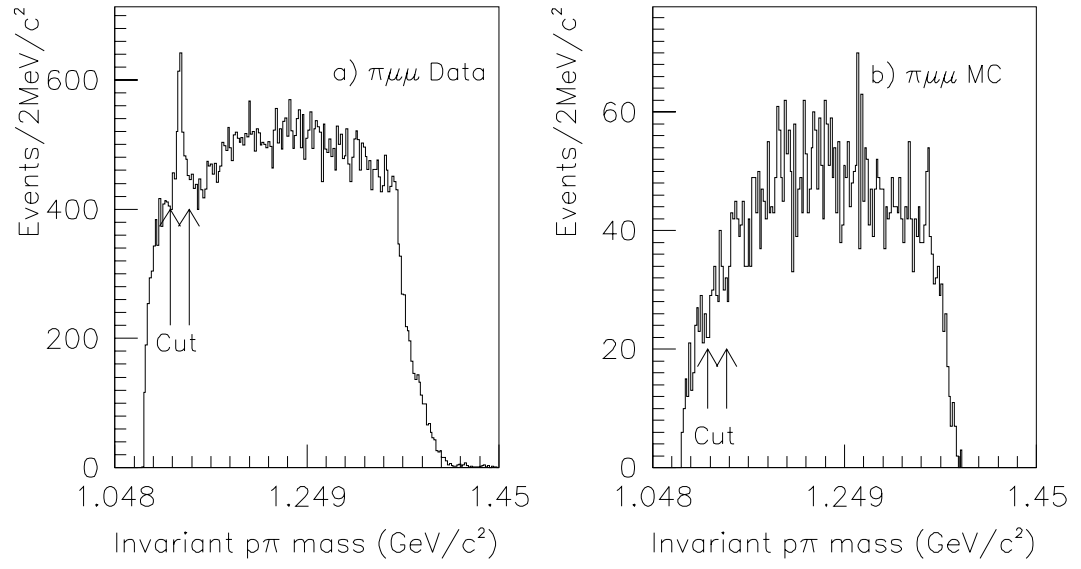
Figure 126. The $p\pi$ invariant mass distributions for both $K_L \to \pi^0 \mu^+ \mu^-$ candidates and $K_L \to \pi^0 \mu^+ \mu^-$ Monte Carlo
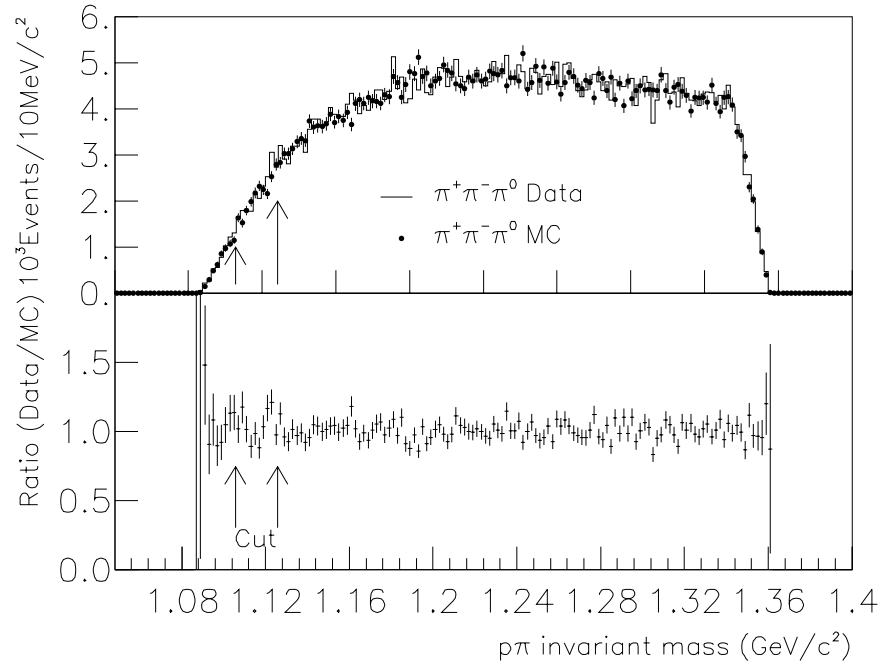
Figure 127. The $p\pi$ invariant mass distributions for both $K_L \to \pi^+\pi^-\pi^0$ candidates and $K_L \to \pi^+\pi^-\pi^0$ Monte Carlo, and the ratio between the two distributions (Data/MC)
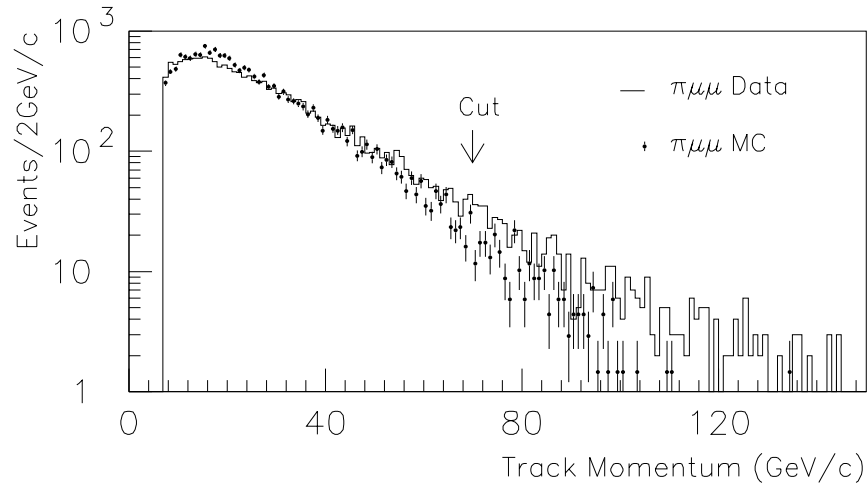


Figure 128. The $\mu^{\pm}$ momentum distributions for both $K_L \to \pi^0\mu^+\mu^-$ data and Monte Carlo
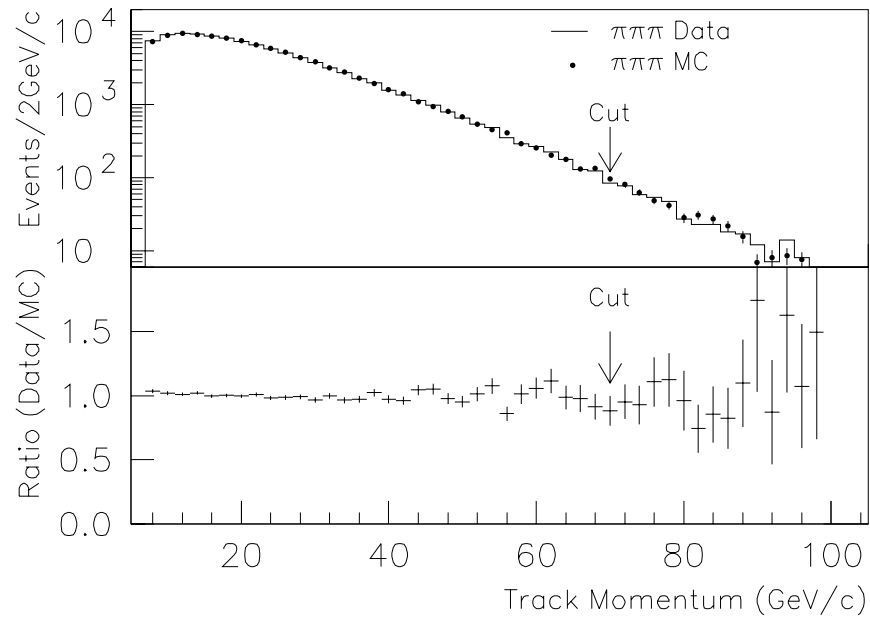
Figure 129. The $\pi^{\pm}$ momentum distributions for both $K_L \rightarrow \pi^+ \pi^- \pi^0$ candidates and $K_L \rightarrow \pi^+ \pi^- \pi^0$ Monte Carlo, and the ratio between the two distributions (Data/MC)

for events which are inconsistent with being from $K_L \to \pi^+\pi^-\pi^0$ decays. The excess at high momentum in the $\pi^0\mu^+\mu^-$ data is due to the presence of $\Lambda$ decays. Figure 129 shows the momentum distribution for pions from $K_L \to \pi^+\pi^-\pi^0$ decays in both the data and the Monte Carlo simulation, and the ratio of the distributions. It is clear from this plot that the acceptance as a function of momentum is understood. The cut at $70\,GeV$ removes $\sim 1.5\%$ of the signal acceptance.

### 10.3.3   Bremsstrahlung Photon Cut

Photons produced by Bremsstrahlung are much more relevant for the $\pi^0 e^+ e^-$ search than to the $\pi^0\mu^+\mu^-$ search, but there is still evidence of this effect in the $\pi^+\pi^-\pi^0$ sample. Figure 130 shows the distribution for the minimum distance between extrapolated upstream track position at the lead-glass and the position of photon clusters at the glass (this cut is described in more detail in section 9.5.3). The excess at small distances is due to external Bremsstrahlung photons and a cut at one lead-glass block width (5.82 cm) is made on both $K_L \to \pi^0\mu^+\mu^-$ and $K_L \to \pi^+\pi^-\pi^0$ candidates. This cut removes 5.9% of the $K_L \to \pi^0\mu^+\mu^-$ data and 4.1% of the $K_L \to \pi^0\mu^+\mu^-$ Monte Carlo.

## 10.4   Efficiencies of $K_L \to \pi^0\mu^+\mu^-$ Analysis Cuts

Table 21 is a listing of the analysis cuts described in this chapter, and the efficiencies for the signal data, the signal Monte Carlo, the $K_L \to \pi^+\pi^-\pi^0$ data, and the $K_L \to \pi^+\pi^-\pi^0$ Monte Carlo. Since the background to this search was low there were no background Monte Carlo simulations done. The cuts that were made were studied with the normalization sample, since it provided a low-background high-statistics sample. The fact that the cuts produced similar efficiencies in both the normalization sample data and Monte Carlo means that the systematic error associated with making these cuts was low. There were no particle identification cuts made on the charged pions in the $K_L \to \pi^+\pi^-\pi^0$ samples.

Table 21. $K_L \rightarrow \pi^0 \mu^+ \mu^-$ Analysis Cuts

| Analysis Cut | $\pi^0 \mu^+ \mu^-$ | | $\pi^+ \pi^- \pi^0$ | |
|---|---|---|---|---|
| | Data | MC | Data | MC |
| Adder Ratio Cut | .987 | .970 | .998 | .999 |
| B and C latch cut | .916 | .998 | .991 | .998 |
| Track Momentum $\leq 70\,GeV$ | .965 | .986 | .996 | .996 |
| $\Lambda$ Mass Cut | .949 | .944 | .961 | .962 |
| Bremsstrahlung $\gamma$ Cut | .941 | .959 | .935 | .944 |
| Final Mass Cut | $2 \times 10^{-4}$ | .940 | .728 | .850 |
| Final $P_t^2$ Cut | $< 0.14$ | .988 | .921 | .930 |

## 10.5    Remaining $K_L \to \pi^0 \mu^+ \mu^-$ Candidates

After all of the cuts were made on the $\pi^0 \mu^+ \mu^-$ sample there are negligible backgrounds remaining. Figure 131 shows the mass versus $P_t^2$ of the remaining $\pi^0 \mu^+ \mu^-$ events in the data sample as well as the $\pi^0 \mu^+ \mu^-$ Monte Carlo, after all other cuts have been made. Signal events were required to have a total $\pi^0 \mu^+ \mu^-$ invariant mass within $12\,MeV/c^2$ of the nominal $K_L$ mass, and a $P_t^2$ of less than $500\,(MeV/c)^2$. The band of events at low mass in the data are consistent with $K_L \to \pi^+ \pi^- \pi^0$ decays, and the few events at high mass are consistent with being from $K_L \to \pi^{\pm} \mu^{\mp} \nu$ decays with extra photon candidates.

To demonstrate how quickly the $K_L \to \pi^+ \pi^- \pi^0$ background is falling below the signal region we fit the upper edge of the $\pi^0 \mu^+ \mu^-$ mass distribution to a Gaussian as an approximation of the $\pi^+ \pi^- \pi^0$ background shape. Figure 132 shows the mass distribution of the events which pass the $P_t^2$ cut in figure 131. If the rate at which the $K_L \to \pi^+ \pi^- \pi^0$ background is falling in figure 132 continues at higher mass, then one event from the background
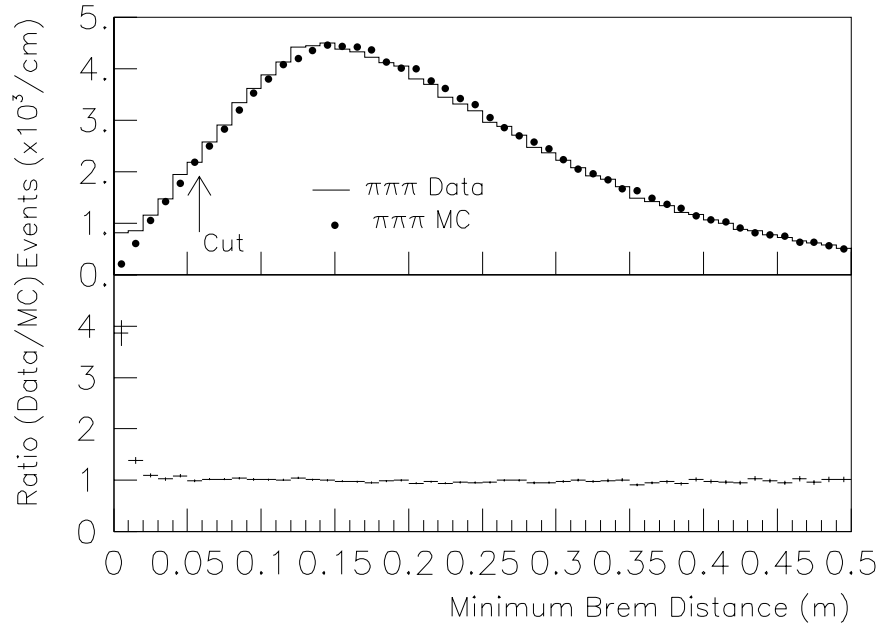


Figure 130. An example of an electron emitting a Bremsstrahlung photon before bending at the plane of the magnet.
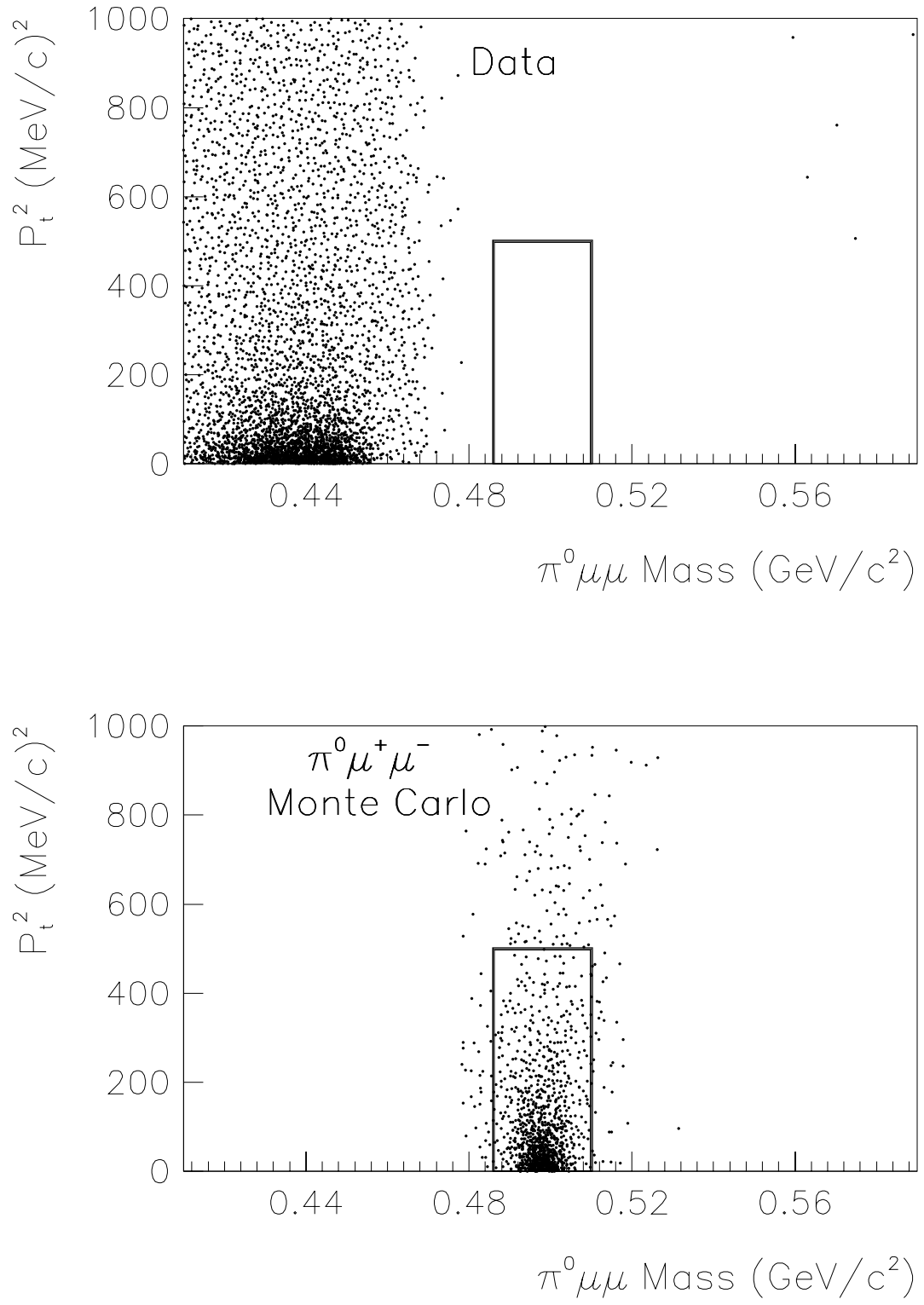
Figure 131. The final mass and $P_t^2$ for all $\pi^0\mu^+\mu^-$ events remaining in both the data and the $\pi^0\mu^+\mu^-$ Monte Carlo after all cuts, where the small box indicates the signal region. There are no remaining signal events in the data

would enter under the peak of the Monte Carlo distribution if the $K_L$ flux were three orders of magnitude larger.

The final mass and $P_t^2$ cuts were chosen to be $\sim 3\sigma$ in both variables. By fitting the $\pi^0\mu^+\mu^-$ Monte Carlo mass distribution (figure 132) the mass resolution is determined to be $3.9 \pm 0.1\, MeV/c^2$. By fitting the resulting $P_t^2$ distribution in the $\pi^0\mu^+\mu^-$ Monte Carlo to an exponential of the form $Ae^{(-bP_t^2)}$ and assuming that the $P_t$ distribution itself is Gaussian, the width of the Gaussian is simply $1/\sqrt{2b}$. The sigma of the $P_t^2$ distribution shown in figure 131 calculated this way is $6.4\, MeV/c$, and so a cut at $500\, MeV/c^2$ is actually equivalent to a $3.5\sigma$ cut.
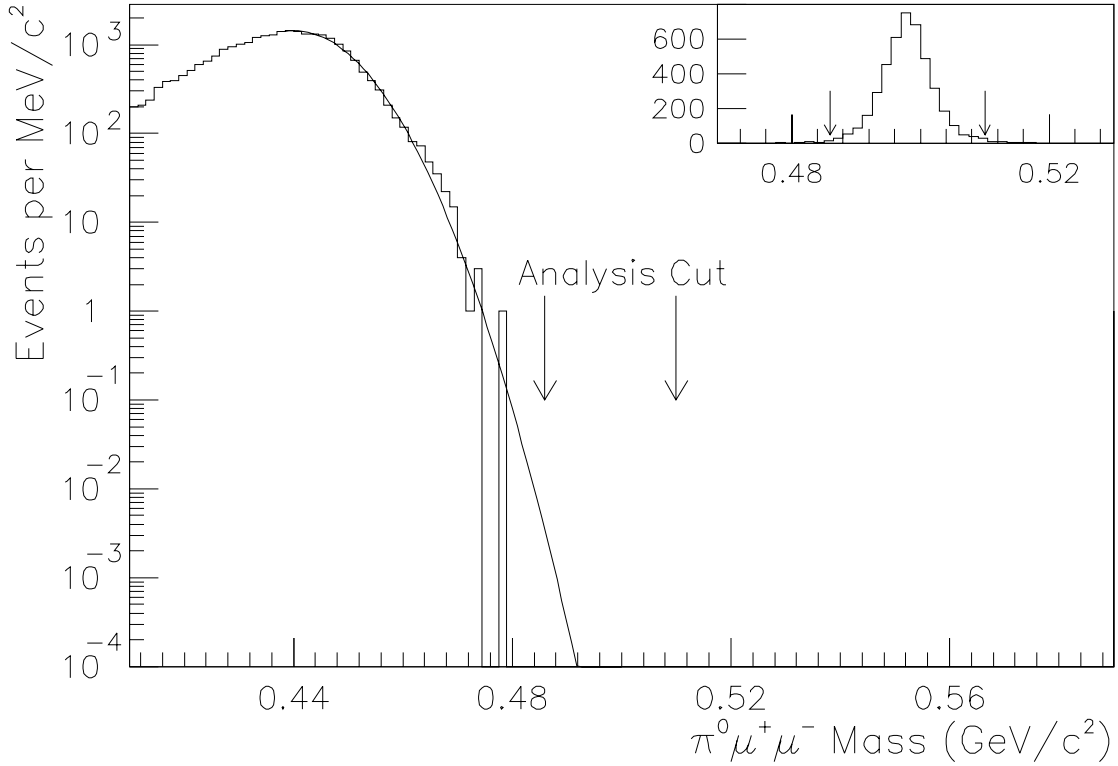
Figure 132. The final mass for all $\pi^0\mu^+\mu^-$ events remaining in both the data and the $\pi^0\mu^+\mu^-$ Monte Carlo after all cuts, where the arrows indicate the signal region, and the function plotted represents an estimate of when a $\pi^+\pi^-\pi^0$ background might enter the peak of the signal region.

## 10.6   $\pi^0\mu^+\mu^-$ Normalization Events

After all cuts were made there were 49624 events which remained in the $K_L \to \pi^+\pi^-\pi^0$ data sample. The only analysis cuts which were not made on the normalization sample were the muon cluster energy cuts. The differences in triggers will be discussed in section 11.3. Figure 133 shows both the final mass and $P_t^2$ distributions for both the $\pi^+\pi^-\pi^0$ data and the Monte Carlo. The tail at the high mass region in the data indicates the level of background contamination, and is likely to be due to semi-leptonic decays. Since there was neither a cluster energy cut nor an $E/p$ cut there is likely to be some contamination due to electrons, but the fraction is less than a tenth of a percent in the signal region and is ignored. The signal region itself is defined as that region where the total invariant $\pi^+\pi^-\pi^0$ mass is within $12\,MeV/c^2$ of the $K_L$ mass, and the total $P_t^2$ is less than $500\,(MeV/c)^2$. The width of the $\pi^+\pi^-\pi^0$ mass distribution is only $(2.72 \pm 0.9)\,MeV/c^2$, and so the resulting cut is more than a $3\sigma$ cut, as is shown by the agreement between the data and the Monte Carlo the total flux of $K_L$'s observed does not depend on varying the mass cut.

By fitting the first 10 channels of the $P_t^2$ distribution to an exponential of the form $A \times \exp(-bP_t^2)$ and assuming that the $P_t$ distribution itself is Gaussian, the width of the Gaussian is $1/\sqrt{2b}$. The sigma of the $P_t$ distribution shown in figure 133 calculated this way is $5.8\,MeV/c$, and so a cut at $P_t^2 < 500\,MeV/c^2$ is equivalent to a $3.8\sigma$ cut. Again, since the data and Monte Carlo $P_t^2$ distributions agree well near the region of the cut the total $K_L$ flux computed does not depend on varying the $P_t^2$ cut.

## 10.7   Conclusion

Figure 132 shows no evidence for the decay $K_L \to \pi^0\mu^+\mu^-$, and the background level is sufficiently low that background estimates from the various sources considered in this chapter are not necessary. In the following chapter we will describe the systematic and statistical errors which enter into the error on the SES for both the $\pi^0 e^+e^-$ and $\pi^0\mu^+\mu^-$ searches, and in the last chapter determine the SES and the 90% confidence level upper limit.
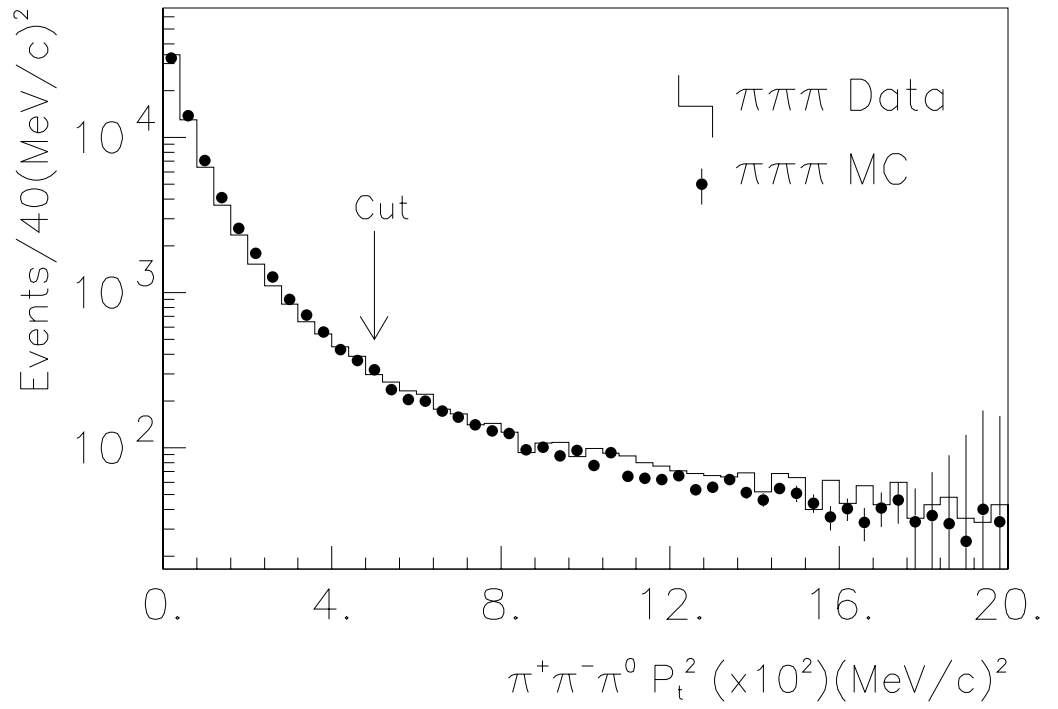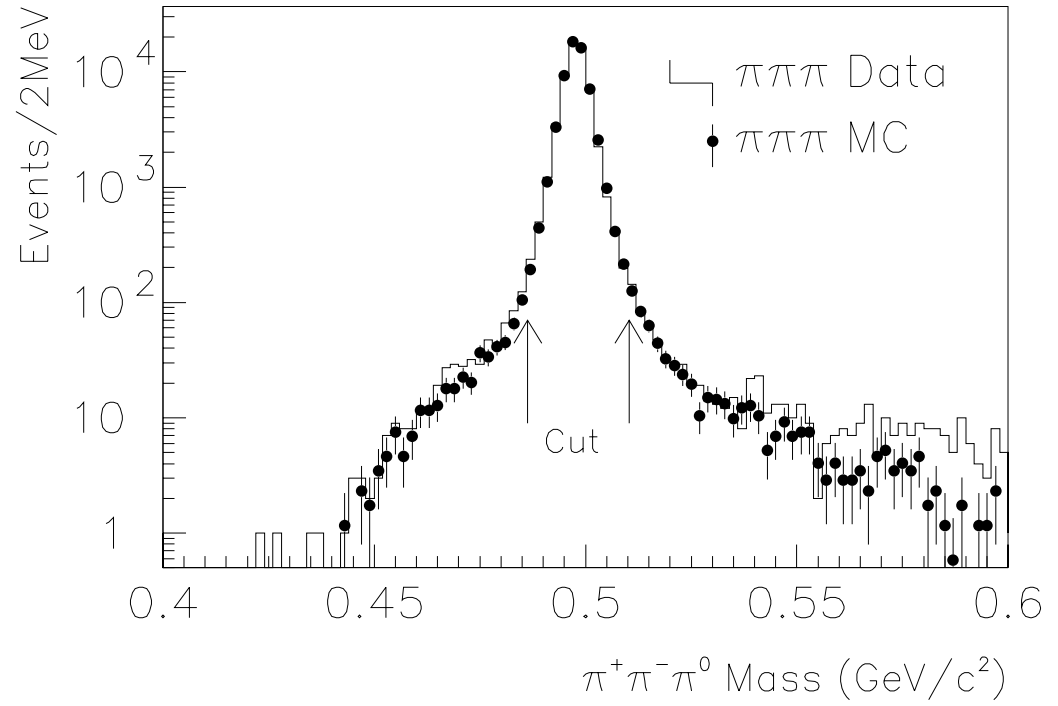
Figure 133. The final mass for all $K_L \to \pi^+\pi^-\pi^0$ events in both data and $\pi^+\pi^-\pi^0$ Monte Carlo after all cuts but those shown, where the arrows indicate the final cuts

# CHAPTER 11

# SYSTEMATIC ERRORS

After all cuts were made in both the $\pi^0 e^+ e^-$ and the $\pi^0 \mu^+ \mu^-$ data sets there were no candidate events, and so the remaining task is to determine the single event sensitivity (SES) for each of these modes, and ultimately the 90% confidence level upper limit. The single event sensitivity of a given decay mode is expressed in the following equation:

$$SES(\pi^0 \ell^+ \ell^-) = BR(\text{norm}) \frac{A(\pi^0 \ell^+ \ell^-)}{A(\text{norm})} \frac{1}{N(\text{norm})} \tag{11.1}$$

where again, $A(\text{mode})$ is the acceptance for that mode, N is the number of events seen, and $BR(\text{mode})$ is the branching ratio for that mode. From this equation it is clear that errors on the single event sensitivity can come from three sources: the experimental error on the normalization branching ratio, the statistical error on the number of normalization events found, and finally, the systematic error on the ratio of acceptances of the signal and normalization modes. The first two sources of error are relatively straightforward to determine, and the last one depends on how well the detector is understood and how tight the analysis cuts are. Each source of error will be discussed in this chapter and in the last section the SES's will be computed for the two signal modes.

Another useful quantity to consider is the total number of $K_L$ particles decaying in the detector within a given momentum range and a given decay volume, or the $K_L$ flux seen by the two-electron trigger. Since the flux calculated this way depends on the absolute acceptance and and not a ratio of acceptances it is a less reliable quantity, since there are cuts on the data which are not well-simulated in the Monte Carlo. The flux is a useful quantity when considering two different normalization samples with similar cuts, however, and is defined in the following way:

$$\text{Flux}(K_L \to \text{mode}) = \frac{N(\text{mode})}{A(\text{mode}) \times BR(\text{mode})} \tag{11.2}$$

Table 22. Decay Modes Used in $K_L \rightarrow \pi^0 \ell^+ \ell^-$ Analyses

| Decay Mode | Branching Ratio | Fractional Error(%) |
|---|---|---|
| $K_L \rightarrow e^+ e^- \gamma$ | $9.1 \pm 0.5 \times 10^{-6}$ | 5.5 |
| $K_L \rightarrow \pi^0 \pi^0$ | $0.909 \pm 0.035 \times 10^{-3}$ | 3.9 |
| $K_L \rightarrow \pi^+ \pi^- \pi^0$ | $0.1238 \pm 0.0021$ | 1.7 |
| $\pi^0 \rightarrow \gamma\gamma$ | $98.798 \pm 0.032 \times 10^{-2}$ | 0.03 |
| $\pi^0 \rightarrow e^+ e^- \gamma$ | $1.198 \pm 0.032 \times 10^{-2}$ | 2.7 |

This quantity is what will be checked when considering the two normalization modes considered in the $\pi^0 e^+ e^-$ SES determination.

## 11.1  Branching Ratio Uncertainties

Table 22 lists the relevant normalization branching ratios and the errors on those quantities, as listed in reference [18]. The overall error on the decay $K_L \rightarrow \pi^0 \pi^0, \pi^0 \rightarrow e^+ e^- \gamma$ is 4.7%, when adding in quadrature the fractional errors on each of the three decays in the chain. The branching ratio uncertainty will prove to be the largest single systematic error associated with the $\pi^0 e^+ e^-$ single event sensitivity.

## 11.2  Statistical Uncertainty

Statistical uncertainties can enter into the error on the single event sensitivities in two ways—either the data statistics or the Monte Carlo statistics. Table 23 lists the statistical uncertainty associated with each of the final samples.

## 11.3  Ratio of Acceptance Uncertainty

The biggest uncertainties in the ratio of acceptances arise from cuts which are made on the signal sample and not on the normalization sample, or from any differences between

Table 23. Statistical Uncertainties in $K_L \to \pi^0 \ell^+ \ell^-$ Analyses

| | $\pi^0 e^+ e^-$ Analysis | | $\pi^0 \mu^+ \mu^-$ Analysis |
|---|---|---|---|
| Sample | $e^+ e^- \gamma$ | $\pi^0 \pi^0$, $\pi^0 \to e^+ e^- \gamma$ | $\pi^+ \pi^- \pi^0$ |
| Normalization Monte Carlo | 1.4 | 2.9 | 0.34 |
| Normalization Data | 6.3 | 7.2 | 0.45 |
| Signal Monte Carlo | 1.1 | | 2.0 |

the trigger requirements for the signal and normalization data. In general the kinematic cuts on all of the samples were loose, so as not to introduce large systematic errors in the ratio of acceptances. In the first part of this section we will describe checks made on the Monte Carlo samples for both the $\pi^0 e^+ e^-$ and the $\pi^0 \mu^+ \mu^-$ analyses, and then describes the analysis-related errors specific to each search.

## 11.3.1 Calorimeter Uncertainties

In parts of this thesis discrepancies have been shown between the expected calorimeter performance and the actual performance. The overall calorimeter energy scale has a shift of about 1%, and the photon energy modeling for highly damaged blocks is not accurate. To check for changes in the ratio of acceptances due to these effects, both the signal and normalization Monte Carlo samples were modified in various ways, and then the change in the acceptances was taken as the associated systematic uncertainty. Because the cuts on the lead-glass were loose, the systematic errors associated with the lead-glass are rather small. Table 24 lists various changes that were made, and the effect that these changes had on the ratio of the $\pi^0 e^+ e^-$ and $e^+ e^- \gamma$ acceptances, and the ratio of the $\pi^0 \mu^+ \mu^-$ and $\pi^+ \pi^- \pi^0$ acceptances.

There were tighter cuts on the calorimeter for the $\pi^0 e^+ e^-$ analysis than for the $\pi^0 \mu^+ \mu^-$ analysis, so the systematics were larger. Furthermore, it is also clear that the ratio of acceptances between $\pi^0 e^+ e^-$ and $e^+ e^- \gamma$ modes is less dependent on changes in calorimeter performance than the ratio of acceptances between $\pi^0 e^+ e^-$ and $\pi^0 \pi^0$, $\pi^0 \to e^+ e^- \gamma$. For

Table 24. Calorimeter Systematic Uncertainties

| Monte Carlo Change | Ratio of Acceptances | | |
|---|---|---|---|
| | $\pi^0 e^+ e^-$ / $e^+ e^- \gamma$ | $\pi^0 e^+ e^-$ / $\pi^0 \pi^0$ | $\pi^0 \mu^+ \mu^-$ / $\pi^+ \pi^- \pi^0$ |
| Shift Lead Glass energies by $-1\%$ | 0.1% | 1.6% | 0.2% |
| Shift Pipe Block energies by $+1.5\%$ other blocks by $+1\%$ | 0.4% | 0.5% | 0.2% |
| Smear Pipe Block energies by 3.7% First Ring of block energies by 2.4% | 0.6% | 1.0% | 0.1% |
| Add $20\,MeV/c^2$ shift and $60\,MeV$ RMS coherent smear | 0.0% | 0.3% | 0.1% |
| Add 2% block-by-block smear in each event | 1.3% | 1.5% | 0.1% |
| Smear the overall gain by 4% in each event | 0.5% | 4.1% | 0.1% |

this reason the SES is calculated using the $e^+ e^- \gamma$ flux, and the flux predicted by the $\pi^0 \pi^0, \pi^0 \to e^+ e^- \gamma$ events is simply as a cross-check.

## 11.3.2 Spectrometer Uncertainties

From looking at events of the type $K_L \to \pi^+ \pi^-$ as shown in figure 70 the extent to which the Monte Carlo does not simulate momentum resolution in the spectrometer is clear. To check for systematic errors based on uncertainties on the spectrometer scale, resolution, or the tails of the momentum resolution the ratio of acceptances was recalculated after each kind of modification. Table 25 lists the change in the ratio of acceptances for the three different combinations of Monte Carlos, for three different changes in the Monte Carlo model of the spectrometer resolution.

Table 25. Spectrometer Systematic Uncertainties

| Monte Carlo Change | Ratio of Acceptances | | |
|---|---|---|---|
| | $\pi^0 e^+ e^-$ / $e^+ e^- \gamma$ | $\pi^0 e^+ e^-$ / $\pi^0 \pi^0$ | $\pi^0 \mu^+ \mu^-$ / $\pi^+ \pi^- \pi^0$ |
| Shift Momentum Scale by 0.05% | 0.1% | 0.2% | 0.1% |
| Smear Momenta by an extra 0.42% | 0.1% | 0.2% | 0.1% |
| Smear every $130^{th}$ track by 14% | 0.2% | 0.3% | 0.5% |

### 11.3.3  Trigger Difference Effects

The trigger differences can severely affect the ratio of acceptances if the overall efficiency of a given trigger is not well-measured. In the search for the decay $\pi^0 e^+ e^-$ the signal and normalization triggers were virtually identical, and since the calorimeter and spectrometer effects have been shown to be small, the trigger differences, which lie only in the amount of energy required in the calorimeter and the number of hits required in the spectrometer, matter even less since the analysis cuts are tighter than the triggers themselves. For the $\pi^0 \mu^+ \mu^-$ search, however, the differences between the two triggers was enormous and therefore careful examination of each difference is indicated. The two most important trigger differences between the $\pi^+ \pi^- \pi^0$ (Minimum Bias) trigger and the $\pi^0 \mu^+ \mu^-$ (di-muon) trigger are the Hadron Shower Veto and the Muon trigger plane requirement, both of which were in the signal trigger but not the normalization trigger. Finally, since the muon trigger plane was located behind 20 interaction lengths of steel, multiple scattering in the steel had to be included in the Monte Carlo for muons but not for charged pions, since hadrons are not expected to reach the muon trigger plane. Therefore, the modeling of multiple scattering was still another difference between signal and normalization modes. These effects and their associated systematic uncertainties are discussed in this section.

Table 26. Muon Trigger Plane Efficiency Studies

| Sample: | $A(\pi^0\mu^+\mu^-)$ | $\frac{\Delta A}{A}$ |
|---|---|---|
| Normal mu3 Efficiency | 2.24% | 0 |
| All mu3 counter efficiencies reduced by 1 $\sigma$ | 2.18% | 2.7% |
| All mu3 counter efficiencies smeared by 1 $\sigma$ | 2.25% | 0.4% |

**Muon Trigger Plane Efficiency**

Section 6.3.1 describes the method used to measure the muon scintillator bank efficiencies. Due to the limited statistics for the different muon calibration runs, many of efficiencies were only measured to a per cent, with some regions of the trigger plane being measured to only 5%. These efficiencies only affect the $\pi^0\mu^+\mu^-$ acceptance and not the $\pi^+\pi^-\pi^0$ acceptance, so uncertainties in the overall efficiency contribute directly to the uncertainty in the ratio of acceptances. To determine how that ratio changes based on how well the efficiencies were measured, two different $\pi^0\mu^+\mu^-$ Monte Carlo samples were generated, besides the nominal $\pi^0\mu^+\mu^-$ Monte Carlo sample, with two different sets of muon trigger plane efficiencies, and then the entire analysis program was performed on all three samples, and the different final acceptances were compared. Table 26 shows how the two different Monte Carlo samples were generated and the resulting $K_L \rightarrow \pi^0\mu^+\mu^-$ acceptance.

When all muon trigger counter efficiencies are reduced by $1\sigma$ the acceptance drop is large, but of course the probability of all of the counters being mismeasured by that much is very low: $(0.32^{32}$, if there are 32 efficiency table entries that were lowered). A conservative systematic error of 1.35%, or half of the decrease of acceptance noted is assigned to this uncertainty.

**Multiple Scattering Simulation**

Section 6.2 describes the effect of muons multiply scattering in the steel before hitting the muon trigger plane. Depending on how the muons are traced through the steel, different counters are hit, and there was a requirement in the dimuon trigger that two non-adjacent

Table 27. Multiple Scattering Simulation Studies

| Sample: | $A(\pi^0 \mu^+ \mu^-)$ | $\frac{\Delta A}{A}$ |
|---|---|---|
| Normal mu3 Efficiency | 2.24% | 0 |
| Muon hits random counter in Mu3 trigger bank | 2.13% | 4.8% |
| Muon is extrapolated to counter—no scattering | 2.17% | 3.1% |

counters in the bank fire. If the multiple scattering simulated in the Monte Carlo is not the same as the actual multiple scattering that occurred in the experiment (because of extra material in the detector or cracks in the steel), then the efficiencies as measured in the muon calibration runs might not be appropriate. Section 7.2.4 describes how the Monte Carlo simulates multiple scattering in the steel while taking into account the efficiencies as measured in the muon calibration run.

To check how multiple scattering affects the overall acceptance, two special Monte Carlo samples were generated, to be compared with the nominal Monte Carlo. The only difference between the three samples is how the decision was made to fire a particular muon trigger bank counter. In one extreme, a random counter was selected to fire, and the counter signal was weighted with the appropriate efficiency. In the other extreme, the muon was extrapolated to a particular counter, with no multiple scattering in the steel, and again the counter fired, weighted with its efficiency. Table 27 shows the results from this study.

Since the $\pi^0 \mu^+ \mu^-$ acceptance changes by 3% when muons are extrapolated to a given counter rather than allowed to scatter in the hadron filter, the actual uncertainty in the multiple scattering itself must be less than that, so again half that change is taken as the systematic uncertainty associated with the multiple scattering simulation.

**Hadron Veto Efficiency**

The Hadron Shower veto was calibrated using only the data from one muon calibration, since there was only one calibration run with enough statistics to measure all the parameters necessary for the simulation. To check for any systematic error associated with not

Table 28. Hadron Shower Veto Efficiency Studies

| Run: | Real Mu1 $\epsilon$ | Simulated Mu1 $\epsilon$ | Difference: |
|------|---------------------|--------------------------|-------------|
| 5186 | $94.04 \pm 0.08\%$ | $95.05 \pm 0.08\%$ | $1.0 + -0.1\%$ |
| 5278 | $94.04 \pm 0.05\%$ | $94.51 \pm 0.05\%$ | $0.5 + -0.07\%$ |
| 5340 | $93.12 \pm 0.3\%$ | $94.71 \pm 0.3\%$ | $1.6 + -0.3\%$ |

re-calibrating the veto at different times during the run, the simulation for single muon efficiency, $\epsilon$, was tested and compared with the measured $\epsilon$ on three different muon calibration data sets, including the run for which the bank was calibrated. The results for those tests are listed in table 28. The average difference between the calculated and actual mu1 efficiency for single muons is $1.01 \pm 0.06\%$.

The efficiency that is important, however, for the $\pi^0 \mu^+ \mu^-$ signal is the efficiency for two muons. This is not simply the product of the single muon efficiencies, since the signals are added before the threshold is checked. To check for the dimuon efficiency, all of the muon calibration runs were searched for events with two muons, where the same cuts on accidental activity as described in section 6.4.2 were made. After all cuts there were only 51 clean dimuon events, and the simulation predicted that the mu1 veto will be on for 15 of those events. The actual Mu1 veto was on for 15 of those events! The overall efficiency of the Mu1 veto for muon pairs is then $(70 \pm 6.4)\%$, which introduces a $9\%$ uncertainty in the overall $\pi^0 \mu^+ \mu^-$ acceptance. This is by far the largest systematic uncertainty in the analysis and is statistics limited by the lack of dimuon test data.

### 11.3.4   Analysis Difference Effects

The only remaining systematic effects that remain to be discussed are those which are caused by the difference between the analysis cuts in the signal mode and those in the normalization mode. In the $\pi^0 e^+ e^-$ analysis, the different cuts are due to the different kinematics of the decay, while in the $\pi^0 \mu^+ \mu^-$ analysis, the different cuts are due to the

different final state particles. This section describes the error associated with each of these cuts.

## $\pi^0 \mu^+ \mu^-$ Analysis

The only analysis cuts which were made on the $\pi^0 \mu^+ \mu^-$ data sample and not on the $\pi^+ \pi^- \pi^0$ data sample were the cuts on the cluster energy associated with the muon. To check the effect of not simulating the Landau distribution in the lead-glass, events from the muon calibration runs were checked. The accidental activity seen here was expected to be less than that from normal running, since the beam was pointed at beam stop, and not the target. The overall efficiency of muon identification cuts in this data was 98.9% per muon, instead of 97.7% per muon as was seen in the Monte Carlo. The extra discrepancy was due to the accidental activity during normal running. The difference of 1% was assigned as a systematic error to the overall efficiency of the cluster energy cut, in order to be maximally conservative.

## $\pi^0 e^+ e^-$ Analysis

The analysis differences between the signal and normalization sample were due to the different kinematics. To check the understanding of the ratio of acceptances for two kinematically different decays the decays $K_L \to e^+ e^- \gamma$ and $K_L \to \pi^0 \pi^0$, $\pi^0 \to e^+ e^- \gamma$ were compared. Table 29 gives the number of events of each type collected for the three different run regions, and the acceptances and prescales for those three parts of the run.

To determine the total number of $K_L$ particles seen over the course of the entire run, the fluxes as determined by both the $\pi^0 \pi^0$,$\pi^0 \to e^+ e^- \gamma$ sample and the $e^+ e^- \gamma$ sample must be multiplied by overall efficiencies. As can be seen in figure 122 there is a 4.4% background underneath the $K_L$ mass peak, which must be subtracted from the total calculated flux. Triggers for the decays $K_L \to e^+ e^- \gamma$ were only taken for a fraction of the run, where the fraction, $91.8 \pm 0.3\%$, was determined using the high statistics mode of $K_L \to \pi^0 \pi^0 \pi^0$,$\pi^0 \to e^+ e^- \gamma$, with $e^+ e^-$ invariant mass above $70 \, MeV/c^2$. There were 9600 decays of this type observed over the course of the entire run [1]. So the total $K_L$ flux as calculated by the number of events in the $e^+ e^- \gamma$ sample must be divided by the fraction of

Table 29. $K_L$ Flux as calculated by different samples

| Date | $e^+e^-\gamma$ | | | $\pi^0\pi^0\,\pi^0 \to e^+e^-\gamma$ | | |
|---|---|---|---|---|---|---|
| | A(mode) (%[†]) | Events | Flux ($\times 10^9$) | A(mode) (%[†]) | Events | Flux ($\times 10^9$) |
| 10/13-10/19 | 0 | 0 | | 0.226/1 | 113 | $2.33 \pm 0.22$ |
| 10/19-10/19 | 1.71/16 | 27 | $2.77 \pm 0.7$ | 0.225/16 | 12 | $3.98 \pm 1.0$ |
| 11/9-1/9 | 1.63/14 | 228 | $21.6 \pm 1.4$ | 0.183/14 | 69 | $24.5 \pm 2.9$ |
| TOTAL | $24.4 \div 0.918^{\ddagger} = 26.5 \pm 1.6$ | | | $30.8 \times 0.956^{\S} = 29.5 \pm 3.1$ | | |

[†] The number in the denominator is the pre-scale on that trigger for that run range.

[‡] The additional flux is due to the fraction of the run when these events were not accepted by the trigger.

[§] The reduction in flux is due to the 4% background under the $\pi^0\pi^0$, $\pi^0 \to e^+e^-\gamma$ mass peak.

the run over which the events were collected. The total flux, based on the $\pi^0\pi^0,\pi^0 \to e^+e^-\gamma$ sample is $29.5 \pm 3.1$ billion $K_L$'s, and the flux based on the $e^+e^-\gamma$ sample is $26.5 \pm 2.5$ billion $K_L$'s, where the errors given are statistical errors only. The two numbers agree to within $1\sigma$ and therefore we conclude that there is no measurable error associated with the different kinematics of the signal and normalization decay, nor is there an error in estimating the single photon acceptance.

### 11.3.5  Uncertainty in the Decay Kinematics

To measure the $K_L \to \pi^0\ell^+\ell^-$ acceptance the Monte Carlo must assume a particular decay distribution of kinematic variables. For the final results the decay distributions generated in the Monte Carlo simulation were flat over the available phase space. If the dominant intermediate process is $K_L \to \pi^0\gamma^*$, however, a vector interaction for the decay may be more appropriate. A vector interaction changes the region of phase space that the decay populates. First of all, the $M_{\ell^+\ell^-}$ distribution is not the same as the flat phase space distributions, due to an orbital angular momentum barrier in the vector interaction case. The decay rate for a vector interaction also has a dependence on the angle between the

$\pi^0$ and the lepton direction, in the center of mass frame of the two leptons. This angular

dependance is due to the fact that the intermediate photon is longitudinally polarized, so

the $e^+e^-$ pair must also be longitudinally polarized, and in a $p$-wave relative to the $\pi^0$ [63].

In the $\pi^0 e^+e^-$ analysis there is a cut which removes events with $M_{e^+e^-}$ less than

$115\,MeV/c^2$. If two different interactions have different expected $M_{e^+e^-}$ spectra, then the

acceptances for those two interactions are different and hence the single event sensitivity

will be different, depending on how the decay is modeled. Figure 134 shows the $\pi^0 e^+ e^-$

acceptance as a function of generated $M_{e^+e^-}$, for a flat phase space Monte Carlo, as well

as the two different generated $M_{ee}$ spectra: one for a vector interaction, and one for a flat

phase space decay. The relative independence of the acceptance as a function of $M_{e^+e^-}$

ensures that this limit does not depend strongly on whether or not the decay is described
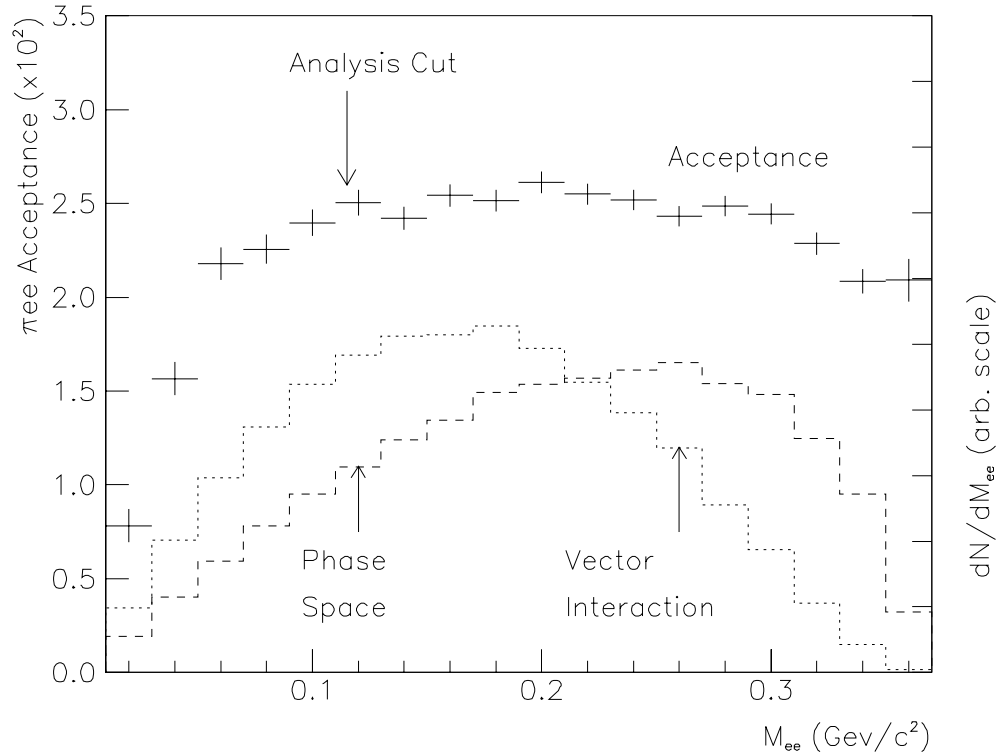


Figure 134. The acceptance as a function of $M_{e^+e^-}$ after all cuts but the one requiring $M_{e^+e^-} > 115\,MeV/c^2$, and the generated $M_{e^+e^-}$ spectra for two different models of $K_L \to \pi^0 e^+ e^-$ decay: a vector interaction and phase space.

by a flat phase space or a vector interaction. In fact, the overall $K_L \to \pi^0 e^+ e^-$ acceptance differs by only $(1.9 \pm 0.2)\%$ for the two different decay distributions. A 1.9% systematic error is therefore assigned to the overall $\pi^0 e^+ e^-$ acceptance to account for this difference.

## 11.4   Summary of Systematic and Statistical Errors

Table 30 gives a summary of all of the systematical and statistical errors associated with the measurement of the $\pi^0 e^+ e^-$ and $\pi^0 \mu^+ \mu^-$ single event sensitivities. After verifying that the $K_L$ fluxes as calculated by the two different two-electron normalization samples are the same, only the $e^+ e^- \gamma$ normalization sample will be used because the kinematics and reconstruction of this decay are more similar to the signal decay.

Table 30. Summary of SES Uncertainties

| Source: | $\Delta \left( \frac{A(\pi^0 \mu^+ \mu^-)}{A(\pi^+ \pi^- \pi^0)} \right) \%$ | $\Delta \left( \frac{A(\pi^0 e^+ e^-)}{A(e^+ e^- \gamma)} \right) \%$ |
|---|---|---|
| Detector Simulation Uncertainties: | | |
| Calorimeter Energy Scale | 0.3 | 0.4 |
| Calorimeter Resolution | 0.2 | 1.5 |
| Spectrometer Momentum Scale | 0.1 | 0.1 |
| Spectrometer Resolution | 0.2 | 0.5 |
| Hadron Shower Veto Efficiency | 9 | 0 |
| Muon Trigger Bank Efficiency | 1.4 | 0 |
| Muon Multiple Scattering | 1.5 | 0 |
| Total Detector Error | 9.2 | 1.6 |
| Analysis Uncertainties: | | |
| Normalization Branching Ratio | 1.7 | 5.5 |
| Muon Cluster Energy Cut | 1.1 | 0 |
| $K_L \rightarrow \pi^0 e^+ e^-$ Interaction Model | 0 | 1.9 |
| Total Analysis Error | 2.0 | 5.8 |
| Statistical Error: | | |
| Normalization Data Statistics | 0.5 | 6.3 |
| Monte Carlo Statistics | 2.0 | 1.8 |
| Total Statistical Error | 2.1 | 6.6 |
| TOTAL | 9.6 | 8.9 |

# CHAPTER 12

# RESULTS

"SGANARELLE: Mais encore faut-il croire quelque chose dans le monde:
qu'est-ce donc que vous croyez?...
DOM JUAN: Je crois que deux et deux sont quatre, Sganarelle,
et que quatre et quatre sont huit."
—*Molière, Dom Juan*

"Moral of the story, simple but it's true
Hey the stars might lie, but the numbers never do" —*Mary-Chapin Carpenter*

After all the cuts have been made, the event samples collected, and the ratios of accep-
tances computed, the single event sensitivities (SES) and the 90% confidence level upper
limits for both the $K_L \to \pi^0 e^+ e^-$ and the $K_L \to \pi^0 \mu^+ \mu^-$ decays can be computed.

## 12.1  $K_L \to \pi^0 e^+ e^-$ Sensitivity

From the 255 $K_L \to e^+ e^- \gamma$ events which were collected over the course of the run, the
$K_L$ flux, defined as the number of $K_L$ particles between 35 and $220\,GeV$ in energy that
decayed between 90 and $160\,m$ from the target, was determined to be $(26.5 \pm 1.6(\text{stat}) \pm
1.5(\text{syst})) \times 10^9$ $K_L$'s. The $K_L \to \pi^0 e^+ e^-$ acceptance for kaons in this window of energy and
decay position is $(2.06 \pm 0.04(syst))\%$, while the $K_L \to e^+ e^- \gamma$ acceptance for kaons in the
same window is 1.50%. The $\pi^0 e^+ e^-$ Monte Carlo used for the final result assumes a decay
distribution which populates the available phase space evenly. The single event sensitivity
for the decay $K_L \to \pi^0 e^+ e^-$ is therefore $(1.84 \pm 0.10(\text{stat}) \pm 0.11(\text{syst})) \times 10^{-9}$. There were
no $K_L \to \pi^0 \ell^+ \ell^-$ candidates remaining after all cuts, with an expected 1.8 background
events. The 90% confidence level upper limit on the branching ratio is therefore

$$B(K_L \to \pi^0 e^+ e^-) < 4.3 \times 10^{-9}$$

which incorporates the systematic and statistical uncertainties on the SES (appendices A and B discuss the effects of SES uncertainties and background predictions, respectively, on upper limits). This is a 20% improvement on the previous limit for this process, and the first to use a two-electron normalization sample, which is ultimately how the branching ratio can be accurately measured. By combing the three most sensitive limits, the "world limit" is now

$$B(K_L \to \pi^0 e^+ e^-)_{\text{world}} < 1.8 \times 10^{-9}$$

There are two orders of magnitude between the new world limit and the highest Standard Model predictions, so there is still room for new physics to be discovered in this mode.

### 12.1.1  Proposed Performance

When the experiment was proposed the SES for the $\pi^0 e^+ e^-$ mode was to have been $\sim 2 \times 10^{-10}$, which would have been a more substantial improvement compared to previous experiments. The single event sensitivity seen in this experiment was a factor of 9 worse than the proposal. As a warning to those who endeavor to improve searches of this type, I list here where the proposed sensitivity of this experiment was lost.

The proposal based its SES calculations on the $\pi^0 e^+ e^-$ limit found by the predecessors of this experiment, E731, for the last 20% of the E731 run. Using this data set, which was taken over a period of one month, the E731 sensitivity to the decay $K_L \to \pi^0 e^+ e^-$ was [57] $SES(K_L \to \pi^0 e^+ e^-)_{\text{E731}} = 1.8 \times 10^{-8}$. The proposal called for an increase in the proton beam intensity by a factor of 3 from the E731 operating intensity. Furthermore, while E731 only had one pure $K_L$ beam, E799 was to use both beams as $K_L$ beams and would run for two months rather than one. The 20 inch Be absorber in the secondary beam was to be removed, which would in turn increase the $K_L$ flux by a factor of 2.6 (and also increase the neutron flux by a factor of 6.7!). Finally, the acceptance was to have been dramatically increased by two factors: first, the instrumentation of the beam-holes with new radiation-hard calorimeters (with an estimate of a factor of 2 increase of acceptance), and second, the fiducial decay volume was to be increased by over a factor of three, thereby improving the acceptance by a factor of $\sim 2.75$ by accepting events further upstream of the original decay

Table 31. Proposed Improvements to E799, compared to E731 one-month data set

| Improvement | Sensitivity Increase |
|---|---|
| Run for two months | 2 |
| Use two $K_L$ beams | 2 |
| Proton intensity: $2 \times 10^{12}$ protons per spill | 3 |
| Remove Be absorber from beam | 2.6 |
| Instrument Beam-holes | 2 |
| Reduce Dead-time | 1.8 |
| Increase Fiducial Decay Volume | 2.75 |
| Total | 310 |

volume. Although E731 ran with approximately 50% dead time, E799 was proposed with an improved data-acquisition system which would run with only $\sim 10\%$ dead time. This improvement implies another factor of 1.8 in sensitivity.

These increases are listed in table 31, and together improve the sensitivity by a factor of 310. At the time of the proposal, neither the new data acquisition system nor the beam-hole calorimeters were available for testing, so as a conservative estimate the proposed $\pi^0 e^+ e^-$ sensitivity was quoted at $2 \times 10^{-10}$, which was a factor of 90 improvement on the previous result, and the expected improvement without those two additions.

## 12.1.2 Actual Performance

In fact the actual $\pi^0 e^+ e^-$ sensitivity was worse than the proposal by a factor of nine. The decreases can be divided into two categories: the $K_L$ flux that the experiment was able to detect online, and a loss of $\pi^0 e^+ e^-$ acceptance.

The increase in kaon flux from removing the absorber from the beam was correctly predicted. However, while the proposed intensity was to be $2 \times 10^{12}$ protons per spill, resulting in $8 \times 10^7 K_L$'s per spill, because of dead-time limitations the experiment only ran at $1.4 \times 10^{12}$ protons per spill, producing $5.3 \times 10^7 K_L$'s per spill. (While the proposal

predicted a kaon to neutron ratio of $1 : 2$, the actual ratio was closer to $1 : 6$). With this large increase in flux, the new data acquisition system was not able to run at the predicted 90% live time, but ran at 45% live. Overall, the actual $K_L$ flux (including dead-time effects) was smaller than the proposed flux by a factor of $\sim 3$. Another effective loss of flux is due to the fact that the Tevatron was only able to deliver approximately 60% of the requested intensity on the target averaged over the run, due to problems with the accelerator, for example, when Tevatron magnets quenched. This is in comparison to the short E731 run, when the accelerator delivered $\sim 75\%$ of the requested intensity, averaged over that month. Also, E799 spent a much larger fraction of time calibrating the calorimeter and testing new calorimeter materials than did E731, which resulted in a loss of 30% of the available beam. This is in comparison with the one-month E731 run, which lost only $\sim 10\%$ of the available running-time to special calibration runs. Putting all these factors together, the overall decrease in $K_L$ flux was roughly a factor of five.

The final $\pi^0 e^+ e^-$ acceptance in E799 was 2.2%, a factor of 4.5 lower than the proposed acceptance of 10%. There are many reasons for this decrease, the three largest being the loss of the beam-hole calorimeters, accidental activity, and the increased trigger thresholds. As was shown in table 11, the accidental veto rates were prohibitively high when the calorimeters were in the beams. Moreover, the $BaF_2$ calorimeter was not resistant enough to radiation damage to be used in this capacity in the first place. The loss of the beam-hole calorimeters translated into an acceptance loss of a factor of two. The acceptance also decreased by about a factor of two from accidental activity. One example of this loss is the fact that 13% of accidental events had an extra HCF-selected cluster, which, if added to a real signal event where all particles reached the lead-glass, would cause the event to be rejected at trigger level. Similarly, 7% of accidental events had at least one (x) or (y) track. When added to a real decay, these tracks would cause the event to be rejected when the analysis cut on tracks was made. Finally, there was also a $\sim 30\%$ loss in acceptance due to a higher lead-glass energy thresholds in both the Hardware Cluster Finder, and the total energy trigger. Both these thresholds had to be higher than anticipated to reduce the trigger rate.

Table 32 lists the differences in sensitivity between the actual experiment and the pro-

Table 32. $\pi^0 e^+ e^-$ Sensitivity Losses compared to Proposal

| Improvement | Sensitivity Loss |
|---|---|
| Flux Losses: | |
| Proton intensity: $1.3 \times 10^{12}$ protons per spill | 1.5 |
| Tevatron Performance | 1.3 |
| Detector Downtime | 1.25 |
| Data Acquisition Dead-time | 2.0 |
| Acceptance Losses: | |
| No Beam-holes | 2.0 |
| Increased trigger thresholds | 1.3 |
| $\Sigma_{cos}^1 \times \Sigma_{cos}^2$ Cut to remove $K_{e3}$ background | 1.18 |
| Accidental Activity: | |
| Hadron Shower Veto | 1.22 |
| Photon Vetoes | 1.16 |
| Back Anti Veto | 1.06 |
| Accidental HCF clusters | 1.15 |
| Accidental drift chamber tracks | 1.07 |
| Total | 27 |

posal, including estimates for a few specific contributions from accidental activity, and one analysis cut which was not included in the proposal (the cut to remove $K_{e3}$ decays). The effects in this table account for most of the difference in sensitivity. After considering only those losses listed in table 32, one would expect that the E799 sensitivity would be a factor of 27 worse than the most optimistic sensitivity calculated, or a factor of 7.8 worse than the proposed sensitivity. The overall decrease measured is a factor of 9 worse than the proposal.

The obvious way to improve a rare decay search is to increase the flux of the decaying particle. But as has been shown here, there are many details which must be taken into consideration, before simply increasing beam intensity and removing absorbers from the

beam. The data acquisition system must be able to withstand the challenge of a much-increased trigger rate, not only because there will be more real decays, but because there will be more accidental activity which can fake real decays. Future experiments cannot place too much attention on the issues of accidental rate reduction and data acquisition. While this experiment would have also benefited from improved electron/pion rejection, as can be seen in table 32 much larger losses were imposed by dead-time and accidental activity vetoing the events, than the 15% loss due to the cut designed to remove the $K_{e3}$ background.

## 12.2 $K_L \to \pi^0 \mu^+ \mu^-$ Sensitivity

There were 49624 $K_L \to \pi^+ \pi^- \pi^0$ events collected in the Minimum Bias trigger. Using the Monte Carlo simulation we determine the acceptance for the decay $K_L \to \pi^+ \pi^- \pi^0$ to be 4.26%, and for $K_L \to \pi^0 \mu^+ \mu^-$ to be $1.4 \pm 0.1\%$, where the $K_L \to \pi^0 \mu^+ \mu^-$ decay was generated with a phase-space distribution. For both decay modes the acceptances quoted are for $K_L$'s with a momentum between $20\,GeV/c$ and $220\,GeV/c$ and which decayed between $90\,m$ and $160\,m$ downstream of the target. The single event sensitivity for the decay $K_L \to \pi^0 \mu^+ \mu^-$ is therefore: $(2.2 \pm 0.01(\text{stat}) \pm 0.2(\text{syst})) \times 10^{-9}$. There were no $\pi^0 \mu^+ \mu^-$ candidates remaining in the data sample after all cuts were made. The 90% confidence level upper limit is therefore

$$B(K_L \to \pi^0 \mu^+ \mu^-) < 5.1 \times 10^{-9},$$

which incorporates the statistical and systematic uncertainties (see section A). This is an improvement of over a factor of 200 from the previous most sensitive search for this mode. After comparison of the final data plot for the $\pi^0 \mu^+ \mu^-$ mode with that of the $\pi^0 e^+ e^-$ mode, it can safely be asserted that the search for $K_L \to \pi^0 \mu^+ \mu^-$ has significantly less background in this experiment than that for $K_L \to \pi^0 e^+ e^-$. While the $\pi^0 \mu^+ \mu^-$ decay is theoretically more complicated since the CP-conserving process is expected to be closer in size to the CP-violating process than for the $\pi^0 e^+ e^-$ decay, it was experimentally a cleaner environment to search for CP-violation. Since the $\mu^+ \mu^- \gamma\gamma$ background to $\pi^0 \mu^+ \mu^-$ searches is expected to be about a factor of two lower relative to the signal than the corresponding background

in the electron mode, this could ultimately be the decay that clarifies the mechanisms of CP-violation. This decay will serve as an important cross-check to the $\pi^0 e^+ e^-$ mode in future searches.

## 12.3 Untangling the Amplitudes

Since there were no events in either data sample after all cuts of course there is no information about the relative sizes of the various amplitudes which contribute to the signal decays. Once several signal events are found, however, it will be important to determine if the signal seen is entirely CP-violating, or if the observed rates are consistent with indirect CP-violation combined with the CP-conserving process. One might speculate as to whether or not the various contributions to the decay $K_L \rightarrow \pi^0 \ell^+ \ell^-$ can ever be untangled, especially given the threat of the radiative Dalitz decay looming on the horizon. In this final section two possible strategies for determining the CP-violating contribution are discussed, given a hypothetical sample of $K_L \rightarrow \pi^0 \ell^+ \ell^-$ events. It should be pointed out that if the observed rate is well above the Standard Model Predictions, then the excess is likely to be due to non-Standard Model directly CP-violating effects, since the CP-conserving and indirectly CP-violating effects are constrained by other measurements. But if CP-violation is completely described by the additional phase $\eta$ in the CKM Matrix, then untangling the amplitudes will require some care. The first method outlined separates the CP-conserving contribution from the CP-violating contribution, and can be used for a sample of $K_L \rightarrow \pi^0 \ell^+ \ell^-$ decays. The second method, while not as powerful for determining the CP-conserving from the CP-violating parts, is the straightforward way to determine the ratio of indirect CP-violation to direct CP-violation, or $\epsilon'/\epsilon_{\pi^0 \ell^+ \ell^-}$.

### 12.3.1 Phase Space Determination

Given that the CP-violating and CP-conserving contributions to the decay $K_L \rightarrow \pi^0 \ell^+ \ell^-$ have very different intermediate states, the region of phase space that each contribution is expected to populate differs as well. For a three body decay, there are two free parameters which define the expected range of phase space. Two possible variables that define all the

parameters of the decay are the $K_L$ center-of-mass energies of the two leptons. However, there many functions of those two variables which can be used to parameterize phase space. If $\mathcal{P}_{K_L}, \mathcal{P}_{\pi^0}, \mathcal{P}_{e^-}$, and $\mathcal{P}_{e^+}$ are the four-vectors of the parent $K_L$, $\pi^0$, the electron, and the positron, respectively, define the variables $s, t_1, t_2$ as:

$$
\begin{aligned}
t_1 &= (\mathcal{P}_{K_L} - \mathcal{P}_{e^+})^2 = m_K^2 + m_e^2 - 2m_K E_{e^+} \\
t_2 &= (\mathcal{P}_{K_L} - \mathcal{P}_{e^-})^2 = m_K^2 + m_e^2 - 2m_K E_{e^-} \\
s &= (\mathcal{P}_{K_L} - \mathcal{P}_{\pi^0})^2 = m_K^2 + m_\pi^2 - 2m_K E_\pi \\
&= m_K^2 + m_\pi^2 + 2m_e^2 - (t_1 + t_2)
\end{aligned}
$$

The decay rates of the two different processes can be expressed as functions of the variables $s$, or $t_1$ and $t_2$. Reference [66] gives the CP-conserving decay rate for $K_L \to \pi^0 e^+ e^-$ as:

$$
\frac{d^2\Gamma_{\text{CP} - \text{conserving}}}{dt_1 dt_2} \sim s \ln^2 \frac{\sqrt{s} + \sqrt{s - 4m_e^2}}{\sqrt{s} - \sqrt{s - 4m_e^2}}.
$$

On the other hand, the electromagnetic penguin is expected to have the following decay rate:

$$
\frac{d^2\Gamma_{\text{CP} - \text{violating}}}{dt_1 dt_2} \sim t_1 t_2 - m_e^2(t_1 + t_2) + m_e^4 - m_K^2 m_\pi^2.
$$

The different parts of the phase space occupied by these two kinds of decays are shown in figures 135 ($\pi^0 e^+ e^-$ mode) and 136 ($\pi^0 \mu^+ \mu^-$ mode). Although the CP-violating and CP-conserving distributions are easily distinguishable, the difference between the two rates is more pronounced in plots of the $s$ distributions of the two different decays. The variable $s$ is equivalent to the square of the $e^+ e^-$ (or $\mu^+ \mu^-$) invariant mass. Figures 137 and 138 show the $s$ distributions for both CP-conserving and CP-violating decays, for both $\pi^0 e^+ e^-$ and $\pi^0 \mu^+ \mu^-$ decays.

Although neither of these methods can distinguish between the direct CP-violating contribution as compared to the indirect CP-violating contribution, since the former is expected to be so much larger than the latter, any sign of CP-violation above the limit imposed by the charged kaon decays would be a sign of direct CP-violation. In the following section we discuss a strategy for untangling the two CP-violating contributions.

Figure 135. The different regions of phase space populated by the two kinds of $\pi^0 e^+ e^-$ amplitudes: a) the two-photon intermediate state (CP-conserving) contribution, and b) the electromagnetic penguin (CP-violating) contribution.
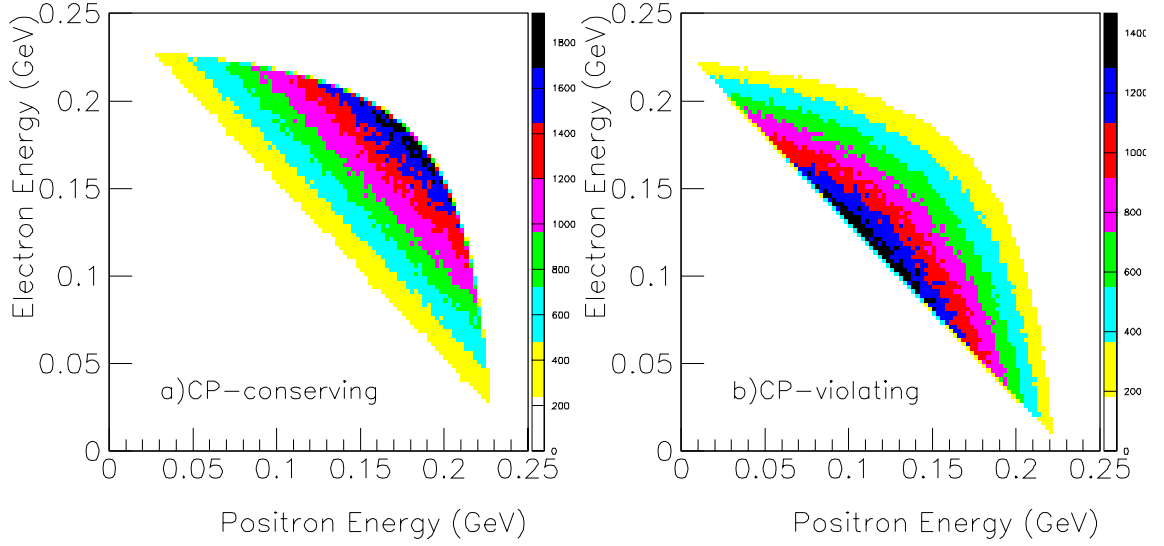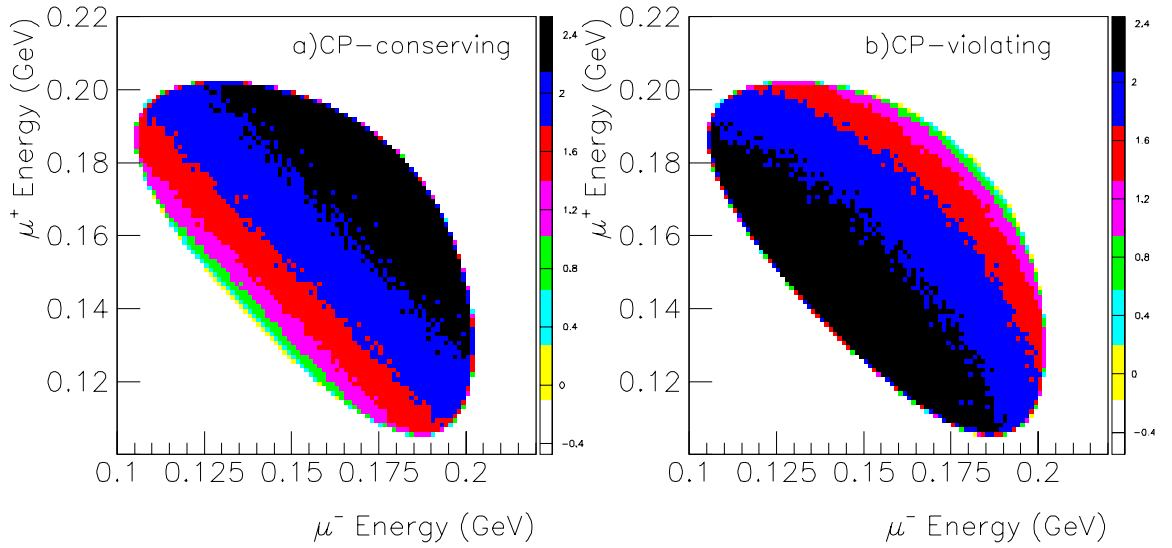


Figure 136. The different regions of phase space populated by the two kinds of $\pi^0 \mu^+ \mu^-$ amplitudes: a) the two-photon intermediate state (CP-conserving) contribution, and b) the electromagnetic penguin (CP-violating) contribution.

Figure 137. The decay distributions as a function of $s$, where $s = m_K^2 + m_\pi^2 - 2m_K E_\pi$, or the square of the $e^+e^-$ invariant mass.

## 12.3.2   Search for $K_{L,S} \to \pi^0 \ell^+ \ell^-$

One strategy which may prove useful is to simultaneously search for both $K_S$ and $K_L$ decays to the states $\pi^0 \ell^+ \ell^-$, much like previous experiments looking for direct CP-violation in the $K \to \pi\pi$ system. Although in E799 the fiducial decay volume began many meters downstream of the target where the kaons were produced, one might imagine a scenario in which one collected $\pi^0 \ell^+ \ell^-$ decays close to the production region, so one could collect both $K_L$ and $K_S$ decays and see the quantum interference effect. Reference [12] describes in detail the correspondence between the observed rates of the decay $K_L \to \pi^0 \ell^+ \ell^-$ and the actual amplitudes of each of the three contributions to $K_L \to \pi^0 \ell^+ \ell^-$. A procedure for using this to extract the direct CP-violating part will be outlined here.

Consider the case where a pure $K^0$ beam is produced by collisions of protons on a target. The $K^0$ is then a superposition of $K_L$ and $K_S$ states, as follows:

$$|K^0 > \quad \sim \quad \frac{1}{\sqrt{2}} \left( e^{-i\mathcal{M}_L \tau} |K_L > + e^{-i\mathcal{M}_S \tau} |K_S > \right)$$
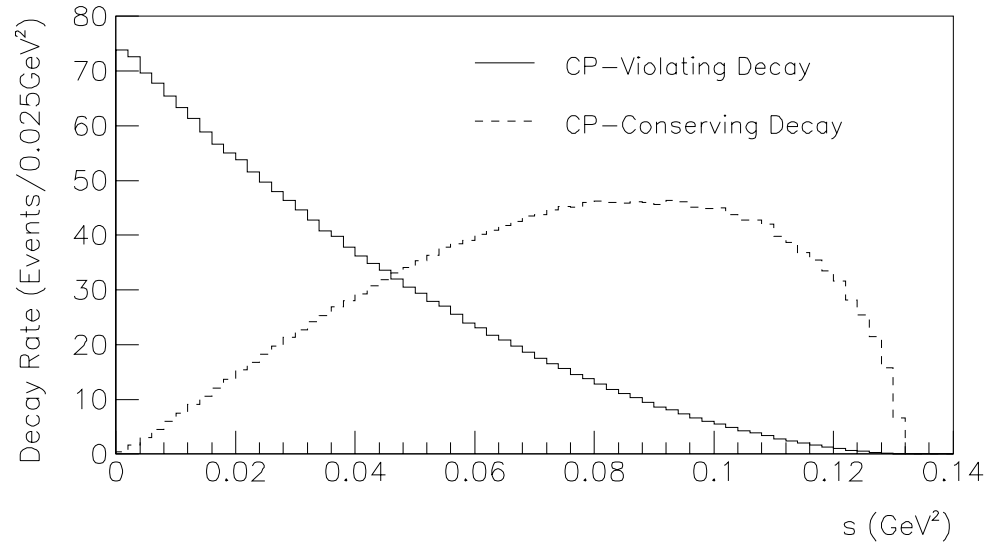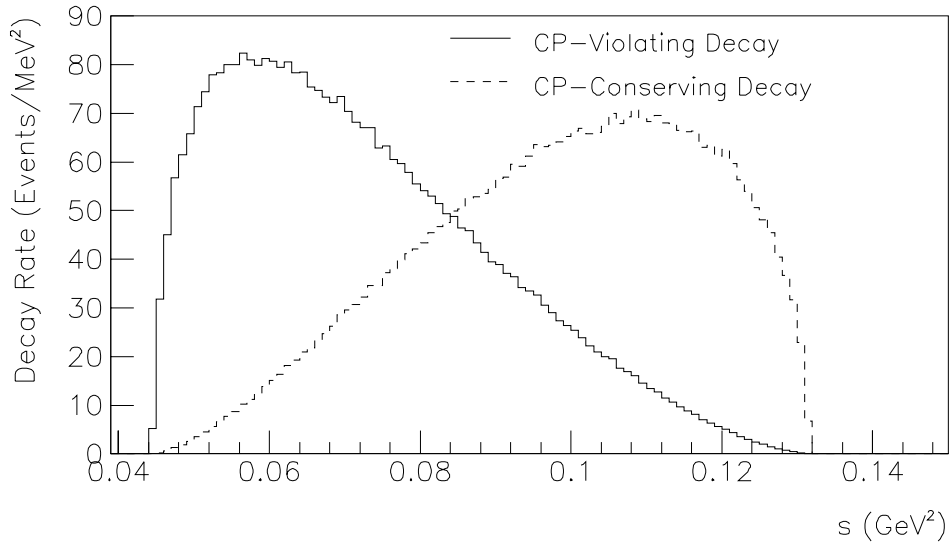


Figure 138. The decay distributions as a function of $s$, where $s = m_K^2 + m_\pi^2 - 2 m_K E_\pi$, or the square of the $\mu^+ \mu^-$ invariant mass.

$$\sim \quad \frac{1}{\sqrt{2}} \left( e^{-i\mathcal{M}_L \tau} (|K_2> + \epsilon |K_1>) + e^{-i\mathcal{M}_S \tau} (|K_1> + \epsilon |K_2>) \right), \text{where}$$

$$\mathcal{M}_L \quad = \quad m_L - i\frac{\Gamma_L}{2}, \text{and}$$

$$\mathcal{M}_S \quad = \quad m_S - i\frac{\Gamma_S}{2}.$$

$m_L, m_S$ are the $K_L$ and $K_S$ masses, respectively, and $\Gamma_L, \Gamma_S$ are the decay rates of the $K_L$ and $K_S$ particles, respectively. Given the definitions

$$A_{1,2} = < \pi^0 e^+ e^- |T| K_{1,2} > \tag{12.1}$$

the decay amplitude can then be expressed as

$$| < \pi^0 e^+ e^- |T| K^0 > |^2 \quad = \quad \frac{1}{2} \left[ |A_2 + \epsilon A_1|^2 e^{-\Gamma_L \tau} + |A_1|^2 e^{-\Gamma_S \tau} \right]$$
$$+ \frac{1}{2} \left[ 2Re(A_1 * A_2 + \epsilon |A_1|^2) e^{-i(M_l - M_s)\tau} \right]$$

The three different proper life-time regions of the above equation give the needed information. The decay rate at low $\tau$ determines the indirect CP-violating contribution to the process $K_L \rightarrow \pi^0 e^+ e^-$. The decay rate at large $\tau$ is due to both the CP-conserving and direct CP-violating contributions. Finally, there is the interference region which would clearly indicate the presence of the phase $\eta$ in the CKM matrix. The direct CP-violating amplitude could then be inferred.

Figure 139 shows the neutral kaon decay rate as a function of proper time for both $\pi^0 e^+ e^-$ and $\pi^0 \mu^+ \mu^-$ final states, and for three different sizes of Direct CP-violating amplitudes. In this plot the $K_2 \rightarrow \pi \ell \ell$ amplitude is defined as follows:

$$A_2 = A_{2\gamma} + i\mathcal{R}|\epsilon|A_1,$$

where $A_{2\gamma}$ (the CP-conserving term) is set at $|\epsilon|$, and $A_1$ and $\mathcal{R}$ are defined as real, which is not necessarily true. The $\pi^0 \mu^+ \mu^-$ decay is expected to have roughly the same size CP-conserving amplitude but a factor of five lower CP-violating contributions. As advertised, the $\pi^0 e^+ e^-$ differences as a function of the size of the CP-violating term are clearly larger than the differences in the $\pi^0 \mu^+ \mu^-$ case. However, one disadvantage in the $\pi^0 e^+ e^-$ decays is that the long-lifetime region is dependent on both the direct CP-violating term as well
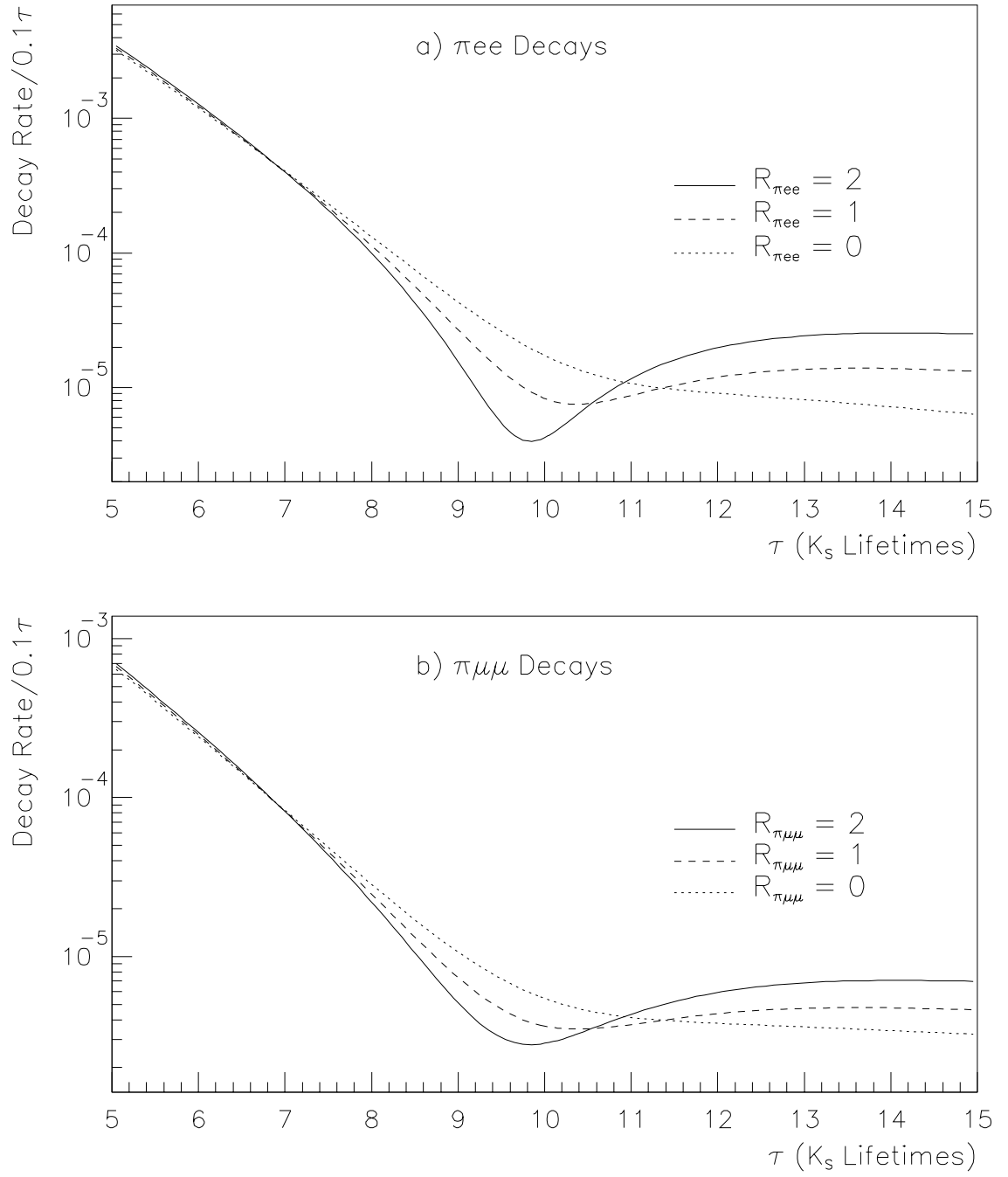
Figure 139. The decay rates of $K \to \pi^0 \ell^+ \ell^-$ as a function of time (arbitrary scale) for three different values of $\mathcal{R}_{\pi^0 \ell^+ \ell^-}$, where $i|\epsilon|\mathcal{R}_{\pi^0 \ell^+ \ell^-}$ is the direct CP-violating contribution to the $K_2 \to \pi^0 \ell^+ \ell^-$ amplitude. Figure a) is the electron mode, figure b) is the muon mode.

as the CP-conserving term, and the $\pi^0\mu^+\mu^-$ decays are less dependent on the direct CP-violating term. As a result, one could presumably use the $\pi^0\mu^+\mu^-$ mode to constrain the CP-conserving piece, and then determine the CP-violating part from the $\pi^0 e^+ e^-$ graph. Conversely, if one had enough events in the long life-time region one can use the phase space techniques outlined in the previous section to determine the relative sizes of the CP-conserving and CP-violating amplitudes.

## 12.4   Conclusion

This experiment has clearly shown that at high energies both the $\pi^0 e^+ e^-$ and the $\pi^0\mu^+\mu^-$ decays of the $K_L$ can be pursued at comparable sensitivities. The branching ratio limits described in this thesis underscore the need to minimize accidental activity when searching for such rare processes. The decays $\pi^0\ell^+\ell^-$ may hopefully someday determine the underlying mechanisms for CP-violation.

# Appendix A

# Upper Limits and Systematic Uncertainties

In this section the method used to determine the 90% confidence level upper limit is discussed, as is the contribution to that limit given a particular uncertainty on the single event sensitivity.

## A.1   Definition of Confidence Level

When the number of events seen $(n)$ is small, Poisson statistics must be used in order to take into account the discreteness of $n$. The Poisson distribution, $f(n; \mu)$, defined as the probability of observing $n$ events when $\mu$ events are expected, has the following value [18]:

$$f(n; \mu) = \frac{\mu^n e^{-\mu}}{n!} \tag{A.1}$$

So, for example, in the search described in this thesis for the decay $K_L \rightarrow \pi^0 e^+ e^-$, there were 2.1 total background events expected, and none seen. The probability of the background fluctuating to 0 is:

$$f(0; 2.1) = \frac{1.8^0 e^{-2.1}}{0!} = e^{-2.1} = 12\% \tag{A.2}$$

The 90% confidence level (CL) limit is defined as the number for which there is a 90% chance that the process one is looking for has a lower branching ratio than that number. For a large number of seen events and predicted background events, the 90% CL limit can be significantly larger than the single event sensitivity. To account for all background processes and errors the 90% CL limits are traditionally given.

If 0 events have been observed, then what remains is to determine $\mu$, the number of events expected, given that the probability of observing less than $\mu$ events is 90%. Another way to determine this is that one must determine the number for which the probability of that number of events fluctuating to 0 is 10%.

$$
\begin{aligned}
f(0; \mu) &= e^{-\mu} \\
&= 0.10 \\
\mu &= \ln(10) \\
&\simeq 2.303
\end{aligned}
$$

Therefore, there is a 90% chance that fewer than 2.3 events are predicted to occur, given that there were 0 events observed. Therefore the single event sensitivity is multiplied by 2.3 for the 90% confidence level limit, if one ignores the error on the single event sensitivity. In the next section we will discuss how the 90% CL limit chances when one considers the systematic error on the single event sensitivity.

## A.2   Determination of Confidence Level including Error

In the case where there are no events seen, the probability of observing $\mu$ events is simply $\exp(-\mu)$. To determine the effect of a Gaussian error on the single event sensitivity, the limit is simply convoluted over all possible numbers of events. Let $\sigma$ be the fractional error on the single event sensitivity. The probability of observing $\mu$ events, assuming there are no events seen, is then [68]:

$$
P_0(\mu) = \frac{\int_0^\infty e^{-\mu x} e^{-\frac{(x-1)^2}{2\sigma^2}} dx}{\int_0^\infty e^{-\frac{(x-1)^2}{2\sigma^2}} dx} \tag{A.3}
$$

By multiplying out the square in the exponent and changing the limits, the above equation becomes:

$$
P_0(\mu) = \frac{\int_0^\infty e^{-\frac{x^2}{2\sigma^2} - (\mu - \frac{1}{2\sigma^2})x - \frac{1}{2\sigma^2}} dx}{\int_0^\infty e^{-\frac{(x-1)^2}{2\sigma^2}} dx} \tag{A.4}
$$

By completing the square in the numerator and changing variables the above equation becomes:

$$P_0(\mu) = e^{-(\frac{\sigma^2}{2}\mu^2 - \mu)} \frac{\int_{-\mu\sigma^2}^{\infty} e^{-\frac{(x'-1)^2}{2\sigma^2}} dx'}{\int_0^{\infty} e^{-\frac{(x-1)^2}{2\sigma^2}} dx} \tag{A.5}$$

where

$$x' = x + \mu\sigma^2 \tag{A.6}$$

Now, assuming the fractional error $\sigma$ is small compared to unity, then one can ignore the value of the extra integral which is added by extending the limits of the integrand from between 0 and $\infty$ to between $-\infty$ and $\infty$. The integrals in the numerator and denominator cancel and for a 90% confidence level limit, one simply solves the following equation for $\mu$:

$$
\begin{aligned}
P_0(\mu) &= e^{-(\frac{\sigma^2}{2}\mu^2 - \mu)} \\
ln(10) &= \frac{\sigma^2}{2}\mu^2 - \mu \\
\mu &= \frac{1 - \sqrt{1 - 2\sigma^2 \ln(10)}}{\sigma^2} \\
&= ln(10)\sqrt{1 + ln(10)\sigma^2}
\end{aligned}
$$

By expanding the square root in powers of $\sigma^2$, and keeping only the first three terms, (ignoring terms of order $\sigma^4$), the equation becomes:

$$
\begin{aligned}
\mu &\simeq \ln(10) + \ln^2(10)\frac{\sigma^2}{2} \\
&= ln(10)\left(1 + \frac{ln(10)}{2}\sigma^2\right) \\
&= 2.303\left(1 + 1.15\sigma^2\right)
\end{aligned}
$$

ignoring terms of order $\sigma^4$. When $\sigma$ is set equal to 0, one recovers equation A.3. For a 10% uncertainty in the single event sensitivity, the 90% confidence level limit increases by 1.15% from the limit with no uncertainty, and for a 20% uncertainty in the single event sensitivity, the limit changes by 4.6%. Equation A.7 can only be used when there are no events observed in the final sample and when the fractional errors on the single event sensitivity are much less than one and Gaussian.

# Appendix B

# Background Level Predictions and Upper Limits

In this section the method of determining an upper limit incorporating the number of background events predicted is discussed. The purpose of this section is to describe how to set a 90% confidence level limit on the signal process, given a predicted number of background events.

## B.1    Definition of Confidence Level

As was mentioned in Appendix A, the 90% confidence level limit on a specific process is defined as the limit for which the probability of the process occurring less than the limit quoted is 90%. When there is no background process, the probability of a certain number of events being seen is based solely on the Poisson probability of the number of signal events being seen. The Poisson probability for $n$ signal events being observed is simply

$$f(n; \mu) = \frac{\mu^n e^{-\mu}}{n!} \tag{B.1}$$

where $\mu$ determines the 90% confidence level limit, if $f(n; \mu)$ is set to 0.10. In the case where there are $n$ events observed, and $\mu_B$ background events predicted, one must again solve for a number of signal events observed, only this time one must include the probability of observing both the signal and background events, and normalize the probability distribution to unity. In other words,

$$f_B(n; \mu, \mu_B) = \frac{\sum_{all\, n';\, n' + n_B = n} f(n', \mu) f(n_B; \mu_B)}{\sum_{n_B = 0}^{n} f(n_b; \mu_B)} \tag{B.2}$$

Since the signal and background are presumed to be uncorrelated, the probability of observing $n'$ signal events multiplied by the probability of observing $n_B$ background events is equal to the probability of observing $n' + n_B$ total events.

$$f_B(n; \mu, \mu_B) = \frac{\sum_{n'=0}^{n} f(n' + n_B; \mu + \mu_B)}{\sum_{n_B=0}^{n} f(n_B; \mu_B)} \tag{B.3}$$

When the numbers $n$, and $\mu_B$ are small, the probabilities are simply the Poisson probabilities:

$$
\begin{aligned}
f_B(n; \mu, \mu_B) &= \frac{\sum_{n'=0}^{n} \frac{(\mu+\mu_B)^{n'} e^{-\mu+\mu_B}}{n'!}}{\sum_{n_B=0}^{n} \frac{\mu_B^{n_B} e^{-\mu_B}}{n_B!}} \\
&= \frac{e^{-\mu+\mu_B} \sum_{n'=0}^{n} \frac{(\mu+\mu_B)^{n}}{n!}}{e^{-\mu_B} \sum_{n_B=0}^{n} \frac{\mu_B^{n_B}}{n_B!}}
\end{aligned}
$$

For a 90% confidence level limit, set $f(n; \mu, \mu_B)$ equal to 0.10, set n equal to the number of events observed, and $\mu_B$ equal to the number of events predicted, and solve for $\mu$. In the case where the number of events observed is non-zero, the equation must be solved for $\mu$ analytically. However, in the case where there are no events seen, the sums in the above expression are simply unity. The factor $\exp(-\mu_B)$ cancels in the numerator and the denominator and the expression is simply:

$$f_B(n = 0; \mu, \mu_B) = e^{-\mu} \tag{B.4}$$

as is the case for no background events predicted. In other words, if there are no events seen in the final signal sample, then the upper limit does not depend on the number of background events predicted. Of course, if the number of background events predicted is many more than 0, then the background prediction might be suspect, but this does not directly effect the prescription for determining the 90% confidence level limit.

# REFERENCES

[1] K.S. McFarland, phd thesis, Univerisity of Chicago, November 1993

[2] D. Roberts, phd thesis, Univerisity of California, Los Angeles, 1993, November

[3] M. Weaver, phd thesis, Univerisity of California, Los Angeles, 1994, June

[4] J.R. Patterson, phd thesis, Univerisity of Chicago, 1990, December

[5] V. Papadimitriou, phd thesis, Univerisity of Chicago, 1990, December

[6] L.K. Gibbons, phdthesis, Univerisity of Chicago, 1993, August

[7] B. Schwingenheuer, phd thesis, Univerisity of Chicago, 1994, September

[8] T. Nakaya, phd thesis, Osaka Univerisity, 1995, September

[9] A.J. Malensek, Fermilab, 1981, October, FN-341

[10] R. Ford and W. Nelson, SLAC, 1978, June, UC-32

[11] W. Nelson and H. Hirayama and D.W.O. Rogers, The EGS4 CODE SYSTEM, SLAC, 1985, December, SLAC-265

[12] M. Atiya *et al*, Kaon Physics in the 1990s: Rare Decays and CP Violation, Fermilab, 1989, March, FERMILAB-CONF-89/56

[13] L. Littenberg and G. Valencia, Rare and Radiative Kaon Decays, Fermilab, 1993, March, FERMILAB-Pub-93-004

[14] J. Bartelt *et al* (CLEO Collaboration), Measurement of Charmless Semileptonic Decays of B Mesons, Cornell Lab for Nuclear Studies, 1993, September, CLNS-93-1240

[15] J. S. Hagelin and S. Kelley and T. Tanaka, Supersymmetric Flavor Changing Neutral Currents: Exact Amplitudes and Phenomenological Analysis, Maharishi International University, 1992, September, MIU-THP-92/59

[16] T. Nakaya et al., A Measurement of the Branching Ratio of $K_L \rightarrow e^+ e^- \gamma \gamma$ , Osaka University, 1994, March, OULNS93-09

[17] A. J. Buras and M. E. Lautenbacher and M. Misiak and M. Munz, Direct CP Violation in $K_L \rightarrow \pi^0 e^+ e^-$ Beyond Leading Logarithms, Max Planck Institut fur Physik, 1994, February, MPI-Ph/94-11

[18] Particle Data Group, Review of Particle Properties, Phys. Rev., **D45**, 1992

[19] M. Laval and M. Moszynski and R. Allemand and E. Cormoreche and P. Guinet and R. Odru and J. Vacher, Barium Flouride-Inorganic Scintillator for Subnanosecond Timing, Nuclear Instruments and Methods, **206**, 1983, 169-176

[20] S. Majewski and D. Anderson, Radiation Damage Test of Barium Flouride Scintillator, Nuclear Instruments and Methods, **A241**, 1985, 76-79

[21] E. Murakami et al., Properties of $BaF_2$ Scintillators in Charged Particle Detection, Nuclear Instruments and Methods, **A253**, 1986, 163-165

[22] R. N. Cahn and G. Goldhaber, Experimental Foundations of Particle Physics, Cambridge University Press, 1988

[23] W. Pauli, Neils Bohr and the Development of Physics, Pergamon Press, 1955

[24] J.D. Jackson, Classical Electrodynamics, John Wiley & Sons, 1975, 638-641

[25] J.D. Jackson, Classical Electrodynamics, John Wiley & Sons, 1975, 712-713

[26] M. Lavel *et al*, Nucl. Instr. and Meth. **A241**, 76, 1983

[27] M. Moszynski *et al*, Nucl. Instr. and Meth. **A226**, 534, 1984

[28] L.G. Landsberg, Phys. Rep. **128**, 302, 1985

[29] H. Leutwyler and M. Roos, *Z. Phys.* **C25**, 91, 1984

[30] M. Neubert, Phys. Lett. **B264**, 455, 1991

[31] M. Ciuchini and E. Franco and G. Mareinelli and L. Reina, Phys. Lett. **B301**, 263, 1993

[32] G. Buchalla and A. J. Buras and M. K. Harlander, Nucl. Phys. **B349**, 1-47, 1991

[33] L. Wolfenstein, Phys. Rev. Lett., **51**, 1945, 1983

[34] L. Wolfenstein, Phys. Rev. Lett., **13**, 562, 1964

[35] Ford, Phys. Rev. Lett., **25**, 1370, 1970

[36] P. Krolak et al., Phys. Lett. **B320**, 407, 1994

[37] J.-M. Gerard and T. Nakada, Phys. Lett. **B261**, 474, 1991

[38] J. H. Christenson and J. W. Cronin and V. L. Fitch and R. Turlay, Phys. Rev. Lett. **13**, 138-140, 1964

[39] J. Schwinger, Phys. Rev. **91**, 720-723, 1953

[40] Smith et al. , Phys. Lett. **B234**, 191, 1990

[41] , Steinberg et al., Phys. Rev. Lett. **33**, 41, 1974

[42] Barnes et al., Phys. Lett. **B199**, 147, 1987

[43] L. K. Gibbons et al., Phys. Rev. Lett. **70**, 1203-1206, 1993

[44] G. D. Barr et al., Phys. Lett. **B317**, 233-242, 1993

[45] V. Papadimitriou et al., Phys. Rev. **D44**, 573-576, 1991

[46] G. D. Barr et al., Phys. Lett. **B284**, 440-447, 1992

[47] W. M. Morse et al., Phys. Rev. **D45**, 36-41, 1992

[48] P. Heiliger and L. M. Sehgal, Phys. Rev. **D47**, 4920-4938, 1993

[49] G. Ecker and A. Pich and E. de Rafael, Nucl. Phys. **B291**, 692-719, 1987

[50] J. M. Flynn and L. Randall, Nucl. Phys. **B326**, 31, 1989

[51] J. M. Flynn and L. Randall, Nucl. Phys. **B334**, 580, 1990

[52] C. O. Dib and I. Dunietz and F. J. Gilman, Phys. Rev. **D39**, 2639, 1989

[53] M. I. Dobroliubov and A. Yu. Ignatiev, Mod. Phys. Lett. **A17**, 1677-1682, 1988

[54] C. Alliegro et al, Phys. Rev. Lett. **68**, 278, 1992

[55] G. Donaldson et al, Phys. Rev. **D14**, 2839-2856, 1976

[56] A. S. Carroll et al, Phys. Rev. Lett., **44**, 525-528, 1980

[57] L. K. Gibbons et al, Phys. Rev. Lett., **61**, 2661-2664, 1988

[58] A. Barker et al, Phys. Rev. **D41**, 3546-3547, 1990

[59] L. Littenberg, Phys. Rev. **D39**, 3322, 1989

[60] K. E. Ohl et al, Phys. Rev. Lett., **64**, 2755-2758, 1990

[61] R.H. Dalitz, Proc. Phys. Soc., **A64**, 667, 1951

[62] N.M. Kroll and W. Wada, Phys. Rev. **98**, 1355, 1955

[63] H. Greenlee, Phys. Rev. **D42**, 3724, 1992

[64] G.D. Barr et al., Phys. Lett. **B240**, 283, 1990

[65] G. Donaldson et al., Phys. Rev. **D9**, 2960, 1974

[66] J. F. Donoghue and B. R. Holstein and G. Valencia, Phys. Rev. **D35**, 2769-2775, 1987

[67] J. Bijens and G. Ecker and J. find Gasser, Nucl. Phys. **B9**, 2960, 1974

[68] Robert D. Cousins and Virgil L. Highland, Nucl. Instrum. and Meth. **A320**, 331-335, 1992

[69]  T. D. Lee and C. N. Yang, Phys. Rev., **104**, 254, 1956

[70]  C. S. Wu *et al*, Phys. Rev., **105**, 1413, 1957

[71]  T. D. Lee and R. Oehme and C. N. Yang, Phys. Rev., **106**, 340-345, 1957